Epitaxial Cobalt-Ferrite Thin Films for Room Temperature Spin Filtering

Ana V. Ramos

DOCTORAL THESIS
UNIVERSITE PIERRE ET MARIE CURIE

Ecole Doctorale de Physique et Chimie des Matériaux

Presented by

Ana V. RAMOS

To obtain the degree of

DOCTEUR DE L'UNIVERSITE PIERRE ET MARIE CURIE

Epitaxial Cobalt-Ferrite Thin Films for Room Temperature Spin Filtering

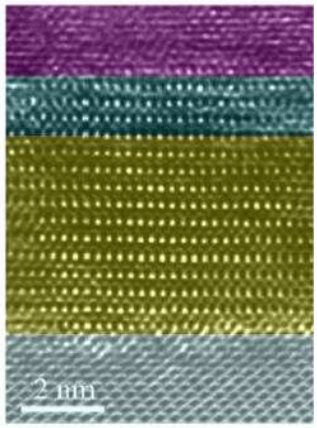

Defended on September 12, 2008

Before the thesis committee :

Mr Albert Fert	President
Mr José Maria De Teresa	Reader
Mr Stéphane Andrieu	Reader
Mr Jagadeesh Moodera	Examinator
Mr Yves Guldner	Examinator
Mme Martine Gautier-Soyer	Thesis director
Mr Jean-Baptiste Moussy	Thesis advisor

ABSTRACT

Remarkable progress in the growth of complex magnetic oxides has sparked renewed interest in physical phenomena traditionally inaccessible at room temperature. One prime example is spin filtering, which can potentially produce highly spin-polarized electron currents by the spin-selective transport of electrons across a magnetic tunnel barrier. Successful spin filtering at room temperature could significantly impact future generations of spin-based device technologies not only because spin-filters may function with 100% efficiency, but because they may be combined with any non-magnetic metallic electrode, thus providing a versatile alternative to half-metals or systems that require coherent spin-polarized tunneling. In this thesis, we present a complete study of the material cobalt ferrite ($CoFe_2O_4$), whose insulating behavior and high Curie temperature (793 K) make it a very good candidate for spin filtering at room temperature. $CoFe_2O_4$ thin films and associated multilayers were grown by oxygen plasma-assisted molecular beam epitaxy. Their structural, chemical and magnetic properties were studied by a number of *in situ* and *ex situ* characterization techniques, as these are known to significantly impact the spin-filter capability of complex magnetic oxides. $CoFe_2O_4$-based spin-filter tunnel junctions were then prepared for spin-polarized tunneling experiments involving either the Meservey-Tedrow technique or tunneling magnetoresistance (TMR) measurements. In the case of the latter experiments, we also payed special attention to the magnetization reversal behavior of the $CoFe_2O_4$ spin-filter barrier and its magnetic counter-electrode (Co or Fe_3O_4), which was a crucial step towards the successful measurement of TMR. In both cases, spin-polarized transport measurements reveal significant spin-polarization of the tunneling current at low temperature, and at room temperature in the case of the TMR. In addition, the TMR ratio follows a unique bias dependence that has been theoretically predicted to be the signature of spin filtering in magnetic tunnel barriers. We therefore show that $CoFe_2O_4$ tunnel barriers provide a model system to investigate spin filtering in a wide range of temperatures.

RESUME

Les progrès remarquables réalisés dans la croissance des oxydes magnétiques complexes ont suscité un regain d'intérêt pour l'étude des phénomènes physiques traditionnellement inaccessibles à température ambiante. Un parfait exemple est le filtrage de spin, qui permet de générer des courants d'électrons fortement polarisés en spin grâce au transport sélectif des électrons à travers une barrière tunnel magnétique. L'observation du filtrage de spin à température ambiante pourrait avoir un impact important sur les générations futures des dispositifs pour l'électronique de spin non seulement parce que les filtres à spin peuvent avoir une efficacité de 100%, mais aussi parce qu'ils peuvent être combinés avec une électrode métallique, constituant ainsi une alternative à l'utilisation des électrodes démi-métalliques ou aux systèmes nécessitant un transport tunnel cohérent. Dans cette thèse, nous présentons une étude approfondie du matériau ferrite de cobalt ($CoFe_2O_4$), dont le caractère isolant et la température de Curie élevée (793 K) en font un très bon candidat pour le filtrage de spin à température ambiante. L'élaboration des couches minces de $CoFe_2O_4$ et des multicouches associées a été réalisée par épitaxie par jets moléculaires assistée par plasma d'oxygène. Les propriétés structurales, chimiques et magnétiques ayant un effet déterminant sur l'efficacité du filtrage de spin, celles-ci ont été étudiées par plusieurs méthodes de caractérisation *in situ* et *ex situ*. Des jonctions tunnel à base du filtre à spin $CoFe_2O_4$ ont ensuite été préparées pour des mesures de transport tunnel polarisé en spin, soit par la méthode de Meservey-Tedrow, soit par des mesures de magnétorésistance tunnel (TMR). Dans ce dernier cas, nous avons porté une attention particulière au retournement magnétique de la barrière tunnel de $CoFe_2O_4$ et de la contre électrode magnétique (Co ou Fe_3O_4), une étape cruciale avant toute mesure de TMR. Dans les deux cas, les mesures de transport tunnel polarisé en spin ont révélé des polarisations significatives du courant tunnel à basse température, et à température ambiante pour les mesures de TMR. Par ailleurs, nous avons trouvé une dépendance unique entre la TMR et la tension appliquée qui reproduit celle prédite théoriquement pour les barrières tunnel magnétiques. Nous démontrons ainsi que les barrières tunnel de $CoFe_2O_4$ constituent un système modèle pour étudier le filtrage de spin dans une large gamme de températures.

ACKNOWLEDGEMENTS

First and foremost, I would like to begin by acknowledging the members of my thesis committee : Albert Fert, Jagadeesh Moodera, Yves Guldner, Jose Maria De Teresa and Stéphane Andrieu. I thank them for taking the time out of their exceedingly busy schedules to read this manuscript and participate in the thesis defense. I am especially grateful to those who traveled from abroad in order to be present at the defense.

Next, my heart-felt thanks go to all the colleagues, friends and family who contributed to the realization of this project. Without their support—whether scientific, administrative or loving—my thesis would not have been the extraordinary experience that it was. The list is long, but every single person deserves recognition...

Martine Gautier-Soyer, my thesis director. For her trust, friendship and support over the past 5 years. For introducing me to Picard. For helping me grow as a scientist, as a professional and as a person. And especially for the immense opportunities that she opened for me.

Jean-Baptiste Moussy, my supervisor and most dedicated colleague. For his constant encouragement and loyalty, and for the hours of shared enthusiasm and frustration. For the rides to Paris in the "JB-mobile."

Marie-Jo Guittet, whose exceptional role can not be explained in just a few words. For the beautiful samples that she taught me to realize, for the endless hours of discussion beside the MBE, for the invigorating afternoon walks, for her gateau au chocolat and her *exceptional* canelés. And especially for never leaving my side in the most difficult times, like only a mother would do...

All of the members of the "Groupe Oxydes" : Hélène Magnan, Antoine Barbier, Odile Bezencenet, Sylvia Matzen. For making the day to day work life that much more lively.

Elisabeth Bouchaud and Serge Palacin, the directors of the SPCSI. For providing me with the opportunity to do my thesis research in their laboratory, and for the remarkably generous support in complicated situations.

Christophe Gatel, my closest collaborator and loyal friend. For the long hours spent beside the TEM not seeing the light of day, for the intense discussions about $CoFe_2O_4$, antiphase boundaries, exchange coupling... For so generously housing me on each of my trips to Grenoble, for teaching me how to make crêpes. And most importantly, for always listening when I needed to talk and constantly offering the right advice.

Frédéric Ott and Michel Viret. For the polarized neutron reflectivity measurements and for the fervent discussions about the exchange coupling mechanism in the $CoFe_2O_4/Fe_3O_4$ bilayers.

Pascale Bayle-Guillemaud. For so generously hosting me in her laboratory on numerous occasions.

Bénédicte Warot-Fonrose and Etienne Snoeck. For the fruitful collaboration with the TEM and EELS studies.

Richard Mattana, Cyrile Deranlot and Frédéric Petroff. For the time dedicated to the preparation and pattering of my samples, for the exciting TMR experiments, and for the valuable transfer of knowledge on spin-polarized tunneling.

Cristian Mocuta and Stefan Stanescu. For giving me the opportunity to share the ESRF experience.

Jagadeesh Moodera, my adoptive thesis advisor and collaborator. For so openly welcoming me as a part of his group, and for being such a generous host. For providing me with numerous great opportunities both in his lab and beyond, for introducing me to his most important colleagues, for dragging me around with him for entire week-long conferences, for the long hours of discussion and brainstorming, and most importantly, for being so understanding when external elements perturbed my ability to work.

Tiffany Santos, my fellow spin filter expert, role model and close friend. For the countless hours spent loading system 3, connecting samples, pumping down on the ^{3}He bath... For giving so much of her valuable time to my experiments, especially having her own thesis to manage. For being my

conference buddy, for sharing life stories, and for simply being such an encouraging friend.

Guoxing Miao, my role model for hard work and determination. For so eagerly accepting to help with my experiments, and for allowing me to participate in his. For being an excellent teacher, and for his persistent sense of humor and positive attitude despite the incalculable hours spent in lab.

The rest of the Moodera crew : Jenny, Karthik, Marius, Martina. For the unforgettable times at MMM, at the APS and at coffee break.

Markus Münzenberg and Georg Müller. For the pleasure of collaborating long distance on a beautiful piece of scientific work.

Igor Mazin. For the extremely valuable discussion regarding the spin polarization in our SPT measurements.

Mairbek Chshiev. For showing such enthusiasm and interest in my work and for the long discussions comparing our experimental and theoretical methods. And especially for being a honest and caring friend.

Craig Carter, my professor, long-time mentor, colleague and close friend. For all of the exceptional opportunities that he trusted and provided me with. For his passion for château's in France. For his honest understanding about work and life, and for the priceless advice about the most important decisions... Without him, I would not be where I am today.

April Julich Perez, the MIT-France Program coordinator. For providing me with the generous financial support to collaborate with the Moodera group at the Francis Bitter Magnetic Laboratory, MIT.

My family : My father Jesus, my mother Elena and especially my sister Cecilia. For their love and encouragement throughout my long studies, and for continuously supporting me through all of my life decisions.

Patrick, Julie and Yves, my adoptive family. For their continuous presence in my life, for the marvelous moments shared over dinners, movies, concerts... For their open demonstration of generosity and love.

And finally all of my other friends and loved ones, both in the US and in France. In particular Flo, Périne, Aurore, Umut, Rabee, Cindy, Vanessa,

Sarah S., Nadjia, Sarah W. and Rachel. We have shared joy, anger, laughter, tears, excitement, frustration and most importantly love. Your presence throughout my thesis has helped me maintain the important work-life balance that has made these years some of the most enjoyable ever.

CONTENTS

LIST OF FIGURES

LIST OF TABLES

1. INTRODUCTION

This thesis will study the spin filter effect, which is a phenomenon belonging to the ever-growing field of spin-electronics (or spintronics). In its most simple definition, research in spintronics strives to develop electronic devices that take advantage not only of the charge of the electron, but also its *spin*. The use of this second degree of freedom allows electron currents to be controlled by a magnetic field, which in certain situations provides a advantageous alternative to the more standard electric potential. Today, spin-based technologies include magnetoresistive (MR) read heads in hard disk drives, magnetic field sensors and, most recently, magnetoresistive random access memory (MRAM). Future applications hope to integrate spins into semiconductor technologies such as spin field-effect transistors (spin-FET) and spin light emitting diodes (spin-LED) [1, 2, 3]. Quite obviously, spintronics involves much more than the control of electrons by a magnetic field. There is an extensive number of distinct physical phenomena (magnetic and electronic) to be considered, which in turn must be optimized using the right combination of materials. All it takes is a glance at the periodic table to realize that the possibilities are endless.

This leads to the next important point about spintronics: *Spintronics is also a Materials Science.* We will see throughout this thesis that the optimization of the materials system is crucial to the successful output of a functioning device, and that two seemingly identical systems differing only by one or two material components, may yield completely different results. The beauty of spintronics therefore lies in this interweaving of physics and materials science which leads to discoveries having both fundamental and technological importance.

The field of spintronics was launched by the discovery of Giant Magnetoresistance (GMR) in Fe/Cr multilayer structures by the groups of A. Fert and P. Grünberg in 1988 [4, 5]. This effect was obtained by toggling the Fe layers, separated by Cr spacers, into parallel (P) and antiparallel (AP) magnetic states via manipulation by an external magnetic field. The result, when electric transport measurements were performed, was two distinct resistance states (low, high) corresponding to the respective (P, AP) magnetic

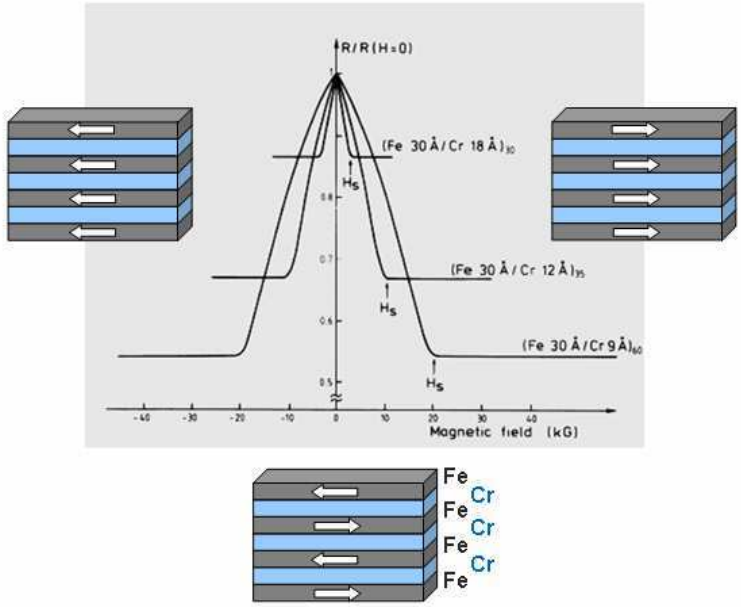

Fig. 1.1: GMR curves of Fe/Cr superlattices measured at 4.2K. The current and applied magnetic field are along the same [110] direction, that is, in the plane of the films [4].

configurations. An example of the first experimental GMR curves is depicted in Figure 1.1. The technological implications of this discovery were immediately recognized by the scientific community: the GMR effect introduced a novel and efficient way of obtaining two clear resistance states corresponding to the (0,1) logic states in a data storage device by simply sweeping an external magnetic field. In fact, within ten years, GMR read heads in hard disks were introduced into the market by IBM, quickly replacing the previous methods of data storage. Thanks to their monumental discovery of the GMR effect, A. Fert and P. Grünberg were recently awarded the 2007 Nobel Prize in Physics.

At the same time that GMR was experiencing its scientific and technological boom, a second magnetoresistive phenomenon known as Tunneling Magnetoresistance (TMR) also began to interest physicists in the field. Even before the experimental demonstration of GMR, theoretical studies by M. Jullière predicted a similar MR effect in magnetic tunnel junctions (MTJs) consisting of two ferromagnetic (FM) electrodes separated by a non-magnetic insulator (I) [6]. In such a FM/I/FM structure, the tunneling current traveling from one FM electrode to the other could also experience two distinct resistance states depending on the relative magnetic configuration of the

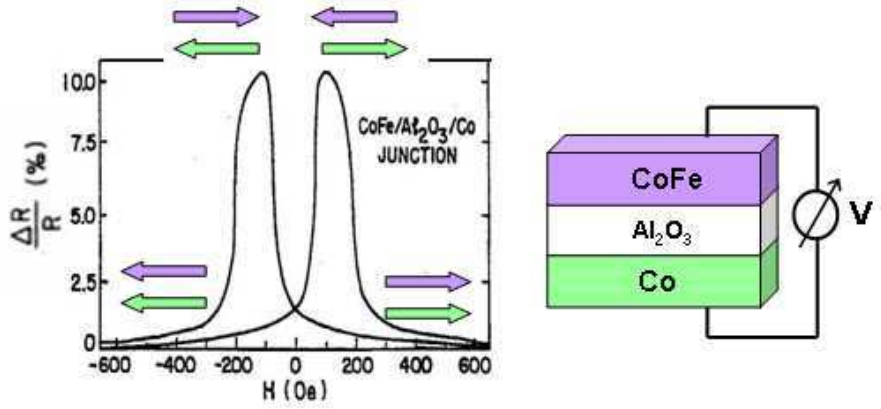

Fig. 1.2: Room temperature TMR in a $Co/Al_2O_3/CoFe$ tunnel junction [7].

electrodes. Jullière's most significant contribution was the development of a simple analytical model that directly related the magnitude of the measured TMR to the spin polarization (P) of the two FM electrodes :

$$TMR = \frac{2P_1P_2}{1 - P_1P_2} \tag{1.1}$$

where P was defined as a function of the density of states of spin-up and spin-down electrons $N_{(\uparrow,\downarrow)}$ at the Fermi level (E_F):

$$P = \frac{N_\uparrow(E_F) - N_\downarrow(E_F)}{N_\uparrow(E_F) + N_\downarrow(E_F)} \tag{1.2}$$

The Jullière model therefore implied that in order to maximize TMR, and consequently the performance of the hypothetical device, all one needed to do was find the ferromagnetic electrodes with the highest possible P at room temperature.

Nearly 20 years after the development of the Jullière model, J. S. Moodera *et al.* demonstrated the first room temperature TMR in MTJs containing two polycrystalline transition metal electrodes (Co, CoFe, NiFe) separated by an amorphous aluminum oxide (Al_2O_x) barrier [7] (see Figure 7.3). The MR values obtained with this system largely surpassed those belonging to the GMR spin valves [8], thus proving the long-awaited interest of TMR. However, it quickly became clear that P values above 50% would be difficult to obtain with the classic FM transition metals, and that a new set of electrode materials needed to be found. Researchers naturally turned to a

family of materials known as *half-metals*, which by definition have only one spin orientation present at the Fermi level, and therefore $P = 100\%$. A few classic examples of half-metals (all of which are also oxides) include CrO_2, $La_{0.7}Sr_{0.3}MnO_3$ and Fe_3O_4. The introduction of complex magnetic oxides into the field of spintronics therefore came as a result of this search for the materials with the highest P.

In the present thesis, we will study yet another complex magnetic oxide: cobalt-ferrite or $CoFe_2O_4$. $CoFe_2O_4$ is not a half-metal, but a ferrimagnetic insulator with a Curie temperature well above 300 K. However, as we will see in the following seven chapters, the combination of $CoFe_2O_4$ with a non-magnetic electrode such as platinum generates a sort of *artificial half-metal*, potentially capable of generating highly spin-polarized electron currents by a phenomenon known as the *spin-filter effect*. The study of spin filtering in $CoFe_2O_4$ tunnel barriers will be presented in this thesis as follows:

1. A first chapter introducing the general context of spintronics, and the important role played by innovative materials in this field of research.

2. A second chapter describing the background of spin-polarized tunneling and the spin filter effect. Cobalt-ferrite will be introduced as a potential candidate for room temperature spin filtering.

3. A third chapter describing the wide range of experimental techniques used throughout this thesis project. These will include techniques for thin film growth, structural and chemical analysis, magnetic measurements, tunnel junction fabrication, and finally spin-polarized transport measurements.

4. A very important fourth chapter covering the in-depth study of the epitaxial growth, chemical and structural properties of our epitaxial $CoFe_2O_4(111)$ tunnel barriers. The successful measurement of spin filtering in our $CoFe_2O_4$ barriers was truly made possible by this careful optimization of the materials properties.

5. A fifth chapter presenting the optimization of the magnetic properties of $CoFe_2O_4$ single layer tunnel barriers, followed by their spin-polarized transport characteristics. Here the spin filter effect in $CoFe_2O_4$ is measured using the Meservey-Tedrow technique.

6. A sixth chapter presenting the first of the two fully epitaxial MTJ systems studied in this thesis : $Pt(111)/CoFe_2O_4(111)/Fe_3O_4(111)$. Chapter 6 will extensively cover the particularly interesting magnetic prop-

erties of $CoFe_2O_4/Fe_3O_4$ bilayers in light of their integration into full MTJs.

7. A seventh chapter presenting the second of our MTJs : $Pt(111)/CoFe_2O_4(111)/\gamma\text{-}Al_2O_3(111)/Co$. Again, the magnetic properties of $CoFe_2O_4/Co$ bilayers will be discussed, followed by a presentation of the TMR measurements. The magneto-transport results will be discussed in detail and compared to those obtained in Chapter 5, as they provide much information about the spin filtering properties of $CoFe_2O_4$.

8. Finally, an eighth chapter concluding the ensemble of results presented in Chapters 4-7. This chapter will finish with a few perspectives for future studies with $CoFe_2O_4$ spin filters.

9. The appendix describes the results of a related side project, in which our knowledge of the growth of epitaxial Al_2O_3 tunnel barriers was applied to the well-known $Co/Al_2O_3/Co$ MTJ. In this study we describe the growth, materials characterization and spin-polarized tunneling properties of epitaxial $Co/\alpha\text{-}Al_2O_3(0001)$ bilayers for the future integration into the fully epitaxial version of the classic MTJ system.

2. SPIN-POLARIZED TUNNELING AND SPIN FILTERING

The following chapter will provide a brief overview of the fundamentals of spin-polarized tunneling (SPT), leading to the discovery of the spin filter effect. Much of the focus will be placed on the different methods used to demonstrate spin filtering, as well as the key examples of spin filter materials. We will finish by introducing cobalt-ferrite as a new candidate for room temperature spin filtering by discussing the ensemble of physical and materials properties at the origin of this effect.

2.1 Spin-Polarized Tunneling

2.1.1 The Basics

Electron tunneling is one of the most widely studied quantum mechanical phenomena, having particular importance in spintronics. In simple terms, it may be described as the attenuation of an electron wave function across a potential barrier such that there is a finite probability of finding the electron on the other side. Electron tunneling is of course only possible through a barrier that is thinner than the decay length of the electron wave. The most straightforward realization of this scenario is in a metal-insulator-metal (M/I/M) tunnel junction, depicted schematically in Figure 2.1, in which an electron originating from one electrode will "tunnel" to the second electrode when a bias voltage is applied. This applied voltage acts upon the Fermi level of the two electrodes, forcing them out of equilibrium, and thus triggering the flow of a tunneling current from the higher energy electrode to that of lower energy. A detailed description of the historical and theoretical background of electron tunneling may be found in [9].

The simplest model for tunneling based on the scenario pictured in Figure 2.1-a, tells us that the transmission coefficient of an electron of energy E may be expressed as:

$$T(E) \propto exp\left(-\frac{2d}{\hbar}\sqrt{2m(\Phi - E)} \right) \tag{2.1}$$

where d is the barrier thickness, m is the effective mass of the electron

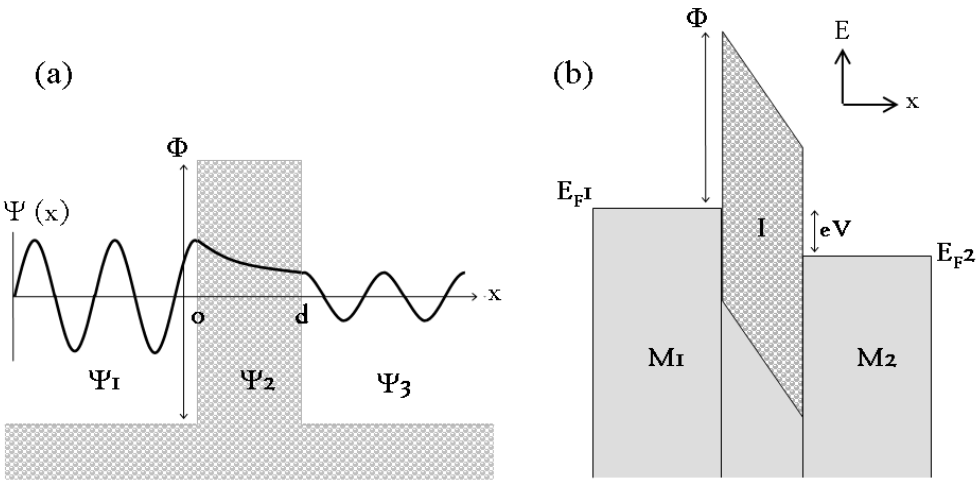

Fig. 2.1: Schematic representation of the tunneling effect depicting (a) the electron wave function traveling from left to right across the potential barrier, and (b) the application of a bias voltage on a M/I/M tunnel junction.

and Φ is the potential barrier. This simple expression already reveals a very important point about the factors governing the electron transmission : the tunneling probability depends *exponentially* on the barrier thickness and on the square root of the potential barrier height. This exponential dependence is one of the keys to spin filtering, as we will see later in this chapter.

A more complete expression for the tunneling current may be derived from the Fermi golden rule which takes into account the density of states (DOS) of each of the two electrodes, $N_{1,2}(E)$, the transmission probability through the barrier, described as the square of a matrix element $|M|^2$, and the probability that the states of the first electrode be occupied and the second electrode be empty, related to the Fermi-Dirac distribution $f(E)$ [10]. The tunneling current from electrode number 1 to electrode number 2 when a bias voltage eV is applied, is therefore given by:

$$I_{1\to 2}(V) = \int_{-\infty}^{+\infty} N_1(E) \cdot N_2(E+eV)|M|^2 f(E)[1-f(E+eV)]dE \quad (2.2)$$

Bardeen further showed that the transmission matrix element $|M|^2$ is in fact independent of E [10]. Assuming that the tunneling current is dominated

by electrons right near the Fermi level (E_F), $f(E) \sim eV\delta(E - E_F)$. After integration, the total tunnel current, $I = I_{1\to2} - I_{2\to1}$, is given by :

$$\frac{I}{V} \propto |M|^2 N_1(E_F) N_2(E_F) \tag{2.3}$$

This reduced expression for the tunneling current was later adopted by Jullière in order to develop his TMR model (see Section 7.2.1).

Another major advancement in tunneling theory was provided by Simmons, who generalized the Bardeen formalism for a $M_1/I/M_2$ structure with dissimilar electrodes [11]. Phenomenologically, this is equivalent to a tunnel junction with a trapezoidal barrier, which Simmons then approximated by an *average* barrier height, $\overline{\varphi}$. Using the Wentzel-Kramers-Brillouin (WKB) approximation to derive the appropriate matrix elements $|M|^2$, he obtained the following equation for the tunneling current density (J):

$$\begin{aligned} J(V) = \frac{J_0}{d^2}\left(\overline{\varphi} - \frac{eV}{2}\right) \exp\left[- Ad\sqrt{\overline{\varphi} - \frac{eV}{2}}\right] \\ - \frac{J_0}{d^2}\left(\overline{\varphi} + \frac{eV}{2}\right) \exp\left[- Ad\sqrt{\overline{\varphi} + \frac{eV}{2}}\right] \end{aligned} \tag{2.4}$$

Simmons also showed that in the tunneling regime, that is for $eV \leq \overline{\varphi}$, Equation 2.4 behaves as

$$J \sim \alpha V + \beta V^3 \ , \tag{2.5}$$

which explains the parabolic shape of the conductance curves ($G \equiv dI/dV$) commonly observed in experiments. Furthermore, the Simmons equation correctly maintains the exponential dependence of J on d and $\sqrt{\overline{\varphi}}$. As a result, Equation 2.4 is widely used to derive *effective* barrier heights and thicknesses from experimental $J(V)$ curves in MTJs and other tunneling systems. We use the term *effective* here because the barrier characteristics felt by the tunneling electrons are often influenced by impurity states or other defects in the barrier.

The major shortcoming of the Simmons model lies in the assumption that the tunneling characteristics are symmetric with applied voltage, whereas the opposite is usually observed when $M_1 \neq M_2$. To overcome this, Brinkmann modified the Simmons model to include an additional parameter $\Delta\varphi$, dubbed the barrier assymetry [12]. Nevertheless, the added complexity and number variable parameters in Brinkmann model render it less reliable when fitting experimental $J(V)$ curves.

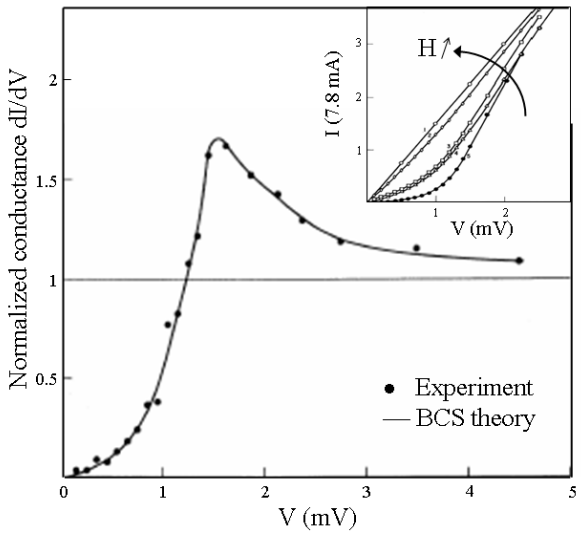

Fig. 2.2: Pioneering tunneling experiments in a $Al/Al_2O_3/Pb$ tunnel junction as measured by Giaever [13]. The dI/dV curve at 1.6K, $\mu_0 H$=0 clearly shows the presence of the BCS energy gap at low V. Inset : I(V) curves for $\mu_0 H$=0 to 0.27T, revealing the SC transition in the Pb layer.

2.1.2 Detecting Spins

Before describing the first experimental demonstration of spin-polarized tunneling, it is important to mention the work of Giaever whose pioneering experiments with metal-insulator-superconductor (M/I/SC) tunnel junctions paved the way for the SPT experiments to follow. Giaever's investigation of the current-voltage ($I(V)$) characteristics of a $Al/Al_2O_3/Pb$ tunnel junction revealed that when the superconducting Pb layer was driven to its normal state via the application of a magnetic field greater than its critical field (H_c), the tunneling $I(V)$ curves went from non-linear to linear [13, 14]. In the superconducting regime, the tunneling current was surprisingly reduced at low V. Further investigation of the conductance ($G(V)$ or $dI/dV(V)$) curves in the SC state revealed a striking resemblance with the Bardeen-Cooper-Schrieffer (BCS) theoretical quasiparticle DOS in a SC (see Figure 2.2). In fact, Giaever showed that these two are proportional, thus providing the first experimental verification of the BCS theory. This remarkable discovery was awarded the Nobel Prize in Physics in 1973.

Giaever's discovery triggered a new wave of theoretical studies attempting to incorporate the role of DOS and many-body effects (found in supercon-

ductors and ferromagnets) into Bardeen's original tunneling model (see for example [15]). While a review of these developments is beyond the scope of this thesis, the important point to retain is that *the tunneling properties of any tunnel junction are dominated by the local DOS at the electrode/barrier interface* [16], where the electrode may be a normal metal or a SC. Tunneling is therefore specific to the *electrode/barrier couple*, and not to the individual bulk properties. For example, tunnel junctions containing the same electrode but different tunnel barriers may behave very differently [17, 18, 19], making the choice of materials for SPT measurements critical.

The first demonstration of SPT was put forward by Meservey and Tedrow in 1970, who extended Giaever's study of the M/I/SC tunnel junction to the case where M is a ferromagnetic metal (FM) [17]. Their original experiments provided the fundamental basis for the field of SPT as we know it today. By analyzing the tunneling characteristics of a FM/I/SC junction, Meservey and Tedrow successfully demonstrated Zeeman splitting in the SC quasiparticle DOS upon the application of an external magnetic field. This effect was recognized by the decomposition of each of the two main peaks in the zero-field dI/dV curve into distinct peaks located at $\pm\mu_B H$ of the main peaks, and corresponding to the spin-up and spin-down quasiparticle states (see Figure A.3). Furthermore, the use of FM Ni as the metallic electrode resulted in Zeeman-split dI/dV curves that were visibly asymmetric—as opposed to those observed for a non-magnetic metal—indicating that the tunneling current was indeed spin-polarized. Meservey and Tedrow's first SPT experiments in an $Ni/Al_2O_3/Al$ tunnel junction are shown in Figure 2.4 [20].

Because the SC DOS is spin dependent in the presence of an applied magnetic field, Meservey and Tedrow showed that the SC electrode plays the role of a *spin detector* that may be used to analyze the polarization of tunneling currents. Al was (and still is) the preferred SC because of its high H_c ~5T, its elevated T_c in the thin film form (T_c = 2-4K), and its long spin lifetime due to low spin-orbit scattering. The spin polarization (P) at the Fermi level of the FM in a FM/I/SC junction may therefore be determined from the extent of asymmetry in the dI/dV curves. A very reasonable estimation is obtained using the following relationship which assumes that the conductance is proportional to $N_1 N_2$:

$$P(E_F) \sim \frac{(\sigma_4 - \sigma_2) - (\sigma_1 - \sigma_3)}{(\sigma_4 - \sigma_2) + (\sigma_1 - \sigma_3)} \tag{2.6}$$

where $\sigma_{1,2,3,4}$ are the relative heights of the four conductance peaks, as shown in Figure A.3-c. A more accurate value of P may be extracted by fitting the dI/dV curves to Maki-Fulde theory which describes the DOS of a SC taking into account the influence of Zeeman splitting, orbital depairing,

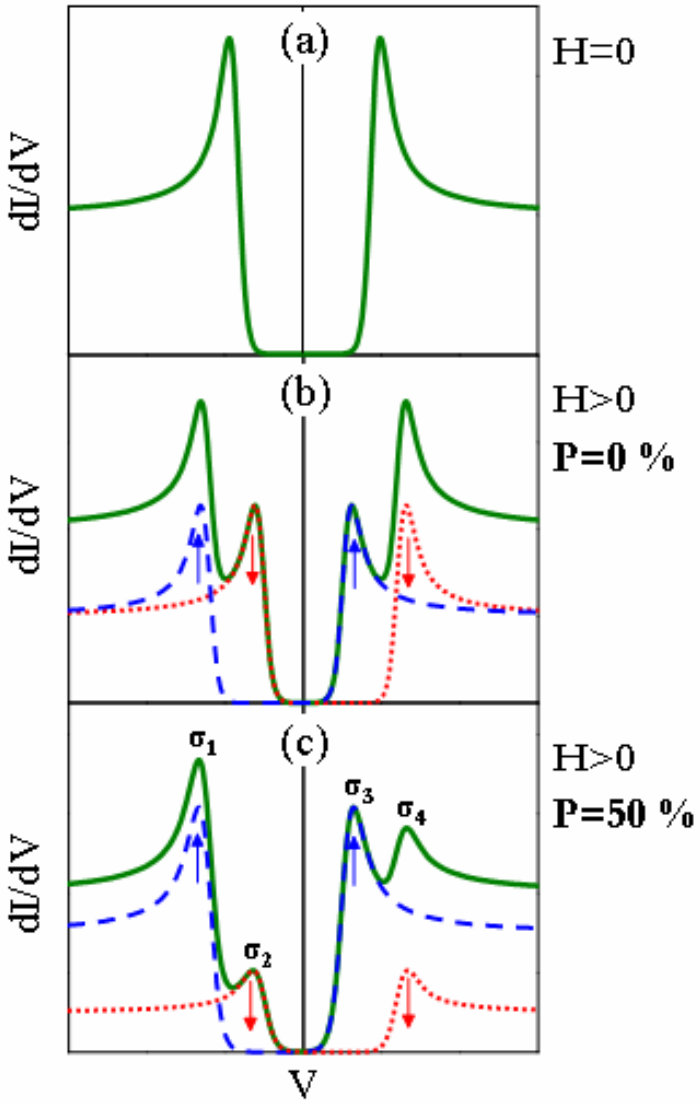

Fig. 2.3: Conductance (dI/dV) curves versus bias voltage for M/I/SC tunnel junctions as measured by the Meservey-Tedrow technique. (a) Zero-field curve representing the SC energy gap centered about $V = 0$. (b) dI/dV in an applied magnetic field showing the Zeeman split DOS. The blue and red dotted lines indicate the deconvolved spin-up and spin-down DOS respectively. The green curve corresponds to the total conductance and is symmetric, indicating that P=0. (c) dI/dV in an applied field when a FM metal is used as the current source. Here, the spin-up DOS is visibly greater than the spin-down DOS resulting in an asymmetric curve and P=50%.

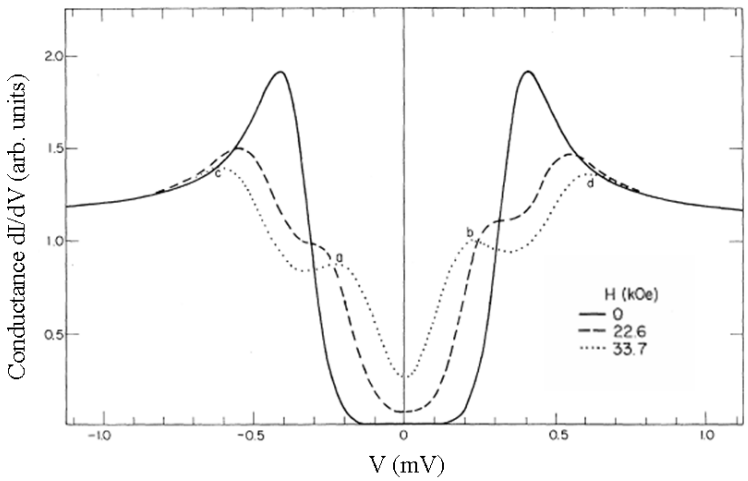

Fig. 2.4: Meservey and Tedrow's first SPT experiment with an $Al/Al_2O_3/Ni$ tunnel junction. The three curves correspond to measurements at $\mu_0 H = 0$, 22.6 and 33.7 kOe. The asymmetry of these dI/dV curves indicate that the tunneling current originating from the Ni electrode is spin-polarized.

spin-orbit coupling and many body effects [21]. The details of this model will not be developed here.

Following the pioneering work with Ni, subsequent SPT measurements with Fe, Co and Gd electrodes yielded similar results, thus proving the effectiveness of the newly-developed Meservey-Tedrow technique [22]. Interestingly, systematic studies of P as a function of the FM layer thickness, t, showed that for t of only $\sim$1 nm, P already attained the bulk value [17]. This introduced the very important issue of interface sensitivity in SPT measurements. Because the tunneling characteristics are governed only by the last few monolayers of FM, the structural and chemical quality of the FM/I interface is crucial to the successful measurement of P.

The most unexpected finding from this series of SPT studies was that, in all cases, P was found to be positive for the $3d$ FM transition metals, suggesting that spin-up electrons dominated the tunneling current. This was in contradiction with the well established electronic band structure calculations [23] predicting that the spin-down d bands were the most prominent at the Fermi level. This controversial result sparked a doubt about the interpretation of P : *How does one precisely define the TUNNELING spin polarization?*

Because Equation 1.2 clearly did not suffice, a more precise definition of P was adopted in the case of a tunneling current:

$$P = \frac{N_{\uparrow}(E_F)|M_{\uparrow}|^2 - N_{\downarrow}(E_F)|M_{\downarrow}|^2}{N_{\uparrow}(E_F)|M_{\uparrow}|^2 + N_{\downarrow}(E_F)|M_{\downarrow}|^2} \tag{2.7}$$

This revised definition of P takes into consideration, not only the spin-dependent DOS as the Fermi level, but also quite naturally the spin-dependent matrix elements governing the electron transmission across the tunnel barrier.

A very good definition of the tunneling P based on Equation 2.7 is that given by Mazin, in which the square of the Fermi velocity, v^2, is the most important element to consider in $|M_{\uparrow,\downarrow}|^2$ [24]. According to Mazin, it is the electrons with an effective mass, m_e^*, closest to that of a free electron, that are most mobile (i.e. highest v^2) and that will therefore dominate the tunneling current. In the case of the $3d$ ferromagnets, these "itinerant electrons" are generally attributed to *sp–d* hybridized bands at the FM/I interface. Similarly, electrons that are highly localized, as are the majority of the spin-down d electrons in the $3d$ ferromagnets, will be highly suppressed in the tunneling current. Mazin's treatment of P encompasses most of the elements of $|M_{\uparrow,\downarrow}|^2$, used individually in previous attempts to redefine P, into one straightforward definition. These include m_e^*, first considered by Stearns [25], and the importance of interface bonding, brought forth by Tsymbal and Pettifor [26]. While all of these studies emphasize the importance of the choice of the tunnel barrier in FM/I/SC junctions, which by modifying the band structure at the FM/I interface significantly affects the different electron mobilities, none address the possibility of effects generated by the choice of SC spin detector. We will see later in this thesis, that the SC electrode may in fact also have an influence on the tunneling properties observed by the Meservey-Tedrow technique.

2.1.3 Tunneling Magnetoresistance

Shortly after Meservey and Tedrow introduced the phenomenon of SPT in FM/I/SC tunnel junctions, Jullière proposed a model explaining the magneto-transport properties of the magnetic tunnel junction (MTJ)—that is, a tunnel junction in which both electrodes are FM metals [6]. Rather than using the BCS DOS of a SC electrode to analyze the spin-polarized tunnel current, Jullière considered the effect that the relative magnetization of the two FM electrodes could have on the tunnel current traveling between them. Jullière based his model on the concept of spin conservation, which implies that *tunneling can only occur between bands of the same spin orientation* on either

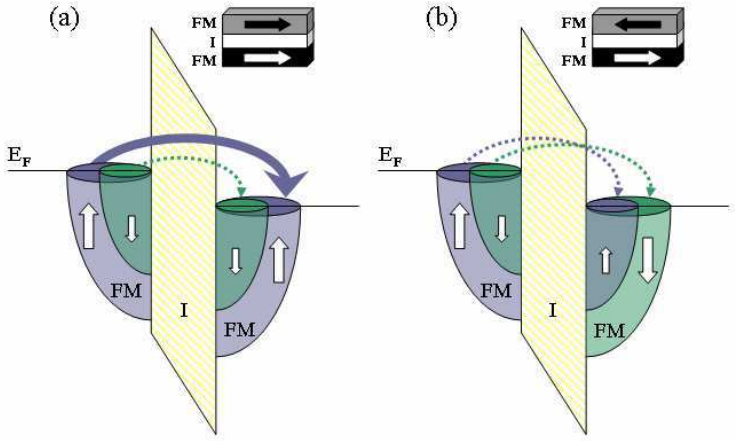

Fig. 2.5: Schematic representation of TMR in a magnetic tunnel junction. (a) In the parallel magnetic state, the majority spins tunnel readily from one FM electrode to the other leading to a low resistance state. (b) In the antiparallel configuration, neither majority not minority spins tunnel easily, and the resistance is high.

side of the barrier.

Without going further into the theory of the Jullière formalism, one can already begin to understand phenomenologically what might happen when the relative magnetizations of the two electrodes are switched. For two FM's with the same spin orientation at E_F (i.e. both positively or both negatively polarized), the majority spin-dominated tunneling current will flow freely when the two electrodes are aligned magnetically in parallel (P, not to be confused with spin-polarization). However, in the antiparallel (AP) alignment, the axis of spin quantization is inverted in one of the electrodes, making the number of states in the receiving electrode available to accept the oppositely-polarized electrons originating from the source very limited. Tunneling in the AP configuration will therefore be difficult. This is schematically illustrated in Figure 2.5. In the case of oppositely polarized metals, the resistance states will be reversed.

Assuming that the tunneling probability is independent of spin or magnetization orientation, and that G is proportional to $N_1 N_2$ as in Equation 2.3, Jullière more rigorously showed that the the tunneling conductance in the P and AP magnetic states may be written as:

$$G_P = G^{\uparrow\uparrow} + G^{\downarrow\downarrow} \propto N_1^{\uparrow} N_2^{\uparrow} + N_1^{\downarrow} N_2^{\downarrow} \tag{2.8}$$

$$G_{AP} = G^{\uparrow\downarrow} + G^{\downarrow\uparrow} \propto N_1^{\uparrow} N_2^{\downarrow} + N_1^{\downarrow} N_2^{\uparrow} \tag{2.9}$$

Because $G_P \neq G_{AP}$, the FM/I/FM tunnel junctions must exhibit a magnetoresistance, known as tunneling magnetoresistance (TMR), that is defined as the normalized conductance difference between the P and AP magnetic states:

$$TMR \equiv \frac{G_P - G_{AP}}{G_{AP}} = \frac{R_{AP} - R_P}{R_P} \tag{2.10}$$

The second definition of TMR in terms of the resistances R_P and R_{AP} is often preferred by experimentalists who, in their TMR measurements, obtain a direct measure of these values. We note that this definition of TMR results in a *negative* value when the FM electrodes are oppositely polarized.

Finally, by combining Equations 2.7, 2.8 and 2.9, Jullière obtained his well-known formula for the TMR in a MTJ with different FM electrodes:

$$TMR = \frac{2P_1P_2}{1 - P_1P_2} \tag{2.11}$$

where P_1 and P_2 are the spin polarizations of the two electrodes taking into account the transmission probability given by the matrix elements $|M_{\uparrow,\downarrow}|^2$.

The Jullière model must of course be used with caution, as it makes some assumptions that in reality over-simplify the physics of the MTJ. In particular, it ignores the influence of interface bonding effects on the matrix elements that govern the transmission of the different tunneling electrons, as was discussed in Section 8.1.3. A more accurate TMR model proposed by Slonczewski further considers the influence of the internal exchange field in each of the FM electrodes on the spin-dependent potential barrier felt by the tunneling electrons [27]. This model therefore includes the presence of interfaces on either side of the tunnel barrier that themselves contribute to P. Nevertheless, Equation 2.11 can be very helpful for predicting or analyzing the magnitude of the TMR in systems where the polarization of at least one of the electrodes is known. It is particularly successful with junctions containing transition metal electrodes and Al_2O_3 tunnel barriers.

As was mentioned in Chapter 1, it took nearly 20 years for scientists to confirm Jullière's theory experimentally. This was in part due to the technical difficulties associated with tunneling systems: the electrode/barrier interfaces must be clean and smooth, the barrier must have few defects and no

pinholes, and a patterning method (either by shadow masking or by lithography) must be developed in order to reduce junction dimensions down to the micron scale. Also the magnetic properties of the FM electrodes must be carefully engineered such that two independent switching events are observed, leading to distinct P and AP magnetic states. This is obtained by either choosing two FM electrodes with sufficiently different coercive fields (H_{c1}, H_{c2}), or by blocking one of the electrodes via an exchange coupling with an antiferromagnetic (AF) pinning layer such as CoO [28].

Moodera's successful demonstration of TMR in $Co/Al_2O_3/CoFe$ MTJs [29], depicted in Figure 1.2 of the introductory chapter, launched a tremendous wave of experimental and theoretical investigations on TMR that has yet to settle down today. While a review of the advancements in TMR [30] would be much too extensive to include here, it is worth noting that the highest TMR values currently reported soar above 470% at room temperature and above 800% at 5K [31]. These are obtained in fully epitaxial MTJs containing MgO tunnel barriers and CoFeB electrodes. In fact, the extremely high TMR obtained in this particular epitaxial system is the perfect example of the insufficiency of the Jullière model. High TMR was first predicted theoretically for epitaxial Fe/MgO/Fe MTJs by Butler *et al.* [32]. This phenomenal effect is attributed to the unique band symmetry of the epitaxial Fe/MgO interface which gives rise to a much slower decay for majority states in the barrier than for minority states. The result is a sort of band "filtering" across the MgO barrier (not to be confused with "spin filtering" in Section 2.2) that produces a very highly spin-polarized tunneling current. After some encouraging preliminary results [33, 34], Butler's theoretical prediction of giant TMR in Fe/MgO/Fe was independently confirmed by Yuasa *et al.* [35] and Parkin *et al.* [36] in 2004, and has since improved with the optimization of the materials properties of the electrodes and the Fe(or CoFe, CoFeB)/MgO interface [37].

2.2 Spin Filtering

As we have begun to see in Chapter 1 and Chapter 5.3, the generation of highly spin-polarized electron currents is one of the dominant focusses in the field of spintronics. Applications involving spin injection into semiconductors and other devices such as MTJs and ultra sensitive spin detectors all share the common need to maximize spin-polarization in order to obtain higher efficiency. For this purpose, spin filtering is one very promising phenomenon, both from a fundamental and from a technological stand point, that involves the spin-selective transport of electrons across a *magnetic tunnel barrier*.

This is in contrast to the classic MTJs discussed in Section 7.2.1, in which the tunnel barrier is a standard non-magnetic insulator. Spin filtering at room temperature could potentially impact future generations of spin-based device technologies not only because spin filters may function with 100% efficiency [38], but they can be combined with any non-magnetic metallic electrode, thus providing a versatile alternative to half-metals or fully epitaxial MgO-based tunnel junctions that require a high level of perfection during device fabrication.

2.2.1 Phenomenological Origin

The spin filter effect originates from the exchange splitting of the energy levels in the conduction band of a magnetic insulator. As a consequence, the tunnel barrier heights for spin-up and spin-down electrons, $\Phi_{\uparrow(\downarrow)}$, are not the same, leading to a higher probability of tunneling for one of the two spin orientations [39]. More precisely, $\Phi_\uparrow$ and $\Phi_\downarrow$ will differ by a magnitude of $2\Delta E_{ex}$ (symmetrically about an average barrier height $\overline{\Phi}$), where ΔE_{ex} is the exchange splitting of the first level of the conduction band. Even a modest ΔE_{ex} can lead to very efficient spin filtering thanks to the exponential Φ-dependence of the tunneling current density:

$$J_{\uparrow(\downarrow)} \propto \exp\Big(- \Phi_{\uparrow(\downarrow)}^{1/2} d \Big) \tag{2.12}$$

The spin filter efficiency or "polarization" of the FM tunnel barrier, P_{SF}, may therefore be defined as:

$$P_{SF} = \frac{J_\uparrow - J_\downarrow}{J_\uparrow + J_\downarrow} \tag{2.13}$$

What makes the spin filter unique, is that its efficiency depends on the barrier parameters $\overline{\Phi}$, ΔE_{ex} and d, as opposed to the FM electrode in a classic MTJ where the DOS at the Fermi level largely determines P. The combination of a non-magnetic metallic electrode with a spin filter barrier therefore has the potential generating currents with $P \rightarrow 100\%$, if the barrier parameters are properly optimized. In this ideal case, the result is the creation of an artificial half-metal.

2.2.2 Measurement Techniques

Because the combination of a non-magnetic metal with a spin filter barrier (NM/SF) is analogous to the FM/I bilayer used in classic SPT experiments, spin filters are easily integrated into both magnetic and superconducting tunnel junctions. The spin filter effect may therefore be quantified either

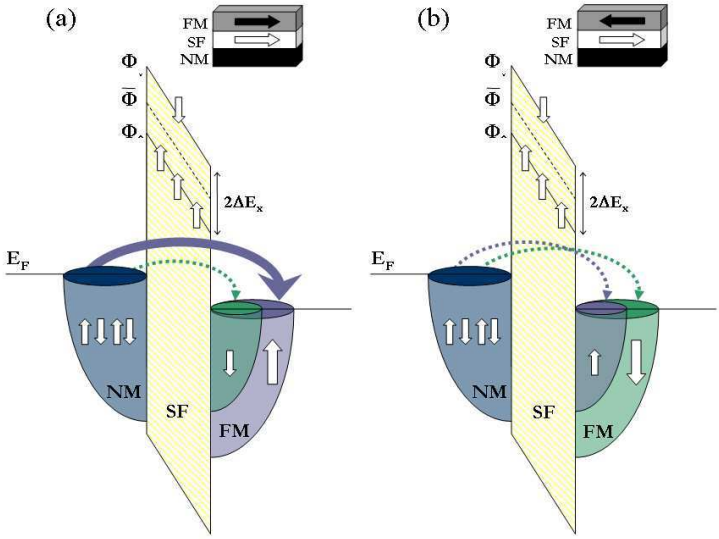

Fig. 2.6: Schematic representation of TMR in a spin filter tunnel junction. In the P configuration (a), spin-up electrons encountering a lower barrier height tunnel freely across the spin filter and are accepted by the large number of available spin-up states in the FM electrode. Conversely, in the AP configuration (b), the FM electrode has few available spin-up states to accept the dominantly spin-up tunneling current.

by TMR measurements or by the Meservey-Tedrow technique, as will be discussed here.

Spin Filter TMR

Analyzing the spin filter efficiency of a FM tunnel barrier using the TMR method requires a tunnel junction structure of the type NM/SF/FM. In this scenario, TMR originates from the relative magnetic orientation of the *spin filter and the FM electrode*. When these have the same spin orientation at E_F, the tunnel current will be high when there is a large number of available spin states in the receiving FM electrode—that is, when the two are magnetically parallel. Similarly, in the AP configuration, tunneling will be scarce and the resistance high. The major advantage of TMR measurements is that they are not limited to low temperature, as in the case for the Meservey-Tedrow technique. These are therefore best suited to study high temperature spin filters.

Because the second FM electrode in a spin filter MTJ serves as the spin detector, it is important to choose a FM metal whose SPT properties are well established. The $3d$ transition metals are therefore a good choice. Using the analogy to the classic MTJ, a reasonable estimate of the spin filter efficiency may be obtained by substituting P_{SF} for P_2 in the Jullière formula:

$$TMR = \frac{\Delta R}{R} = \frac{2P_1 P_{SF}}{1 - P_1 P_{SF}} \tag{2.14}$$

where P_{SF} is defined as in Equation 2.13.

A theoretical description of the spin filter tunnel junction was proposed by Saffarzadeh, who used a free-electron approximation similar to that in the Slonczewski model, but this time with an internal exchange energy inside the SF tunnel barrier [40]. In addition to the basic assumptions of an electron wave vector perpendicular to the interfaces and the conservation of spin during tunneling (i.e. no spin flip), Saffarzadeh also integrated a non-symmetric barrier shape and an effective mass m^* of the electrons into his model. Using the transfer matrix method to numerically calculate the spin-dependent transmission coefficients in the model system Al/EuS/Fe, where EuS is the FM tunnel barrier and Fe the FM electrode, Saffarzadeh revealed a unique property in the NM/SF/FM system : *TMR increases with increasing bias voltage up to a certain value, followed by a decrease for higher biases.* This is graphically represented in Figure 2.7.

This *increasing* TMR(V) dependence is especially interesting because it is the exact opposite of what is observed in conventional MTJs. The intrinsic TMR(V) dependence in conventional MTJs is well known to decrease with increasing V [41] largely due to inelastic magnon excitations in the non-magnetic tunnel barrier [42]. On the other hand, the increasing TMR(V) dependence found in spin filter tunnel junctions may be explained by the spin-split nature of the conduction band in the spin filter, which essentially dominates over magnon effects for a significant range of applied V. Upon the application of sufficient bias, the spin-oriented electrons with the lower Φ (spin-up in the case of EuS) acquire a preferential tunneling pathway across their corresponding conduction band as it nears the Fermi level. This indirect tunneling mechanism is often referred to as Fowler-Nordheim (F-N) tunneling [43]. The result is an increase of their tunneling probability with respect to the opposite spin (spin-down) electrons, and thus an increasing TMR(V) dependence. Eventually, V is high enough that the opposite spin conduction band (spin-down) also approaches E_F. At this point, the TMR ratio attains its maximum and then gradually begins to decrease, assisted eventually by magnon excitations. The increasing TMR(V) dependence first predicted by Saffarzadeh has since been accepted to be the signature of spin filtering in

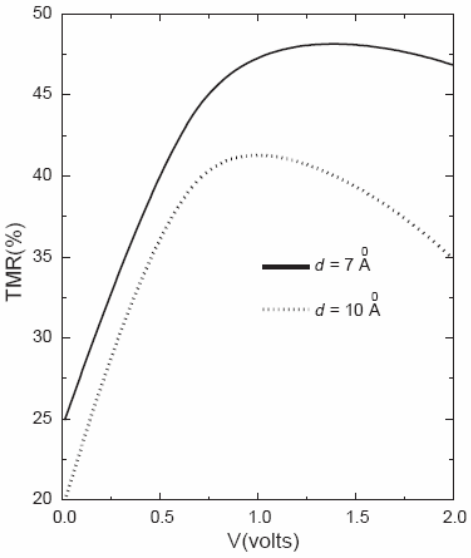

Fig. 2.7: Theoretical TMR versus bias voltage dependence in a Al/EuS/Fe spin filter tunnel junction as calculated by Saffarzadeh [40]. The TMR(V) curves are shown for EuS barrier thicknesses of 7 Å and 10 Å.

MTJs containing a magnetic barrier.

Despite the physical soundness of Saffarzadeh's predictions, the signature increase of the TMR versus V curves was only very recently observed experimentally by Nagahama *et al.* in Al/EuS/Al_2O_3/Co spin filter tunnel junctions [44]. For all of the other known spin filter systems, it is supposed that the spin filter tunnel barriers were not of sufficiently high quality to observe this unique TMR(V) dependence, especially in the case of oxide spin filters (see Section 2.3). In Nagahama's tunnel junctions, the TMR(V) curves are characterized by three tunneling regimes, as may be seen in Figure 2.8-b. The first, starting at zero bias, corresponds to a direct tunneling regime in which both spin-up and spin-down electrons tunnel across the band gap of the EuS barrier. A second tunneling regime appears at ±0.8 V when the bias V is high enough for the spin-up electrons to tunnel via the spin-up conduction band of the EuS barrier. This F-N tunneling regime is characterized by the increasing TMR(V) dependence described above. Finally, when V is so high that the second spin-down conduction band also passes below E_F, F-N tunneling becomes accessible to both spin-up and spin-down electrons, leading to a maximum in the TMR followed by a systematic decrease thereafter. In their analysis of the experimental TMR(V) curves, Nagahama *et al.* went as far as to quantitatively attribute the onset of F-N tunneling at ±0.8

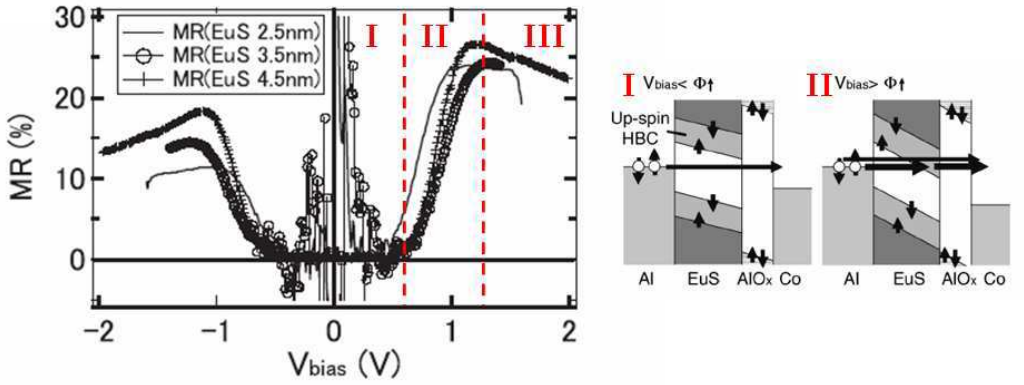

Fig. 2.8: Experimental TMR versus bias voltage curves in Al/EuS/Al_2O_3/Co tunnel junctions with various thicknesses of EuS. The TMR(V) curves may be decomposed into three regimes : I. Direct tunneling across the EuS + Al_2O_3 band gap ; II. Fowler-Nordheim tunneling for only spin-up electrons leading to increasing TMR(V) ; III. Fowler-Nordheim tunneling for both spin-up and spin-down electrons and gradually decreasing TMR(V). From [44].

V to the tunnel barrier height $\Phi_\uparrow$. Furthermore, they compared the extent of the spin-selective F-N tunneling regime (i.e. regime II) to the magnitude of the exchange splitting in the conduction band, although competition between spin filter tunneling and magnon excitations at higher V and leads to an experimental value that is lower than the theoretical exchange splitting determined by band structure calculations. Nagahama's work with EuS spin filter tunnel junctions therefore showed that important information about the spin filter barrier parameters may be extracted directly from the quantitative analysis of experimental TMR(V) curves.

Meservey-Tedrow Technique

The most straightforward measurement of the spin filter efficiency in a FM tunnel barrier remains the Meservey-Tedrow technique, which as described in Section 8.1.3, directly probes the relative density of spin-up and spin-down electrons in the tunneling current produced by the spin filter via the spin-dependent DOS of a SC spin analyzer. From an experimental point of view, the procedure and analysis of a Meservey-Tedrow measurement with a NM/SF/SC tunnel junction is itself identical to that of its FM/I/SC counterpart. Equation 2.6 is therefore used to determine P_{SF} from the experimental

dI/dV curves, as was shown in Figure A.3.

One novel feature that may arise in the case of the NM/SF/SC system is the presence of a significant internal exchange field in the SC electrode due to an exchange interaction with the FM tunnel barrier. This effect is only observed when there is direct contact between the FM layer and SC electrode. As predicted by Sarma [45] and de Gennes [46] in the 1960's, the quasiparticles in the SC electrode may exchange couple with the FM cations in the spin filter barrier by a boundary scattering mechanism at the SF/SC interface (see Figure 2.9-inset). As a result, the SC thin film of thickness, d, effectively feels a uniform exchange field acting only on the electron spins, and not on the electron motion, if d is less than the superconducting coherence length, ξ. This internal exchange field in turn leads to an enhanced Zeeman splitting in the SC quasiparticle DOS, and even the presence of Zeeman splitting at zero applied magnetic field. Figure 2.9 shows an example of the SF/SC exchange interaction in a Au/EuS/Al tunnel junction, where enhanced Zeeman splitting is clearly observed at $\mu_0 H = 0$ T [47]. Another consequence of this field-spin interaction is that the critical field of SC film is prematurely reached upon the application of an external field, as may be seen by the dotted curve in Figure 2.9 corresponding to an applied field of only 0.15 T.

The enhanced Zeeman splitting in the Al superconducting DOS has in fact been observed, not only in EuS, but in all of the europium chalcogenide spin filters : EuS, EuSe and EuO [39, 47, 38, 48]. As we will see in the following section, these strongly ferromagnetic insulators have since paved the way for a growing number of studies involving new materials for spin filtering.

2.3 From Eu Chalcogenides to Complex Magnetic Oxides : The Diverse Spectrum of Spin Filter Materials

2.3.1 Eu Chalcogenides

The *first* spin filter to be revealed by the Meservey-Tedrow technique was EuS [47]; hence the important number of theoretical and experimental studies based on this model material. As explained in the previous section, Moodera *et al.*'s pioneering SPT measurements with Al/EuS/Au tunnel junctions were particularly interesting because they revealed Zeeman splitting in the *zero-field conductance curve*, due to the exchange interaction between the conduction electrons in the SC Al electrode and the strongly ferromagnetic Eu^{2+} cations (μ = 7-8 μ_B). To determine the spin filter efficiency of the EuS

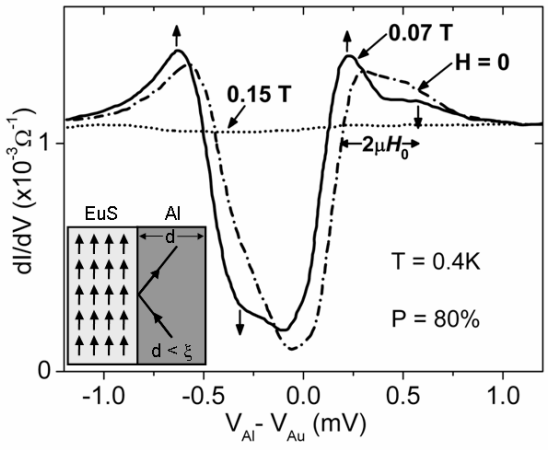

Fig. 2.9: Dynamic conductance versus bias voltage curves in a Au/EuS/Al spin filter tunnel junction, measured by the Meservey-Tedrow technique at various applied magnetic fields [47]. The spin-split quasiparticle DOS in the Al superconductor shows clear signs of an exchange interaction with the EuS layer, as may be seen by the enhanced Zeeman splitting in the 0 T and 0.07 T curves.

barrier, the dI/dV curves in Figure 2.9 were fitted using Maki-Fulde theory [21], yielding a notably large value of $P_{SF} = 80 \pm 5\%$. Also extracted from the 0.07 T curve in Figure 2.9 was the magnitude of the effective magnetic field in the Al layer induced by the EuS, given that the Zeeman splitting is equal to $2\mu_0 H_0$. The result is an effective field $H_0 = 3.46$ T as opposed to the applied field $H_{appl} = 0.07$ T.

Evidence of the spin filter effect in EuS was also identified from the junction resistance, R_j, versus temperature curves. For $T > T_C$, these display the increasing $R_j(T)$ behavior typically found in semiconductors. On the other hand, when $T < T_C$, the lowering of $\Phi_\uparrow$ due to the onset of exchange splitting in the conduction band results in a significant drop in R_j with decreasing T. In fact, R_j decreases as much as 65% with respect to its maximum value at T_c, confirming the significant exchange splitting and P_{SF} expected at low T.

Motivated by the work of Moodera *et. al.*, LeClair *et al.* further proved the spin filtering capacity of EuS via TMR measurements in spin filter MTJs [49]. This work was again of major importance to the development of spin filters, as it was the first to successfully integrate a spin filter barrier into a MTJ. In their Al/EuS(5 nm)/Gd tunnel junctions, LeClair *et al.* measured TMR $\sim 100\%$ at 2K which corresponds to $P_{SF} = 87\%$, in very good

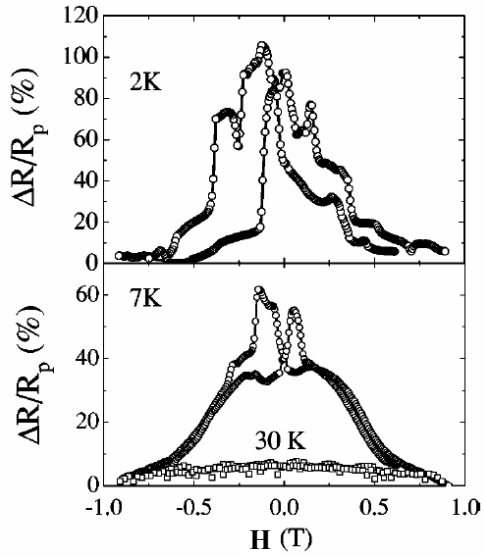

Fig. 2.10: TMR at 2K, 7K and 30K in an Al/EuS/Gd spin filter tunnel junction [49].

agreement with the previous Meservey-Tedrow measurements. A few degrees higher in temperature, TMR decreased significantly, disappearing completely above the T_c of EuS (16K). As may be seen in Figure 2.10, the MR signal contains significant amount of noise which was attributed to instabilities in the EuS magnetization, although this could potentially be due to instabilities in the Gd layer as well (see Figure 2.11-b for EuO below). A possible exchange coupling between the EuS and Gd layers could also explain the observed noise [50].

A close relative of EuS, EuSe was the second Eu chalcogenide to be considered for spin filtering [38]. However, its magnetic properties are quite different from EuS, leading to a spin filtering behavior unique to this material. In fact, EuSe has an interesting magnetic phase diagram that passes from an antiferromagnetic state at zero field to a ferrimagnetic and then ferromagnetic state with increasing H_{appl}. In other words, the application of an external magnetic field induces an exchange splitting in the conduction band of EuSe that increases with increasing H_{appl}. The result is a spin filter whose P_{SF} increases from zero to nearly 100% at $H_{appl} = 1.2$ T. Similarly, R_j in the Ag/EuSe/Al tunnel junctions used to demonstrate spin filtering in EuSe revealed a significant decrease with increasing H_{appl} (rather than with decreasing T), due to the field-induced exchange splitting of the conduction

band.

While both EuS and EuSe have proven to be highly efficient spin filters with model SPT and R_j characteristics, their low magnetic ordering temperatures of 16.6 K (T_C^{EuS}) and 4.6 K (T_N^{EuSe}) are such that spin filtering is only possible in the liquid helium temperature range. In an effort to obtain spin filtering at higher temperature, T. S. Santos and J. S. Moodera took on the task of elaborating an EuO spin filter expected to have a higher T_c (69 K) and greater $2\Delta E_{ex}$ (0.54 eV) [48]. The growth of stoichiometric EuO in the ultra-thin film form, as opposed to the more stable and non-magnetic Eu_2O_3, was a particularly difficult task that required careful interface engineering and optimization of growth conditions. Santos and Moodera showed that the insertion of a 5 nm-thick Y layer in between the EuO barrier and the metallic counter electrode helps stabilize the oxidation of the EuO, leading to optimized SPT characteristics. Figure 2.11-a shows the results of a Meservey-Tedrow measurement in a Al(4.5 nm)/EuO(4.5 nm)/(5 nm)Y/Al(10 nm) junction, revealing spin-split DOS in the Al SC and asymmetry corresponding to $P_{SF} = 29\%$. Again, as was the case with EuS and EuSe, the presence of an exchange interaction at the Al/EuO interface produces Zeeman splitting in the zero field curve. The $R_j(T)$ characteristics of the Al/EuO/Y/Al tunnel junction also show a spectacular drop of two orders of magnitude at T_c.

As a complement to the Meservey-Tedrow experiments, Santos *et al.* also performed TMR experiments in EuO-based MTJs with a Gd counter electrodes [50], analogous to the EuS-based MTJs studied by LeClair *et al.* (See Figure 2.10). In a Cu/EuO/Gd junction, they successfully measured high TMR = 280% at low bias ($V = 40$ mV), confirming the high spin filter efficiency of EuO. This TMR, shown in Figure 2.11-b, displays a gradual increase to a high resistance state due to the gradual switching of Gd, followed by an abrupt drop down to low resistance corresponding to the rapid switching of EuO. Due to the gradual switching and low remanence of Gd, the Gd and EuO layers never attain a fully antiparallel state, thus explaining the pointed shape of the antiparallel resistance peak in the TMR curve, rather than the plateau typically observed in MTJs.

Much like LeClair's Al/EuS/Gd tunnel junctions, the TMR curves of the EuO-based system show evidence of instabilities attributed to the switching of Gd. Significant instabilities were also observed when the bias voltage was varied, making it difficult to study the TMR(V) dependence. Not surprisingly, a closer look at the magnetization ($M(H)$) curves of the EuO/Gd bilayers paired with preliminary polarized neutron reflectivity measurements suggest the presence of an exchange coupling that could very well be responsible for the instabilities and unusual shape of the TMR curves. Nevertheless,

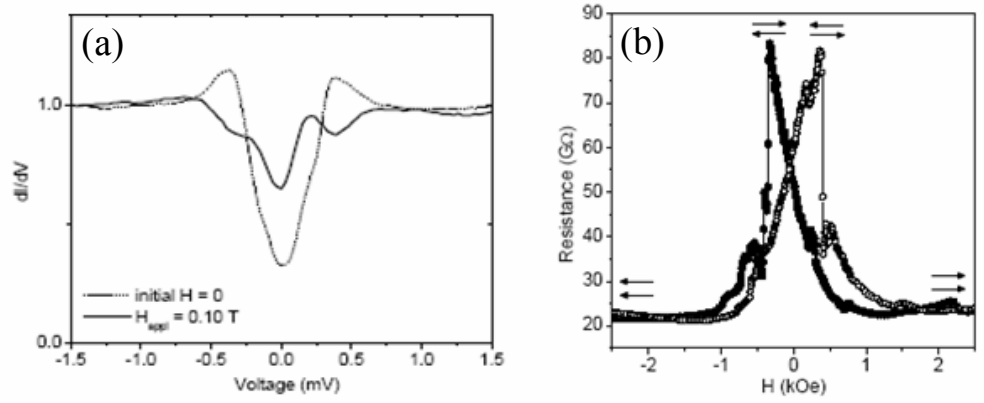

Fig. 2.11: SPT experiments with EuO. (a) dI/dV curves in a Al(4.5 nm)/EuO(4.5 nm)/(5 nm)Y/Al(10 nm) tunnel junction at zero magnetic field and at $H = 0.10$ T. Asymmetric Zeeman splitting is observed both with and without the applied field, revealing the high spin filtering capacity of EuO. (b) TMR in a Cr/Cu(5 nm)/EuO(7.5 nm)/Gd(12 nm)/Al(14 nm) MTJ, yielding a value of 280% at 8 K.

the Cu/EuO/Gd tunnel junctions produce very good results, indicating that the presence of an exchange coupling between the FM barrier and FM electrode in this spin filter MTJ system does not completely depolarized the tunneling current nor suppress the TMR.

2.3.2 Perovskites

Following EuO, the next step towards high temperature spin filtering was naturally to explore the magnetic transition metal oxides. The perovskite $BiMnO_3$ (BMO) was the first of these complex materials to be considered [51]. Its T_c around 100 K provided a potentially significant increase in the temperature range for spin filtering, while the robust nature of this oxide also made it an interesting candidate for spin filter studies. As in the case of EuS and EuO, the spin filter efficiency of BMO was demonstrated using TMR measurements in a $La_{2/3}Sr_{1/3}MnO_3/SrTiO_3/BiMnO_3/Au$ (LSMO/STO/BMO/Au) tunnel junction where the STO ($\sim$1 nm) layer served to decouple the LSMO and BMO magnetic layers. MR measurements for these MTJs showed quite successful results, with TMR values reaching 50% for certain junctions (see Figure 2.12-a). Using the Jullière model with $P_1 = 90\%$ for the LSMO elec-

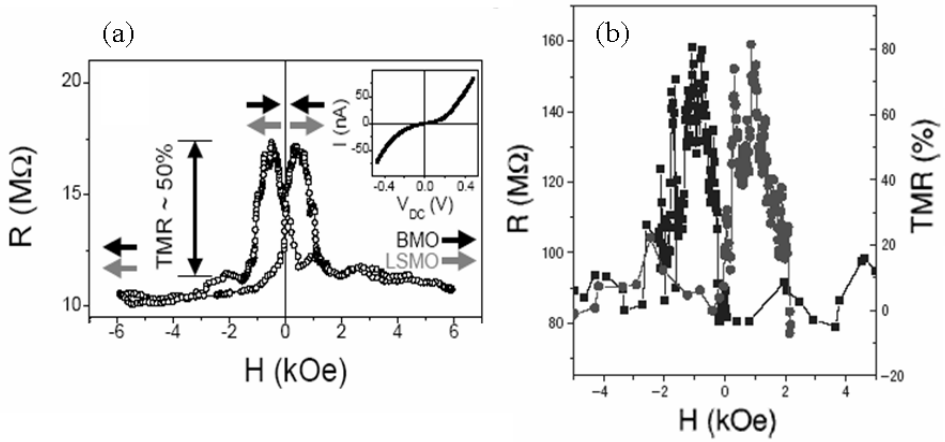

Fig. 2.12: $R(H)$ curves for perovskite-based spin filter tunnel junctions : (a) LSMO(25 nm)/STO(1 nm)/BMO(3.5 nm)/Au measured at 3 K and (b) LSMO(25 nm)/STO(1.6 nm)/LBMO(4 nm)/Au measured at 4 K.

trode [52], a spin filter efficiency value $P_{SF} = 22\%$ was obtained for the BMO layer. The positive sign agrees well with the expected lower barrier height for spin-up electrons.

At higher temperatures still below the bulk T_c of BMO, the TMR value decreased rapidly, completely disappearing above 40 K. This rapid disappearance of the TMR effect was attributed to a possible decrease in the coercivity of the BMO layer with increasing T, as well as likely related to a decrease in the T_c of the ultra thin films. Such a decrease in T_c is consistent with an observed reduction of the saturation magnetization by 50% in the 3 nm films with respect to the bulk moment of 3.6 μ_B per formula unit. Finally, the TMR(V) dependence of the BMO-based junctions showed a sharp decrease with increasing V, in contrast with the signature increasing dependence predicted by Saffarzadeh [40] and experimentally verified by Nagahama *et al* [44]. This suggests that spin flip events generated by defects in the barrier outweigh the spin filter effect, leading to a decreasing TMR(V) curve.

Following the encouraging results obtained for BMO, an appreciable improvement was made to the spin filter efficiency of this perovskite system by partially substituting the Bi^{3+} cations with La^{3+} to form $La_{0.1}Bi_{0.9}MnO_3$ (LBMO) [53]. The result was higher TMR values in tunnel junctions containing LSMO bottom electrodes, both with and without the STO spacer. Figure 2.12-b shows the $R(H)$ curve for a LSMO/STO/LBMO/Au tunnel junction yielding 81% TMR. This value corresponds to a spin filter efficiency

Tab. 2.1: Spin Filter Materials

Material	Magnetic Nature	T_c (K)	μ (μ_B)	Structure	E_g (eV)	$2\Delta E_{ex}$ (eV)	P_{SF} (%)
EuS	FM	16.6	7.0	FCC	1.65	0.36	86 [47, 49]
EuSe	AF	4.6	7.0	FCC	1.8	—	100 [38]
EuO	FM	69.3	7.0	FCC	1.12	0.54	29 [48]
$BiMnO_3$	FM	105	3.6	perovskite	—	—	22 [51]
$NiFe_2O_4$	ferri-M	850	2.0	spinel	0.98	1.2	22 [54]
$CoFe_2O_4$	ferri-M	796	3.0	spinel	0.8	1.28	??

of 35%. In the case of a LSMO/LBMO/Au, the TMR measurement reduces to 22%. This is still an improvement compared to the BMO spin filter for which no TMR was reported when the STO spacer was removed. The difference between the LBMO and BMO spin filter efficiencies was attributed to the improved quality of the LBMO films.

Another noticeable difference between BMO and LBMO was that R_j in the former showed an increasing dependence with decreasing T, whereas in the latter, R_j decreased with decreasing T. Because the model spin filter is expected to show a decreasing $R_j(T)$ dependence, this result further confirms the improved quality of the LBMO barriers. However, the LBMO barriers did not show much improvement in the TMR versus T dependence, leaving the door open for other materials with the potential for spin filtering at higher temperatures.

2.3.3 Ferrites

The search for new materials with the capability of spin filtering at room temperature has sparked renewed interest in the spinel ferrites, whose magnetic and electronic properties are most appropriate for high temperature applications. The spinel ferrites are a family of mixed oxides with the general formula XFe_2O_4 where X is a divalent transition metal cation such as Fe^{2+}, Mn^{2+}, Ni^{2+} or Co^{2+}. With the exception of Fe_3O_4, all are insulating and ferrimagnetic with a Curie temperature above 700 K. While the conductive Fe_3O_4 has been most widely studied as a half-metallic electrode in traditional MTJs [55], the developing field of spintronics has turned its attention to its insulating relatives for their potential to behave as room temperature spin filter tunnel barriers.

Spin filtering in a ferrite tunnel barrier was first demonstrated with $NiFe_2O_4$ via TMR measurements in LSMO/$NiFe_2O_4$/Au tunnel junctions [54]. Before any transport measurements were performed, a careful study of the magnetic

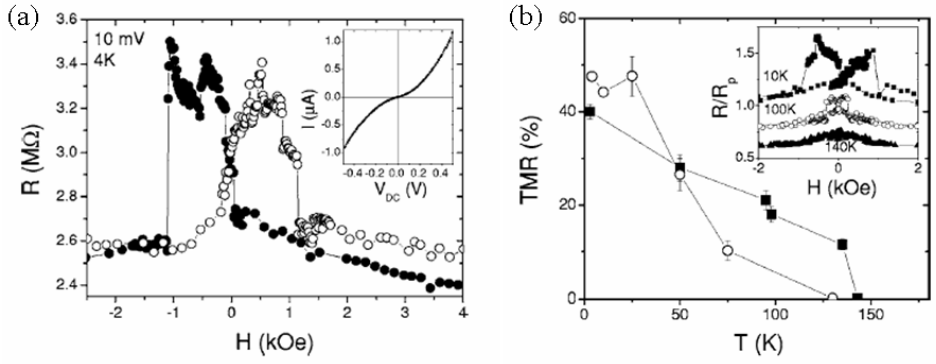

Fig. 2.13: TMR in a LSMO/$NiFe_2O_4$/Au tunnel junction. a) $R(H)$ curve measured at 4 K, and yielding 40% TMR. The current-voltage characteristics are shown in the inset. b) Temperature dependence of the TMR ratio in a LSMO/$NiFe_2O_4$/Au junction with (circles) and without (squares) STO at the LSMO/$NiFe_2O_4$ interface.

and electronic properties of $NiFe_2O_4$ showed that this material, in the thin film form, is extremely sensitive to the conditions used during sample growth. For example, the conductivity of $NiFe_2O_4$ may change significantly, varying from insulating to metallic behavior if the oxygen pressure in the growth chamber is insufficient. Furthermore, it was found that the saturation magnetization of the films increases with decreasing thickness due to cationic site inversion in the thinner $NiFe_2O_4$ layers. These preliminary studies suggested that structural and chemical defects may play a determinant role in the spin polarized transport properties of $NiFe_2O_4$ as well.

Figure 2.13 shows the result of a typical $R(H)$ measurement, measured at 4 K, for a LSMO/$NiFe_2O_4$/Au tunnel junction. The observation of TMR is an indication that $NiFe_2O_4$ acts as a spin filter. From this measurement, one may apply the Jullière where P_1 and P_{SF} are the spin polarizations of the LSMO and $NiFe_2O_4$ layers respectively. Taking $P_1 = 90\%$, a spin filter efficiency $P_{SF} = 19\%$ was obtained for the $NiFe_2O_4$ spin filter. Further studies show that this value may be slightly improved to 22% by inserting a thin STO layer in between the LSMO and $NiFe_2O_4$.

The positive sign of P_{SF} is somewhat surprising as it is contrary to what is expected from the electronic band structure calculations for $NiFe_2O_4$. One proposed explanation attributes the positive polarization to the difference in the spin-dependent effective masses for spin-up and spin-down electrons ($m^*_\uparrow < m^*_\downarrow$) [54]. Further theoretical studies related to this system, and using more complex elliptic band models, suggest that the decay rates of spin-up

and spin-down electrons may in fact lead to an inversion of the sign of TMR [56]. Another possible source for this unexpected result could be defects in the $NiFe_2O_4$ barrier that provide alternative tunneling pathways other than direct tunneling across the electronic band gap. In either case, the origin of this discrepancy remains unclear.

The temperature dependence of the TMR ratio in the $NiFe_2O_4$-based tunnel junctions was also an important parameter to consider, as the ultimate goal in this system was to measure spin filter effects at room temperature. The results shown in Figure 2.13-b reveal a rapid decrease of the TMR ratio with increasing T. Above 140 K, well below the expected T_c = 850 K of $NiFe_2O_4$, TMR is no longer observed. The disappearance of TMR could be due to a decrease of the $NiFe_2O_4$ coercive field at high temperature, or to a drop in the T_c of LSMO caused by nonstoichiometry at the LSMO/$NiFe_2O_4$ interface. Furthermore, in the case of even a small nonstoichiometry in either of the oxide films, defect states in the barrier and/or at the interfaces very probably lead to spin scattering events or direct tunneling without spin filtering. These effects become more prominent at higher temperatures and bias voltages.

The TMR(V) curves for the $NiFe_2O_4$-based tunnel junctions showed a systematic decrease in TMR with increasing V, much like that observed for BMO, and which is not the theoretically expected behavior for a spin filter. Again, defect states such as those discussed for the TMR versus T curves likely play an important role in the observed bias dependence as well. The ensemble of SPT results obtained from the $NiFe_2O_4$-based MTJs therefore confirm the critical importance of mastering the structural and chemical quality of spinel spin filters in order to obtain results at high temperature, and in particular all the way to 300 K.

2.4 $CoFe_2O_4$: A New Candidate for Room Temperature Spin Filtering

In this thesis, we endeavor to demonstrate that spin filtering at room temperature is indeed possible with another material from the spinel ferrite family : *cobalt-ferrite or* $CoFe_2O_4$. $CoFe_2O_4$ (CFO) is a very good candidate for room temperature spintronics applications thanks to its ferrimagnetic nature, high Curie temperature (793 K), and good insulating properties. As we will see in detail below, electronic band structure calculations from first principles methods predict $CoFe_2O_4$ to have a band gap, E_g, of 0.8 eV and an exchange splitting, $2\Delta E_{ex}$, of 1.28 eV between the minority (low energy) and majority (high energy) levels in the conduction band

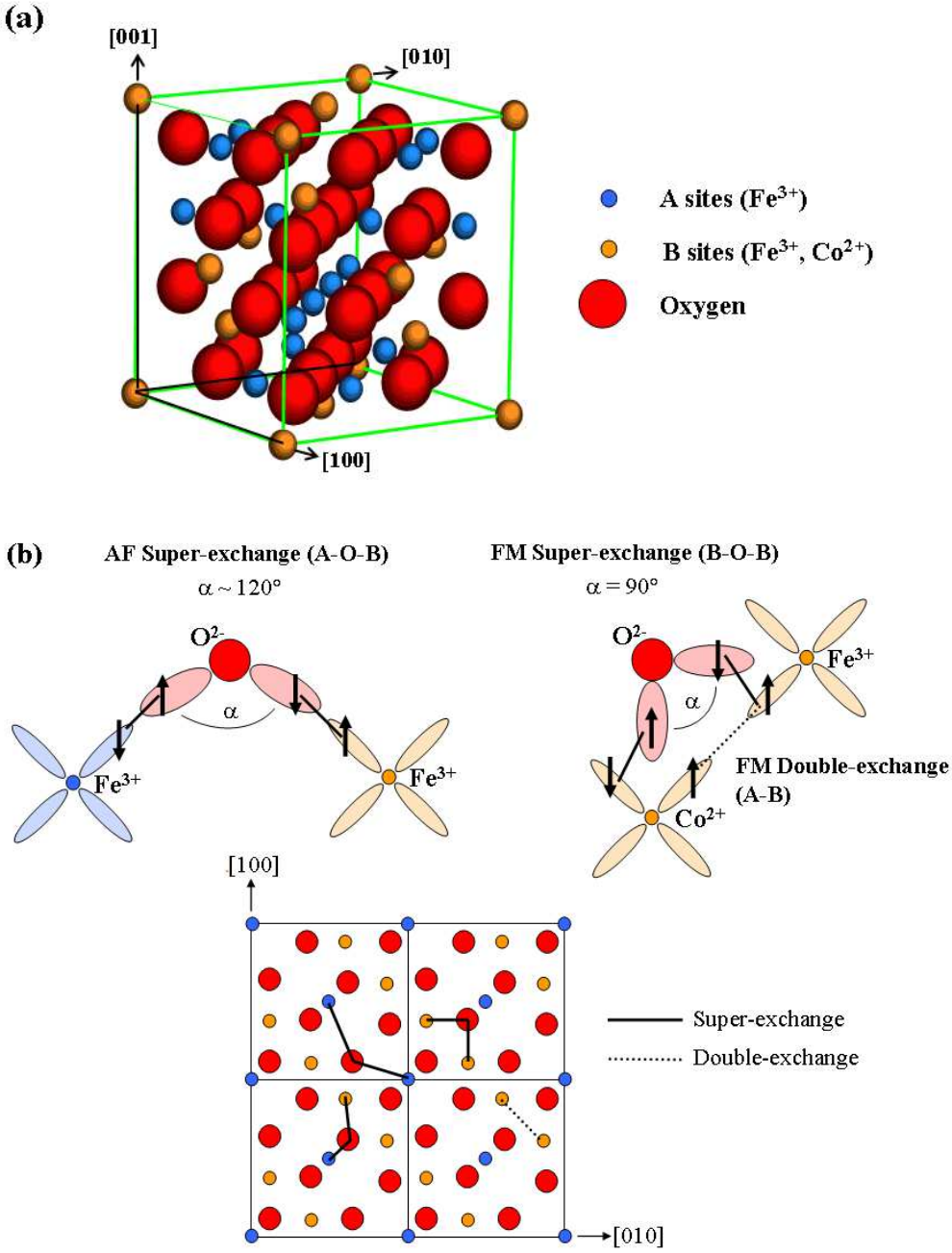

Fig. 2.14: a) Schematic representation of the inverse spinel unit cell of $CoFe_2O_4$. b) Magnetic exchange interactions in $CoFe_2O_4$, shown in the (001) plane.

[57], thus confirming its high potential to be a very efficient spin filter, even at room temperature. We emphasize that $CoFe_2O_4$ is expected to have a *negative* spin polarization, as opposed to its Eu chalcogenide and perovskite counterparts (see Section 2.4.3). Recently, a tunneling spectroscopy study of $CoFe_2O_4/MgAl_2O_4/Fe_3O_4$ double barrier tunnel junctions revealed optimistic results for the spin-filter efficiency of $CoFe_2O_4$ [58]. However, the polarization (P) and TMR values obtained in this work were indirectly extracted from a complex model developed to fit experimental current-voltage curves rather than from direct Merservey-Tedrow or TMR measurements. In the present work, we will use both of these SPT techniques to unequivocally demonstrate the spin filter capabilities of $CoFe_2O_4$.

2.4.1 Structure

The ideal $CoFe_2O_4$ crystal has an inverse spinel structure consisting of an FCC oxygen sublattice and a distribution of cations in both the tetrahedral (A) and octahedral (B) interstitial sites. The unit cell contains a total of 56 atoms which may be broken down into 32 O^{2-}, 16 Fe^{3+} and 8 Co^{2+}. More precisely, the Fe^{3+} cations occupy 1/8 of the available A-sites, while 1/2 of the available B-sites are filled in equal proportion by the remaining Fe^{3+} and Co^{2+}. Its lattice parameter is most widely accepted to be 8.392 Å, although this value varies slightly from one study to another [59, 60, 61, 62]. A schematic representation of the inverse spinel unit cell belonging to $CoFe_2O_4$ may be seen in Figure 2.14.

2.4.2 Magnetism

The magnetic properties of $CoFe_2O_4$ arise from several exchange couplings between the different cations. The predominant interactions are *super-exchange* interactions in which Fe^{3+} and Co^{2+} couple via an overlap of their $3d$ orbitals with the $2p$ orbitals of an intermediate oxygen anion. When the overlap angle, α, is greater than 90° the interaction is strongly antiferromagnetic, whereas when $\alpha = 90°$ the interaction is weaker and ferromagnetic. Another ferromagnetic interaction also occurs by the direct transfer of the seventh electron in Co^{2+} ($3d^7$) towards the empty d-levels in Fe^{3+} ($3d^5$). This *double-exchange* is again rather weak and often confused or masked by the ferromagnetic super-exchange interaction. The principal exchange interactions in $CoFe_2O_4$ and their energies (in units of k_B) may be summarized as follows [61]:

1. An antiferromagnetic super-exchange interaction involving the overlap of Fe_A^{3+} with Fe_B^{3+} or Co_B^{2+} across the $2p$ orbitals of an intermediate O^{2-}.

This A-O-B exchange is the strongest in $CoFe_2O_4$, with an energy J_{AF} = -24 k_B.

2. An second antiferromagnetic super-exchange interaction involving only Fe_A^{3+} cations, again via an O^{2-}. The energy of the A-O-A exchange is J_{AF} = -19 k_B.

3. A ferromagnetic super-exchange interaction that couples Fe_B^{3+} to Co_B^{2+} at $\alpha = 90°$. The energy of this B-O-B exchange is low compared to the antiferromagnetic couplings, giving $J_F = 4\ k_B$.

4. A direct ferromagnetic double-exchange interaction in between Fe_B^{3+} and Co_B^{2+} that is masked by the super-exchange involving the same cations.

As is the case for all the spinel ferrites XFe_2O_4, the net magnetic moment, μ, of $CoFe_2O_4$ is obtained by adding up the interactions between Fe_A^{3+}, Fe_B^{3+} and Co_B^{2+}. Because the 5 μ_B of the $Fe_{A,B}^{3+}$ cations cancel out in the antiferromagnetic A-O-B coupling, μ is determined by the moment of Co^{2+}. The result for $CoFe_2O_4$ is $\mu_{CoFe2O4} = 3\ \mu_B$. In a similar manner, $\mu_{NiFe2O4} = 2\ \mu_B$, $\mu_{Fe3O4} = 4\ \mu_B$, etc. Finally, it is worth noting that these spinel ferrites rarely exhibit a perfect inverse spinel structure. Studies have shown that the migration of X^{2+} cations from B to A sites occurs readily [63], leading to a "mixed" spinel whose μ and electronic band structure may vary significantly from the inverse scenario.

2.4.3 Electronic Band Structure

Theoretical work using first principles calculations has in fact demonstrated the effect of structural modifications such as cationic site inversion on the electronic band structure and magnetic moment of the principal spinel ferrites [57]. In the case of $CoFe_2O_4$, the *inverse spinel* scenario yields a theoretical band gap of 0.80 eV, while the exchange splitting of the conduction band is 1.28 eV (see Figure 2.15). As mentioned earlier, the exchange splitting is such that the lowest energy level of the conduction band corresponds to spin-down states. The result should therefore be a lower tunnel barrier height for spin-down electrons and thus negatively polarized spin filtering. These predictions are certainly highly encouraging for the spin filter capability of $CoFe_2O_4$. When taking into consideration a complete site inversion of Co^{2+} cations and thus a *normal spinel* structure, μ increases dramatically to 7 μ_B [57]. As a consequence there is a largely amplified exchange splitting in the conduction band, and therefore the theoretical possibility of even higher

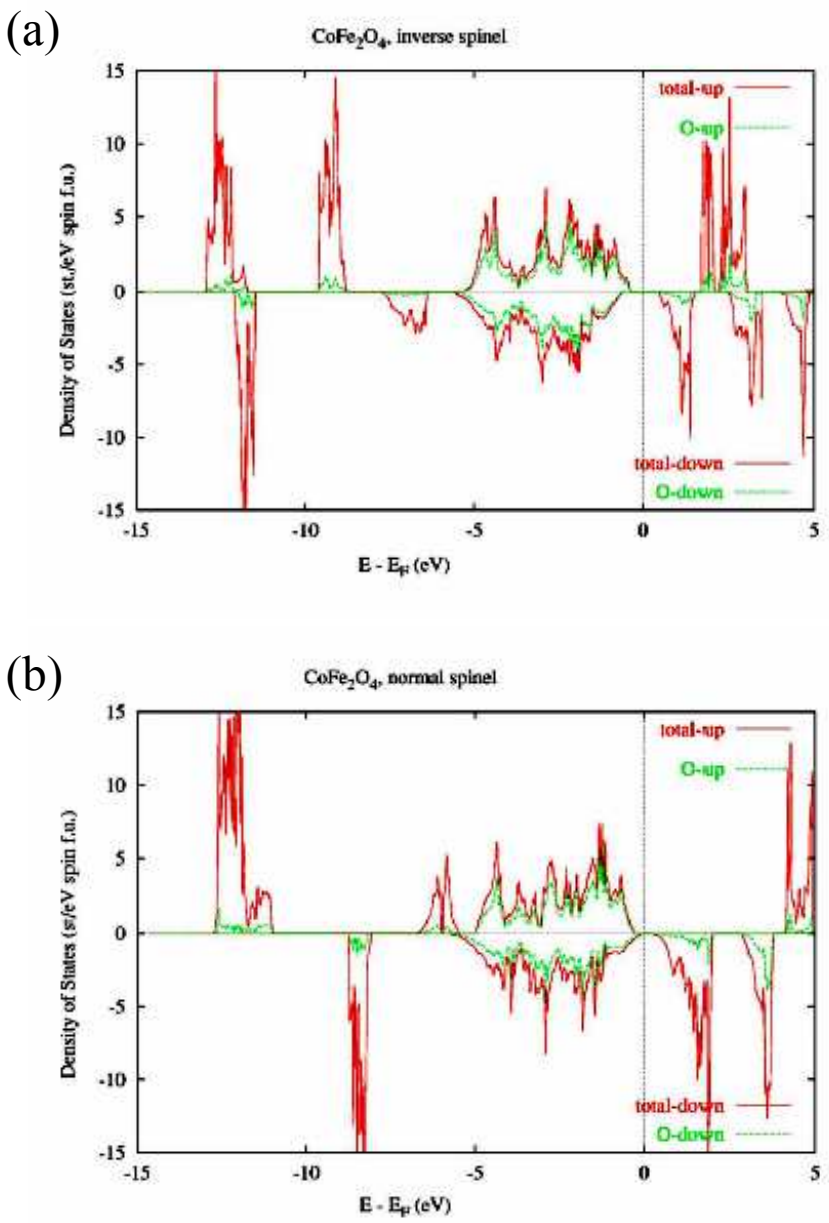

Fig. 2.15: Spin decomposed total densities of states, per formula unit, for $CoFe_2O_4$ in the inverse spinel (a) and normal spinel (b) structures, as calculated by density functional theory using the local density + U approximation. The effect of Co^{2+} site inversion on the band gap and exchange splitting is evident in these calculations. Figures from [57].

spin filtering efficiencies. Unfortunately, the increased ΔE_{ex} is counterbalanced by a decrease in E_g, which leads to a normal spinel $CoFe_2O_4$ which is nearly half-metallic. Nevertheless, the 1.28 eV of exchange splitting in the insulating inverse spinel is largely sufficient for purposes of spin filtering.

The effect of defects such as cationic site inversion, presence of Co^{3+} and oxygen vacancies, predicted theoretically but undetermined experimentally, will thus form one of the key motivations behind the spin polarized tunneling experiments in this thesis. As we will see in Chapter 5, preliminary studies varying the oxygen vacancy concentration in our films do indeed suggest that these have a significant effect of the spin filter efficiency of $CoFe_2O_4$. Although a more detailed investigation involving these and other types of point defects is not presented in this thesis, such studies should form an important part of the future work to be done on $CoFe_2O_4$ and other potential room temperature spin filters.

3. EXPERIMENTAL METHODS : FROM THIN FILM GROWTH TO SPIN-POLARIZED TUNNELING

In this chapter we will describe the ensemble of experimental techniques used throughout this thesis. We have granted this topic a chapter of its own, rather than integrating it into the forthcoming chapters, in order to avoid drowning out the important experimental results with technical details. The goal here is thus to introduce a sort of reference that the reader may refer back to if needed to understand the results and physical interpretations in Chapters 4-7. We will begin by presenting the growth of epitaxial magnetic oxides by molecular beam epitaxy (MBE), which is of course the heart of this thesis. Without the MBE, nothing else would have been possible. Next we will continue on to the numerous *in situ* and *ex situ* characterization techniques used to verify the structural, chemical and magnetic properties of our films. Finally, we will conclude with a detailed description of the different magneto-transport techniques used to measure the electronic properties and spin polarized tunneling in our $CoFe_2O_4$-based systems.

3.1 Epitaxial Growth of Spinel Ferrite Thin Films

3.1.1 Molecular Beam Epitaxy

Nearly all of the films studied throughout this thesis have been grown by molecular beam epitaxy (MBE). The only exception, as we will see in Chapter 4, is the growth of Pt(111) buffer layers which have been fabricated by the sputtering technique at the Unité Mixte de Physique CNRS/Thales in Palaiseau, France. The fundamental basis of simple material deposition by MBE consists in generating a molecular flux of the metal or semiconductor to be deposited by evaporating a solid source of this material from a Knudsen effusion cell. The condensation of the evaporated metal on a crystalline substrate leads to the growth of a single crystalline film. This film is considered *epitaxial* when the crystalline lattice of the substrate and that of the deposited film are geometrically coherent. In other words, the crystalline substrate in essence imposes its lattice on the growing film such that, in addition to the other physical constraints imposed by the deposi-

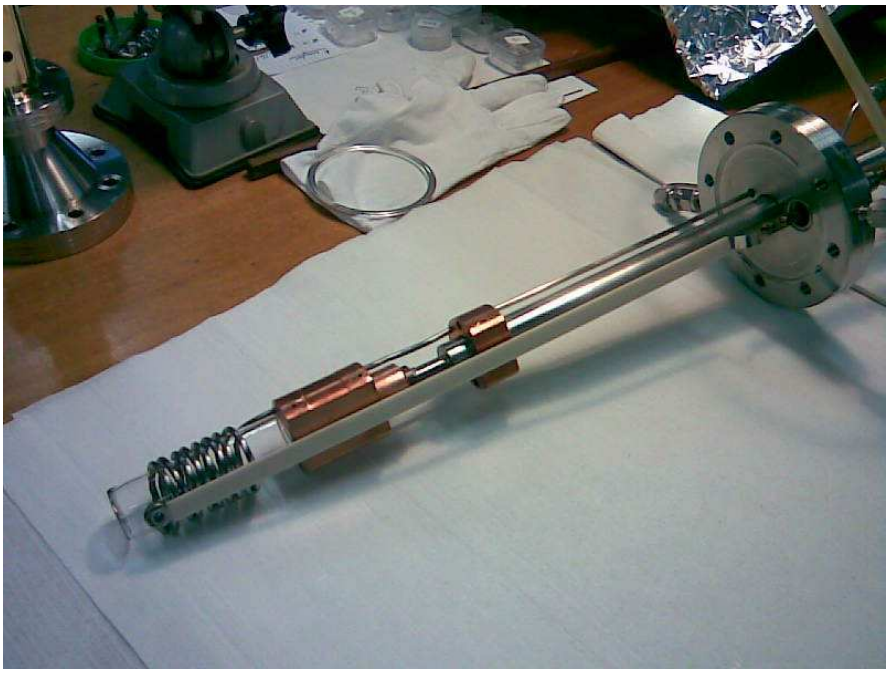

Fig. 3.1: Image of the rf oxygen plasma source used to grow our epitaxial oxide films. At the end of the source one can distinguish the radio frequency quartz cavity containing one single effusion hole to release the oxygen atoms.

tion conditions, only a geometrically compatible phase may form. In order to avoid the contamination of the deposited film during growth, the MBE chamber must imperatively be maintained under ultra high vacuum (UHV) conditions (base pressure $\sim 5.10^{-11}$ mbar). Not surprisingly, this constraint makes MBE a very delicate and complex deposition technique.

In the case of growing an oxide film, one may once again evaporate a solid source of the desired oxide material and have it deposit directly on the substrate. However, the loss of oxygen due to the UHV conditions in the MBE chamber makes it difficult to obtain a film that is fully stoichiometric. Yet another method consists in introducing a flux of oxygen into the chamber which in turn reacts with a metallic flux (of one or more metals) on the substrate surface to form the desired oxide phase. The advantage of this coevaporation method is that the stoichiometry of the final product may be controlled by adjusting the intensity of the oxygen flow. In the present thesis, a flow of *atomic oxygen* was used as the oxidizing agent in our MBE system, which has the advantage of being much more reactive than standard

molecular O_2. We therefore address this specific technique by the name *oxygen plasma-assisted MBE*. The amount of atomic oxygen introduced into the evaporation chamber, and thus the oxidation conditions of the growing film, is controlled via two parameters : the radio frequency (rf) power of the oxygen plasma source, and the partial oxygen pressure inside the plasma source ($P_{O_2}^{plasma}$). An image of the rf oxygen plasma source installed in the MBE chamber is shown in Figure 3.1.

A photograph of the entire MBE system as well as a schematic representation of the main deposition chamber are shown in Figure 3.2. In the deposition chamber, we can identify two *in situ* characterization techniques : reflection high energy electron diffraction (RHEED) and Auger electron spectroscopy (AES). In addition to these two techniques, an x-ray source and hemispherical analyzer situated in an adjacent analysis chamber allow for *in situ* x-ray photoelectron spectroscopy (XPS) measurements as well. As we will see in the following sections, the ensemble of these incorporated techniques allowed for the thorough investigation of the structural and chemical properties of our ferrite films and multilayers *before* surface contamination from exposure to air.

3.1.2 Growth Conditions

The growth of our $CoFe_2O_4(111)$ thin films by oxygen-assisted MBE was inspired by the previously-optimized growth of $Fe_3O_4(111)$ on α-$Al_2O_3(0001)$ substrates [64, 65]. Throughout this thesis, films ranging from 3 to 30 nm in thickness were grown on high quality α-$Al_2O_3(0001)$ (sapphire) substrates specially optimized for epitaxial growth. Their structure is corindon which is based on a HCP lattice. Before depositing any oxide, the substrates were systematically cleaned in two steps :

1. A chemical rinse in an aqueous solution of ammonia (NH_3) and hydrogen peroxide (H_2O_2). This step is performed outside the MBE, before mounting the substrate on the substrate holder.

2. A plasma cleaning inside the MBE chamber under moderate oxidizing conditions (rf power 350 W, oxygen pressure in the plasma source cavity ($P_{O_2}^{plasma}$) of 0.13 Torr). This second step was also applied for samples containing a Pt(111) buffer layer deposited on the sapphire substrate.

All $CoFe_2O_4$ films were deposited at 450°C with a P_{O_2} in the plasma source cavity ranging from 0.2 to 0.4 Torr. Unlike the growth of Fe_3O_4, the spinel phase of $CoFe_2O_4$ could be stably grown in a significantly wide range of $P_{O_2}^{plasma}$, allowing us to study the properties of this material as a function of

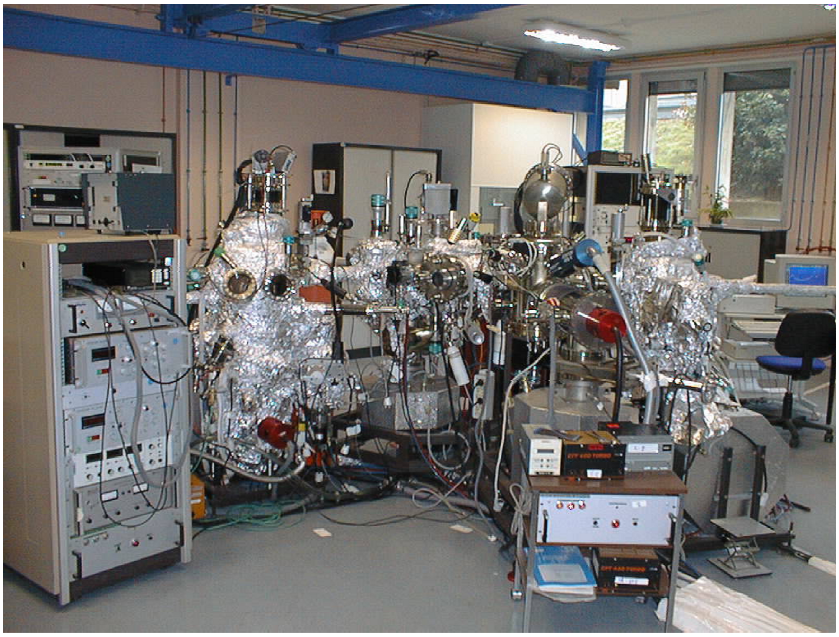

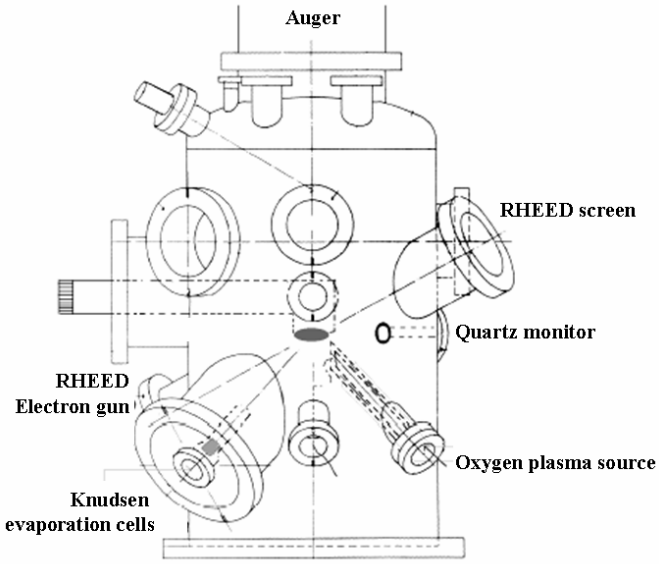

Fig. 3.2: Photograph of the entire MBE system used to grow our $CoFe_2O_4$-based thin films and multilayers. A schematic diagram of the deposition chamber is shown below.

the extent of oxidation (i.e. presence of oxygen vacancies). Again, the base pressure in the MBE chamber was 10^{-11} mbar, and the oxygen partial pressure during deposition 10^{-8} mbar. Because the previously optimized growth of Fe_3O_4 was performed at an oxide deposition rate of 0.18 nm/min, we chose to maintain this same total deposition rate for the growth of $CoFe_2O_4$. In other words, the partial Fe deposition rate of 0.09 nm/min used for Fe_3O_4 was subdivided into 0.03 and 0.06 nm/min partial Co and Fe rates respectively in order to achieve a 1:2 Co to Fe ratio. The metallic fluxes were calibrated using a piezoelectric quartz monitor installed in the main chamber and then verified by TEM imaging of the film thickness. Having fixed the total metal flux from the start, it was by changing $P_{O_2}^{plasma}$ that we were able to optimize the growth conditions for $CoFe_2O_4$.

Aside from $CoFe_2O_4(111)$ single layers, several $CoFe_2O_4$-based multilayer systems have been studied. These include $CoFe_2O_4(111)/Fe_3O_4(111)$, $CoFe_2O_4(111)/\gamma$-$Al_2O_3(111)$, $CoFe_2O_4(111)$/Co(0001) and $CoFe_2O_4(111)/\gamma$-$Al_2O_3(111)$/Co(0001). Occasionally a polycrystalline layer of Au was deposited on top of the epitaxial heterostructures as a protective capping layer.

The growth conditions for Fe_3O_4 were nearly identical to those of $CoFe_2O_4$, only that $P_{O_2}^{plasma}$ never exceeded 0.2 Torr in order to avoid over oxidizing to Fe_2O_3. Again the metallic Fe deposition rate was held constant at 0.09 nm/min in order to maintain a total oxide rate of 0.18 nm/min. Therefore, the growth of the $CoFe_2O_4/Fe_3O_4$ bilayers could be done in one step without cooling down between layers. Once the $CoFe_2O_4$ finished, the sample was rotated away from the metal and oxygen fluxes, the Co cell closed with a shutter, the Fe flux raised from 0.06 to 0.09 nm/min, and $P_{O_2}^{plasma}$ lowered to 0.2 Torr. After about 15 minutes of stabilization time, the sample was rotated back into the flux to continue the deposition.

The $CoFe_2O_4(111)/\gamma$-$Al_2O_3(111)$ bilayers were also grown in one step at 450°C. For the proper growth of Al_2O_3, the Al flux was fixed at 0.05 nm/min (0.1 nm/min total oxide rate) and $P_{O_2}^{plasma}$ held the same as for $CoFe_2O_4$. The reduced oxide deposition rate and higher $P_{O_2}^{plasma}$ assured an Al_2O_3 film that was single crystalline and fully oxidized.

Finally, only the growth of Co was performed at low temperature (25°C). This was done to minimize the reaction of Co with the neighboring oxide to form CoO and a substoichiometric $CoFe_2O_4$ or Al_2O_3. The rate of Co deposition was generally around 0.2 nm/min. The growth of the Co-containing multilayers therefore required an interruption for cooling down, before continuing to deposit Co.

3.2 In situ *Characterization*

3.2.1 *Reflection High Energy Electron Diffraction*

Undoubtedly the most important *in situ* characterization technique in our MBE system was reflection high energy electron diffraction (RHEED). The major advantage of this technique is that it allowed us to follow the structure of the film being deposited *in real time* throughout the entire growth process.

The RHEED measurement consists in aiming an electron beam at the sample surface with an incident angle of 1-4° such that only the last few monolayers of atoms at the surface are probed (approximately 1 nm deep). In our measurements, the energy of the incident electron beam was 30 keV. The incident electrons are then mainly elastically scattered, giving rise to a diffraction pattern representing the reciprocal lattice of the surface along the direction perpendicular to the incident beam. The diffraction patterns are captured on a fluorescent screen and then recorded and digitized by a CCD camera.

According to the dynamic theory of diffraction in two dimensions (i.e. a surface), the expected diffraction pattern is determined by the intersection of the rods of the reciprocal lattice with the Ewald sphere. This should result in an image with spots. However, because of the energy of the incident electrons, the radius of the Ewald sphere is much greater than the interatomic distances, the resultant diffraction pattern takes on the form of rods. This effect is further accentuated by the dispersion of the incident beam angle and the two-dimensional nature of thin film surface. Only in the case of a rough surface, in which the incident electrons manage to traverse the islands on the surface (the case of transmission), does one observe spots in the diffraction diagram. The appearance of spots on a RHEED pattern during the growth of a thin film is therefore indicative of poor surface quality [66].

For the growth of the spinels ($CoFe_2O_4$, Fe_3O_4 and γ-Al_2O_3) on α-Al_2O_3 (0001) or Pt(111), we have studied the RHEED patterns along the $[10\bar{1}0]$ and $[1\bar{1}00]$ directions in reciprocal space. These are shown in Figure 3.3 for the superposition of the corindon and spinel lattices. The streaks observed on each of the RHEED patterns therefore represent the reciprocal lattice along the chosen directions. An example of the RHEED patterns of a sapphire substrate and a Fe_3O_4 film along $[10\bar{1}0]$ and $[1\bar{1}00]$ are shown in Figure A.1, with the streaks corresponding to the green and red dots in Figure 3.3 respectively. If during the course of a deposition, the spinel layer begins to deviate from the desired phase (towards (Co,Fe)O in the case of insufficient oxygen pressure, towards $(CoFe)_2O_3$ in the opposite case), the streaks will in the RHEED patterns will change such that they are no longer associated

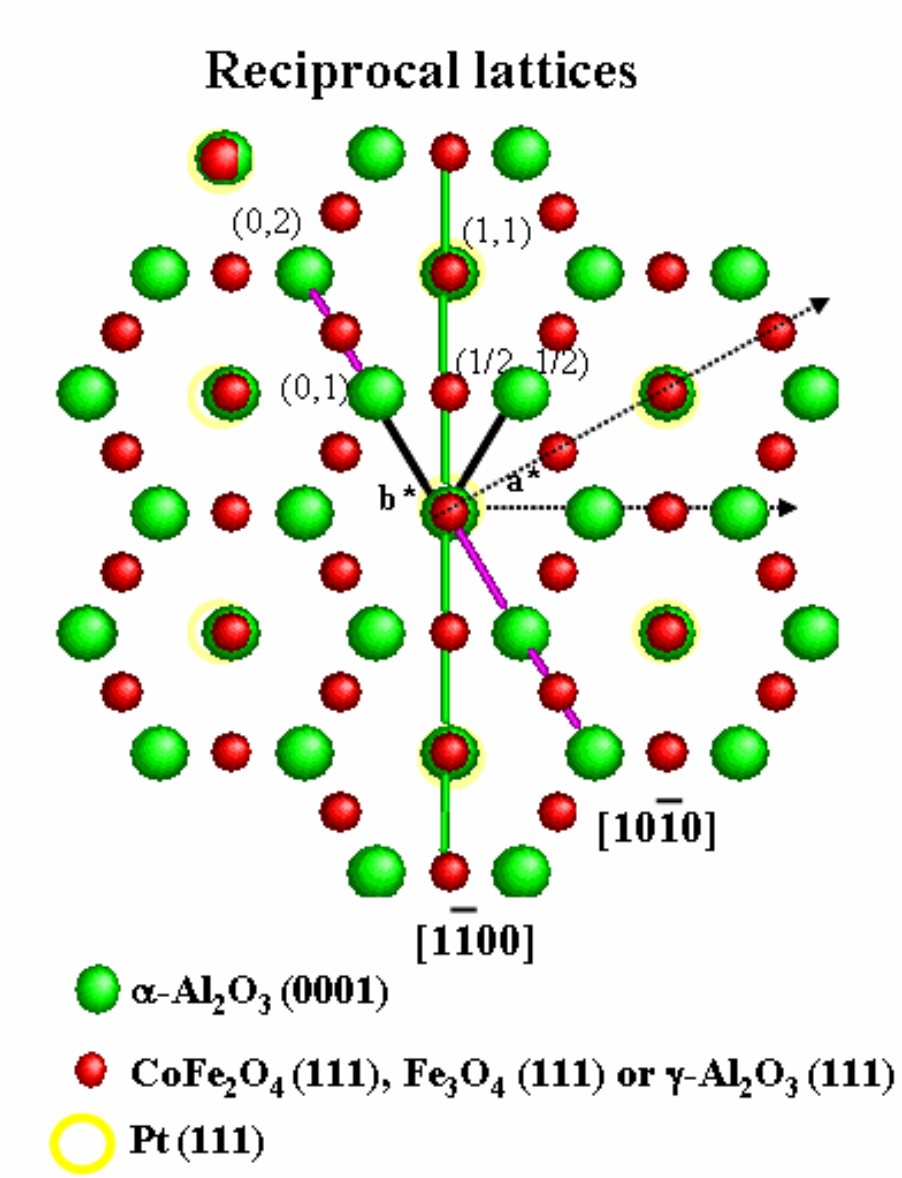

Fig. 3.3: Superposition of the hexagonal corindon and cubic spinel lattices. The labels [10$\bar{1}$0] and [1$\bar{1}$00] correspond to the RHEED observation directions used throughout this study, and are indicated in the hexagonal lattice basis.

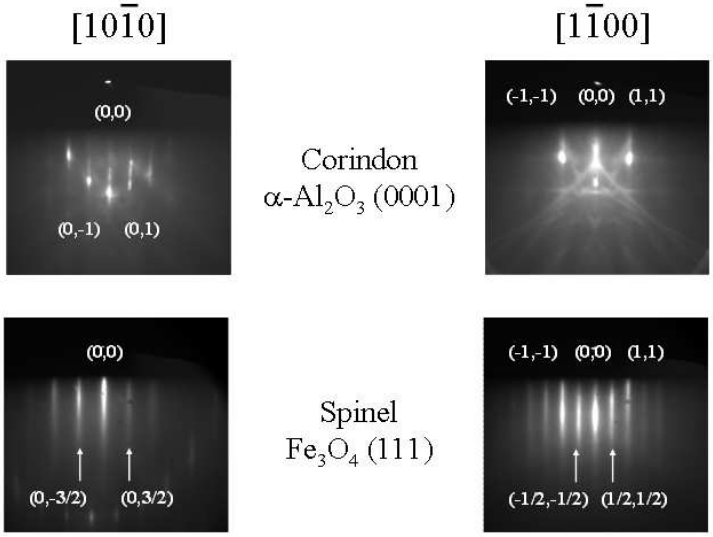

Fig. 3.4: Example of the RHEED patterns obtained along [10$\bar{1}$0] and [1$\bar{1}$00] for a sapphire substrate and a spinel Fe_3O_4 film. The rods observed for each oxide correspond to the respective reciprocal lattices depicted in Figure 3.3.

with spinel lattice. We are therefore able to follow the structure of our film throughout the course of deposition and modify, if necessary, the growth conditions in order to assure a final film of the highest possible quality.

3.2.2 Electron Spectroscopies

X-ray Photoelectron Spectroscopy

As was mentioned earlier in Section 3.1.1, the MBE used to elaborate our $CoFe_2O_4$-based thin films was equipped with a UHV x-ray photoelectron spectroscopy (XPS) analysis chamber which allowed us to verify the composition of our films before exposure to air. XPS is a technique that probes the binding energy (E_B) of the electrons in a given material by the photoelectric effect. In a simplified model, the material will emit a photoelectron if the energy of the incident photon is sufficient to strip an electron from a core level into the vacuum. This is schematized in Figure 3.5. The energy conservation law may be expressed as follows :

$$E_K = h\upsilon - E_B - \varphi_{spec} \tag{3.1}$$

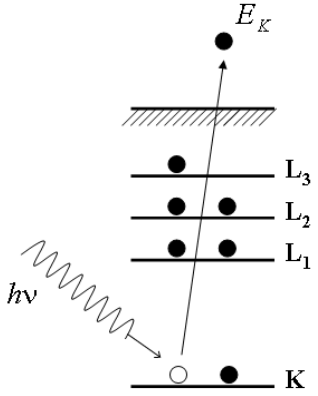

Fig. 3.5: Simplified schematic representation of the photoelectric effect which is the basis of XPS.

where E_K is the kinetic energy of the emitted photoelectron, $h\upsilon$ the energy of the incident photon, E_B the binding energy of the core electron and φ_{spec} the work function of the spectrometer. Each chemical element in the material will therefore have a characteristic E_K,E_B peak energy and form. Furthermore, comparison of the relative peak areas allows for a quantitative analysis of the composition of the sample.

XPS is a technique limited to the analysis of surfaces and thin films because the energy of the incident photons is such that the photoelectron escape depth of only a few nanometers (depending on the material). For example, in our experimental conditions, the depth probed using the Fe2p peaks is on the order of 3 nm. Our XPS measurements were performed using both Al Kα ($h\upsilon$ = 1486.6 eV) and Mg Kα ($h\upsilon$ = 1253.6 eV) non-monochromatized x-ray sources depending on the chemical constituents of the samples. While oftentimes Al Kα is the radiation of choice, we used a Mg Kα source for all specimens containing Co (i.e. $CoFe_2O_4$, Co) in order to avoid overlap with parasitic Auger peaks in the Co2p binding energy range.

The chemical analysis of our $CoFe_2O_4$ thin films and $CoFe_2O_4$-based multilayers by XPS involved mainly the Fe2p and Co2p peaks, because their shape depends greatly on the chemical state of these atoms. In the case of Fe, the Fe2p peak is always split in two due to spin orbit coupling ($Fe2p_{1/2}$, $Fe2p_{3/2}$). However, in the oxidized state, an additional satellite peak appears in between the $Fe2p_{1/2}$ and $Fe2p_{3/2}$ components: for FeO (purely Fe^{2+}) this peak is situated 4.5 eV above the $Fe2p_{3/2}$ component, while in the case of Fe_2O_3 the satellite occurs 8 eV above the $Fe2p_{3/2}$ component. Because the Fe

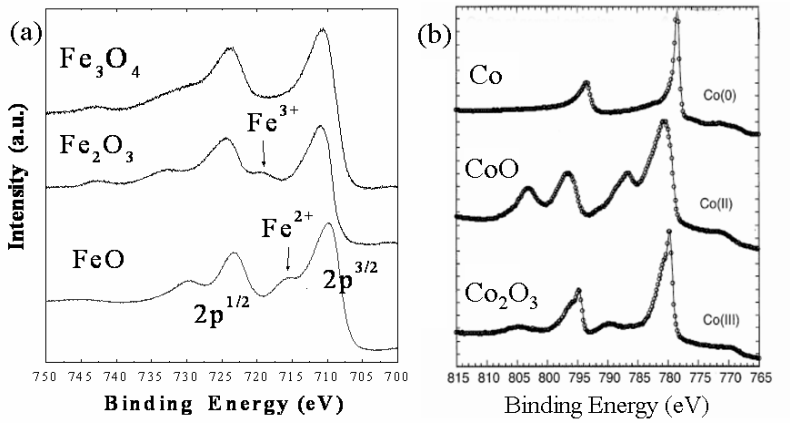

Fig. 3.6: Reference XPS spectra for the Fe2p (a) and Co2p (b) peaks in the different oxidation states. In the case of Fe2p, the placement of the intermediate satellite peak marked with an arrow (or lack thereof) indicates the oxidation state of the Fe ions. For Co2p, it is the peak shape that distinguishes one oxidation state from another. (a) is taken from [64] and (b) from [67].

ions in $CoFe_2O_4$ are fully Fe^{3+}, we should expect to see a Fe2p peak identical to that of Fe_2O_3. In the particular case of Fe_3O_4, the presence of Fe^{2+} and Fe^{3+} in a 1:1 ratio leads to the equal presence of both satellites and thus an unresolved structure between the two spin-orbit components [64]. The absence of a resolved satellite peak is therefore characteristic of a Fe_3O_4 layer. Figure 3.6-a contains reference peaks of the three possible combinations of Fe oxidation states.

Regarding the Co2p binding energy range, we also expect to see a significant change in peak shape when going from metallic Co to fully oxidized Co_2O_3. In Figure 3.6-b, we identify the three possible Co oxidation states, and in particular that of CoO which corresponds to Co^{2+}. Because the Co cations in $CoFe_2O_4$ are purely Co^{2+}, we should expect to observe the same peak shape in our samples. All in all, even if the *in situ* RHEED studies already contain valuable information about the structure at the surface of our films, the XPS data is essential as it reflects the chemical composition of a considerably larger portion of the entire film thickness.

Auger Electron Spectroscopy

Even more surface sensitive than the XPS technique is Auger electron spectroscopy (AES), which detects the emission of secondary electrons following the ionization of an atom by an exterior excitation (photon or electron). In our measurements, we have used an electron beam of 2-3 keV as the source of excitation. The Auger effect is a three-step process :

1. An incident electron strips an electron from a core level and is itself backscattered, leaving behind a hole.

2. An electron from a higher energy level relaxes down to recombine with the hole, transferring its extra energy to a third electron called the Auger electron. This is known as *non-radiative* relaxation.

3. The energy transfer to the third Auger electron results in its being stripped from its energy level and its ejection from the atom.

These three steps are schematically illustrated in Figure 3.7.

Although the Auger relaxation process competes with radiative relaxation (fluorescence), its occurrence is much more probable in the light elements and in excitations involving the K levels. AES is therefore most useful for detecting surface contamination by atoms such as C, N and O, and for detecting the oxidation state of light metals such as Al. In our experiments, we primarily used AES to study the oxidation state of our Al_2O_3 barriers because the metallic Al and AlO_x peaks are readily distinguishable, which is less so the case in XPS. Finally, AES was best adapted for our ultra-thin Al_2O_3 barriers (t = 1-2 nm) because it is more sensitive to weak signals than XPS while also having a higher surface sensitivity for the typical electron beam energies used (the Auger electron escape depth in Al *LMM* transition using an electron beam of 3 keV is only $\sim$1 nm for example).

3.3 Structural and Chemical Characterization Electron Microscopies

3.3.1 Transmission Electron Microscopy

Transmission electron microscopy (TEM) is an extremely valuable tool for the structural characterization of epitaxial thin films. Thanks to this technically complex method, one can obtain high resolution images in real space (image mode) of the crystalline structure of a film with a magnification starting around 10^3 and reaching atomic resolution as high as 10^6. TEM also

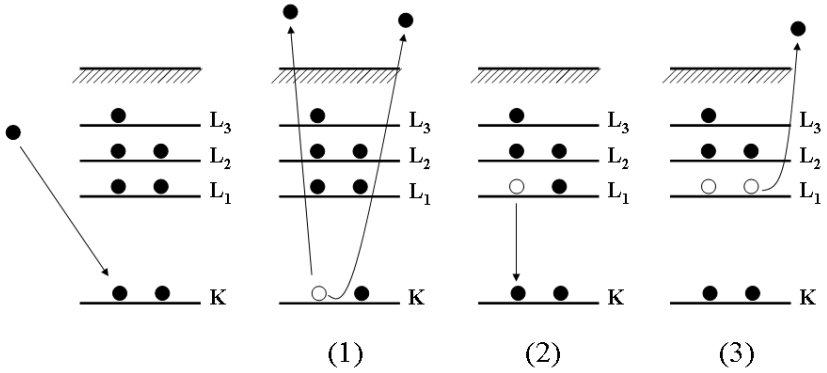

Fig. 3.7: Schematic representation of the three steps of the Auger effect after excitation by an incident electron beam (KL_1L_1 transition).

offers the possibility of studying a sample in reciprocal space (diffraction mode) in order to better analyze the epitaxial relationship between different layers.

In our study of epitaxial $CoFe_2O_4$-based heterostructures, TEM was particularly useful for several aspects :

- Characterization of sample interfaces (i.e. crystallinity, roughness)
- Verification of sample thickness
- Identification of film structure
- Identification of structural defects such as dislocations and antiphase boundaries (APBs)
- Analysis of mechanical strain in epitaxial heterostructures

All of this information was critical to the complete understanding of the epitaxial growth as well as to the optimization of our samples for future magnetic and electronic measurements.

The TEM images presented in this thesis were obtained thanks to a close collaboration with two laboratories in France : the DSM/DRFMC/SP2M laboratory at CEA-Grenoble and the CEMES-CNRS laboratory in Toulouse. The majority of the high resolution TEM (HRETEM) images were obtained at Grenoble using a JEOL 4000EX microscope having a point resolution of 0.17 nm. Cross-sectional samples were prepared by cutting along the (112) planes before thinning by mechanical grinding down to 20 μm in thickness.

The final thinning was performed by Ar ion-milling (using a Precision Ionic Polish System) in order to achieve electron transparency. Plane view specimens were also thinned in the same manner.

3.3.2 Geometric Phase Method

Aside from the visual characterization described above, HRTEM images are rich in information about other structural and mechanical properties. A number of different image treatment techniques permit the extraction of this information. The geometric phase method is one such technique that measures the local displacement and strain fields in a specimen from experimental HRTEM images of a crystalline specimen [68, 69]. The phase image is obtained through several computational manipulations of the Fourier transform of the original image, which contains all information about the periodicity and orientation of the sample. The isolation of selected diffraction spots using a digital circular aperture, followed by an inverse Fourier transform of the selected spots, generates a phase image that is extremely sensitive to displacements of the selected atomic planes. This method is currently used for to study the local strain fields created by defects such as dislocations and antiphase boundaries, the detection of nanocrystals and the study of epitaxial strain in multilayers. In this work, we will see that the geometric phase method may provide an interesting insight on the the epitaxial growth mode of oxides having similar structures (see Chapter 4). This analysis was especially useful in the characterization of our Pt/$CoFe_2O_4$/γ-Al_2O_3/Co MTJs.

3.3.3 Electron Energy Loss Spectroscopy

A complementary measurement to the structural characterization obtained by TEM is electron energy loss spectroscopy (EELS). This spectroscopic method, which is performed inside the electron microscope and requires the same sample preparation, measures the energy loss of the electrons traversing a specimen due to inelastic interactions. These interactions include excitations in the valence or conduction band of the atoms in the sample, but also core level excitations. The latter of the two represent considerably higher energy losses (>50 eV), and are thus more readily detected by the spectrometer [59]. The unique aspect of EELS measurements is that they are chemically selective, since each element of the periodic table has its own spectrum of energy losses.

For the purposes of this thesis, the most useful application of the EELS technique was to obtain chemical maps of our samples. By detecting the losses corresponding to a specific element's absorption edge (Co L-edge for

example), we could obtain a map of all the areas in the sample where that element could be found. This technique was especially useful for distinguishing $CoFe_2O_4$ from Fe_3O_4 in bilayer samples containing both oxides (see Chapter 4). All of the EELS experiments to be presented were carried out in a Tecnai FEG-Cs corrected TEM with a point resolution of 0.12 nm, and fitted with a Gatan Imaging Filter, at the CNRS-CEMES laboratory in Toulouse.

3.4 Magnetic Characterization

3.4.1 Vibrating Sample Magnetometry

The vibrating sample magnetometer (VSM) is an apparatus that measures the magnetic properties of thin films and small crystals as a function of applied magnetic field and temperature. The great advantage of this technique as opposed to other magnetic measurements such as the superconducting quantum interference device (SQUID) or polarized neutron reflectometry (PNR) is the speed at which data is acquired. A simple magnetization curve can be obtained in a few minutes whereas with a SQUID the same measurement may take a few hours. Also, VSM is well adapted for room temperature measurements, which are crucial to the study of high T_c materials such as $CoFe_2O_4$.

The VSM is composed of an electromagnet which generates a horizontal magnetic field H. The measurement itself relies on the principle of flux and consists in measuring the voltage ϕ that is induced in the detection coils when a magnetic sample is displaced periodically in the applied field (hence the term *vibrating*). The voltage induced by a sample with a magnetic moment μ is linked to the induced flux F by the relation :

$$\phi = -\frac{dF}{dt} \tag{3.2}$$

F is determined by the reciprocity theorem :

$$F = \left(\frac{B}{I}\right)\mu \tag{3.3}$$

where B is the magnetic field generated by the effective current I circulating in the detection coils. Combining the detected ϕ with the equations above, we obtain a measure of μ as a function of H.

Because the measurement of μ is proportional to the volume of the sample, the physical property that we look to analyze, especially in the case of samples with varying thicknesses, is the moment per unit volume, or magnetization M:

$$M = \frac{\mu}{V} \tag{3.4}$$

where V is the volume of the film. The reason why we base the interpretation of the magnetic measurements on M is obvious : we are looking to analyze the intrinsic properties of our $CoFe_2O_4$ films as a function of stoichiometry, structure and thickness. The magnetic moment being directly proportional to the film thickness, we must imperatively eliminate this deceiving effect via the calculation of M in order to directly access the physical phenomena at play. In some cases, the magnetization curves will be represented as the normalized magnetization with respect to the saturation magnetization, M/M_S (taken at the highest possible applied field $\mu_0 H = 2.2$ T). Plotting $M/M_S(H)$ is particularly useful when comparing the coercive fields of various samples with different magnetic moments.

The VSM measurement technique has a few particularities that must not be ignored when interpreting the data. First, in order to obtain the correct value of the measured magnetic moment, the VSM must first be calibrated with a reference. For this we use a small sample of nickel for which the saturation magnetization M_S is rigorously established. This reference sample, which was furnished with the apparatus, has the exact dimensions for optimized signal detection. Nevertheless, the samples that we have studied throughout this work do no have this precise geometry. As a consequence, the value of μ that we measure experimentally is slightly modified depending on how the sample was mounted on the sample holder. We can however obtain a precise measurement of M_S by calibrating the VSM measurements with another magnetic measurement such as SQUID or PNR.

A final detail to consider is that the raw data provided by the VSM is not a direct measurement of the deposited thin film, but rather a superposition of the pyrex sample holder, the tape used to hold the sample in place, the sapphire substrate and the film. Because the combination of the sample holder and substrate contribute a diamagnetic signal (negative slope) to the raw data, this slope must be removed in order to access the signal due solely to the deposited layer.

3.4.2 Polarized Neutron Reflectometry

Polarized Neutron Reflectometry (PNR) [1] is an extremely valuable technique for measuring the magnetic configuration of multilayer systems. In addition to accessing the magnetization amplitude and direction in each layer,

[1] The PNR measurements in this thesis were performed at the Laboratoire Léon Brillouin at CEA-Saclay.

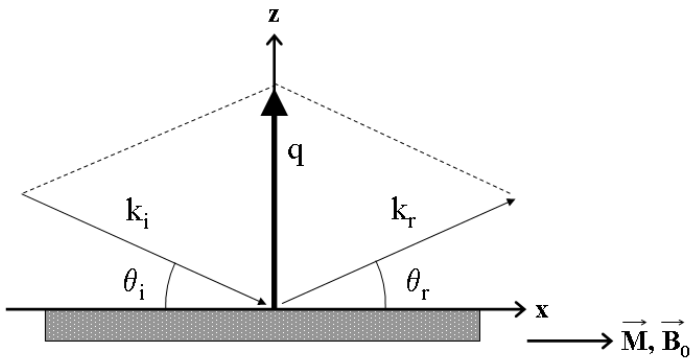

Fig. 3.8: Geometry of a specular reflectivity measurement. A PNR experiment measures the magnetic field perpendicular to the moment transfer vector q_z, which corresponds to the in-plane magnetization of the sample.

PNR provides magnetic and density depth profiles, and the absolute measurement of μ with a resolution of 0.1 μ_B. The main limitation of this technique is that it is only sensitive to in-plane magnetization.

PNR is a specular reflection technique, in which a beam of polarized neutrons is aimed at the sample surface with an incident angle θ_i and is reflected at the same angle $\theta_r = \theta_i$. The reflection may be described by a momentum transfer vector q_z which describes the change in momentum of a reflected neutron after interacting with the atoms in the sample :

$$q_z = \left(\frac{4\pi}{\lambda}\right) sin\theta_i \tag{3.5}$$

were λ is the neutron wavelength and z is the direction perpendicular to the plane of the film. The geometry of a PNR measurement is schematized in Figure 3.8. A typical PNR curve therefore plots the reflected intensity as a function of q_z. In our studies we consider the neutrons that conserve their incident spin orientation after scattering. These are called R^{++} and R^{--} for the "up-up" and "down-down" reflectivity curves respectively, and probe the magnetization of the sample parallel to the applied magnetic field.

Because neutrons are particles with a spin, they not only interact with the nuclei of the atoms in the material, but also with the magnetic field created by the unpaired electrons in magnetic atoms ($\mu_0\vec{M}$). Using a simple model, the neutron-matter interaction in an externally applied magnetic field ($\vec{B}_0$) may therefore be described by the sum of three components :

$$V(r) = V_N(r) + V_M(r) + V_Z(r) \tag{3.6}$$

where V_N, V_M and V_Z are the potentials created by the nuclear interaction, the magnetic interaction and the Zeeman interaction respectively.

These three interactions are further described as follows :

$$V_N(r) = b_n \left(\frac{2\pi\hbar^2}{m} \right) \delta(\vec{r}) \tag{3.7}$$

where b_n as the neutron scattering factor for a particular nucleus, m the neutron mass and $\vec{r}$ the position of the neutron.

$$V_M(r) = -g_n \mu_n \vec{\sigma} \cdot \mu_0 \vec{M} \tag{3.8}$$

where g_n is the neutron nuclear Landé factor, μ_n the nuclear magnetron and $\vec{\sigma}$ the Pauli operator associated to the neutron spin.

$$V_Z(r) = -g_n \mu_n \vec{\sigma} \cdot \vec{B}_0 \tag{3.9}$$

From these equations we can see that the reflectivity curve will depend on the type of atoms in the material (through b_n) as well as the magnetic properties of the sample (through $\mu_0 \vec{M}$). It is important to note that the neutron scattering factor b_n does not increase systematically with increasing atomic mass, unlike the x-ray scattering factor. This means that two elements side by side on the periodic table may have very different scattering factors and thus be easily distinguished by PNR. This was especially useful in the study of our $CoFe_2O_4/Fe_3O_4$ bilayers, in which the two layers were readily distinguishable thanks to the different scattering factors of Co and Fe ($b_{Fe_3O_4} = 51.6$, $b_{CoFe_2O_4} = 44.6$). Finally, PNR is also sensitive to surface and interface roughness effects, thus providing a complementary analysis to other structural characterization techniques.

3.5 Electronic Transport and Spin-Polarized Tunneling

3.5.1 In-plane electronic transport

The basic electronic transport properties of our $CoFe_2O_4$ single layers and multilayer systems were studied in a Quantum Design Physical Properties Measurement System (PPMS) especially designed to measure the electronic properties of magnetic single crystals and thin films in an applied magnetic field up to ± 7 T. Low temperature measurements down to 2 K could be performed thanks to an advanced cryogenic system consisting of both a liquid

nitrogen dewar and a liquid helium dewar. Using the built-in electronics of the PPMS, DC resistance measurements were possible up to 4 MΩ in the four-terminal configuration (see Section 3.5.2). However, with the aid of external Keithley current-voltage sources (K2400, K6514), the resistance limit increased to the GΩ range in the two terminal configuration.

Our study of the transport and magneto-transport properties consisted in two main types of measurements :

1. Resistance versus temperature ($R(T)$), from 2 to 300 K, without applied magnetic field. These served to identify the insulating behavior of our ultra-thin $CoFe_2O_4$ films.

2. Resistance versus applied magnetic field ($R(H)$) at constant temperature. These provided information about the intrinsic magnetoresistance (MR) in our films, calculated using the following definition of MR:

$$MR(\%) = 100 \times \left(\frac{R_H - R_0}{R_0} \right) \tag{3.10}$$

where R_H and R_0 are the measured resistances at a given applied field and at zero field respectively.

All samples were connected for measurements in the current-in-plane (CIP) geometry using either silver paste or indium pressed directly on the film surface for the electrical contacts. Samples were mounted on sample holders especially designed for the PPMS system, allowing for three samples for be measured at a time.

3.5.2 Two Terminal Versus Four Terminal Measurements

There are two different electrical configurations that may be used to obtain a resistance measurement. The simplest of the two, called a "two terminal" measurement, consists in applying a voltage (or a current) in between two electrical contacts, and measuring the induced current (or voltage). The resistance derived from Ohm's law is the sum of the resistance of the sample and the contacts :

$$R = R_{sample} + \sum R_{contact} \tag{3.11}$$

When $\sum R_{contact}$ is negligible with respect to R_{sample}, a two terminal measurement is sufficient to measure R_{sample}. However, as soon as the two resistances are comparable, a different configuration is necessary in order to obtain a precise measurement of the sample.

In order to eliminate the contact resistance, the "four terminal" configuration is preferable. Here two contacts serve to pass a current across the

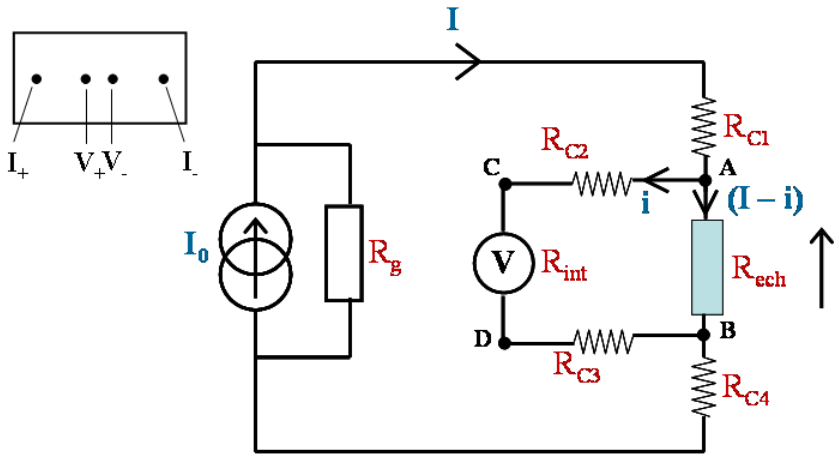

Fig. 3.9: Representation of the four terminal measurement set-up. In the equivalent circuit diagram, A and B are the current contacts (I_+, I_-) and C and D are the voltage contacts (V_+, V_-).

sample, while the induced voltage is measured across two other contacts. Figure 3.9 contains a diagram of the equivalent circuit in a four terminal measurement. If we solve this circuit for the sample resistance, we find :

$$R_{sample}(I - i) = (R_{C2} + R_{C3})i + V_{mes} \tag{3.12}$$

where I is the current applied by the two exterior contacts, i is the current that passes through the voltmeter, and V_{mes} is the measured voltage. The impedance of the voltmeter being extremely high, i is negligible and the contact resistances R_{C2} and R_{C3} may be ignored.

3.5.3 Sample Preparation for TMR Experiments : Optical Lithography

The most significant electronic transport experiments presented in this thesis are those involving tunneling transport across our $CoFe_2O_4$ barriers. Unlike the basic CIP resistance measurements described in Section 3.5.1, tunneling experiments require the samples to be patterned into micron-scale junctions in order to guarantee a barrier free of pin holes that destroy the tunneling effect. For this, two different patterning techniques were used depending on the type of measurement to be performed. For the experiments involving $CoFe_2O_4$-based MTJs (i.e. $Pt/CoFe_2O_4/Al_2O_3/Co$, $Pt/CoFe_2O_4/Fe_3O_4$), an advanced optical lithography technique was used to pattern junctions

ranging from 6 μm^2 to 128 μm^2 in area. The entire lithography procedure was done in the clean room facility at the CNRS/Thales Laboratory in Palaiseau, France.

The optical lithography process consists of four steps in which the junctions pillars are first defined, followed by the shape of the bottom and then top electrodes. The final step consists in depositing the circuitry used to connect the different junctions. In each of the four steps, the desired pattern was defined with the aid of a photoresistive resin which, when shielded from UV illumination by a mask and then developed with a chemical developer, is resistant to Ar etching thus retaining the structure defined by the mask. Before beginning the lithography process, and in between each of the four steps, the samples were cleaned with acetone and ethanol. The four steps are described here as follows :

1. **Definition of the junction pillars -** Using the photoresistive resin and mask technique described above, the pillars are defined on the unpatterned sample surface. An Ar beam etching is next carried out, etching down to the bottom electrode everywhere but where the pillars are defined. This process is controlled by a mass spectrometer, in order to be able to precisely stop the etching as soon as the bottom electrode is reached.

2. **Definition of the bottom electrodes -** In this step, the photoresist masking technique is used to define long strips that run across a row of pillars and form the bottom electrodes. This time, the unmasked portion of the sample is Ar-etched down to the substrate. After etching, a layer of Si_3N_4 ($\sim$200 nm) is deposited over the entire sample for electrical insulation.

3. **Opening of the junctions -** Following the deposition of the Si_3N_4, a hole must be opened in the insulator above the pillar in order to be able to connect the top electrode of the junction. This is done by reactive ion etching (RIE) of the Si_3N_4 by SF_6. The area to be etched is once again defined with the photoresist—the alignment of the mask with the patterned sample being extremely delicate as the holes must lie perfectly on top of the junction pillars.

4. **Deposition of the top contacts and circuitry -** In the final step, the circuitry is patterned not by etching, but by a lift-off technique. A photoresistive resin is once again deposited on the sample and then developed and removed only where the top contacts should go. Next a thick layer of gold is deposited over the entire sample. Finally the

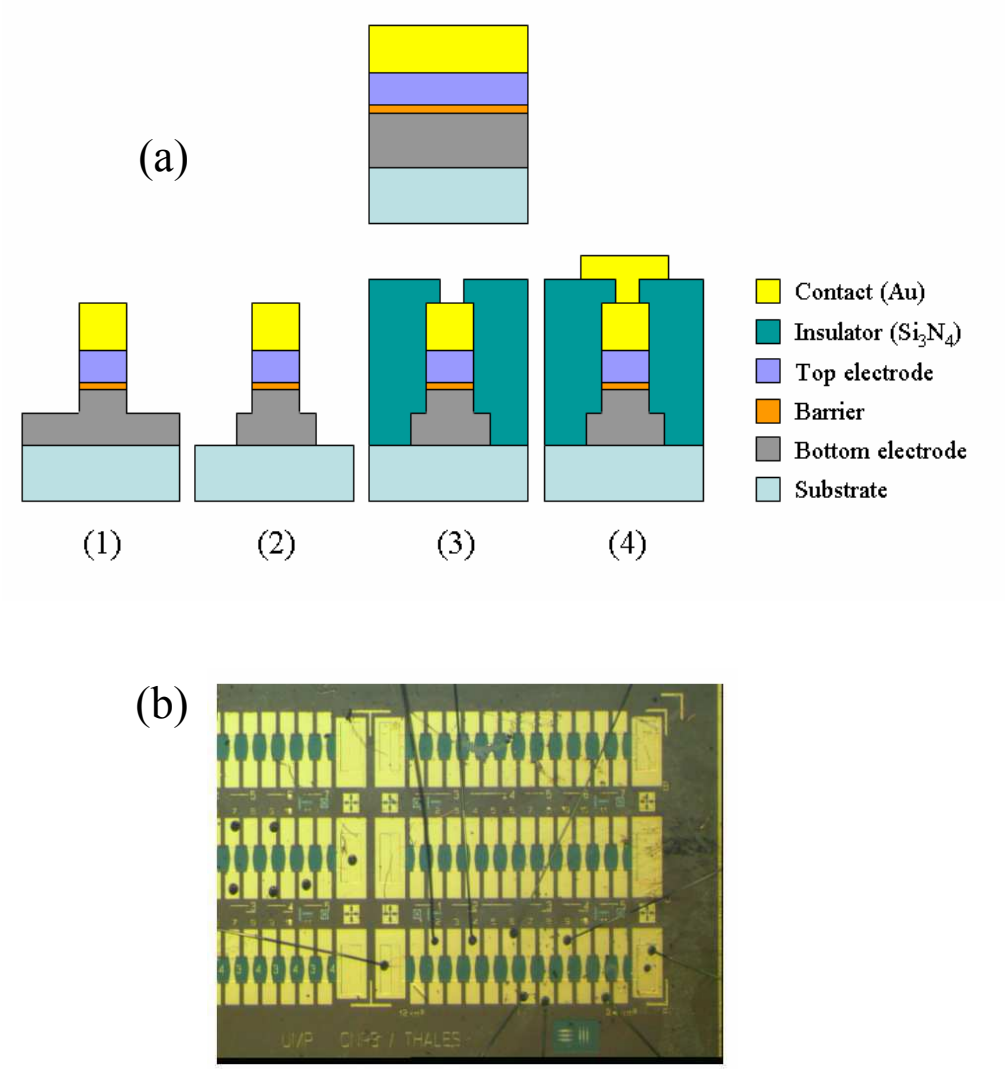

Fig. 3.10: (a) Schematic representation of the four steps of the optical lithography process. (b) Real image, obtained with an optical microscope, of a lithographically patterned sample after electrical connection using a wire bonder.

sample in rinsed in acetone, causing the area covered with resin to "lift off", taking the gold on top along with it. Only the areas containing no resin will therefore remain covered with gold for the electrical connection.

Figure 3.10-a schematically demonstrates a cross section of a sample at each of the four steps of the lithography process. Figure 3.10-b shows an image, obtained with aid of an optical microscope, of a sample after the complete lithography process. One may also identify a few gold wires that connect the top and bottom electrodes of the junction to the electronics. The wiring is connected with the aid of a wire bonder.

3.5.4 Out-of-plane Electronic Transport

TMR experiments were once again carried out at the CNRS/Thales Laboratory in Palaiseau, France. The experimental setup consisted of a cryostat allowing to measure down to 2 K, and an electromagnet capable of applying magnetic fields up to 7 T during resistance measurements.

3.5.5 Sample Preparation for Meservey-Tedrow Experiments

Because the Meservey-Tedrow technique is once again a tunneling experiment, the samples for these measurements needed to be patterned into small junctions as well. However, due to the complexity of this experiment, a simpler patterning technique using shadow masks was preferred over optical lithography. The sample preparation and Meservey Tedrow experiments were performed at the Francis Bitter Magnet Laboratory, MIT, Cambridge MA, USA. The scientists in this laboratory having discovered the Merservey Tedrow technique, their expertise was essential for the successful performance of the experiments on our $CoFe_2O_4$ spin filters.

The tunnel junctions studied by the Meservey-Tedrow technique contained $CoFe_2O_4/\gamma$-Al_2O_3 barriers, and used a thin superconducting Al layer as the spin analyzer. The growth of this thin Al film was critically important because its superconducting properties depend greatly on its structural and chemical quality. $Pt/CoFe_2O_4/\gamma$-Al_2O_3 multilayers were therefore prepared as described in Section 3.1 and then taken to MIT for patterning and deposition of a 4.2 nm Al top electrode in a separate thermal evaporation chamber. The process may be described in 3 steps as follows :

1. **Definition of a 3 mm strip -** The $Pt/CoFe_2O_4/\gamma$-Al_2O_3 system grown on sapphire is etched into a 3 mm strip running along the long

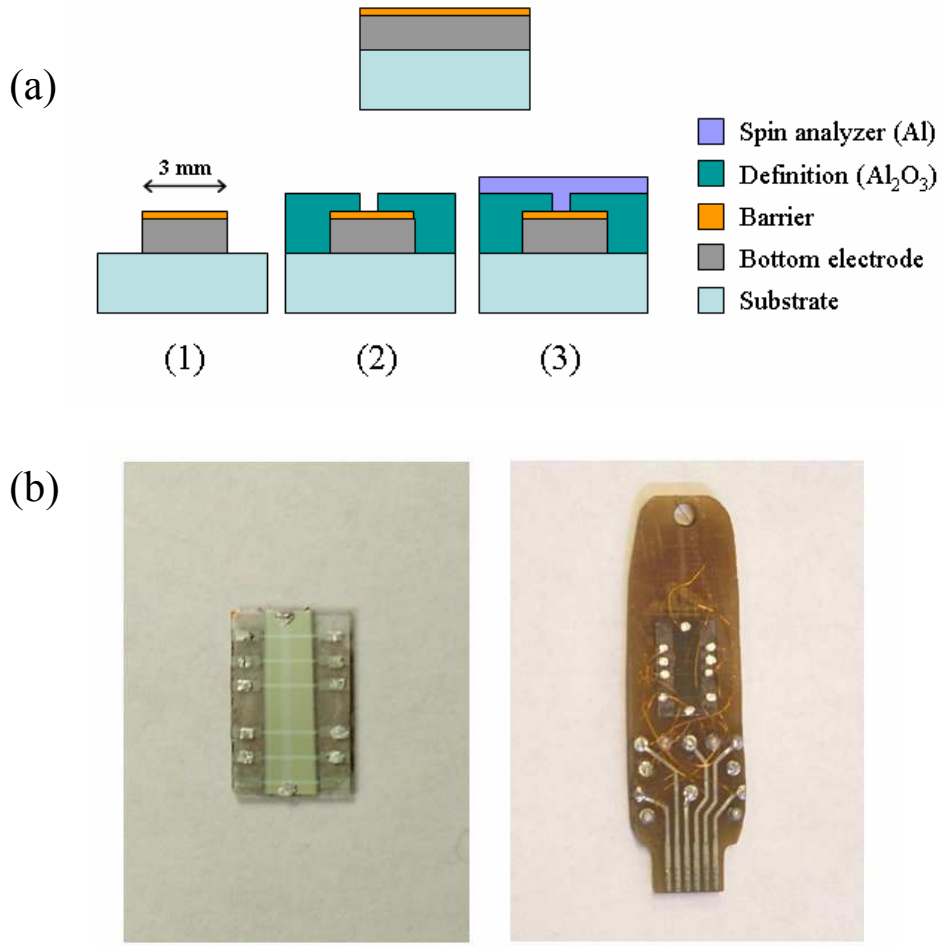

Fig. 3.11: (a)Illustration of the patterning process for the Meservey-Tedrow measurements. The bottom and top electrodes were defined using simple shadow masks. (b) Photograph of two patterned samples. The one on the left is not connected whereas the one on the right is, with the connections made with copper wire and pressed indium. Note that on the left, the long strip whose width was defined by the Al_2O_3 definition layer is visible.

edge of the substrate. This is done by Ar-ion etching, using a 3 mm wide piece of silicon wafer as a mask.

2. **Definition of the bottom electrode -** Before beginning this step, the surface of the exposed γ-Al_2O_3 layer is glow discharge cleaned in an oxygen plasma in order to minimize surface contamination from air. Next, an amorphous alumina definition layer is deposited from an electron beam source, allowing to define the junction width with a simple shadow mask.

3. **Deposition of the Al top electrode -** The sample is then liquid-nitrogen cooled to 77 K, and the 4.2 nm Al electrode deposited through another mask defining cross strips perpendicular to the bottom electrode. The end result is a heterostructure whose junction area is approxiamtely 500×150 μm^2.

Figure 3.11 once again schematically illustrates the Meservey-Tedrow patterning process, as well as showing a photograph of the final patterned and connected sample.

3.5.6 The Meservey-Tedrow Experiment

A successful Meservey Tedrow experiment requires the conductance measurement to be performed well below the T_c of the superconducting Al electrode ($\sim$2.6 K). For this a ^{3}He refrigerator placed inside a ^{4}He cryostat, schematically illustrated in Figure 3.12, was used to cool the samples down to 0.45 K. After lowering the sample into the ^{3}He refrigerator with the aid of a special probe, the refrigerator was evacuated and filled with ^{3}He gas. The temperature was then first lowered to 1.4 K by pumping down on the external ^{4}He bath, causing the ^{3}He to condense into a liquid in the sample space. Further pumping on the ^{3}He bath brought the temperature down to 0.45 K.

The insert of Figure 3.12 shows the equivalent circuit for the complete dI/dV measurement. Dynamic conductance measurements were necessarily performed in the two terminal configuration, for which a small AC voltage ($\sim$20 μV) was superimposed onto the DC voltage used to measure the junction. The resistor R_V acted as a voltage source for both the small AC and DC bias. The change in AC current through the junction was measured with a lock-in amplifier that detected the change in AC voltage across the series resistor R_S, and the result was plotted directly as a $dI/dV(V)$ curve. For the measurements with an applied magnetic field, the Al superconducting

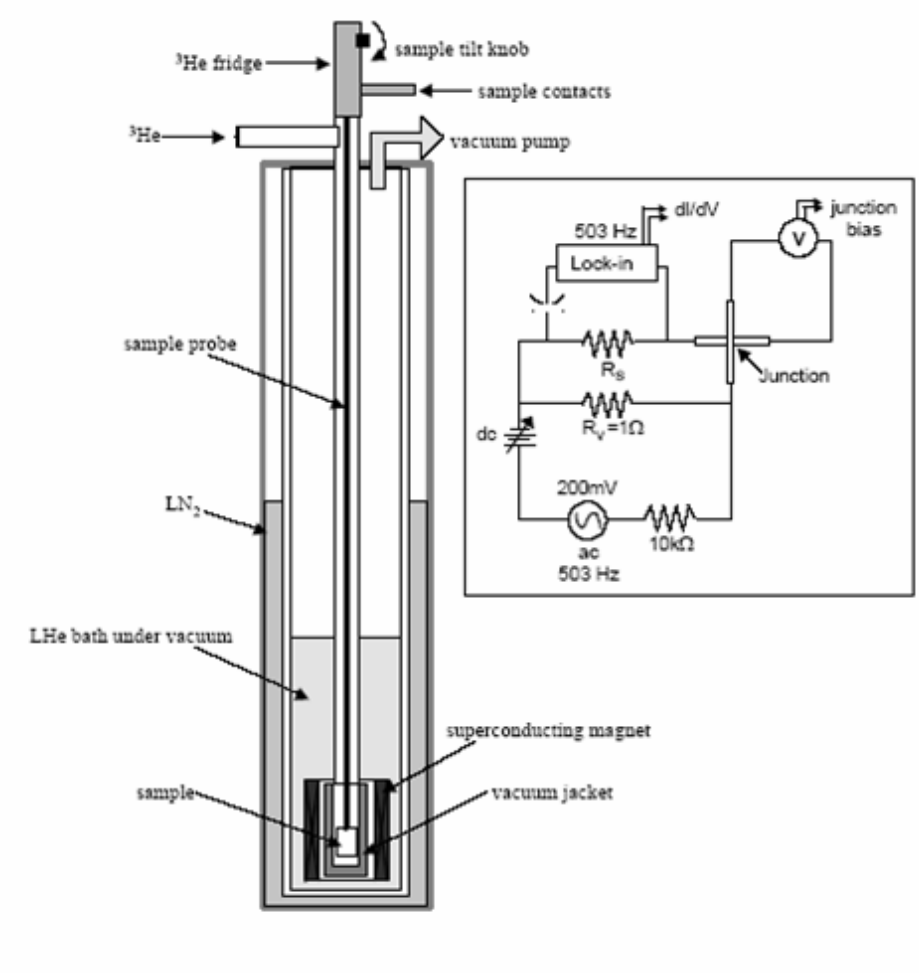

Fig. 3.12: Schematic illustration of the ^{3}He refrigeration used for the Meservey-Tedrow experiments. The custom-built pumping system on the ^{3}He bath allowed samples to be cooled down to 0.45 K. The inset shows the equivalent circuit diagram for the dI/dV versus V measurement in the Meservey-Tedrow technique. Illustration from [50].

film could be precisely aligned parallel to the field thanks to a gear system attached to the sample probe.

4. CHARACTERIZATION OF $CoFe_2O_4$ THIN FILMS AND ASSOCIATED MULTILAYERS

The following chapter presents a in-depth study of the structural and chemical properties of our epitaxial $CoFe_2O_4(111)$ thin films and $CoFe_2O_4$-based multilayers. While much of the experiments presented here may seem trivial or redundant, they are arguably the most important portion in this entire thesis. In fact, without the rigorous optimization of the materials properties of the different systems, none of the key results presented in Chapters 5-7 would have been possible. This is largely due to the complexity of the spinel ferrites, and in particular of $CoFe_2O_4$, whose magnetic and electronic properties are extremely sensitive to both structural and chemical defects. It is therefore imperative that we dedicate an entire chapter to this materials study. Chapter 4 will be broken down into three main sections : the first describing $CoFe_2O_4$ single layers, the second describing $CoFe_2O_4/Fe_3O_4$ bilayers, and the third describing $CoFe_2O_4/Al_2O_3/Co$ trilayers and their variants. These three sections correspond to the different tunnel junction systems discussed in the upcoming chapters.

4.1 $CoFe_2O_4$ Single Layers

4.1.1 Epitaxial Growth : RHEED In situ

The structural study of our epitaxial $CoFe_2O_4(111)$ thin films began inside the MBE growth chamber with *in situ* RHEED performed in real time throughout the entire deposition process. The RHEED patterns were studied along the $[10\bar{1}0]$ and $[1\bar{1}00]$ directions based in the hexagonal real space of the α-$Al_2O_3(0001)$ substrate. Figure 4.1 shows the RHEED patterns along both observation directions of a $CoFe_2O_4$(15 nm) film. Immediately after placing the substrate into the flow of metal and oxygen, smooth streaks corresponding to the (0, 1) and (1, 1)-type planes of the FCC sublattice are observed, indicating that film growth is two-dimensional as of its initial stages. Intermediate (0, 3/2) and (1/2, 1/2) streaks next appear after about 10-15 minutes, corresponding to a film thickness of about 2-3 nm, and revealing the characteristic RHEED pattern of the spinel structure. These

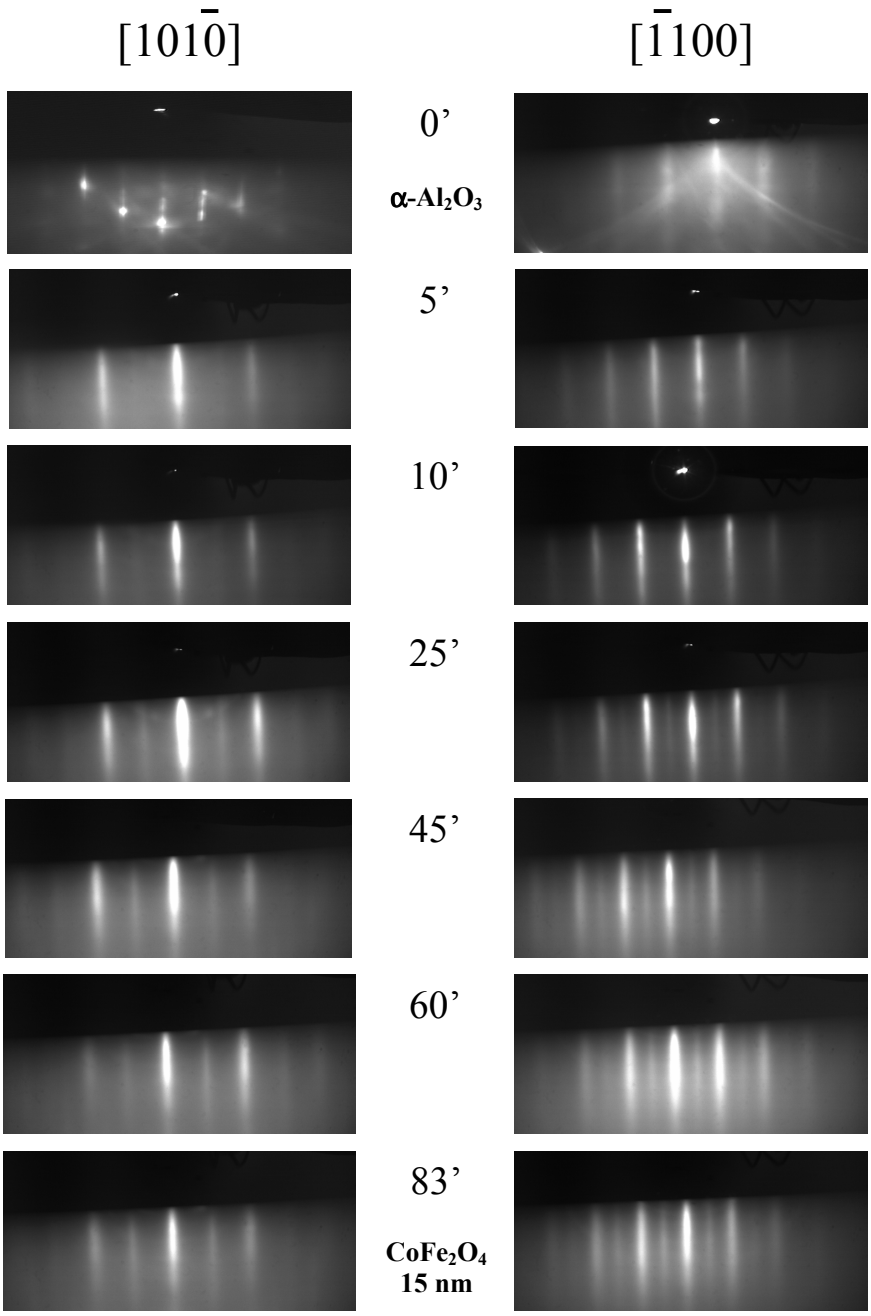

Fig. 4.1: RHEED patterns of a 15 nm $CoFe_2O_4(111)$ film observed along the (a) $[10\bar{1}0]$ and (b) $[1\bar{1}00]$ directions at various stages during growth.

intermediate streaks persist and intensify throughout the entire duration of the deposition, indicating that the desired spinel phase is maintained and that the growth mode remains two-dimensional.

A comparison of the relative spacing between the primary streaks in the RHEED patterns of the α-Al_2O_3 substrate and $CoFe_2O_4$ film allows us to calculate the relative lattice mismatch Δa using the following relationship :

$$\Delta a(\%) = \frac{d_{film} - d_{sub}}{d_{sub}} \tag{4.1}$$

where d_{film} and d_{sub} are the distances between the primary streaks of the film and substrate respectively [1]. The result, based on the RHEED patterns in Figure 4.1, is a mismatch of $8.25 \pm 0.75\%$ as soon as the intermediate spinel streaks appear. This value is in very good agreement with the expected mismatch of 8%, and thus suggests that the films are fully relaxed as of the beginning stages of growth. The fact that our $CoFe_2O_4$ films are fully relaxed (i.e. under no mechanical strain due to the α-Al_2O_3 interface) is very important because $CoFe_2O_4$ is known to be a highly magnetostrictive material [70, 71, 72]. Any epitaxial strain on the $CoFe_2O_4$ tunnel barriers could therefore modify their magnetic properties.

4.1.2 *In situ* Chemical Characterization by XPS

The primary control of the composition of our $CoFe_2O_4$ was performed *in situ* directly after film growth by XPS, which allowed us to verify the stoichiometry of the films before exposure to air. A Mg K_α X-ray source (1253.6 eV), rather than the more standard Al K_α (1486.6 eV), was the incident radiation of choice in order to avoid overlap with Auger peaks in the Co2p binding energy range. We focus our attention on the Fe2p and Co2p peaks in the XPS spectra, as is shown in blue in Figures 4.2 and 4.3 for $CoFe_2O_4$ single layers of 15 nm and 5 nm in thickness respectively. In the energy range corresponding to the Fe2p peak, the observation of a well-defined structure in between the two main $Fe2p_{3/2}$ (711 eV) and $Fe2p_{1/2}$ (724 eV) spin orbit components indicates the presence of Fe^{3+} cations. The shape of the Co2p also signals the presence of Co^{2+} rather than another oxidation state [67]. It is important to note that XPS spectra of the 5 nm layer (Figure 4.3) are identical to those of the 15 nm layer (Figure 4.2), indicating that the chemical quality has been optimized in our ultra-thin $CoFe_2O_4$ films. By

[1] The lattice mismatch may also be calculated using Equation 4.1, taking d_{film} and d_{sub} to be the distance between oxygen cations in the film and substrate sublattices. The O-O distances in $CoFe_2O_4(111)$ and α-$Al_2O_3(0001)$ are 2.97 Å and 2.75 Å respectively leading to $\Delta a = 8\%$ [64].

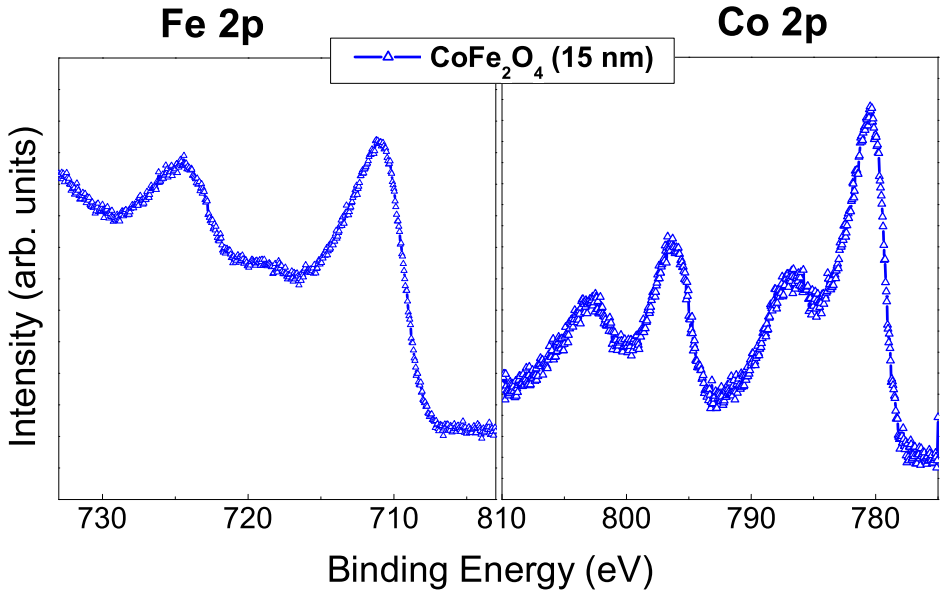

Fig. 4.2: XPS of a $CoFe_2O_4$(15 nm) single layer showing the Fe2p and Co2p peaks, and corresponding to the Fe^{3+} and Co^{2+} oxidation states respectively.

comparing the Fe2p and Co2p peak intensity ratios, we were also able to quantify the Co/Fe/O ratio in our films by fitting the experimental peaks, after background removal, using a standard Shirley function. In all cases, we obtained the correct composition within the accuracy limit of the XPS method, that is within 10% of the expected 14/28/58% ratio.

The complete XPS study of the $CoFe_2O_4$ single layers therefore confirms the proper oxidation state of the Co and Fe atoms as well as their overall composition, validating the specific growth conditions used to elaborate the films. However, it does not give any information about the interstitial site distribution of the Co^{2+} and Fe^{3+} cations—that is, whether they occupy tetrahedral, octahedral or both sites. This shortcoming of the XPS technique must not be ignored because, as was described in Chapter 2, the magnetic properties and electronic band structure of $CoFe_2O_4$ depend drastically on the cationic site distribution [57]. Complementary spectroscopic measurements using a synchrotron light source (see Section 4.1.4 : *X-ray absorption and X-ray Magnetic Circular Dichroism*) are thus necessary to fully understand the chemical order of our $CoFe_2O_4$ thin films.

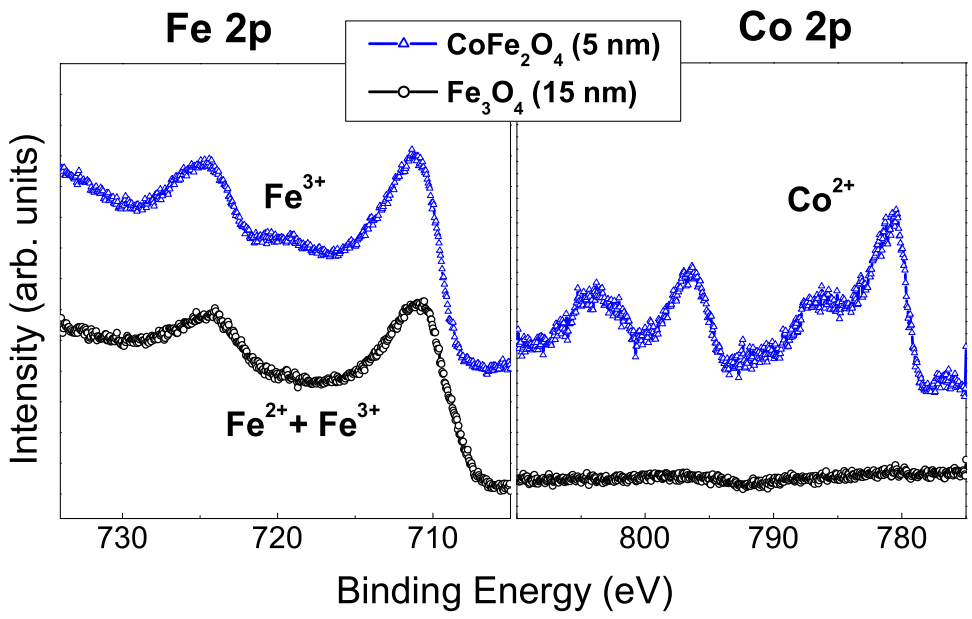

Fig. 4.3: Fe2p and Co2p XPS peaks in a $CoFe_2O_4$(5 nm)/Fe_3O_4(15 nm) bilayer sample. The XPS spectra for the $CoFe_2O_4$ bottom layer alone (triangles) were obtained before subsequent deposition of the Fe_3O_4 top layer (circles), and are thus representative of an ultra-thin $CoFe_2O_4$ single layer.

4.1.3 X-ray Diffraction and Reflectivity

The structural properties of our $CoFe_2O_4$ thin films were studied by X-ray diffraction, X-ray reflectivity and later TEM (see Section 4.2.2). These different techniques allowed us to verify that the basic properties of film thickness, structure and crystallographic orientation, characterized *in situ* from the RHEED patterns, were reproducible once the samples were removed from the UHV chamber. We note that while the RHEED analysis was of critical importance during film deposition, it represents a highly localized area on the sample surface. The additional structural measurements were therefore necessary to be sure that the bulk of the films did not evolve over the course of the deposition, or after exposure to air. Furthermore, the ensemble of the *ex situ* structural measurements offer additional information about film homogeneity, possible unwanted phases, and structural defects.

Figure 4.1.3-a shows a XRD θ-2θ scan for a $CoFe_2O_4$(15 nm) sample deposited directly on an α-Al_2O_3(0001) substrate. Only the [111] family of reflections emerge from the spinel layer, confirming the unidirectional, epitax-

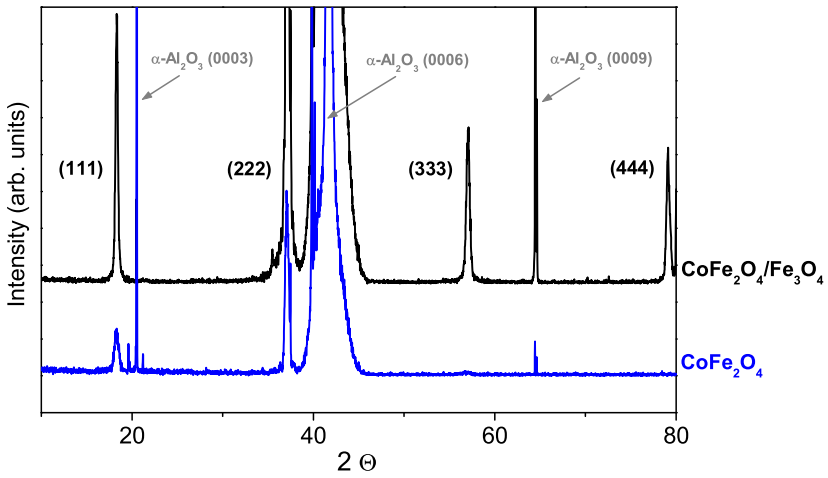

Fig. 4.4: XRD 2-θ scans for a $CoFe_2O_4$(15 nm) single layer (bottom, blue) as well as a $CoFe_2O_4$(5 nm)/Fe_3O_4(15 nm) bilayer (top, black). Both samples were grown directly on α-Al_2O_3(0001) substrates.

ial growth by MBE. In addition, the diffraction patterns of the two bilayers show no trace of parasitic phases throughout the films which rules out the possibility of the formation of oxides such as Co_2O_3 or CoO whose structures differ from the spinel. Identification of the XRD peak-angle locations and application of the Bragg law allowed us to calculate a lattice parameter a of 8.395Å for the $CoFe_2O_4$ single layers, in very good agreement with the generally reported bulk value of 8.392 Å.

X-ray reflectivity measurements additionally allowed us to verify the film thicknesses predicted from the calibration of the atomic fluxes in our MBE setup. In all cases, we successfully fitted the periodicity of the reflectivity oscillations to find thicknesses that agree with the expected values and with a roughness of $\sigma_{rms} = 0.35$ nm for a 15 nm $CoFe_2O_4$ single layer. This remarkably low value lends itself very well to the growth of more complex epitaxial heterostructures.

4.1.4 X-ray Absorption and X-ray Magnetic Circular Dichroism

As was mentioned in Section 4.1.2, the most important chemical information missing from the *in situ* XPS experiments, was the interstitial site distribution of Co^{2+} and Fe^{3+} cations. The site distribution is a particularly

crucial point to consider in the case of $CoFe_2O_4$ spin filter tunnel barriers because electronic band structure calculations predict that the magnetic moment, the band gap and the exchange splitting in the conduction band all change significantly when passing from the inverse spinel to the normal spinel structure [57]—that is, when the Co^{2+} cations go from octahedral to tetrahedral sites (see also Chapter 2, Section 2.4.3). Each of these parameters, in turn, is a determinant factor for the spin filter characteristics of this material.

In order to access the cationic site distribution in our ultra-thin $CoFe_2O_4$ films, we performed X-ray absorption (XAS) and X-ray magnetic circular dichroism (XMCD) experiments at the ESRF synchrotron light source in Grenoble, France. Very briefly, the XMCD spectrum is determined by subtracting two X-ray absorption spectra obtained at a given absorption edge of the selected element: one XAS spectrum is obtained using right circularly polarized light, while the other uses left circularly polarized light. Close analysis of the difference in the two XAS spectra yields information about the local geometry about the selected atom, as well as information about the spin and orbital magnetic moments. In the case of Co and Fe, the XAS and XMCD are commonly measured at the $L_{2,3}$ absorption edge, which corresponds to the excitation of a 2p electron into a 3d state. Because the 3d electron states are responsible for the magnetic properties of the elements, the XAS and XMCD spectra allow us to access their magnetic properties. In the present study, we will show only a qualitative analysis of the Fe $L_{2,3}$ and Co $L_{2,3}$ spectra, allowing us to identify their interstitial site placement. Further studies are in progress using ligand-field multiplet calculations [2] in order to extract information about the magnetic properties of the individual cations.

Figures 4.5-a,b show the Fe $L_{2,3}$ edge XAS and XMCD spectra obtained for a $CoFe_2O_4$(5 nm)/γ-Al_2O_3(1.5 nm) film deposited directly on α-Al_2O_3 and measured in a magnetic field of 0.5, 2 and 3 T at 10 K. The spectra were recorded in the total electron yield mode, allowing us to probe the extreme surface (3-4 nm) of the sample, and thus the $CoFe_2O_4$ layer. Comparing the experimental data with reference spectra for the different iron oxides shown in Figure 4.5-b, we immediately see a close resemblance with the XMCD signal of γ-Fe_2O_3. γ-Fe_2O_3 is itself a spinel oxide (similar to γ-Al_2O_3) containing only Fe^{3+} cations distributed in both octahedral and tetrahedral sites, which agrees very well with the oxidation state and site distribution expected for the Fe cations in $CoFe_2O_4$. The fact that we observe a close resemblance

[2] Future ligand-field multiplet calculations will be performed in collaboration with M.-A. Arrio and P. Sainctavit at the Laboratoire de minéralogie-cristallographie de Paris CNRS/IPGP/UPMC/UDD, and with L. Calmels at the CEMES/CNRS Toulouse.

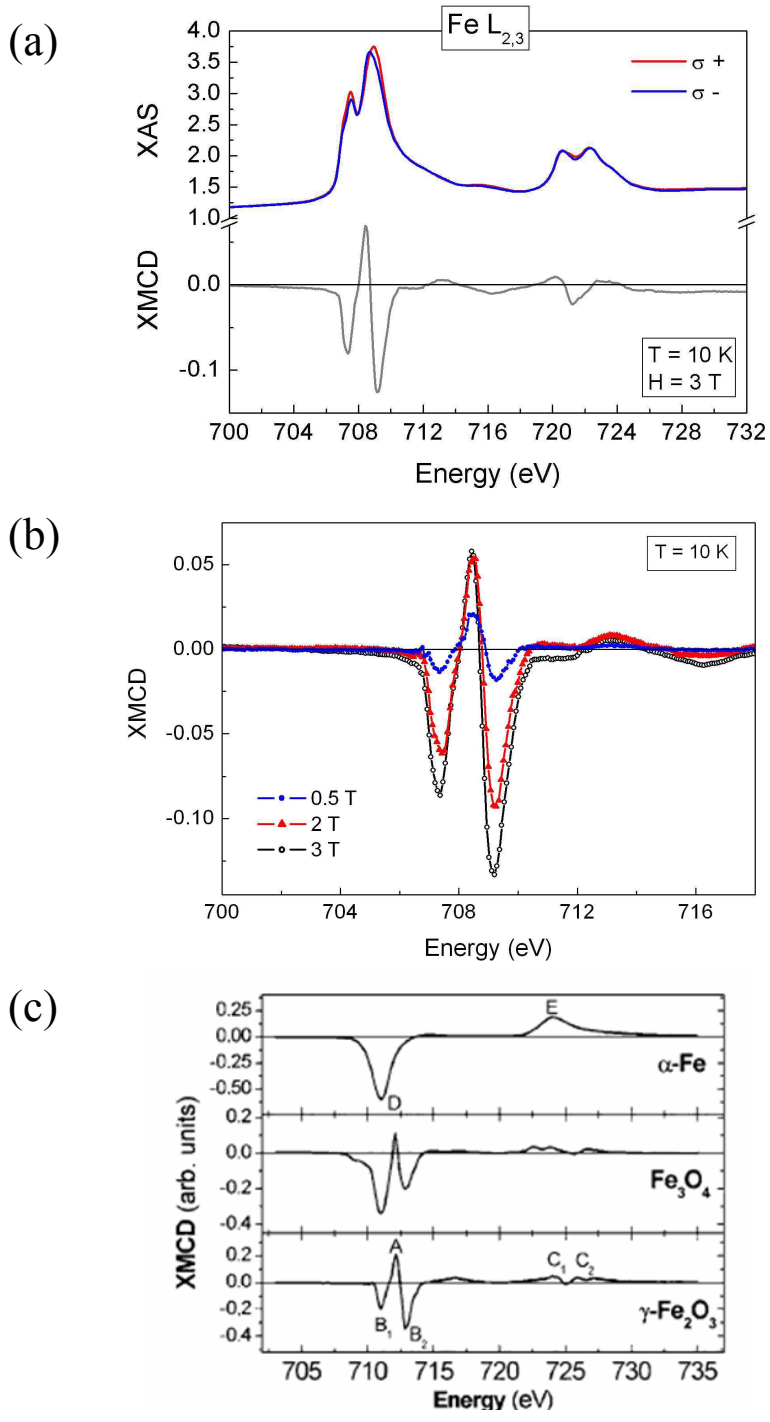

Fig. 4.5: XAS and XMCD spectra at the Fe $L_{2,3}$ absorption edge. (a) Experimental data for a $CoFe_2O_4$(5 nm)/γ-Al_2O_3(1.5 nm) layer measured at 10 K in a magnetic field of 3 T. (b) Experimental XMCD spectra of the same sample in various applied magnetic fields. (c) Reference XMCD Fe $L_{2,3}$ spectra for the different iron oxides taken from [73].

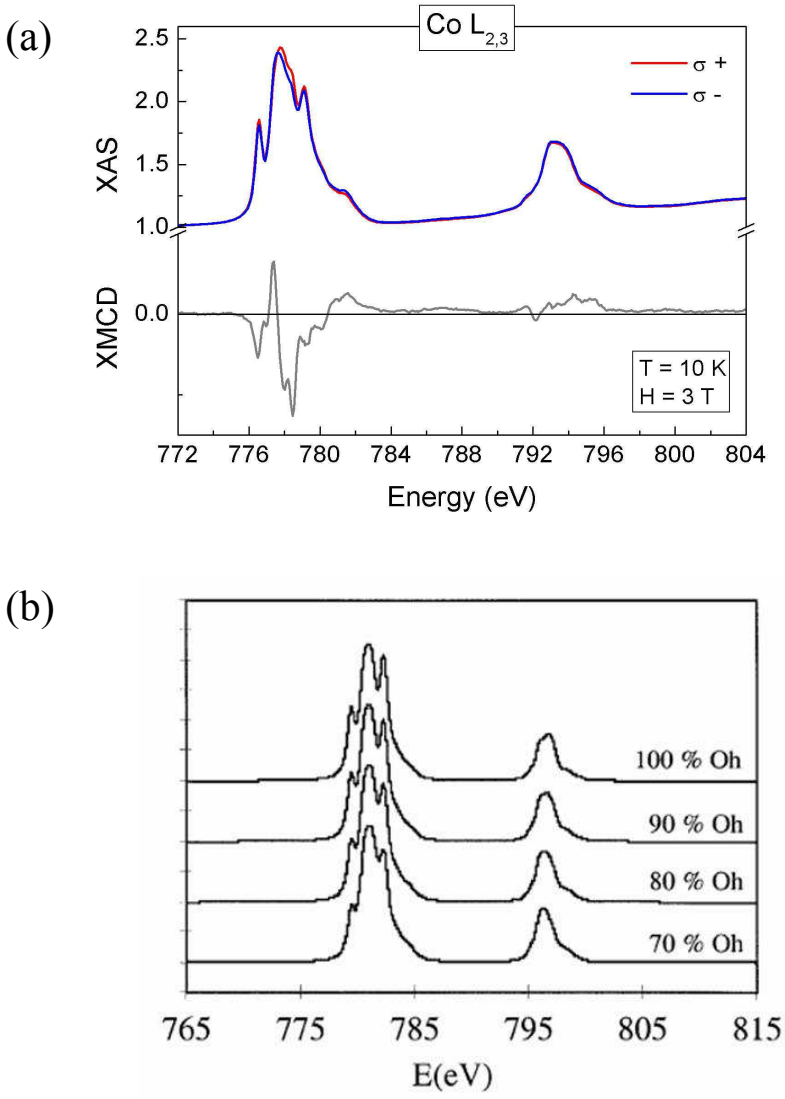

Fig. 4.6: XAS and XMCD spectra at the Co $L_{2,3}$ absorption edge. (a) Experimental data for the same $CoFe_2O_4$(5 nm)/γ-Al_2O_3(1.5 nm) layer as in Figure 4.5 with $T = 10$ K, $H = 3$ T. (b) Calculated XAS spectra using ligand multiplet theory at the Co $L_{2,3}$ edge, and for different values of octahedral site occupation (from [74]).

between these two spectra therefore suggests that we do indeed have an inverse spinel $CoFe_2O_4$ containing fully oxidized Fe^{3+}. Another interesting observation is that the intensity of XMCD signal decreases significantly when then magnetic field is reduced from 3 T to 0.5 T (Figure 4.5-b). This suggests that the $CoFe_2O_4$ film has a very low remanent magnetization, which will be later confirmed in the magnetic characterization by VSM and SQUID in Chapters 5 and 7. Finally, another series of measurements performed at 300 K (not shown) reveal XAS and XMCD spectra very similar to those at low temperature, indicating that the magnetic properties do not vary significantly with temperature. This once again agrees well with the VSM and SQUID measurements to follow.

Also as convincing are the XAS and XMCD spectra obtained at the Co $L_{2,3}$ edge. In this case, we compare the XAS spectra (measured with $\mu_0 H$ = 3 T and T = 10 K) to theoretically calculated reference spectra for Co^{2+} situated in octahedral sites in varying concentrations (Figures 4.6-a,b). The shape and intensity of the different components of the experimental XAS spectrum most closely resemble those of the theoretical spectra containing Co^{2+}_{OCT} in high (100% or 90%) concentration. This result tells us that, not only have we confirmed the 2+ oxidation state of the Co cations, but that the vast majority are located in octahedral interstitial sites, thus confirming the inverse spinel structure of our $CoFe_2O_4$ thin films. The observation of an inverse spinel $CoFe_2O_4$ agrees well with the magnetic moment and insulating behavior measured in our ultra-thin films, as will also be discussed in detail in Chapter 5. This important determination of the cationic site distribution will be extremely valuable for the later interpretation of the spin filter characteristics of our $CoFe_2O_4$ tunnel barriers (see Chapters 5 and 7).

4.1.5 Growth on a Pt(111) buffer layer

Finally, it is worth noting that the growth of $CoFe_2O_4$ may be significantly improved by depositing an epitaxial Pt(111) buffer layer on the α-Al_2O_3(0001) substrate [3]. This is clearly seen in the RHEED patterns, where the intermediate spinel streaks appear much more rapidly (within the first 5 minutes) and are more intense than in the case of $CoFe_2O_4$ deposited directly on α-Al_2O_3 (See Figure 4.12-b for an example of a $CoFe_2O_4$(111)(3 nm) film grown on Pt(111)(20 nm)). XRD measurements of the Pt/$CoFe_2O_4$ samples also reveal 2-θ scans in which the diffraction peaks are narrower, further indicating improved structural quality in these films. By depositing our $CoFe_2O_4$ films on Pt(111), we are therefore able to reduce their thickness down to 3 nm,

[3] Pt(111) buffer layers were grown using the sputtering technique at the Unité Mixte de Physique CNRS/Thales in Palaiseau, France.

while maintaining structural and chemical properties comparable to those of thicker films deposited directly on α-Al_2O_3. In this manner, we optimize our $CoFe_2O_4$ layers for use as a tunnel barriers.

The positive effect of the Pt underlayer has previously been observed in the growth of other iron oxides such as Fe_2O_3 [75], and has been attributed to a decreased number of structural defects such as misfit dislocations and antiphase boundaries in the iron-oxide layer. The magnetic properties of $CoFe_2O_4$ being so sensitive to its structural quality, we expect the growth of our $CoFe_2O_4(111)$ barriers on the Pt buffer layers to lead to improved magnetic behavior, as will be discussed in Chapter 5.

4.2 $CoFe_2O_4/Fe_3O_4$ Bilayers

$CoFe_2O_4(111)/Fe_3O_4(111)$ bilayer samples were fabricated with the intention of optimizing their structural, chemical and magnetic properties for the insertion into the fully epitaxial MTJ system : $Pt(111)/CoFe_2O_4(111)/Fe_3O_4(111)$. Here $Fe_3O_4(111)$ plays the role of ferromagnetic counter electrode. The interest of the $CoFe_2O_4$ barrier/Fe_3O_4 electrode combination lies in several unique properties of the two spinel ferrites. The predicted half-metallic behavior of Fe_3O_4 [76] makes it a very good candidate for an electrode material with high spin polarization at room temperature. Furthermore, the nearly identical structure of these two materials is expected to lead to an epitaxial system with a near-perfect interface, minimizing detrimental effects of interface anomalies on the polarization of one or both of the ferrimagnetic layers. The correlation between the structural and chemical properties and the magnetic behavior (presented in Chapter 6) will thus be critical to understanding future magnetotransport measurements on this system.

4.2.1 RHEED and XPS

The RHEED and XPS analysis of our epitaxial $CoFe_2O_4(111)/Fe_3O_4(111)$ bilayers was quite similar to that of the $CoFe_2O_4(111)$ single layers. We will thus only present a brief overview of the principal results of these measurements before continuing on to the more significant microscopy studies.

The growth of the $CoFe_2O_4(111)/Fe_3O_4(111)$ bilayers was systematically performed in one step inside the MBE chamber, allowing us to follow the RHEED patterns of both layers without interruption. Because Fe_3O_4 has the same spinel structure and nearly-identical lattice parameter as $CoFe_2O_4$, no significant change in the RHEED patterns is observed when passing from

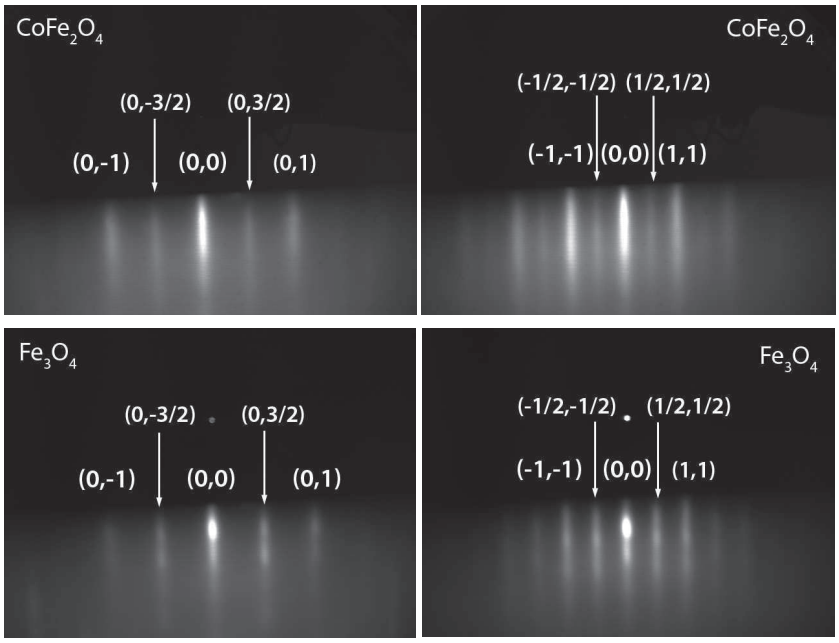

Fig. 4.7: RHEED patterns of a $CoFe_2O_4$(5 nm)/Fe_3O_4(15 nm) bilayer sample along $[10\bar{1}0]$ (left) and $[1\bar{1}00]$ (right). Here the RHEED patterns were obtained once the deposition of each individual layer was finished. The intermediate (0, 3/2) and (1/2, 1/2) streaks have been labeled for clarity.

one layer to the other, as may be clearly seen in Figure 4.7. The only eventual evolution, in the case of Fe_3O_4, is that the intermediate streaks ultimately attain the same intensity as the primary streaks whereas in the case of $CoFe_2O_4$, these streaks remain less intense throughout the entire deposition. This discrepancy in the RHEED patterns of $CoFe_2O_4$ and Fe_3O_4 has been observed in previous studies using different deposition methods [59], but the origin remains unclear. Once again the real time, *in situ*, RHEED analysis demonstrates the successful two-dimensional, epitaxial growth of our $CoFe_2O_4(111)/Fe_3O_4(111)$ bilayers on α-$Al_2O_3(0001)$ substrates.

In situ XPS measurements of our $CoFe_2O_4/Fe_3O_4$ bilayers were exceptionally performed with an interruption after the growth of each layer, allowing us to verify the chemical state of the bottom and top layers directly after their respective depositions. The second layers were deposited only after the stoichiometry of the bottom layers was mastered, as was described in Section 4.1.2. The main goal of this study was to verify the existence of two distinct $CoFe_2O_4$ and Fe_3O_4 layers without intermixing of the Co atoms. The black spectra in Figure 4.3 show the Fe2p and Co2p peaks of the top Fe_3O_4 layer in

a $CoFe_2O_4$(5 nm)/Fe_3O_4(15 nm) bilayer sample. The evolution of the Fe2p peak from $CoFe_2O_4$ to Fe_3O_4 may be clearly identified, with the intermediate satellite completely disappearing in the case of Fe_3O_4. The smooth plateau in between the $Fe2p_{3/2}$ and $Fe2p_{1/2}$ main peaks thus indicates the presence of Fe^{2+} and Fe^{3+} in equal proportion, as is expected for Fe_3O_4. Furthermore, the XPS spectrum of the top Fe_3O_4 layer lacks any signal in the Co2p energy range. Because XPS allows us to probe the top 3 nm of the 15 nm upper layer, we may thus conclude that there is no large scale diffusion of cobalt into and across the Fe_3O_4 film. Of course, we must be weary of this analysis because XPS measurements in this system do not probe the Fe_3O_4 layer down to the interface with $CoFe_2O_4$. More precise chemical measurements were therefore necessary to prove the existence of a clean bilayer interface, free of Co interdiffusion (See Section 4.2.2).

4.2.2 Microscopy studies of $CoFe_2O_4/Fe_3O_4$

TEM

The structural properties of our $CoFe_2O_4$ thin films and $CoFe_2O_4/Fe_3O_4$ bilayers were carefully studied by TEM. Because the TEM results for the $CoFe_2O_4$ single layers were identical to the $CoFe_2O_4/Fe_3O_4$ bilayers, we will focus our discussion on the latter of the two, which are representative of both systems. Images at both high and low magnifications were taken over a significant portion of each of the films allowing for a detailed analysis representing the entirety of the samples.

In the plane view, we began by looking at the diffraction pattern of our bilayer system, which immediately revealed its remarkably high epitaxial quality . Figure 4.8 shows the diffraction pattern of a $CoFe_2O_4(111)/Fe_3O_4(111)$ bilayer sample, in which all of the principal spots have been identified, demonstrating the perfect superposition of the spinel lattice on the hexagonal α-Al_2O_3 substrate. From this pattern, we recognize the $2/\sqrt{3} \times 2/\sqrt{3}R30$ epitaxial relationship schematized in Figure 3.2 and corresponding to the experimentally measured RHEED patterns in Figure 4.7. The existence of Moiré interference spots with six-fold symmetry about the α-Al_2O_3 peaks further testifies to the high epitaxial quality of the samples. This figure is representative of all of the samples presented in this work and proves that we have successfully grown single crystalline epitaxial spinel films.

In the cross-sectional view, the samples were prepared along the $[11\overline{2}]$ zone axis for observation at low magnification and high resolution (HRTEM). Figure 4.9-a shows a low magnification micrograph of a $CoFe_2O_4/Fe_3O_4$ sample in which one may easily identify the oxide film which is perfectly homoge-

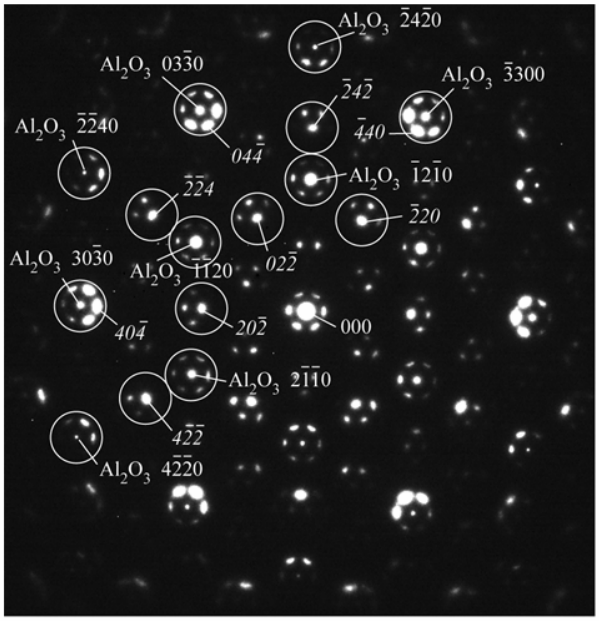

Fig. 4.8: TEM plane view diffraction pattern of a $CoFe_2O_4$(5 nm)/Fe_3O_4(15 nm) bilayer grown on α-Al_2O_3. The diffraction spots corresponding to each of the constituents have been identified. Those belonging to the spinel films are labeled only with numbers, whereas those belonging to the sapphire substrate contain the addition label "Al_2O_3".

neous and smooth across nearly one micron of substrate surface. In the case of the bilayer samples, we do not see any contrast at the $CoFe_2O_4$/Fe_3O_4 interface. This observation is contrary to that published in a previous study by Chapline *et al.*, who in similar $CoFe_2O_4$/Fe_2O_4 bilayers with a (001)-directional growth observed a continuous line which delimits the two spinel films [77]. This result is somewhat surprising as one would expect that, in the case of a fully epitaxial system, the extreme similarity in structure and chemistry between these two iron oxides would inhibit the observation of any distinctive mark at their interface. We thus believe that the lack of such a visible interface in our low magnification micrographs is not alarming, but rather indicative of a truly single-crystalline, epitaxial system in the case of the bilayer samples. Finally the low magnification micrographs yield film thickness that correspond well with the expected values given by the calibration of the metallic fluxes in our MBE chamber and the deposition time during growth.

Figures 4.9-b,c show typical HRTEM micrographs of a $CoFe_2O_4$(5 nm)/ Fe_3O_4(15 nm) bilayer on its α-Al_2O_3 substrate. In this image, one may clearly

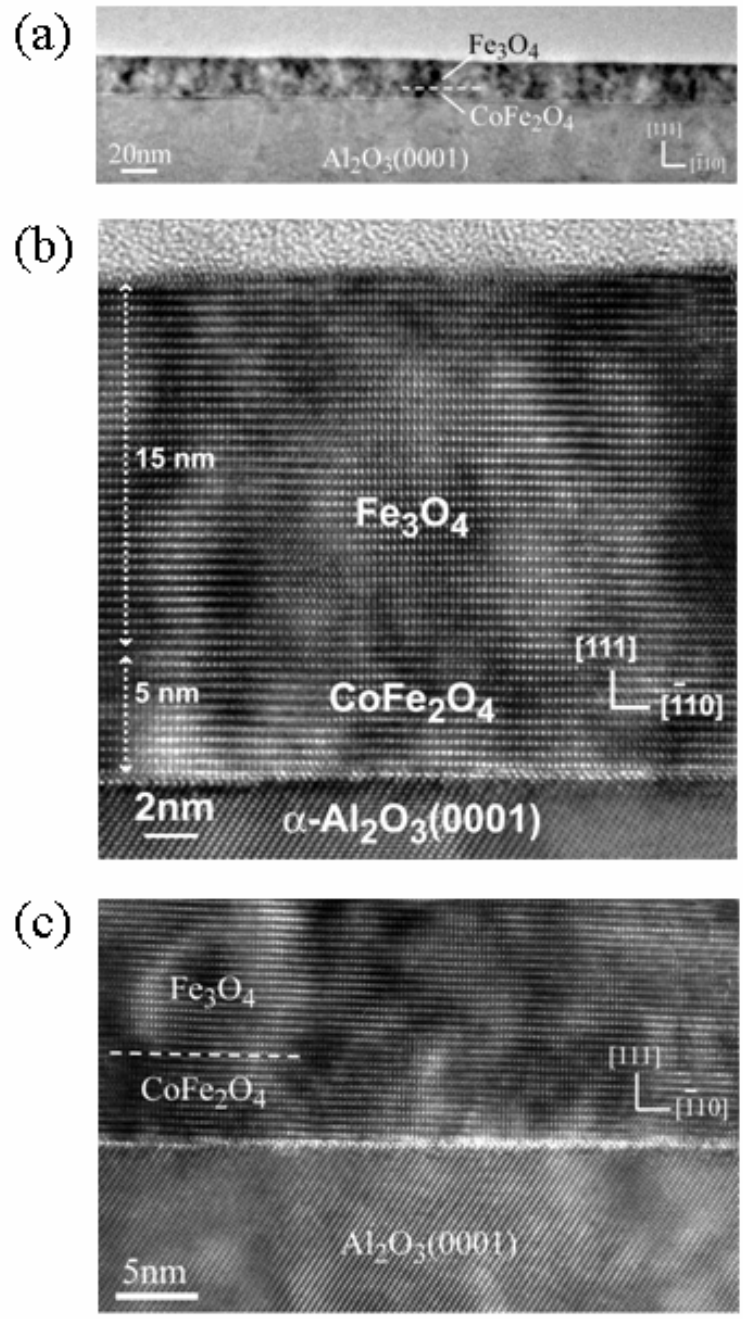

Fig. 4.9: Cross-sectional TEM images of a $CoFe_2O_4$(5 nm)/Fe_3O_4(15 nm) bilayer sample viewed along the $[11\bar{2}]$ zone axis. Figure (a) is a low magnification image, while (b) and (c) are in high magnification. The thickness of the $CoFe_2O_4$ and Fe_3O_4 layers have been labeled as a guide to the eye, since they are structurally identical.

identify the (111) planes of Co and/or Fe cations oriented parallel to the substrate surface. The HRTEM images provide detailed information on the structure of our spinel multilayers at the various interfaces—a study which is crucial to the eventual evaluation of the magnetic and magneto-transport properties in these systems. Before discussing the interface properties in detail, we note that the HRTEM images once again evidence the homogeneity and high structural quality of the epitaxial samples.

In Figures 4.9-b,c we observe an α-$Al_2O_3/CoFe_2O_4$ interface which is perfectly flat and abrupt. There is no trace of parasitic phases resulting from the formation of an unwanted Fe/Co oxides during the early stages of film growth. These observations are in very good agreement with the real-time RHEED diffraction patterns in which single-phase, two dimensional growth is observed as soon as the oxide begins to form. The wider view in Figure 4.9-c additionally brings out a series of regularly-spaced contrasts that appear at the substrate/film interface. Such contrasts may be attributed to misfit dislocations that form due to the large mismatch between the α-Al_2O_3 and $CoFe_2O_4$ lattices. The dislocations themselves may not be seen, as they do not affect the (111) planes which are the only ones visible taking the $[11\overline{2}]$ zone axis. The result is a fully relaxed $CoFe_2O_4$ film, in good agreement with our previous RHEED characterization in which we calculated a mismatch between the substrate and the ferrite films that corresponds to that between the bulk lattice parameters.

The existence of misfit dislocations is of particular interest when they occur in the $CoFe_2O_4$ layers, as this material is known to be highly magnetostrictive [78] due to the presence of Co^{2+} in the octahedral sites [79]. One could imagine that the local strain induced by these defects might have a impact on the magnetic properties, most notably the coercivity, in ultra thin $CoFe_2O_4$ layers such as those in our samples. Magnetostrictive effects due to residual strain arising from defects have been reported in $CoFe_2O_4$ powders [72], indeed suggesting that similar effects may be observed in relaxed epitaxial films containing misfit dislocations. On the other hand, we do not expect this effect to be as significant in Fe_3O_4 as its magnetocrystalline anisotropy is negligible compared to that of its cobalt-containing counterpart. A detailed magnetic study of the present samples will naturally follow in Chapters 5 and 6, with special attention given to the improvement of their structural quality (i.e. via the use of a Pt(111) buffer layer), in correlation with their magnetic properties. At this point, we thus wish to reiterate the need to perform a detailed structural and chemical analysis of our samples in order to understand the magnetic and magnetotransport measurements to follow.

Finally, the HRTEM investigation also provides detailed structural information about the $CoFe_2O_4/Fe_3O_4$ interface for the bilayer samples. This

interface is of critical importance for spin filter MTJ's based on these two spinel ferrites, as it the filter efficiency and spin polarization depend strongly on the nature of electrode/barrier interface. In Figure 4.9-b the dashed arrows indicate the thickness of each film, as expected from the MBE deposition times, and thus where the $CoFe_2O_4/Fe_3O_4$ interface occurs. As one may easily see, there is no physical trace of a delimitation between the two films. As mentioned earlier in this section, this result is not surprising because the two spinel ferrites are nearly identical in chemistry and structure. The substitution of one Co^{2+} cation for a Fe^{2+} in $CoFe_2O_4$ hardly affects the lattice parameter of the system (8.397 Å for Fe_3O_4 compared to 8.392 Å for $CoFe_2O_4$), and so no strain or defects are expected when epitaxially growing one film on the other. The presence of contrast or defects at the interface would most likely be due to the presence of parasitic phases, which is clearly not the case in our samples. The lack of a visible interface thus proves the high epitaxial quality of our bilayer systems. Our HRTEM study lacks only information on the chemical quality of the $CoFe_2O_4/Fe_3O_4$ interfaces. Due to the proximity in the atomic masses of Co and Fe, no Z-contrast may be distinguished, and the possibility of Co interdiffusion may not be ruled out. For this reason, we must rely on a complementary chemical analysis in order to prove the bilayer structure of the samples.

TEM observation of antiphase boundaries

One of the most common defects known to appear in epitaxial ferrite thin films are antiphase boundaries (APBs). APBs are stacking defects of the atomic planes in the spinel lattice corresponding to a half lattice translation of the cationic sublattice, whereas the oxygen sublattice remains unchanged. These result from the coalescence of islands with different cationic symmetries (all of which are (111)-oriented) in the early stages of epitaxial growth. In the case of Fe_3O_4, these APBs have been widely studied due to their important effect on the magnetic [80, 65] and magneto-transport [81, 82, 83] properties of this material. In the case of $CoFe_2O_4$, the presence of APBs has been recognized [59], but much less is known about their effect on the physical properties of these films. Nevertheless, it is important to address the observation of APBs in our TEM studies because, as we will see in Chapters 5 and 7, these defects most certainly have affect on the magnetic and spin-polarized tunneling properties of our $CoFe_2O_4$ tunnel barriers.

In order to view the APBs in our films, dark-field TEM images obtained by selecting one of the three (220)-type reflections in the spinel lattice were acquired for both cross-sectional and plane-view samples. In these dark-field micrographs, the antiphase domains are outlined by dark contrasts

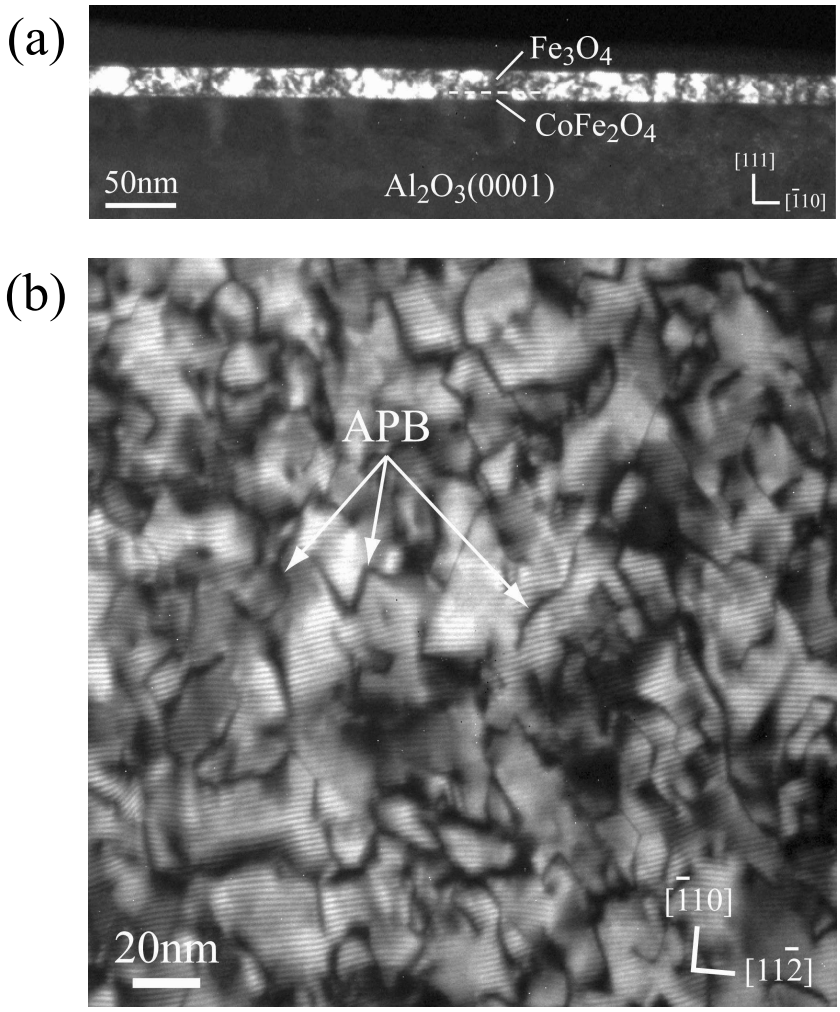

Fig. 4.10: TEM study of antiphase boundaries in a $CoFe_2O_4$(5 nm)/Fe_3O_4(15 nm) bilayer. (a) Cross-sectional dark field image in which the dark contrasts running perpendicular to the plane of the film indicate the presence of APBs that originate in the bottom $CoFe_2O_4$ film and traverse the entire thickness of the bilayer. (b) In the plane-view dark field image, APBs may be easily identified by the dark contrasts lines distributed over its entire surface.

produced when a break of the selected periodicity occurs. Figure 4.10-a,b shows the cross-sectional and plane-view dark-field images of a $CoFe_2O_4$(5 nm)/Fe_3O_4(15 nm) bilayer in low magnification. In the cross-sectional image, the dark contrasts running perpendicular to the plane of the film and across its entire thickness indicate the presence of APBs that nucleate in the $CoFe_2O_4$ layer and then propagate through to the Fe_3O_4. In the plane-view image, APBs are evidenced by two types of dark contrasts: sharp contrasts indicating APBs perpendicular to the layer, and diffuse contrasts corresponding to APBs tilted with respect to the normal of the plane. The jagged, geometrical nature of the contrasts is characteristic of this type of defect. From the dark-field images in Figure 4.10, it is clear that APBs are in fact present in relatively high concentration in our spinel films, making them an important factor to keep in mind when interpreting future magnetic and tunneling experiments.

EELS

In parallel to the structural quality of our films, we analyzed their chemical properties in detail. In the case of the $CoFe_2O_4/Fe_3O_4$ bilayers, the interface introduces and additional possibility for unique magnetic phenomena such as exchange coupling and must be carefully controlled. Furthermore, the chemical properties at the interface may also affect the spin polarization and filter efficiency of $CoFe_2O_4$ tunnel barriers as both of these are largely governed by the barrier/electrode interface [19]. While *in situ* XPS allowed us to control the chemical composition of our films during film deposition, it does not guarantee that the films did not evolve over time once removed from the UHV growth chamber. That is, there is no indication of the potential diffusion of Co from $CoFe_2O_4$ into Fe_3O_4, creating a diffuse interface in the ferrite bilayers. This is also the case in our HRTEM study, where we have proven the high structural quality of the $CoFe_2O_4/Fe_3O_4$ interface, but extracted no information about possible Co interdiffusion. We have thus relied on *ex situ* characterization by EELS, in order to first confirm the 1:2 Co/Fe ratio in the $CoFe_2O_4$ single layers, and secondly to verify the bilayer nature of our $CoFe_2O_4/Fe_3O_4$ system.

Figure 4.11 shows cross-sectional chemical maps obtained for a $CoFe_2O_4$(15 nm)/Fe_3O_4(15 nm) bilayer sample. A thicker $CoFe_2O_4$ layer was used for this study in order to have sufficient material to observe the $CoFe_2O_4/Fe_3O_4$ interface accurately. From both the iron and cobalt maps, one may clearly distinguish the $CoFe_2O_4/Fe_3O_4$ interface at a thickness that corresponds well with that expected from the MBE deposition times. The iron map reveals a difference in Fe concentration between the $CoFe_2O_4$ and Fe_3O_4 layers, which

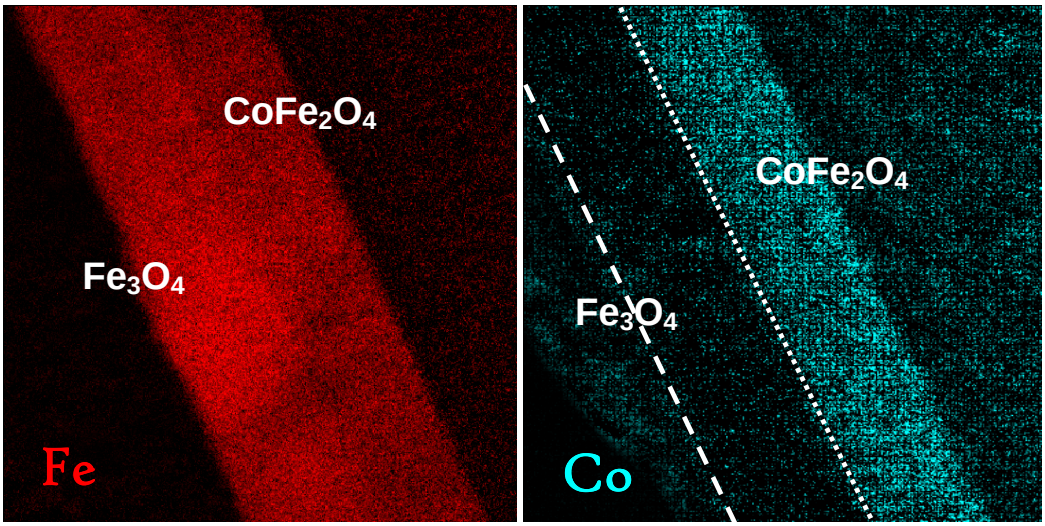

Fig. 4.11: EELS chemical maps of the Fe and Co concentrations in a $CoFe_2O_4$(15 nm)/Fe_3O_4(15 nm) sample, revealing the bilayer nature of this system.

may be seen by the change in intensity when passing from the $CoFe_2O_4$ to Fe_3O_4. Quantitatively, the intensity ratio is approximately 2/3, in very good agreement with the relative Fe concentrations in the two materials. Even more remarkable is the results obtained from the cobalt map. This reveals a bilayer for which all of the Co concentration is restricted to the $CoFe_2O_4$ layer (the spatial resolution is <1 nm), indicating that there is no significant diffusion of Co from $CoFe_2O_4$ to Fe_3O_4. Again, the interface in the cobalt map appears abrupt and further confirms the bilayer structure in our ferrite system.

4.3 $CoFe_2O_4/\gamma$-Al_2O_3/Co trilayers and their variants

The second tunnel junction system that will be presented throughout this thesis uses cobalt as the ferromagnetic electrode in combination with our $CoFe_2O_4$ magnetic tunnel barrier. Co has the advantage of being one of the most widely studied electrode materials in MTJs. Its magnetic properties and spin polarization are well established, thus significantly limiting the unknown parameters in the $CoFe_2O_4$/Co spin filter system. Furthermore, the structure and magnetic properties of the Co layer differ significantly from those of $CoFe_2O_4$, making this a system in which the two layers are readily distinguishable. The originality in this work is that we present Co films that

are epitaxial. In such an epitaxial system, interface effects may once again significantly influence the magneto-transport properties of the spin filter.

Two possible MTJ systems containing Co electrodes have been considered : the first consisting of a Co electrode deposited directly on $CoFe_2O_4$ ($Pt/CoFe_2O_4/Co$), and the second with an ultra-thin epitaxial Al_2O_3 spacer inserted in between the $CoFe_2O_4$ and Co layers ($Pt/CoFe_2O_4/Al_2O_3/Co$). Although we will see in Chapter 7 that only the latter of the two yielded successful MTJs, the MBE growth and characterization of both variants will be presented in detail in this section. In particular, the optimization of the epitaxial Al_2O_3 layer required additional methods of structural and chemical characterization unsolicited in the $CoFe_2O_4/Fe_3O_4$ studies.

4.3.1 Epitaxial growth and RHEED

$CoFe_2O_4$/Co bilayers

The MBE growth of the $CoFe_2O_4$/Co bilayers was very similar to that of the fully spinel systems discussed previously, with the exception that the deposition of the Co electrode was performed at room temperature after the preceding $CoFe_2O_4$ layer was cooled down from 450°C. The result for this system, as seen from the RHEED pattern in Figure 4.12-a for the $[1\bar{1}00]$ growth direction, is a high quality, single crystalline epitaxial film. The RHEED pattern in itself is not sufficient to determine whether the Co film takes on a hexagonal or cubic structure, and so we must rely on complementary TEM studies to answer this question (see Section 4.3.3). Nevertheless, the deposition of Co directly on $CoFe_2O_4$ is quite remarkable as it results in very high quality epitaxial growth *at room temperature*, without the need of a post-deposition anneal.

$CoFe_2O_4/\gamma$-Al_2O_3/Co triayers and full MTJs

The need to insert a crystalline Al_2O_3 layer in between $CoFe_2O_4$ and Co in this MTJ system arises from the exchange coupling between these two magnetic layers, which will be discussed in detail in Chapter 7. In terms of sample preparation, the main challenge in growing fully epitaxial $Pt/CoFe_2O_4/Al_2O_3/Co$ MTJs was in fact the successful elaboration of an epitaxial Al_2O_3 barrier. This Al_2O_3 spacer was grown following a procedure developed previously for the growth of crystalline aluminum oxide tunnel barriers on Fe_3O_4 [84], which involves high temperature deposition (450°C) and maintaining the same pressure in the oxygen plasma source as for the previous spinel layer. Doing so results in the spinel phase γ-Al_2O_3. When the same procedure is applied on for growth on $CoFe_2O_4$, we once again

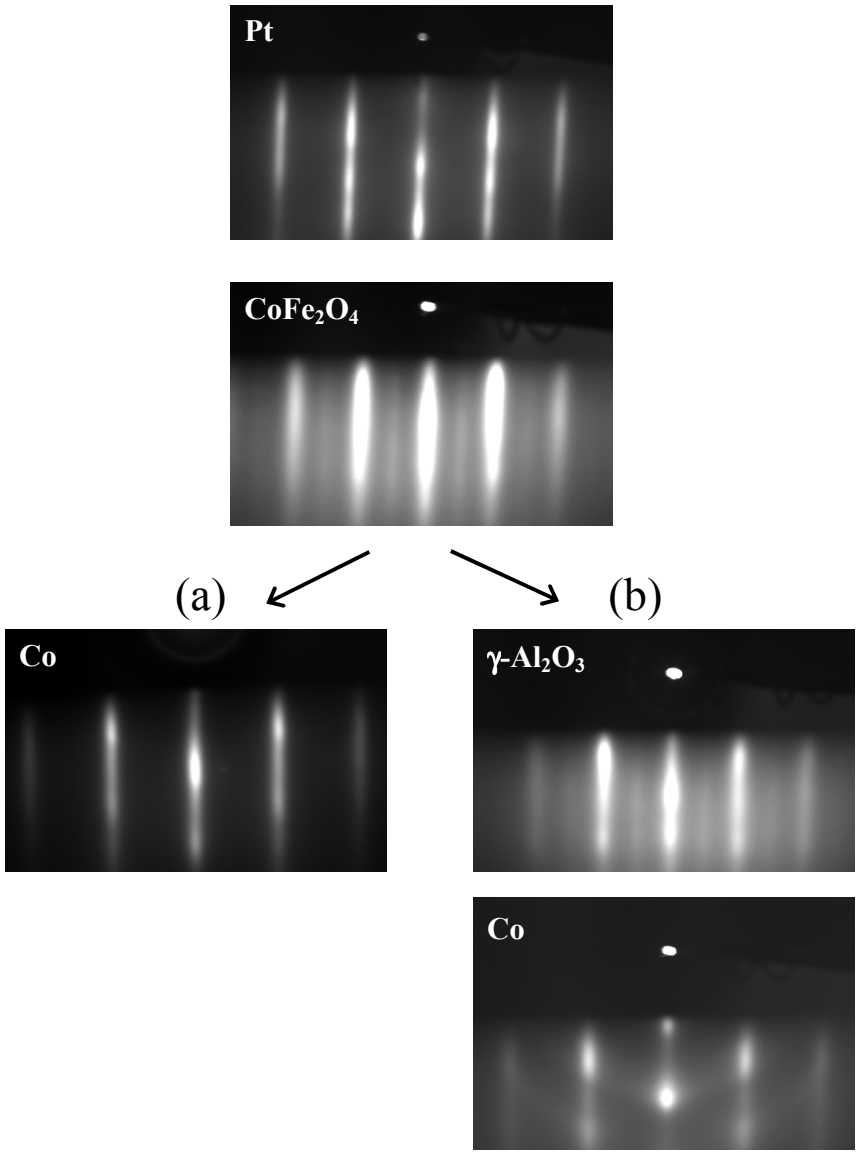

Fig. 4.12: RHEED patterns along the $[1\bar{1}00]$ direction showing two $CoFe_2O_4$-based systems grown on Pt(111). System (a) demonstrates the direct growth of $CoFe_2O_4$ and then Co on Pt(111) : Pt(20 nm)/$CoFe_2O_4$(3 nm)/Co(10 nm). System (b) contains a thin crystalline γ-Al_2O_3 layer in between the $CoFe_2O_4$ and Co : Pt(20 nm)/$CoFe_2O_4$(3 nm)/γ-Al_2O_3(1.5)/Co(10 nm). We note that in (b), the $CoFe_2O_4$ and Al_2O_3 have similar RHEED patterns, indicating that the latter is also a spinel (γ phase).

obtain a high quality epitaxial γ-Al_2O_3, as may be seen by the similarity in the RHEED patterns of the $CoFe_2O_4$ and Al_2O_3 layers in Figure 4.12-b. However, many tests with different Al metal fluxes (i.e. Al_2O_3 growth rates) were necessary before such high quality films were obtained. Figure 4.12-b, which is representative of the entire Pt/$CoFe_2O_4$/Al_2O_3/Co MTJ system, further indicates that Co also grows epitaxially on γ-Al_2O_3, although the slight presence of rings about the RHEED streaks suggests that its crystalline quality is not quite as excellent as Co deposited directly on $CoFe_2O_4$. We also note the exceptional quality of the $CoFe_2O_4$ layer which is only 3 nm thick, thanks to the enhanced growth on Pt.

Real time lattice studies on $CoFe_2O_4/\gamma$-Al_2O_3

Because $CoFe_2O_4$ and γ-Al_2O_3 have the same spinel structure, interesting information regarding epitaxial strain may be obtained using the real time RHEED patterns to track the change in lattice parameter throughout the growth process. This real time lattice analysis in essence records a film of the RHEED patterns, such that the continuous evolution of the lattice mismatch with the substrate may be extracted from the spacing between the primary streaks in conjunction with Equation 4.1.

The results for a $CoFe_2O_4$(3 nm)/γ-Al_2O_3(1.5 nm) bilayer deposited directly on an α-Al_2O_3 substrate are shown in Figure 4.13. Here Δa is calculated taking d_{sub} to be the spacing between the α-Al_2O_3 substrate streaks in our experimental RHEED patterns. The first thing to notice is that the $CoFe_2O_4$ layer undergoes a sudden dilated phase during the initial stages of growth. Its lattice mismatch with the sapphire substrate reaches as high as 13% before rapidly settling down to just over 8%, in good agreement with the value obtained in Section 4.1.1. All of this occurs within the first 6 or so minutes of deposition ($t \sim$1 nm), beyond which the $CoFe_2O_4$ recovers its bulk parameter and remains stable. Not coincidentally, these first 6 minutes also correspond to the period in which no intermediate spinel streaks are yet visible in the RHEED patterns. The presence of such a dilated phase has previously been reported in the growth of epitaxial Fe_3O_4(111) films by MBE [64], and is attributed to an expanded oxygen sublattice deficient in Fe ions. As the growth continues, the unoccupied Fe sites are filled establishing long-range order and compressing the oxygen sublattice down to the bulk spinel value. Assuming a similar situation, our real time lattice studies suggest that the growth of epitaxial $CoFe_2O_4$(111) also involves a preliminary Co,Fe-deficient phase that disappears once enough matter has been deposited. The final result is a fully relaxed $CoFe_2O_4$ film.

Contrary to what is observed for $CoFe_2O_4$, the subsequently deposited γ-

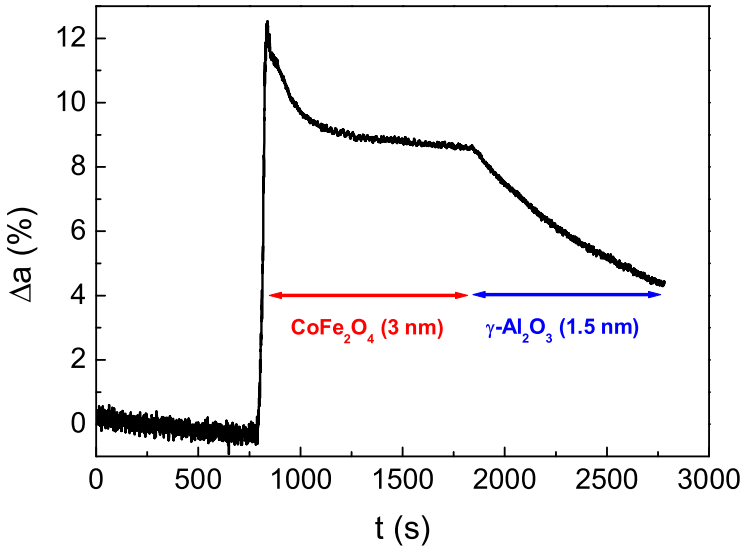

Fig. 4.13: Lattice mismatch as a function of deposition time for a $CoFe_2O_4$(3 nm)/γ-Al_2O_3(1.5 nm) bilayer grown on a α-Al_2O_3 substrate. The data was acquired simultaneously with the film deposition using the real time analysis capabilities of the RHEED technique.

Al_2O_3 does not exhibit a preliminary dilated phase. This may seem surprising at first given that it also has a spinel structure. Applying the argument above, the lack of a dilated phase could be explained by the higher oxygen affinity of the Al cations who bind immediately to the oxygen sublattice without forming an Al-deficient (and thus expanded) phase. However, rather than an abrupt relaxation to the bulk parameter, the γ-Al_2O_3 lattice first takes on that of the $CoFe_2O_4$, before gradually relaxing towards a lower value. This is clearly seen in the second portion of the real time lattice mismatch curve in Figure 4.13. For a 1.5 nm γ-Al_2O_3 layer—limited in thickness by the requirements for a tunnel barrier—this relaxation is only partial, dropping at best to $\sim$4% with respect to the α-Al_2O_3 substrate. If the γ-Al_2O_3 was fully relaxed, the lattice mismatch would be only 2%. As result, we obtain a γ-Al_2O_3 barrier that is under significant tensile stress in the direction parallel to the plane of the film.

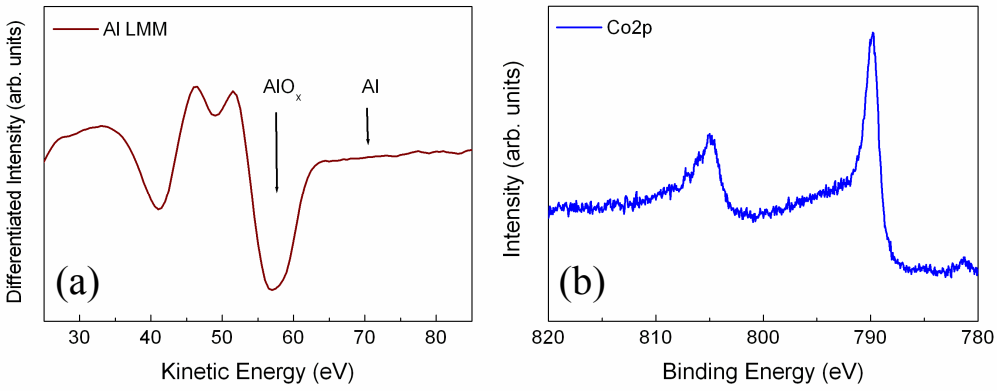

Fig. 4.14: Chemical study of the γ-Al_2O_3 and Co layers in a $CoFe_2O_4$(3 nm)/γ-Al_2O_3(1.5 nm)/Co(10 nm) sample. The degree of Al oxidation was analyzed by AES (a), while the metallic state of the Co was confirmed by XPS (b).

4.3.2 In situ spectroscopies : XPS and AES

One of the major risks in growing multilayer structures that combine several oxide and metallic materials is the diffusion of oxygen and the formation of non-stoichiometric interfaces. To control the chemical quality of our $CoFe_2O_4/\gamma\text{-}Al_2O_3/Co$ multilayers, both XPS and AES spectroscopies were necessary. XPS was most appropriate for identifying the oxidation state of $CoFe_2O_4$ (as described in Section 4.1.2) as well as the lack of oxidation in Co. On the other hand, AES was best suited for analyzing the Al_2O_3(1.5 nm) layer, which should ideally contain fully oxidized Al^{3+}, due to the high surface sensitivity of this technique (< 1 nm) and its chemical sensitivity to the presence of metallic Al.

Because the fabrication process of our $CoFe_2O_4/\gamma\text{-}Al_2O_3/Co$ trilayers required cooling down the sample from 450° to room temperature in between the deposition of Al_2O_3 and Co, *in situ* XPS and AES measurements could be performed on the $CoFe_2O_4/\gamma\text{-}Al_2O_3$ bilayer structure before continuing on to deposit the Co. In the case of XPS, the longer escape length of the photoelectrons ($\sim$3 nm) allowed for the selective analysis of the Co and Fe atoms localized at the metal/oxide interface. The result in a $CoFe_2O_4$(3 nm)/γ-Al_2O_3(1.5 nm) bilayer is identical to the blue curve (triangles) in Figure 4.3 when the oxidation conditions are maintained the same when passing

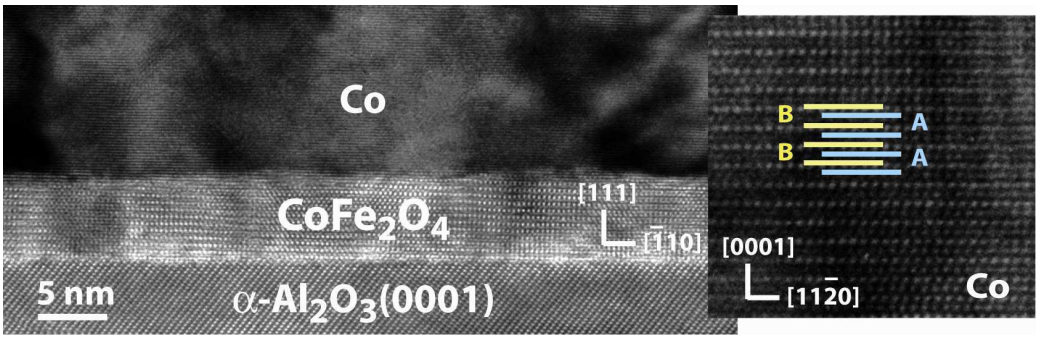

Fig. 4.15: Cross-sectional HRTEM image of a $CoFe_2O_4$(5 nm)/Co(15 nm) bilayer viewed along the $[11\bar{2}]$ zone axis. The right inset represents a zoom of the Co[0002] planes viewed along $[\bar{1}10]$, and revealing an HCP lattice.

from $CoFe_2O_4$ to Al_2O_3. In other words, under these specific conditions (i.e. rf power, oxygen pressure in the plasma source...), the presence of Al_2O_3 in contact with $CoFe_2O_4$ does not modify the chemical state of the Co^{2+} and Fe^{3+}. Similarly, AES measurements show that the γ-Al_2O_3 layer contains no metallic Al. Figure 4.14-a shows the Al *LMM* transition in the AES spectrum of the γ-Al_2O_3(1.5 nm) barrier in the same $CoFe_2O_4$(3 nm)/γ-Al_2O_3(1.5 nm) bilayer. Here, the existence of one sole peak at 56 eV and absence of any peak in the energy range corresponding to metallic Al (70 eV), confirms that our crystalline Al_2O_3 layer is fully oxidized.

Finally, following the deposition of the top Co layer, *in situ* XPS was used to verify its metallic state. In Figure 4.14 we do indeed see that the Co2p energy range contains one single peak at 793 eV corresponding to unoxidized Co. This result reassures us that the room temperature deposition of Co on Al_2O_3 results in an inert interface free of oxygen interdiffusion.

4.3.3 TEM

$CoFe_2O_4$/Co bilayers

In the TEM analysis of our $CoFe_2O_4$/Co system, the separate layers were easily distinguished by imaging the sample along two different zone axes, each of which selectively resolved one of the two layers. Along the $[11\bar{2}]$ zone axis, which is the one used for all of the previous HRTEM images presented in this chapter, we clearly identify the $CoFe_2O_4$ film sandwiched between the sapphire substrate and the Co layer. This is shown in Figure 4.15 for a $CoFe_2O_4$(5 nm)/Co(15 nm) sample. In this image, the (111) planes of Co and

Fe cations are oriented parallel to the substrate surface. The homogeneity and high structural quality of the epitaxial sample are also evident. We observe α-$Al_2O_3/CoFe_2O_4$ and $CoFe_2O_4$/Co interfaces that are abrupt and exhibit no trace of additional phases other than the expected HCP and spinel. The $CoFe_2O_4$ and Co films also appear fully relaxed, in good agreement with the RHEED characterization described in Section 4.3.1. The insert in Figure 4.15 shows a zoom of the (0002) planes in the Co top layer viewed along the $[\bar{1}10]$ zone axis (with respect to the cubic $CoFe_2O_4$). Careful examination of these planes reveals a clear ABAB stacking sequence indicative of an HCP structure, unlike that of the $CoFe_2O_4$ sublayer which is an FCC-based spinel. By TEM, we therefore confirm the high epitaxial quality of the $CoFe_2O_4$ and Co films seen by RHEED, and additionally resolve the crystalline structure of the Co layer.

$CoFe_2O_4/\gamma$-Al_2O_3/Co trilayers : TEM and geometric phase analysis

The TEM studies of our $CoFe_2O_4/\gamma$-Al_2O_3/Co trilayers were particularly interesting due to the structural similarity between the two oxide layers. The HRTEM images in Figure 4.16-a,b demonstrate the high epitaxial quality of a $CoFe_2O_4$(5 nm)/γ-Al_2O_3(1.5 nm)/Co(10 nm) sample. In this figure we observe a single crystalline $CoFe_2O_4(111)/\gamma$-$Al_2O_3(111)$ tunnel barrier sandwiched between the sapphire substrate and Co counter-electrode. However, due to the near perfect epitaxy between the two spinel layers, it is very difficult to distinguish them by eye. In this particular situation, the geometric phase method [69, 68] (see Chapter 3), which measures the local displacement and strain fields in a specimen from experimental HRTEM images, was extremely useful.

Using the geometric phase method, we were able to analyze the strain fields in the $CoFe_2O_4$(5 nm)/γ-Al_2O_3(1.5 nm) barrier, thus unveiling its bilayer nature. Figure 4.16-c shows the strain fields in the in-plane (ε_{xx}) and out-of-plane (ε_{yy}) directions. Along ε_{xx}, the strain field is homogeneous with no visible disruption between the two layers. This indicates that the γ-Al_2O_3, is not relaxed and therefore takes on the lattice parameter of the $CoFe_2O_4$. This is in very good agreement with the RHEED real time lattice studies presented in Section 4.3.1. Because the lattice parameter of γ-Al_2O_3 (7.91 Å) is smaller than that of $CoFe_2O_4$ (8.39 Å), we may qualitatively conclude that the first is strained along (ε_{xx}). However, the strain field along ε_{yy} encounters a strong phase shift at the $CoFe_2O_4/\gamma$-Al_2O_3 interface, as may be seen from the color change from red to dark blue. This suggests that the γ-Al_2O_3 is deformed in the out-of-plane direction with respect to the $CoFe_2O_4$. The ε_{xx} and ε_{yy} strain profiles in Figure 4.12-d further confirm

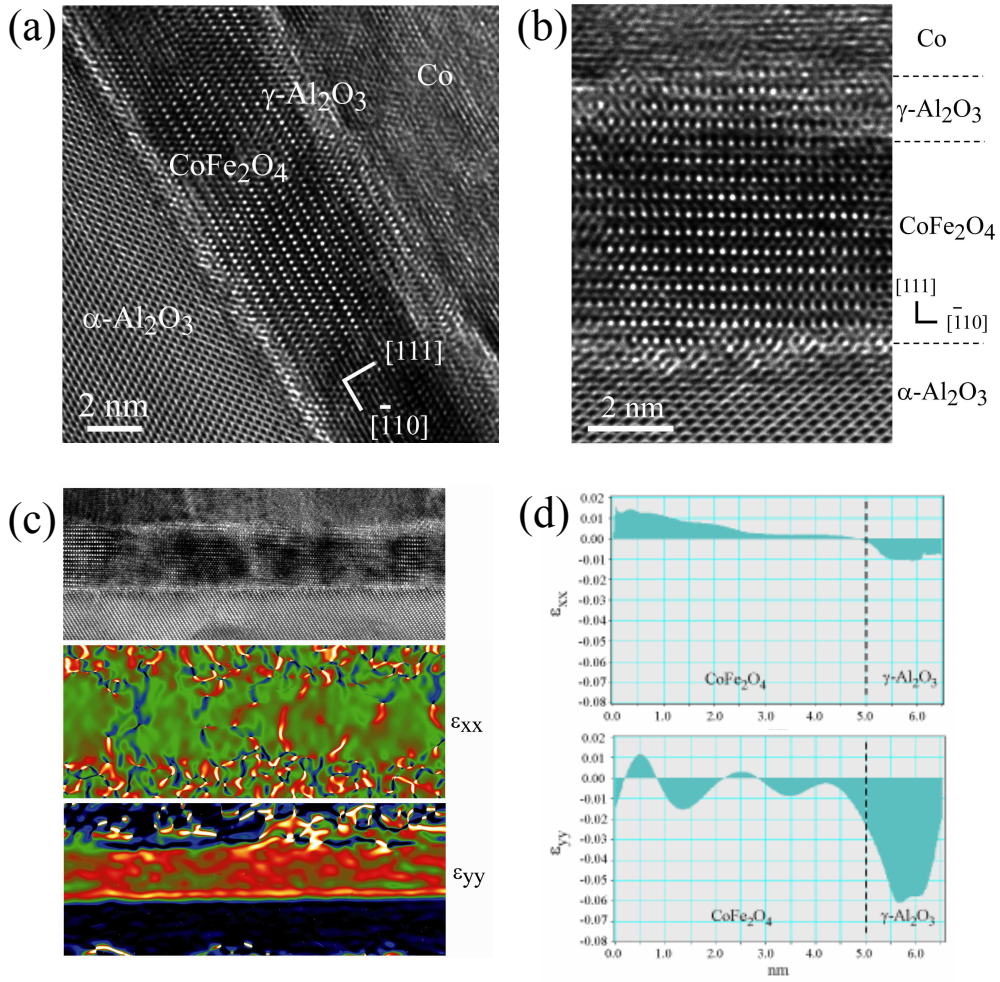

Fig. 4.16: (a),(b) HRTEM images of a $CoFe_2O_4$(5 nm)/γ-Al_2O_3(1.5 nm)/Co(10 nm) trilayer deposited directly on a sapphire substrate. (c) Geometric phase analysis of the strain fields in the $CoFe_2O_4$/γ-Al_2O_3 double barrier, based on the HRTEM image on top. The color map along ε_{xx} (in-plane) contains one single green strip that covers the entire thickness of the $CoFe_2O_4$/γ-Al_2O_3 bilayer, indicating a uniform strain field across the two layers in this direction. However, along ε_{yy} (out-of-plane), the map reveals a sharp color change from red to blue at the expected bilayer interface. From this image, it is clear that the γ-Al_2O_3 is strongly deformed with respect to the $CoFe_2O_4$ along ε_{yy}. (d) Strain profiles further confirm the conclusions extracted from the strain field maps. The deformation at the $CoFe_2O_4$/γ-Al_2O_3 interface along ε_{xx} is insignificant compared to the strong compression in the γ-Al_2O_3 layer observed along ε_{yy}. This compression, yielding -6% strain, allows the 1.5 nm γ-Al_2O_3 to be distinguished from the 5 nm $CoFe_2O_4$. The oscillations seen in the $CoFe_2O_4$ portion of the ε_{yy} profile are an artifact due to light contrasts in the HRTEM image and have no physical meaning.

this interpretation, as they reveal a γ-Al_2O_3 layer (of the expected 1.5 nm thickness) under significant compression along ε_{yy}. This compression is a direct consequence of the tension experienced along ε_{xx}, and results in -6% strain with respect to the $CoFe_2O_4$ lattice. The geometric phase analysis therefore allows us to verify the presence and thickness of the two distinct spinel layers in the tunnel junction. Furthermore, it provides complementary information about the epitaxial growth mode of γ-Al_2O_3 on $CoFe_2O_4$ that complements the results obtained from the real time RHEED studies.

5. $CoFe_2O_4$ SINGLE LAYER SPIN-FILTER TUNNEL BARRIERS

In this fifth chapter addressing the first physical results in this thesis, we focus solely on our $CoFe_2O_4(111)$ single layer tunnel barriers. Following the extensive study of their growth, structural and chemical properties presented in Chapter 4, one final and critical optimization step was necessary before performing spin-polarized tunneling (SPT) measurements. This was of course the optimization of their magnetic properties, which in the case of the ultra-thin tunnel barriers must meet certain specific requirements in order for them to be suitable for spin filter experiments. In this chapter, we will therefore describe the entire process used to optimize the physical properties (magnetic and electronic) in our $CoFe_2O_4$ tunnel barriers, before going on to present the first SPT results. SPT measurements in our $CoFe_2O_4$ single layers were performed by the Meservey-Tedrow technique and reveal, for the first time, successful spin filtering in this material at low temperature.

5.1 Magnetic Properties of $CoFe_2O_4$ single layers

The magnetism in $CoFe_2O_4$ films of different thickness was studied principally at room temperature by VSM. SQUID measurements were later performed only on the ultra-thin films in order to evaluate their behavior at low temperature, after optimization at 300 K. Surprisingly, while a very large number of studies exist on the magnetic properties of thicker epitaxial $CoFe_2O_4$ thin films ($t > 50$ nm), very few address the interesting and important behavior of ultra-thin films of a few nanometers in thickness. Whether or not this lack of information in the literature is related to the difficulty to grow high quality epitaxial films at these thicknesses is questionable. In either case, the materials study presented in Chapter 4 clearly shows that our 3-5 nm $CoFe_2O_4(111)$ layers do indeed meet the structural and chemical requirements of high quality $CoFe_2O_4$, allowing for the magnetic studies to follow.

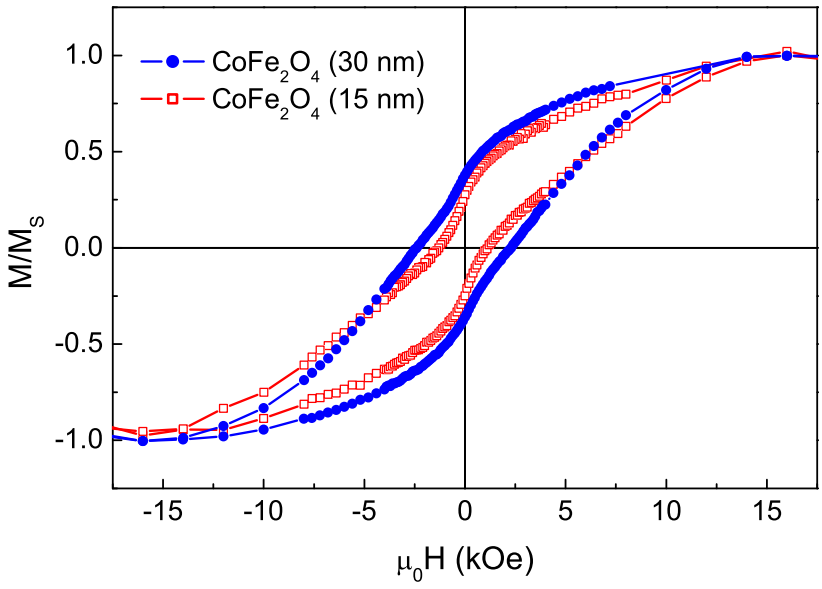

Fig. 5.1: Normalized magnetization curves for thicker $CoFe_2O_4(111)$ films. The blue circles correspond to a 30 nm layer and the red squares to a 15 nm layer. In both cases, the measurements were taken at room temperature with the applied field in the plane of the films.

5.1.1 Magnetism in "thick" $CoFe_2O_4$ films

As was the case in the study of the epitaxial growth of our $CoFe_2O_4(111)$ thin films, the magnetic characterization began with films of significantly greater thickness than that required for tunnel barriers. This was principally done to compare the initial magnetic properties with those found in the literature for thicker $CoFe_2O_4$ films [67, 70, 63, 62, 59]. By "thick" here we mean 30 nm, which is already considerably thinner than the majority of studies existing in the literature. Again room temperature magnetization curves were obtained by VSM, both in the in-plane and out-of-plane geometry. These systematically revealed a magnetic easy axis in the plane of the films, as expected due to shape anisotropy. Within the in-plane measurements, we also checked for any planar angular anisotropy, which proved to be insignificant. This agrees well with the lack of angular dependence found in Fe_3O_4 epitaxial films with a [111] growth direction [65].

Figure 5.1 shows the typical room temperature magnetization loop of a 30 nm $CoFe_2O_4$ layer grown directly on a sapphire substrate (blue circles).

Although in Figure 5.1 the magnetization curve has been normalized for comparison with future measurements, the original, unnormalized curve shows a saturation magnetization $M_s = 315$ kA/m. This corresponds to a net magnetic moment $\mu = 2.5\ \mu_B$ per formula unit, only slightly reduced from the bulk value of 3 μ_B, but not surprising for $CoFe_2O_4$ thin films. Also characteristic of "thicker" $CoFe_2O_4$ thin films is the large coercive field $H_c = \sim$2200 Oe and low remanent magnetization $M_r/M_s = 32\%$. The high coercivity is particularly unique to $CoFe_2O_4$ thin films, and has been extensively studied and attributed to the high magneto-crystalline anisotropy in this specific spinel ferrite [67, 70, 62]. While this large coercivity could be interesting for the application of $CoFe_2O_4$ as a blocking layer in MTJ structures, it is quite undesirable in a spin filter tunnel barrier because the magnetic field required to switch this layer would be inconveniently high. The large H_c is therefore a property that had to be carefully monitored when studying the ultra-thin $CoFe_2O_4$ layers.

To give a second example of the magnetic properties in a thicker $CoFe_2O_4$ film, Figure 5.1 also shows the room temperature magnetization loop of a 15 nm layer (red squares). In this sample, we once again observe a magnetic moment on the order of 2.4 μ_B and a remanent magnetization of 28%. The coercivity of the 15 nm sample, on the other hand, does drop more significantly to 1200 Oe. This decrease in H_c is in fact a trend that is repeatedly observed with the decrease of $CoFe_2O_4$ thickness, as will be addressed in the following Section 5.2.

5.1.2 Magnetism in ultra-thin $CoFe_2O_4$ films

Having found the magnetic properties in our thicker $CoFe_3O_4$ films to be comparable with those in the literature, we quickly moved on to films of 5 nm in thickness which were much closer to those needed for tunnel barrier applications. In Figure 5.2 which displays the room temperature magnetization loop of a $CoFe_2O_4$(5 nm) film grown directly on a sapphire substrate, we immediately see that the ultra-thin layer maintains its ferromagnetic behavior. The net magnetic moment in this case is 2.3 μ_B at saturation, which is very close to that of the 30 nm film. On the other hand, the measured coercivity, $H_c = 170$ Oe, is significantly reduced with respect to the 30 nm layer. This observation is in fact consistent with the increased presence of antiphase boundaries (APBs) commonly observed in spinel ferrite thin films with decreased thickness [85, 65]. Because these structural defects break the crystalline order in the films, the result is a reduction of the magneto-crystalline anisotropy and thus the coercive field, as may be clearly seen in the present sample.

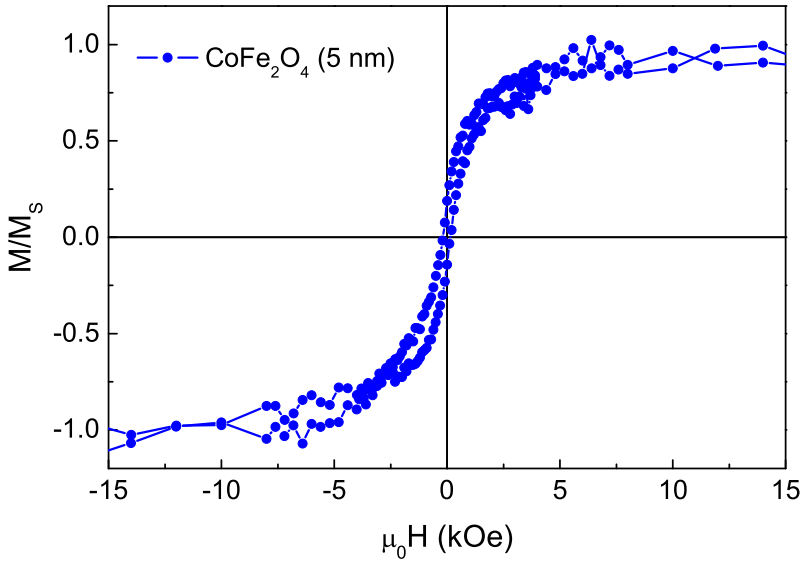

Fig. 5.2: Room temperature magnetization curve for a $CoFe_2O_4$(5 nm layer), displaying clear ferromagnetic behavior and a magnetic moment of 2.3 μ_B.

As we mentioned earlier in Section 5.1.1, the reduced H_c is in fact quite positive in terms of the magnetic properties of a spin filter tunnel barrier. The only doubt to keep in mind for future SPT measurements is whether the increased number of defects in the crystalline structure of magnetic tunnel barrier could eventually create defect states in the band gap, generating spin flip events during tunneling, and thus reducing the overall spin polarization (see Section 5.3 and Chapter 7 for more discussion on this topic).

In addition to the changes in μ and H_c, we also observe a drop in M_r/M_s from 32% at 30 nm to 20% at 5 nm. This could eventually have a negative effect on the magnitude of the TMR observed in a full MTJ system for which the switching of the second magnetic electrode occurs at low magnetic field.

Finally, we note that the magnetic properties of our $CoFe_2O_4$(111) films, when reduced even further to 3 nm in thickness, are nearly identical to those of the 5 nm film shown in Figure 5.2. We therefore do not display the magnetization loop for these samples.

5.1.3 Optimization with a Pt(111) buffer layer

Earlier in Chapter 4, we mentioned that our $CoFe_2O_4$(111) thin films were also grown by introducing a 20 nm Pt(111) buffer layer in between the

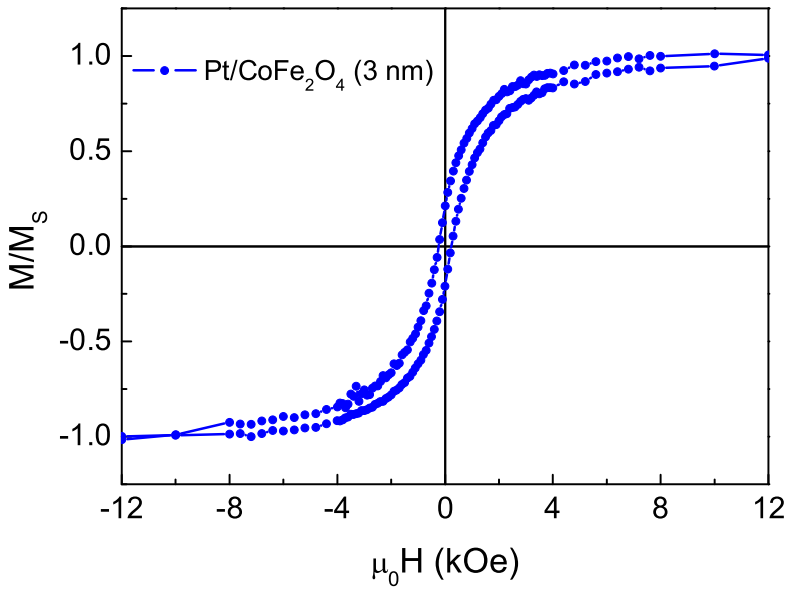

Fig. 5.3: Magnetic properties of an optimized $CoFe_2O_4$(3 nm) barrier grown on a Pt(111) buffer layer. The hysteresis loop was once again obtained at room temperature, with H in the plane of the film.

substrate and the film. In this case, the thickness of the films could be reduced to 3 nm, while *increasing* μ from 2.3 μ_B to 2.7 μ_B. Furthermore, H_c increased slightly to 220 Oe, indicating improved structural quality and thus a potential reduction of structural defect and impurity defect states in the barrier band gap. We note that all of the Pt/$CoFe_2O_4$ and $CoFe_2O_4$ samples that were compared were aligned identically with respect to the applied magnetic field in order to exclude deceiving geometry effects on the measured magnetic signal. The magnetization loop of a Pt(20 nm)/$CoFe_2O_4$(3 nm) sample is shown in Figure 5.3.

The effect of the Pt buffer on the magnetic properties of the ultra-thin $CoFe_2O_4$ was observed repeatedly and is clearly tied to the narrower XRD peaks and higher intensity RHEED patterns observed during the structural characterization of these films (see Chapter 4). The reduction of certain defects such as misfit dislocations and APBs in the Pt-buffered layers (which typically modify the quality of the XRD and RHEED patterns) are likely responsible for the improvement of the magnetic order in the $CoFe_2O_4$ films,

leading to the higher coercivity and magnetic moment. Again, the optimization of the magnetic properties of our $CoFe_2O_4$(3 nm) thin films by growing them on a Pt buffer layer turns out to be very useful, because the Pt buffer is a very good candidate for a non-magnetic electrode in spin filter MTJ structures. Not coincidentally, Pt(111) will indeed later serve as the bottom electrode in all of our $CoFe_2O_4$-based MTJs.

5.1.4 Magnetic properties of $CoFe_2O_4/\gamma$-Al_2O_3 double tunnel barriers

In Chapter 4, we presented the growth and materials properties of a second double tunnel barrier containing both $CoFe_2O_4$(111) and γ-Al_2O_3(111). As was briefly mentioned in that chapter, and as will be described in detail in Chapter 7, the insertion of an ultra-thin γ-Al_2O_3 spacer in between the $CoFe_2O_4$ barrier and Co counter-electrode allowed us to obtain perfect magnetic decoupling between the two magnetic layers in this particular MTJ system. After having optimized the growth of the $CoFe_2O_4$(3 nm)/γ-Al_2O_3(1.5 nm) double tunnel barriers, the natural next step was to verify that the γ-Al_2O_3, although non-magnetic, did not affect the magnetic properties of the $CoFe_2O_4$.

The room temperature VSM magnetization measurement of a $CoFe_2O_4$(3 nm)/γ-Al_2O_3(1.5 nm) double tunnel barrier deposited on a Pt(20 nm) buffer layer is shown in Figure 5.4-a. The hysteresis loop for this sample is nearly identical to that shown in Figure 5.3, confirming that the γ-Al_2O_3 has no effect on the magnetic behavior in the $CoFe_2O_4$. While this result may at first seem trivial, it is not necessarily so. The high temperature deposition of the γ-Al_2O_3 top layer is in essence equivalent to a 10-15 minute anneal at 450°C for the $CoFe_2O_4$ bottom layer, increasing the risk of atomic interdiffusion or phase change due to over-oxidation of the Co^{2+} cations. It is therefore quite reassuring for the future magneto-transport measurements in this thesis that the magnetic properties of the single $CoFe_2O_4$(3 nm) and double $CoFe_2O_4$(3 nm)/γ-Al_2O_3(1.5 nm) tunnel barriers are identical.

5.1.5 Low temperature SQUID measurements

After having fully optimized the magnetic properties of the $CoFe_2O_4$(3 nm) and $CoFe_2O_4$(3 nm)/γ-Al_2O_3(1.5 nm) tunnel barriers at room temperature, it was important to verify that the low temperature magnetization curves did not present any unpleasant surprises with respect to the room temperature characterization. Doing so also provided a reference for the Meservey-Tedrow (Section 5.3) and low temperature TMR measurements (Chapter 7) to follow, both of which were performed below 4 K. Magneti-

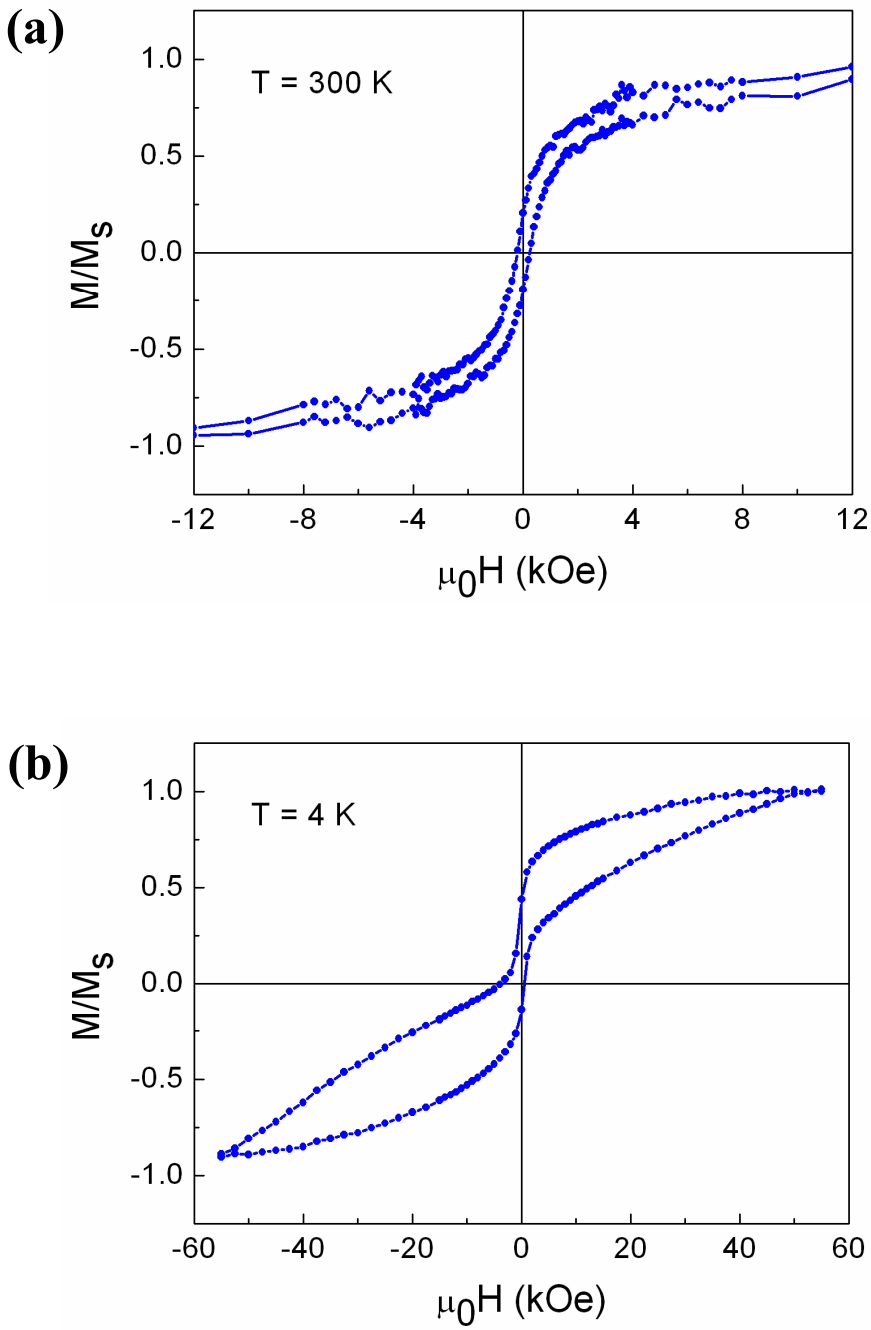

Fig. 5.4: Magnetic properties of a $CoFe_2O_4$(3 nm)/γ-Al_2O_3(1.5 nm) double tunnel barrier. (a) Normalized in-plane magnetization loop measured by VSM at room temperature. (b) Normalized in-plane magnetization measured by SQUID at 4 K. Here the irreversibility of the magnetic loop is evident, revealing the difficulty to saturate the $CoFe_2O_4$ at low temperature.

zation measurements at 4K were therefore obtained by SQUID [1], since this measurement temperature was well below the limits of our VSM system. Once again, no significant difference was found between the $CoFe_2O_4$(3 nm) and $CoFe_2O_4$(3 nm)/γ-Al_2O_3(1.5 nm) systems, and so only the results from the latter are shown in Figure 5.4-b.

The magnetization loop in Figure 5.4-b indicates that H_c and M_r/M_s are somewhat affected by the drop in temperature, increasing to 500 Oe and 40% respectively in comparison to the 220 Oe and 20% obtained at room temperature. The increase in M_r/M_s is obviously beneficial for tunneling experiments. The increase in H_c from 220 Oe to 500 Oe, although not necessarily desirable, is also relatively minor and therefore not worrisome. What is more intriguing is the shape of the hysteresis loop, which never actually closes, even at $H = 6$ T. This indicates that, after the main switching event at 500 Oe, the $CoFe_2O_4$ layer has an extremely difficult time saturating, resulting in a hysteresis loop that is entirely irreversible. One could suspect that the presence of APBs or other defects, which already affected the magnetization behavior at room temperature, could result in an accentuated effect at low temperature. Because the spin-polarized transport properties, especially in the case of TMR measurements, are largely dependent on the magnetization reversal characteristics of the magnetic layers in an MTJ, we can expect the low temperature magnetic properties of our $CoFe_2O_4$ tunnel barriers to inevitably have an impact on the magneto-transport measurements to follow. This will particularly be the case in the TMR measurements described in Chapter 7.

5.2 In-plane Electronic Transport Measurements

Before inserting the $CoFe_2O_4$(3 nm) thin films as tunnel barriers in full MTJ structures, we of course had to verify that these were indeed insulating. Both the thicker and ultra-thin samples were therefore characterized for their in-plane electronic properties using the PPMS system described in Chapter 3. Measurements were performed in the four-terminal configuration, although two-terminal measurements would have sufficed given the high resistivities observed.

The resistivity versus temperature curve ($\rho(T)$) for a $CoFe_2O_4$(15 nm) film grown directly on sapphire is shown in Figure 5.5. This curve demonstrates typical insulating behavior, following an Arrhenius law down to 150 K. Below 100 K, the experimental resistance was greater than the measure-

[1] SQUID measurements were performed at the Unité Mixte de Physique CNRS/Thales in Palaiseau, France.

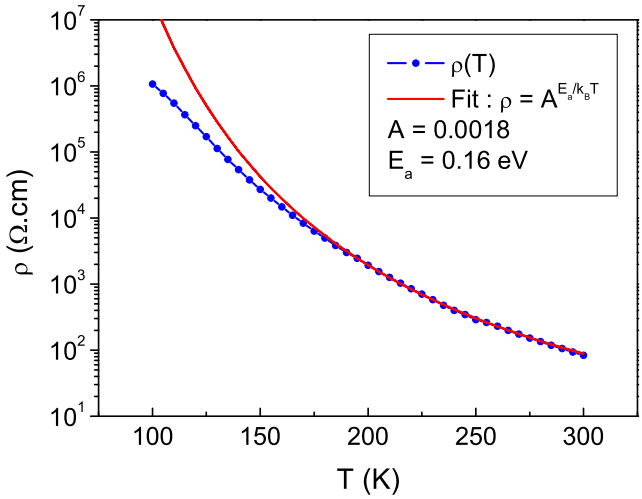

Fig. 5.5: In-plane resistivity versus temperature dependence in a $CoFe_2O_4$(15 nm) film, revealing typical insulating behavior and high resistivity at room temperature. The corresponding Arrhenius fit is also shown. The $\rho(T)$ curves of ultra-thin $CoFe_2O_4$ films are not shown because the room temperature resistances were already too high to provide a clean measurement.

ment capacities of the voltmeter in our PPMS system, limiting how far we could descend in temperature. The resultant room temperature resistivity for this sample is $\rho = 85$ Ωcm.

In the case of the 5 and 3 nm films, the room temperature resistivities were equivalent to that of the 15 nm film, confirming that the insulating behavior of the ultra-thin films is unaffected by the decrease in films thickness. In fact, all films ranging from 3 to 30 nm in thickness resulted in room temperature resistivities around 100 ± 20 Ωcm. Unfortunately for the ultra-thin samples, the resistances measured at room temperature were already so high that complete $\rho(T)$ curves could not be obtained, and are therefore not shown here. Nevertheless, these simple electronic measurements confirm that our ultra-thin $CoFe_2O_4$ layers do indeed have the insulating properties necessary to be used as tunnel barriers.

5.3 Spin-polarized Tunneling in $CoFe_2O_4$: Meservey-Tedrow Technique

5.3.1 The initial Meservey-Tedrow measurement

The most direct measurement of the spin polarization in a spin filter tunnel barrier is the Meservey-Tedrow technique, which was described in detail in Chapter 2. For our $CoFe_2O_4$ tunnel barriers, we chose to focus the Meservey-Tedrow experiments on the $CoFe_2O_4$(3 nm)/γ-Al_2O_3(1.5 nm) double barrier system, as it was more representative of the tunnel barriers used for our Pt/$CoFe_2O_4$/γ-Al_2O_3/Co MTJs (Chapter 7). Furthermore, the fact that the tunnel barrier samples were inevitably exposed to air during transport and before deposition of the Al superconducting electrode made them that much more susceptible to contamination and damage. Capping the $CoFe_2O_4$ with γ-Al_2O_3 therefore provided an added security, protecting the $CoFe_2O_4$ spin filter, and increasing the probability of a successful measurement. All of the experiments presented in the following section were performed at the Francis Bitter Magnet Laboratory at MIT, Cambridge MA. The tunnel junction preparation and patterning technique are described in Chapter 3.

The initial Meservey-Tedrow experiment was performed on a Pt(20 nm)/ $CoFe_2O_4$(4 nm)/γ-Al_2O_3(1 nm) sample covered with 4.2 nm of Al superconductor. The oxidation conditions used during the growth of this particular $CoFe_2O_4$ barrier were $P_{O_2}^{plasma}$ = 0.20 Torr, which is the lower limit of the range of $P_{O_2}^{plasma}$ used to grow $CoFe_2O_4$ in our MBE system. The room temperature tunnel junction resistance-area product (R_jA) was on the order of 0.01 Ωcm^2, giving the impression that the junction was shorted. However, when the sample was cooled to liquid nitrogen temperature (77 K), R_jA increased significantly to 12.8 Ωcm^2, indicating that tunneling was indeed present. Between liquid nitrogen and liquid helium temperature on the other hand, the junction resistance no longer evolved, yielding a final R_jA = 13.5 Ωcm^2 at 4 K. The major increase in R_jA between room temperature and 77 K was a first indication of tunneling through the $CoFe_2O_4$ barrier, as such an increase is not observed when tunneling through Al_2O_3 alone.

As it turns out, the temperature evolution and magnitude of R_jA would become an important indication of the quality of all the tunnel junctions to be measured. In fact, only those junctions whose R_jA increased from room temperature down to 77 K, but remained stable below that, yielded any significant polarization in the dynamic conductance curves. Furthermore, polarization was only measured in junctions whose R_jA was less than 35 Ωcm^2 at 4 K. All junctions with resistances above this limit failed to produce polarization. Because the evolution and magnitude of R_jA are largely

dependent on the number of impurity states in the tunnel barrier band gap, we can be certain that the junctions that yielded successful SPT results were those containing the fewest number of structural and chemical impurities.

In preparation for the Meservey-Tedrow experiment, the sample was cooled down to 0.45 K thanks to the special pumping system in the ^{3}He cryostat. During the final descent in T, we measured the superconducting critical temperature (T_c) of the Al electrode, and finding $T_c = 2.6$ K, the high quality of the spin analyzer was confirmed.

The tunneling dynamic conductance (dI/dV) versus bias voltage (V) was first measured with zero applied magnetic field, as shown in Figure 5.6-a. In this particular sample, measurements were performed in the two-terminal configuration because only one working voltage contact associated with the junction was available. The zero-field conductance curve in Figure 5.6-a is symmetric with sharp peaks on either side of $V = 0$, showing a 0.68 meV superconducting energy gap for Al and negligible leakage. These properties confirm the high quality of the $CoFe_2O_4/\gamma$-Al_2O_3 barrier and Al top electrode.

One noticeable feature in the zero-field curve is the observation of two additional peaks at ± 0.73 meV. These are a consequence of the two-terminal configuration of the transport measurements, and have no physical meaning with respect to the $Pt/CoFe_2O_4/\gamma$-Al_2O_3/Al tunnel junction. In fact, these peaks delimit the superconducting energy gap of a second tunnel junction in between the indium contacts and the Al superconductor. Exposure to air inevitably causes the last few monolayers of Al to oxidize, thus forming a thin layer of AlO_x in between the Al electrodes and the In contacts. The result is a tunnel junction that itself generates peaks in the dI/dV curve. Because the measurements were taken in the two terminal configuration, the contact resistance also contributes to the overall tunneling experiment, thus explaining the presence of a second set of peaks in the dI/dV curve.

Returning to the SPT experiment in our $Pt/CoFe_2O_4/\gamma$-Al_2O_3/Al tunnel junction, the application of a magnetic field revealed Zeeman splitting of the Al quasiparticle density of states. This could be recognized by the decomposition of the two main conductance peaks in the zero-field curve into distinct peaks corresponding to the spin-up and spin-down states on either side of the main peaks. Furthermore, the Zeeman-split dI/dV curves are visibly asymmetric, indicating that the tunneling current is indeed spin polarized. Figures 5.6-b,c show the conductance curves obtained at $H = 2.9$ T and $H = 3.3$ T. Applying the relation described in Chapter 2 (Equation 2.6)—which provides an estimation of P by comparing the relative spin-up and spin-down peak heights in the experimental dI/dV curves—to the 2.9 T and 3.3 T curves in Figures 5.6-b,c, yields a spin polarization $P = 6\%$. This

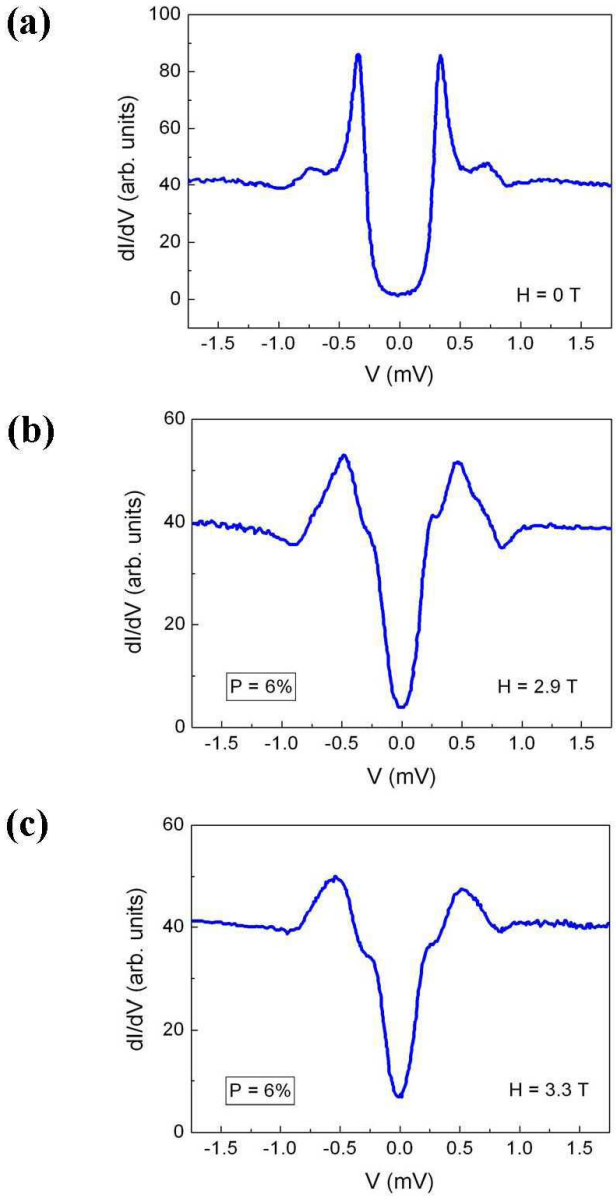

Fig. 5.6: Meservey-Tedrow experiments for a Pt(20 nm)/$CoFe_2O_4$(4 nm)/γ-Al_2O_3(1 nm)/Al(4.2 nm) tunnel junction at 0.45 K. $P_{O_2}^{plasma}$ during growth of the $CoFe_2O_4$ barrier was 0.20 Torr (sample 1). The dynamic dI/dV curves are shown for measurements at (a) zero applied magnetic field, (b) 2.9 T and (c) 3.3 T. Here the asymmetry in the conductance curves (b) and (c) corresponds to a tunneling current spin polarization of 6%, thus revealing spin filtering in the $CoFe_2O_4$ barrier.

polarization may only be explained by spin filtering in the $CoFe_2O_4$ barrier, as no other magnetic layer exists in the junction. This result therefore marks the first successful revelation of spin filtering in a $CoFe_2O_4$ tunnel barrier.

The observation of a non-negligible spin filter effect is very encouraging, especially since this is the first such direct measurement by the Meservey-Tedrow technique with a ferrite tunnel barrier. However the magnitude of P is significantly lower than what should be expected given the theoretical exchange splitting in the conduction band of $CoFe_2O_4$ [57]. The most probable cause of reduced P being defect states in the barrier—which could lead to spin scattering or spin-insensitive tunneling—the next natural step was to modify a growth parameter in order to improve the quality of our $CoFe_2O_4$ ultra-thin films. In the following section, we will consider the effect of oxygen vacancies in the spinel structure (due to insufficient oxidation conditions during growth) as one potential cause for the reduced polarization. Before moving on to this study, however, we can not ignore the fact that the positive polarization measured in the present Meservey-Tedrow experiment does not agree with the negative polarization predicted for $CoFe_2O_4$ in band structure calculations. The question of the sign of P is a significantly more complicated issue that will be addressed in Section 5.3.4.

5.3.2 Optimizing the SPT results : Effect of oxidation

Following the first successful Meservey-Tedrow measurement in our $CoFe_2O_4$ spin filter tunnel barriers, we proceeded to fabricate new $Pt/CoFe_2O_4/\gamma\text{-}Al_2O_3$ samples in which the oxidation conditions during growth were modified with respect to the original sample described in Section 5.3.1. As was presented in Chapter 3, one major advantage that was found in the MBE growth of $CoFe_2O_4$ was that the correct spinel phase and correct cation oxidation states could be obtained using a significantly large range of oxygen pressures in the plasma source ($P_{O_2}^{plasma}$). The structural and chemical characterization of all $CoFe_2O_4$ layers grown between $P_{O_2}^{plasma} = 0.2$ Torr and $P_{O_2}^{plasma} = 0.4$ Torr revealed no visible difference in the crystalline structure, stoichiometry and cation oxidation states. Their magnetic properties visibly did not vary either. This means that any difference that might exist in these films was likely due to point defects that were undetectable by standard characterization techniques. The first defects that come to mind are of course oxygen vacancies, which again in small concentrations are nearly impossible to quantify by standard chemical characterization techniques.

Several other $Pt(20\,nm)/CoFe_2O_4(3\,nm)/\gamma\text{-}Al_2O_3(1\,nm)/Al(4.2\,nm)$ tunnel junctions were therefore prepared for SPT measurements using a $P_{O_2}^{plasma}$ ranging from 0.2 to 0.4 Torr. Interestingly, a variation in the SPT charac-

Tab. 5.1: Summary of Meservey-Tedrow Experiments

Sample	$P_{O_2}^{plasma}$ (Torr)	R_jA (Ωcm^2) T = 77 K	R_jA (Ωcm^2) T = 4 K	P (%)
1	0.20	12.8	13.5	6
2	0.24	13.5	15.0	12
3	0.26	13.9	15.0	26

teristics was observed only for samples grown between 0.2 and 0.26 Torr. We will therefore concentrate on the results from three sample sets with $P_{O_2}^{plasma}$ = 0.2, 0.24 and 0.26 Torr. Again, because the structural and chemical characterization of both samples proved to be nearly identical, there was no straightforward way to quantify the difference between them. We therefore were limited to comparing P in the SPT measurements as a function of $P_{O_2}^{plasma}$, without knowing exactly what $P_{O_2}^{plasma}$ corresponded to physically in the samples. For the purpose of this comparison, the three samples that gave varying results by the Meservey-Tedrow technique—that is, the samples fabricated at $P_{O_2}^{plasma}$ = 0.20, 0.24 and 0.26 Torr—will from now on be called samples 1, 2, and 3 respectively.

As was the case with sample 1 in Section 5.3.1, R_jA in samples 2 and 3 increased significantly from room temperature to 77 K, and then remained stable down to 4 K. The resistance values in each of the three samples are summarized in Table 5.3.2. The zero-field dI/dV curves similarly revealed a clear Al superconducting energy gap with sharp peaks at $\pm$0.43 eV, and negligible leakage. In the case of sample 3, the measurement was performed in the two-terminal configuration (as opposed to sample 2 which was four-terminal), leading to the appearance of two additional peaks at higher V. Once again, these peaks may be completely ignored for the purposes of this study.

The application of a magnetic field resulted in the Zeeman splitting of the Al superconductor quasiparticle density of states in both samples 2 and 3. Furthermore, the four spin-dependent DOS peaks are clearly asymmetric, as may be seen for both samples in Figure 5.7-b,c,e,f.

In sample 2 ($P_{O_2}^{plasma}$ = 0.24 Torr), dI/dV curves were obtained at H = 3.3 T and 3.7 T. In both cases, the calculation of P using the Equation 2.6 yielded a value of about 12%. In addition, because this tunnel junction was measured in the four-terminal configuration, the dI/dV curves were nearly noise-free, allowing us obtain a more precise value of P by fitting them to Maki theory

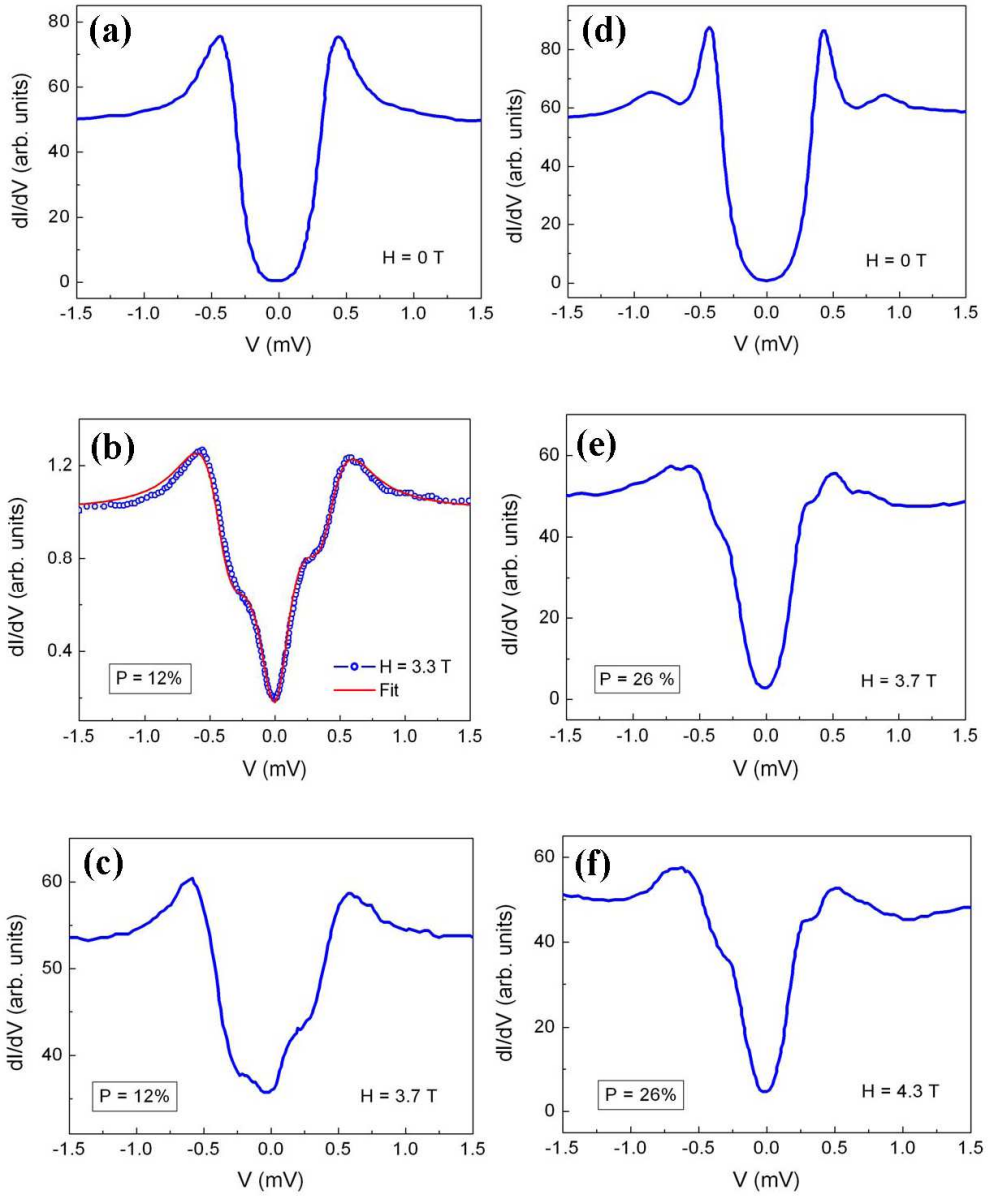

Fig. 5.7: Meservey-Tedrow experiments in two Pt(20 nm)/$CoFe_2O_4$(3 nm)/γ-Al_2O_3(1 nm)/Al(4.2 nm) tunnel junctions, both fabricated under increased oxidation conditions for the $CoFe_2O_4$. Figures (a)-(c) are the $H = 0$ T, 3.3 T and 3.7 T curves for a sample grown at $P_{O_2}^{plasma} = 0.24$ Torr (sample 2), revealing $P = 12\%$. In addition the curve in (b) at 3.3 T was fitted using Maki theory leading to a similar value of $P = 12.5\%$. Figures (d)-(f) correspond to the $H = 0$ T, 3.7 T and 4.3 T measurements of a sample grown at $P_{O_2}^{plasma} = 0.26$ Torr (sample 3), with $P = 26\%$. The results from this study clearly reveal the effect of increased oxidation conditions on the spin polarization of $CoFe_2O_4$.

[21] with the aid of the Cocoa SPT program [2]. Again briefly, Maki-Fulde theory describes the DOS of a SC taking into account the influence of Zeeman splitting, orbital depairing (c), spin orbit scattering (b) and susceptibility enhancement (e_0). In Figure 5.7-b we see that the $H = 3.3$ T curve may in fact be well fitted using this model. The fitting parameters used were the following : $T_c = 2.8$ K, $T = 0.45$ K, $H = 3.31$ T, $c = 0.08$, $b = 0.03$ and $e_0 = 0.7$. The result is $P = 12.5\%$, which agrees well with the approximative value obtained by comparing the relative spin-up and spin-down peak heights, thus justifying the exclusive use of Equation 2.6 to calculate P from the dI/dV curves obtained in the two-terminal configuration (samples 1 and 3). The increased value of P in sample 2 with respect to sample 1 begins to suggest that the stronger oxidation conditions may indeed have a positive effect on the spin filter efficiency of the $CoFe_2O_4$ barrier.

This trend was further confirmed by the SPT measurement of sample 3 ($P_{O_2}^{plasma} = 0.26$ Torr), which for an applied magnetic field of $H = 3.7$ T, yielded $P = 26\%$. Again, due to the noisier curves obtained in the two-terminal configuration, P in this sample was determined using Equation 2.6 rather than by Maki theory fitting. The dI/dV curves for sample 3 at $H = 3.7$ T and $H = 4.3$ T are shown in Figures 5.7-e,f. Beyond $P_{O_2}^{plasma} = 0.26$ Torr, no higher polarization was measured, indicating that the $CoFe_2O_4$ barriers reached saturation at this point.

The SPT results for the series of three Pt/$CoFe_2O_4$/γ-Al_2O_3/Al tunnel junctions described in this section reveal a systematic increase in P as a function of the oxidation conditions used during growth of the $CoFe_2O_4$ spin filters up to $P_{O_2}^{plasma} = 0.26$ Torr. Assuming that the oxygen vacancy concentration decreases with increasing $P_{O_2}^{plasma}$, we may qualitatively conclude that the presence of oxygen vacancies in $CoFe_2O_4$ is detrimental to the spin filter efficiency. Oxygen vacancies, even in very small concentration, are likely to create defect states in the spin filter band structure that have little or no exchange spitting, generate spin scattering events, and lead to spin-insensitive tunneling. Because the SPT characteristics of a spin filter are extremely sensitive to such perturbations in the tunneling current, even minor deviations from the optimal oxidation conditions during the growth of $CoFe_2O_4$ seriously affect its capability to act as an efficient spin filter.

Finally, it is worth emphasizing that the changes in oxygen vacancy concentration from sample 1 to sample 3 were undetectable by all standard structural, chemical and magnetic characterization techniques. Only the tun-

[2] The Cocoa SPT program was developed by E. Verduijn of the Applied Physics Department, Technical University of Eindhoven to fit experimental dI/dV curves obtained by the Meservey-Tedrow technique.

neling experiments presented above were sensitive enough to detect an effect related to these minor defects. This study therefore brings up another important point about SPT measurements : Not only are these extremely useful in understanding the magneto-transport properties and electronic band structure of magnetic thin films, but these may very well also be the most sensitive and accurate method for detecting the presence of defects in such systems.

5.3.3 Junction Resistance Temperature Dependence

Further evidence that oxygen vacancies influence the tunneling properties of our $CoFe_2O_4/\gamma$-Al_2O_3 barriers was seen in the junction resistance (R_j) versus temperature dependence of the Pt/$CoFe_2O_4/\gamma$-Al_2O_3/Al junctions. In particular, we were interested in the extent to which R_j increased when cooling down from room temperature to liquid He temperature (4 K). The increase in resistance, measured by the temperature resistance ratio $R_{ratio} = R_j(4K)/R_j(300K)$, is plotted in Figure 5.8 for a series of fifteen junctions whose $P_{O_2}^{plasma}$ during growth varied from 0.2 to 0.4 Torr. In this plot we immediately observe a substantial decrease in R_{ratio} for the junctions deposited between 0.2 and 0.26 Torr, followed by a plateau or saturation beyond 0.26 Torr. This saturation agrees well with that measured in P_{SF}. The large R_{ratio} in the low-oxidized junctions (corresponding to Samples 1 and 2 above) is characteristic of a tunnel barrier containing defect states in the band gap, which are likely generated by oxygen vacancies in the $CoFe_2O_4$. The defect states should act to lower the effective barrier height of the tunneling electrons, and thus induce a stronger $R_j(T)$ dependence. Because they are associated with oxygen bands (*sp*-type) that are weakly hybridized with the *d*-bands from the Co and Fe, their exchange splitting is much weaker that that of the *d*-states in the conduction band. The expected consequence is a significant reduction of P_{SF}, in good agreement with our SPT experiments.

The evolution of the resistance values with increasing oxidation conditions also indicated a decrease in the number of defect states in the band gap for the higher oxidized samples. This may be seen in the insert of Figure 5.8, were the values at 4 K are plotted. The R_j values are somewhat scattered due to the large error induced by the thickness uncertainty from one junction to another. Even a variation of a few angstroms in barrier thickness can cause R_j to change by an order of magnitude due to the exponential dependence of the tunneling current density on this parameter. It is worth noting that the resistance increase is relatively small, compared to the increase in R_{ratio}, because the effect of defect levels is less dominant at low temperature. Also, because the R_{ratio} is self-normalized, it is a more reliable parameter than R_j alone. Nevertheless, there is a clear increasing trend in the $R_j(P_{O_2}^{plasma})$

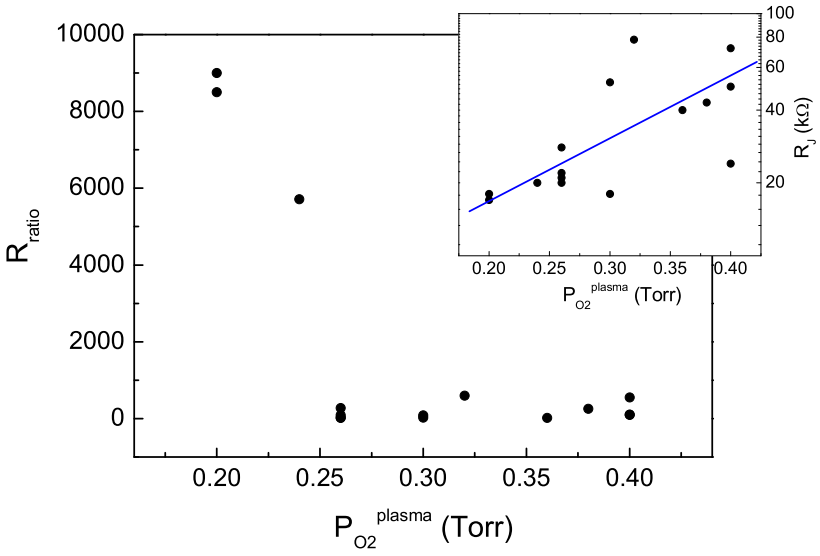

Fig. 5.8: Tunnel junction temperature resistance ratio ($R_j(4K)/R_j(300K)$) as a function of oxidation conditions for 15 junctions with $P_{O_2}^{plasma}$ = 0.2 - 0.4 Torr. The insert shows the distribution of the junction resistances at 4 K, plotted in semi-log scale, with the blue line serving as a guide to the eye.

distribution. This result again suggests that for the lower oxidized samples, *sp*-type defect states in the band gap generated by oxygen vacancies lower the effective barrier height, thus lowering R_j and P_{SF} in these junctions.

The $R_j(T)$ results for the series Pt/$CoFe_2O_4$/γ-Al_2O_3/Al tunnel junctions described in this section therefore reinforce the conclusions drawn from the SPT experiments. They in fact indicate that for $P_{O_2}^{plasma} < 0.26$ Torr, the $CoFe_2O_4$ barriers contain enough defect states due to oxygen vacancies to lower the effective tunnel barrier height, thus significantly increasing the $R_j(T)$ dependence. The predominant *sp* character of these states makes them less sensitive to exchange splitting, thus explaining the reduction in P_{SF}. Above 0.26 Torr, the temperature resistance ratio shown in Figure 5.8 saturates, in good agreement with the measured P_{SF}, and suggesting that tunneling is dominated by *d* states in the conduction band.

5.3.4 Discussion

In this final section, we discuss the complex issue which is the sign of $P_{CoFe2O4}$ measured systematically in our Meservey-Tedrow experiments. As was described in Chapter 2, electronic band structure calculations predict the exchange splitting in the conduction band of $CoFe_2O_4$ to lower the energy of the spin-down band and raise that of the spin-up band [57]. We would therefore expect a lower tunnel barrier height for spin-down electrons, and thus *negatively* polarized spin filtering, whereas the opposite is systematically observed. The Meservey-Tedrow technique being undoubtedly the most direct measurement of P in a tunneling current, this unexpected result must be an indication of some additional factor, other than the DOS in the $CoFe_2O_4$ conduction band, influencing the overall mechanism for spin-polarized tunneling. Without further experimental or theoretical confirmation, the interpretation of this phenomenon remains non-trivial. Nevertheless, in comparing the experimental conditions and samples used for the Meservey Tedrow and TMR (see chapter 7) measurements, two main differences stand out. The first is the detector electrode, which is either Al or Co. The second is the bias voltage applied for the two tunneling experiments. The effect of these two factors on the sign of P_{SF} is addressed below. Again, these remain open to discussion, and should be verified in the future by further experimental and theoretical investigations.

The measurement of an unexpected P has already been observed in Merservey-Tedrow experiments involving other systems. Most notably is the work of Thomas *et al.* which measured a positive P in the quasiparticle DOS of the SC Al electrode in $Co/SrTiO_3/Al$ tunnel junctions [86], whereas TMR experiments in $Co/SrTiO_3/La_{2/3}Sr_{1/3}MnO_3$ MTJs had already determined the $Co/SrTiO_3$ barrier/electrode combination to be negatively polarized by De Teresa *et al.* [19]. In the case of the MTJs, the polarization of Co was deduced from the Jullière formula assuming that the polarization of the $SrTiO_3/La_{2/3}Sr_{1/3}MnO_3$ interface was positive, based on previous studies of this half-metallic electrode [52]. In the work of Thomas *et al.*, one conjecture that they had was that the wave function symmetry of the Al detector may actually determine the sign of P.

In the case of our $Pt/CoFe_2O_4/\gamma\text{-}Al_2O_3/Al$ tunnel junctions, the effect of the Al detector electrode wave symmetry could be especially relevant if the alignment of the bands in the epitaxial barrier with the those of the Al resulted in the preferential detection of the highly delocalized *sp* electrons, and thus positive P. This is all the more likely as electronic band structure calculations show that $sp-d$ hybridization in $CoFe_2O_4$ is weak [57], resulting in highly mobile, delocalized *sp* electrons. The only structural difference

between the tunnel junctions used for Meservey-Tedrow and our futur TMR experiments being the detecting electrode (Al or Co respectively), it is quite possible that the Al detector electrode wave symmetry be in fact responsible for the positive sign of P measured in the Meservey-Tedrow case. An intriguing experiment to verify this hypothesis would be to substitute the SC Al spin detector with another transition metal SC whose electronic band structure is dominated by d-type bands. More on this potential experiment will be discussed in Chapter 8.

Another example of unexpected SPT results is the work of Worledge and Geballe, who measured a negative polarization in $SrRuO_3$ with $SrRuO_3$/ $SrTiO_3$/Al tunnel junctions by the Meservey-Tedrow technique [87]. This unique result proved that Al electrodes do not always detect positive P, thus excluding this as an explanation for our results or those of Thomas et al.. Worledge and Geballe correlated their unique SPT result to the theoretical work of Mazin [24], which we will also use to help explain our results with $CoFe_2O_4$. Before describing the details of this work, we recall that in Chapter 2, the polarization of a tunneling current was more precisely defined by Equation 2.7, in which the DOS for spin-up and spin-down electrons at the Fermi level were weighted by the spin-dependent matrix elements $|M_{\uparrow(\downarrow)}|^2$ governing the transmission of both types of electrons across the tunnel barrier. In the case of a spin filter, P_{SF} was defined as a function of the tunneling current densities (Equation 2.13), where $J_\uparrow$ and $J_\downarrow$ intrinsically contain these spin-dependent tunnel matrix elements in them. Based on these definitions, it becomes evident that P may not be entirely determined by the DOS of the ferromagnet or spin filter material if the difference between $|M_\uparrow|^2$ and $|M_\downarrow|^2$ is significant. This is exactly the basis of Mazin's work, which presented a simplified version of this scenario in which the weighing factor was taken to be the the square of the Fermi velocity $v^2_{\uparrow(\downarrow)}$ [24]. Because $J_{\uparrow(\downarrow)} \propto \langle Nv^2\rangle_{\uparrow(\downarrow)}$, Mazin was able to define a new spin polarization which he named P_{Nv^2} :

$$P_{Nv^2} = \frac{\langle Nv^2\rangle_\uparrow - \langle Nv^2\rangle_\downarrow}{\langle Nv^2\rangle_\uparrow + \langle Nv^2\rangle_\downarrow} \tag{5.1}$$

as opposed to the classic spin polarization which he called P_N :

$$P_N = \frac{N_\uparrow - N_\downarrow}{N_\uparrow + N_\downarrow} \tag{5.2}$$

In other words, P_N is the P determined by spin-polarized photoemission which probes more deep, localized d states. In a transition metal such as Ni, P_N is negative in clear agreement with band structure calculations. In the case of $CoFe_2O_4$, P_N is also expected to be negative, again from band

structure calculations. However, P_{Nv^2}, is meant for electron transport or tunneling where the mobility of the band electrons are to be considered. This second definition of P is likely that which governs the tunneling mechanism in Merservey-Tedrow SPT experiments [88].

Next, by a series of band structure simulations using Fe and Ni as model ferromagnets, Mazin showed that depending on the extent of the hybridization between the *sp* and *d* bands at the Fermi level, the difference between P_N and P_{Nv^2} could vary quite significantly. In other words, when the *sp* and *d* spin channels are highly hybridized and thus the area of their respective Fermi surfaces comparable (as is the case for Fe), the incorporation of the additional factor v^2 into the definition of P does not lead to significant modifications. P_N and P_{Nv^2} should therefore be similar in magnitude and sign. On the other hand, if the hybridization between *sp* and *d* channels is weak, one may single out the "light" *sp* pockets from the "heavy" *d* pockets on the Fermi surface. This being the case for Ni, the *d* bands are therefore more localized compared to the *sp* bands and hence have much lower mobility [89]. In this latter scenario, the multiplicative factor v^2 becomes very important and leads to a P_N that is dominated by the "heavy" *d* pockets, while P_{Nv^2} is dominated by the "light" *s* pockets. As Mazin clearly showed for the case of Ni, P_N and P_{Nv^2} may in fact be radically different and even of opposite sign.

We now go further to imagine two different tunneling experiments : one which probes the DOS and thus P_N (spin-polarized photoemission being the typical example), and one that is strongly influenced by the transition matrix elements and thus probing P_{Nv^2}. According to Mazin, if the $sp-d$ hybridization at the Fermi level of the ferromagnet is weak, one might very well measure opposite signs for P.

Returning to the case of $CoFe_2O_4$ and our Meservey-Tedrow experiments, the main question to answer is *which definition of P is probed?* To answer this we consider the conditions under which the experiment is performed. In order to probe the spin at the superconducting energy gap of the Al spin analyzer, the Meservey-Tedrow experiment is necessarily performed at extremely low bias voltage (< 2 mV). This means that the bands in the $CoFe_2O_4$ tunnel barrier are hardly deformed and that transport occurs via direct tunneling across the band gap. In this direct tunneling regime, $J_{\uparrow(\downarrow)}$ is naturally determined by a number of factors in addition to the tunnel barrier heights given by the DOS in the conduction band (See Equations 1.4 and 1.12). According to Mazin, $v^2_{\uparrow(\downarrow)}$ can not be ignored in the Mersevey-Tedrow experiment, making P_{Nv^2} the reasonable definition to consider.

Of course, this interpretation assumes that Mazin's arguments, originally developed for tunneling in classic MTJs, are also valid for the spin filter MTJ

scenario. While the role played by the electron mobility in the bands of the FM tunnel barrier is less obvious in the case of spin filtering, it is clear that P must be governed by additional transfer matrix elements that in turn take into consideration the nature of the *sp* and *d* bands in $CoFe_2O_4$. Furthermore, the fact that we are working with a fully epitaxial spin filter also introduces the possibility of additional factors including band symmetry filtering [32], resonant tunneling [90, 91] and band alignment with the energy levels of the Pt and Al electrodes—all of which form part of $|M_{\uparrow(\downarrow)}|^2$ and may potentially invert the sign of P. We therefore believe that such transfer matrix elements must be considered when interpreting the spin filter P measured by the Meservey-Tedrow technique.

Looking more closely at the electronic band structure of $CoFe_2O_4$, we see that the DOS in the conduction band contains *d* states that are highly localized and dissociated from the *sp* states contributed by the oxygen anions [57]. $sp-d$ hybridization is therefore weak, suggesting that P_{Nv^2} may indeed be *sp*-dominated and very different from P_N, in agreement with Mazin's predictions. The intriguing results from our Meservey-Tedrow experiments therefore suggest that P_{SF} is not necessarily determined by the DOS in the conduction band of the spin filter alone. In the case of $CoFe_2O_4$, whose complex electronic band structure contains distinct *sp* and *d* channels, the mechanism for spin filtering in the low-bias regime could apparently favor the transmission of *sp* electrons, leading to the observation of a positive P.

Following these results, what would be most interesting of course would be to compare the SPT measurements obtained by the Merservey-Tedrow technique with another measurement that probed the DOS and thus P_N rather than P_{Nv^2}. In Chapter 7, we will see that by performing TMR experiments at significantly higher bias voltage, we gain access to a different tunneling regime for which the spin polarization of $CoFe_2O_4$ is apparently negative, in good agreement with the theoretical DOS and the expected P_N.

6. $CoFe_2O_4/Fe_3O_4$ BILAYERS FOR SPINEL-BASED TUNNEL JUNCTIONS

Chapter 6 will cover the first of the two $CoFe_2O_4$-based spin filter MTJ systems studied in this thesis. The magnetic electrode will be Fe_3O_4, which as described in Chapter 4, was chosen for its predicted half metallic behavior and structural and chemical similarity to $CoFe_2O_4$. The $CoFe_2O_4/Fe_3O_4$ fully epitaxial system is especially unique because it is *fully oxide*. We will see that very interesting properties arise in the magnetic and spin-polarized tunneling (SPT) behavior of this bilayer combination, as a result of the oxide nature of the interface. The first part of the chapter will therefore be dedicated entirely to the magnetic properties of $CoFe_2O_4/Fe_3O_4$ bilayers. By combining a number of different experimental techniques, we will attempt to understand the fascinating but complex phenomena that arise at the spinel-spinel interface.

6.1 Magnetic Properties of the $CoFe_2O_4/Fe_3O_4$ system

6.1.1 Room temperature magnetization curves

The principal motivation behind the magnetic characterization of the $CoFe_2O_4/Fe_3O_4$ (barrier/electrode) combination was to see if it was possible to obtain an antiparallel magnetic state between the two layers, which in turn would permit future TMR experiments. In other words, the goal was to determine whether the $CoFe_2O_4$ and Fe_3O_4 films display two independent switching events despite the fact that they are directly in contact with each other.

The magnetic switching behavior of $CoFe_2O_4$(5 nm)/Fe_3O_4(15 nm) bilayers was therefore studied by VSM at room temperature. As was the case with the $CoFe_2O_4$ single layers, the bilayer samples showed a ferromagnetic easy axis in the plane of the films, with no in-plane angular anisotropy. Figure 6.1 shows a typical hysteresis loop of the bilayer samples. The $M(H)$ loop contains two inflection points around 100-200 Oe and 3000 Oe, hereafter called H_{s1} and H_{s2} respectively, which correspond to two independent switching events and suggest that an antiparallel magnetic state may be attained.

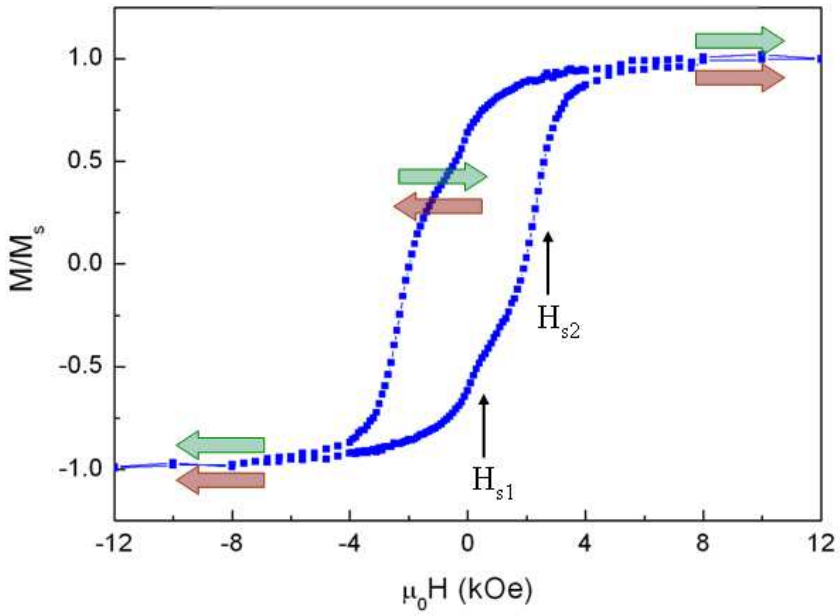

Fig. 6.1: Room temperature normalized magnetization loop for a $CoFe_2O_4$(5 nm)/Fe_3O_4(15 nm) bilayer measured in the plane of the film. The two inflection points labeled H_{s1} and H_{s2} correspond to the switching of the $CoFe_2O_4$ and Fe_3O_4 layers respectively.

The first question that must be treated given these experimental results is which of the two layers H_{s1} and H_{s2} correspond to. To answer this, we began by comparing the experimental magnetization height ratio of the two magnetic components in Figure 6.1 to the theoretically expected ratio from the known saturation magnetizations of $CoFe_2O_4$ and Fe_3O_4 (see Equation 6.1). Taking $M_{CoFe_2O_4}$(5 nm)=250 kA/m and $M_{Fe_3O_4}$(15 nm)=370 kA/m [65], we obtain the following expected magnetization height ratio :

$$\frac{\mu_{CoFe2O4}}{\mu_{Fe3O4}} = \left(\frac{M_{CoFe2O4}}{M_{Fe3O4}}\right)\left(\frac{t_{CoFe2O4}}{t_{Fe3O4}}\right) \approx 0.23$$

Here the value of 0.23 corresponds very well with the ratio observed experimentally in Figure 6.1, leading us to conclude that the $CoFe_2O_4$ layer switches first (H_{s1}). While the natural reaction may be to find this interpretation counterintuitive knowing that the H_c of thicker $CoFe_2O_4$ films tends to be in the thousands of Oe, it is important to consider the magnetic properties specific to the ultra-thin $CoFe_2O_4$ films. We recall that the $M(H)$ loop of the

5 nm $CoFe_2O_4$ single layer (Chapter 5) shows an H_c of 200 Oe, while that of a 15 nm Fe_3O_4 single layer is ∼300 Oe [65]. From this data, it thus becomes evident that the $CoFe_2O_4$ may in fact switch first, as seems to be the case in the present system. The minor hysteresis loop of the supposed $CoFe_2O_4$ contribution to the magnetization curve is also shown in the inset of Figure 6.2-a. Its shape and coercivity are remarkably similar to the magnetization curves of a $CoFe_2O_4$(5 nm) single layer, futher suggesting that the first layer to switch is indeed the $CoFe_2O_4$. The second switching field should therefore correspond to the Fe_3O_4. Surprisingly however, H_{s2} is over 3000 Oe, which is ten times greater than the coercivity of a single Fe_3O_4 layer. This result may only be explained by the presence of an exchange coupling at the interface between the two films causing the Fe_3O_4 coercivity to explode.

6.1.2 Low temperature magnetization curves

In order to better examine the switching behavior between the $CoFe_2O_4$ and Fe_3O_4 layers, we measured the in-plane magnetization at various temperatures down to 150 K. The result was a systematic and dramatic accentuation of the two phase hysteresis loop with decreasing T, as may be seen by the measurement at 150 K in Figure 6.2-a. At this particular temperature, H_{s2} increases to 8000 Oe, which is a trademark sign that a powerful exchange coupling is present. As for H_{s1}, this remains nearly unchanged suggesting that even at low temperature, the coupling interaction favors the rapid switching of $CoFe_2O_4$. A detailed discussion of the possible mechanisms governing these results will follow in Section 6.2. The low temperature VSM measurements reinforce the notion that an antiparallel magnetic state is present and stable thanks to the strong exchange coupling between the two layers at their interface.

Taking a closer look at the temperature dependence of the $CoFe_2O_4$(5 nm)/Fe_3O_4(15 nm) $M(H)$ curves, we find that H_{s2} varies remarkably linearly with T (see the inset of Figure 6.2-b). Because H_{s2} is directly related to the energy of the exchange coupling (E_{ex}) at the $CoFe_2O_4/Fe_3O_4$ interface, this means that E_{ex} also displays a linear temperature dependence. The origin of this linear $E_{ex}(T)$ dependence will remain unresolved throughout this thesis, and would require a more theoretical analysis of the present system taking into account the local magnetic configuration at the bilayer interface and the different possible exchange interactions between Fe and Co cations. The discussion in Section 6.2 presents a possible phenomenological scenario which reasonably explains the observed results. However, further analytical calculations, not presented in this thesis, would further clarify the intriguing linear evolution of $H_{s2}(T)$.

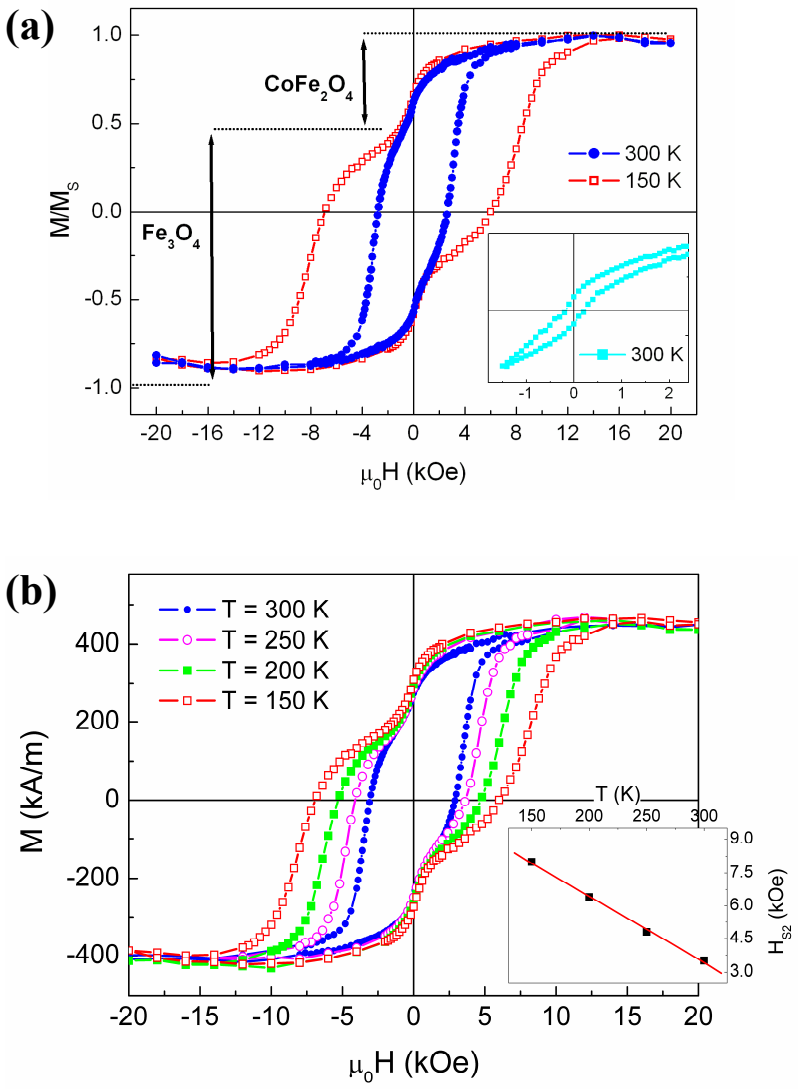

Fig. 6.2: Magnetization curves for a $CoFe_2O_4$(5 nm)/Fe_3O_4(15 nm) bilayer measured at various temperatures. In (a), the $CoFe_2O_4$ and Fe_3O_4 contributions are identified for the room temperature and 150 K measurements. The inset of (a) also shows the room temperature minor loop of the $CoFe_2O_4$ layer, which is comparable to the hysteresis loop of a 5 nm $CoFe_2O_4$ single layer. In (b), the unnormalized measurements at 300, 250, 200 and 150 K are superposed, revealing a linear evolution in H_{s2} as a function of T (insert).

Despite the uncertainty about the evolution of H_{s2} as a function of T, the room temperature and low temperature $M(H)$ results already reveal quite a bit of information regarding the magnetization reversal behavior in our $CoFe_2O_4$(5 nm)/Fe_3O_4(15 nm) bilayers. The mere shape of the curves suggests that, as the magnetic field is lowered from the saturated and "parallel" (P) state past the zero-field mark, the $CoFe_2O_4$ layer switches quite readily both at high temperature and at room temperature. Once in the "antiparallel" (AP) state, a strong exchange coupling between $CoFe_2O_4$ and Fe_3O_4 stabilizes the system in this configuration, making it extremely difficult for the Fe_3O_4 to switch. Only when the applied magnetic field becomes strong enough to overcome E_{ex} at the $CoFe_2O_4/Fe_3O_4$ interface, does the Fe_3O_4 finally let go, aligning itself with the $CoFe_2O_4$ and returning the system to a P configuration. What is most unique in this system is therefore that the energetically stable or "blocked state" *occurs after the $CoFe_2O_4$ has switched*, which is rare in exchange coupled systems involving two ferro- or ferrimagnetic layers. Furthermore, the intrinsic coercivities of the $CoFe_2O_4$(5 nm) and Fe_3O_4(15 nm) films alone (on the order of 200 to 300 Oe for both) are so close that it is impossible to predict which of the two layers should act as the "hard" and "soft" ferromagnet (FM). Only when the two are put directly in contact with each other, does it finally become clear that the $CoFe_2O_4$ acts as the blocking layer after its own magnetic reversal.

6.1.3 Insertion of a thin γ-Al_2O_3 spacer

The origin of the enlarged coercivity in the $CoFe_2O_4$(5 nm)/Fe_3O_4(15 nm) bilayer samples was further analyzed at room temperature by preparing a similar bilayer sample in which the $CoFe_2O_4$ and Fe_3O_4 layers were separated by a 3 nm γ-Al_2O_3 spacer. In this case, the enlarged portion of the magnetic hysteresis loop shown in Figure 6.1 is reduced to a coercivity of 400 Oe (see Figure 6.3), which is much closer to the usual H_c of a Fe_3O_4(15 nm) single layer. The switching of the $CoFe_2O_4$(5 nm) in this case may not be distinguished as it too close to that of the Fe_3O_4. This measurement proves that the enhanced coercivity observed in the $CoFe_2O_4$(5 nm)/Fe_3O_4(15 nm) samples results exclusively from a magnetic interaction localized at the bilayer interface, and not from the intrinsic properties of either of the individual layers.

6.1.4 In-plane Magnetoresistance Measurements

Another method to study the magnetic order (or disorder) in our $CoFe_2O_4$(5 nm)/Fe_3O_4(15 nm) bilayer samples was to perform current-in-plane (CIP)

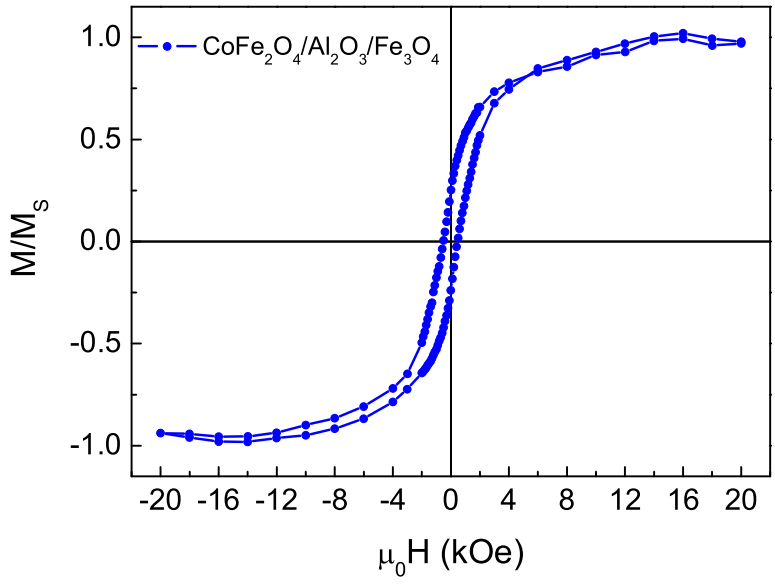

Fig. 6.3: Normalized magnetization curve for a $CoFe_2O_4$(5 nm)/γ-Al_2O_3(3 nm)/Fe_3O_4(15 nm) trilayer demonstrating the effect of a nonmagnetic spacer on the magnetic properties of the $CoFe_2O_4/Fe_3O_4$ bilayer system.

electronic transport measurements using the PPMS system described in Chapter 3. This was done by directly placing electronic contacts on the top Fe_3O_4 layer for measurements in the four terminal configuration. Because the resistivity difference between a 5 nm $CoFe_2O_4$ layer (see Chapter 5) and a 15 nm Fe_3O_4 film [83] is of the order of 10^3, we could safely assume that all of the current passed in the Fe_3O_4 layer.

The electronic transport in Fe_3O_4 is governed by the FM double exchange interaction between Fe^{2+} and Fe^{3+} cations, which in turn permits electron hopping and thus conduction. When this FM double exchange is disturbed by the presence of defects or other magnetic interactions, the resistance versus applied magnetic field ($R(H)$) curves in Fe_3O_4 exhibit significant magnetoresistance (MR). Measuring the MR in Fe_3O_4 thin films therefore directly probes the level of magnetic disorder, which in the case of our $CoFe_2O_4/Fe_3O_4$ system could eventually be caused by the exchange interactions at the bilayer interface. Logically, a peak or maximum in the $MR(H)$ curve should correspond to the applied field for which the magnetic disorder is greatest [92, 81]. A schematic illustration of the CIP transport measurement in our

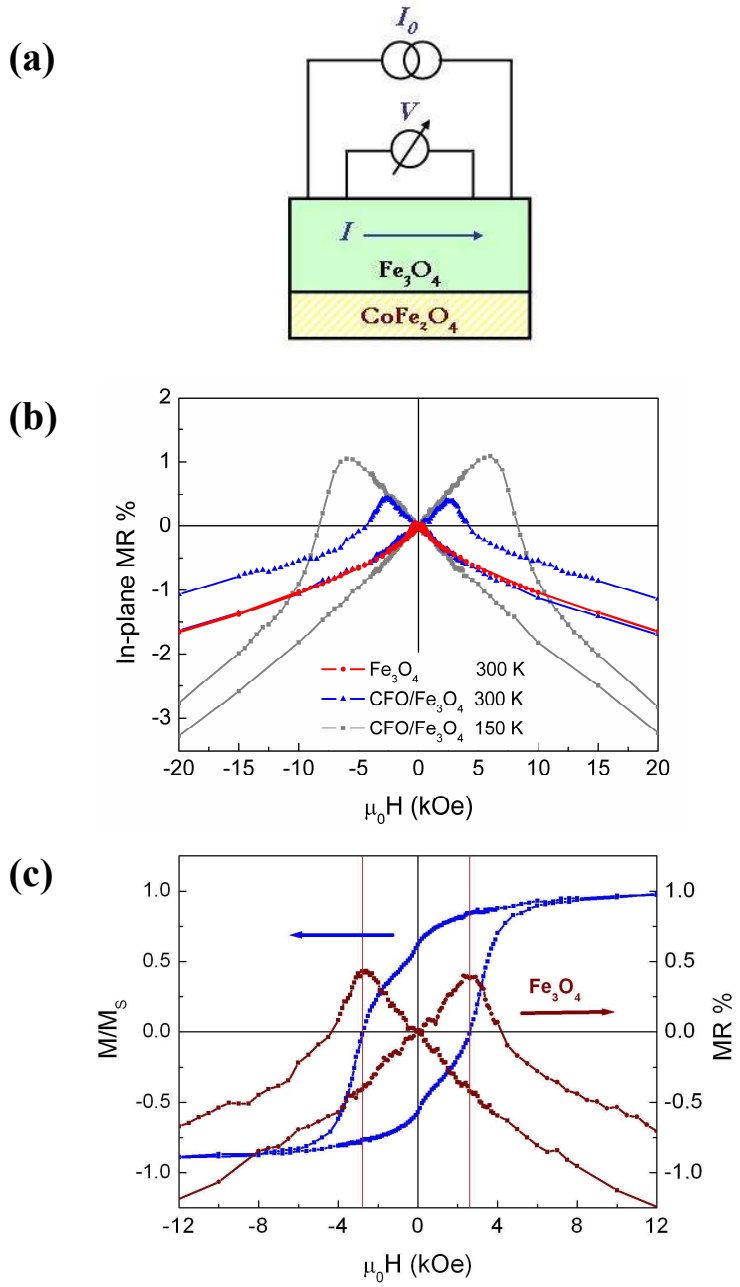

Fig. 6.4: Current-in-plane magneto-transport measurements in a $CoFe_2O_4$(5 nm)/Fe_3O_4(15 nm) bilayer. (a) Schematic representation of the experimental setup, with the applied current running through the Fe_3O_4 layer. (b) Magnetoresistance measurements in the $CoFe_2O_4/Fe_3O_4$ sample at 300 K and at 150 K. The MR curve for a Fe_3O_4 (15 nm) layer is also shown at 300 K as a reference. (c) Comparison of the room temperarture MR curve with the corresponding magnetization loop, showing the clear alignment between the MR peaks and the coercive field.

$CoFe_2O_4/Fe_3O_4$ bilayers is shown in Figure 6.4-a.

One very important point to note about the transport properties of Fe_3O_4 thin films, is that these exhibit an intrinsic MR due to the magnetic disorder caused by the presence of antiphase boundaries [93, 81, 82]. The intrinsic MR at 300 K for a Fe_3O_4(15 nm) single layer grown in our MBE chamber under similar conditions to our $CoFe_2O_4/Fe_3O_4$ bilayers is shown in red (circles) in Figure 6.4-b. In blue (triangles) and in gray (squares) are the MR curves for a $CoFe_2O_4$(5 nm)/Fe_3O_4(15 nm) bilayer at 300 K and 150 K respectively. From these measurements it is quite clear that the MR in the Fe_3O_4 is dramatically modified in the bilayer case, indicating that an additional magnetic disorder is created by the interface with $CoFe_2O_4$. In other words, the exchange coupling between $CoFe_2O_4$ and Fe_3O_4 must result in a local magnetic configuration at the interface that significantly disturbs the FM interactions in the Fe_3O_4.

To extract further information from the MR curves of our $CoFe_2O_4/Fe_3O_4$ bilayers, we next superposed the room temperature curve in Figure 6.4-b with the corresponding $M(H)$ hysteresis loop. Doing so, as may be seen in Figure 6.4-c, reveals a near-perfect alignment between the MR peaks and the coercive field, or point of zero magnetization, in the bilayer hysteresis loop. Because the coercive field in this hysteresis loop corresponds to the field of highest magnetic disorder *of the entire sample, both layers combined,* this result tells us that the Fe_3O_4 film necessarily "feels" the disorder imposed by the $CoFe_2O_4$, via the exchange interaction at the interface.

Finally, in order to better interpret the dynamics of magnetic switching behavior, we compared the derivatives of the $R(H)$ and $M(H)$ curves at 150 K. The low temperature curves were chosen simply because the inflection points at H_{s1} and H_{s2} in the magnetic measurement were better defined than at room temperature. In the case of $M(H)$, the derivative dM/dH exhibits two clear peaks naturally corresponding to the switching events H_{s1} and H_{s2}. On the other hand, the derivative of $R(H)$ contains only one peak which aligns perfecly with that of H_{s2} in dM/dH (see Figure 6.5). This simple analysis is extremely valuable for several reasons. First, the single peak in dR/dH validates the assumption that all of the applied current in the transport measurements passes solely through one layer : the Fe_3O_4. Secondly, its alignment with H_{s2} also confirms that the Fe_3O_4 is the second layer to switch, as was originally deduced from the magnetization height ratio in the $M(H)$ measurements in Section 6.1.

The dR/dH characteristics therefore tell us that as the applied magnetic field is lowered from saturation, past the switching of the $CoFe_2O_4$ layer, the magnetic configuration throughout the entire Fe_3O_4 film does not change significantly. This may be seen by the lack of any noticeable peak in dR/dH

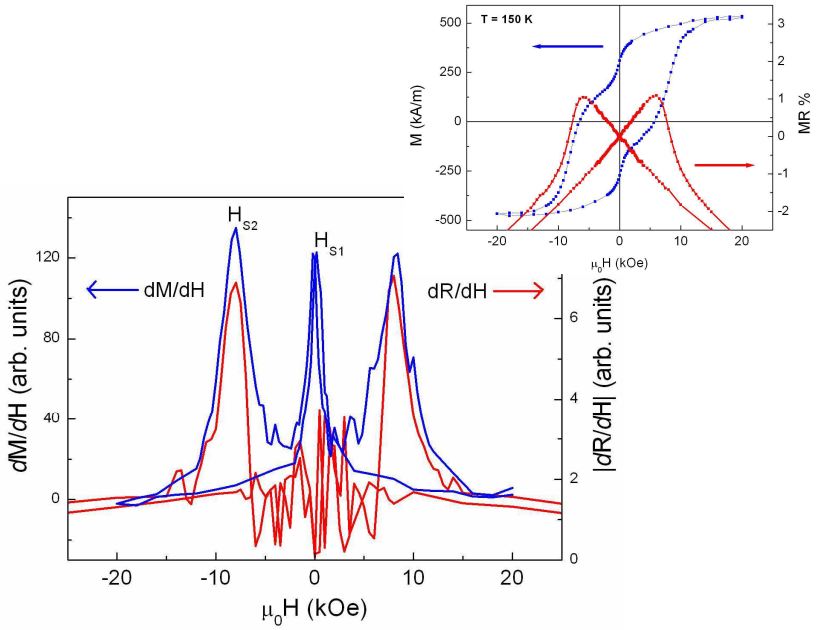

Fig. 6.5: Comparison of the derivatives of the magnetization and magnetoresistance curves in a $CoFe_2O_4$(5 nm)/Fe_3O_4(15 nm) sample at 150 K. dR/dH exhibits one single peak (symmetric for $\pm H$) which aligns perfectly with H_{s2} of dM/dH—that is, with the switching of Fe_3O_4.

from $H = 20$ kOe down to $H = H_{s2}$ [1]. In other words, the local magnetic configuration at the $CoFe_2O_4/Fe_3O_4$ interface must be such that only the $CoFe_2O_4$ is affected by its own reversal, while the Fe_3O_4 stays fixed. Only when H becomes great enough to overcome E_{ex}, is the Fe_3O_4 finally released from the blocked configuration, switching rapidly to realign with the direction of the applied magnetic field. A detailed discussion of a possible magnetic configuration at the $CoFe_2O_4/Fe_3O_4$ interface, taking into consideration the observations made from the dR/dH characteristics, will be presented in Section 6.2.

[1] The noise in dR/dH around -5 kOe $< \mu_0 H <$ 5 kOe is due to a change in the step size in the $R(H)$ measurements, and did not result in any reproduceable peaks in multiple measurements.

6.1.5 Polarized Neutron Reflectivity

As was described in Chapter 3, polarized neutron reflectivity (PNR) is an extremely valuable tool for the characterization of magnetic multilayers with complex exchange interactions. In the study of our $CoFe_2O_4/Fe_3O_4$ bilayer system, PNR provided a complementary analysis of the magnetic reversal behavior to the VSM and PPMS measurements, in particular thanks to its ability to extract magnetization depth profiles across the entire thickness of the films and at different applied magnetic fields. Following the acquisition of the reflectivity curves, these were fitted using the SimulReflec program [2], by a model that took into consideration the following parameters for each of the sample constituents (See Chapter 3, Section 3.4.2):

- t = thickness (nm).
- ρ = material density (g/cm^3), fixed at 1.36 for Fe_3O_4 and 1.35 for $CoFe_2O_4$.
- b = neutron scattering factor (fm), theoretically 51.6 for Fe_3O_4 and 44.6 for $CoFe_2O_4$.
- μ = magnetic moment (μ_B).
- σ = rms rugosity (nm), fixed at 0.3 for the all of the layers based on previous x-ray reflectivity measurements.

PNR measurements on a $CoFe_2O_4$(5 nm)/Fe_3O_4(15 nm) bilayer deposited directly on α-Al_2O_3 began at the maximum applied magnetic field allowed by the magnet in the neutron spectrometer, which was 1.2 T. The room temperature magnetization curve of this sample being closed (i.e. reversible) at 1.2 T (Figure 6.1), we could assume that our bilayer system was saturated and in the P magnetic state. The reflectivity curve and simulation parameters for the $CoFe_2O_4$(5 nm)/Fe_3O_4(15 nm) bilayer at H = -1.2 T and T = 300 K are shown in Figure 6.6-a. In this figure we see that we are able to successfully reproduce the experimental R^{++} and R^{--} curves using a bilayer model in which the thickness, scattering factor and magnetic moment of the $CoFe_2O_4$ and Fe_3O_4 layers correspond reasonably well with those expected for a 5 nm and 15 nm film of each material respectively (the thickness was systematically overestimated by about 20% in all measurements). This first, simple PNR

[2] Developed by the Laboratoire Léon Brillouin at CEA-Saclay for the simulation of x-ray and neutron reflectivity measurements. See also http://www-drecam.cea.fr/llb/prism/programs/simulreflec/simulreflec.html.

(a)

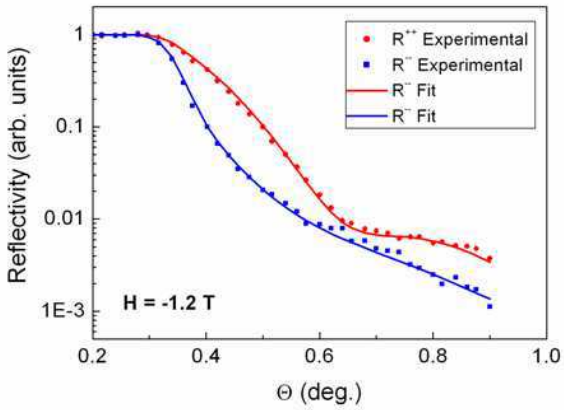

H = -1.2 T	*t* (nm)	*b* (fm)	μ (μ_B)
$CoFe_2O_4$	6.5	48.4	-1.9
Fe_3O_4	18.9	50.6	-3.1

(b)

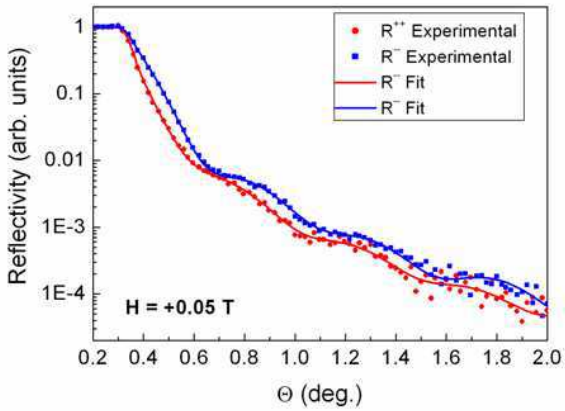

H = +0.05 T	*t* (nm)	*b* (fm)	μ (μ_B)
$CoFe_2O_4$	1.9	45.1	+0.34
Interface	5.5	48.7	-0.98
Fe_3O_4	18.2	50.9	-1.8

Fig. 6.6: Room temperature PNR curves for a $CoFe_2O_4$(5 nm)/Fe_3O_4(15 nm) bilayer at -1.2 T (a) and +0.05 T (b). The tables below each graph show the fitting parameters used to simulate the experimental curves, and thus extract information about the magnetic configuration in the films.

measurement therefore further confirms the bilayer nature of the sample via a *magnetic* rather than structural or chemical characterization technique.

In the following experiment, we next swept the field from H = -1.2 T, past the first switching event at H_{s1}, to H = +0.05 T. The experimental reflectivity curve obtained at the new field of 0.05 T is shown in Figure 6.6-b. This second measurement was once again fitted using the SimulReflec program, and was only reproducible using a model that contained a *positive* μ for a portion of the $CoFe_2O_4$ layer, whereas for Fe_3O_4, μ remained *negative*. We note that when fitting all of the reflectivity curves at intermediate magnetic fields, the total thickness of the bilayer was fixed to that originally found for the measurement at 1.2 T. This important result confirms the presence of an AP magnetic state for a given magnetic field between H_{s1} and H_{s2}, while also proving that the $CoFe_2O_4$ film is indeed the first to switch. We note that the negatively magnetized portion of the bilayer had to be broken down into two sublayers of 5.5 nm and 18.2 nm, the first having a reduced magnetic moment with respect to the second. The thickness of the $CoFe_2O_4$ layer was also determined to be 1.9 nm, thinner than the expected 5 nm. We believe that the second 5.5 nm layer may correspond to an intermediate zone at the $CoFe_2O_4/Fe_3O_4$ interface that actually includes some of both materials. The reduced moment in this interfacial zone could be explained by the averaged moments of the positive $CoFe_2O_4$ and negative Fe_3O_4 contributions, as well as by a possible progressive switching of the spins on either side of the interface due to a more complicated local magnetic configuration (see Section 6.2).

In continuation to the PNR experiment at H = 0.05 T, we proceeded to gradually increase the applied magnetic field from 0.05 T up to 1.2 T, this time tracing the magnetization loop past the second switching event at H_{s2}. Seven additional reflectivity curves were obtained, and from them, the corresponding magnetization depth profiles were plotted. These are all shown in Figure 6.7. We note that μ depicted in these profiles is the projection of the total magnetic moment in the film along $\vec{H}$, meaning that the reduction of μ may be attributed to a rotation away from the direction of $\vec{H}$. For H = 0.05 T, 0.1 T and 0.15 T, the magnetization depth profiles display an antiparallel state, in good agreement with the $M(H)$ curve (Figure 6.7-a). As the field is increased in this regime, the Fe_3O_4 layer slowly loses some of its magnetic moment, in gradual preparation for the switching event at H_{s2}. The $CoFe_2O_4$, on the other hand, remains fixed and stable. At H = 0.2 T (Figure 6.7-b), the magnetization of Fe_3O_4 suddenly turns positive, indicating a rapid magnetic reversal at a magnetic field that again agrees well with H_{s2} in the $M(H)$ curve. Finally, for H = 0.25 T, 0.3 T, 0.35 T and 1.2 T (Figure 6.7-c), we see that once the Fe_3O_4 layer has switched, the two

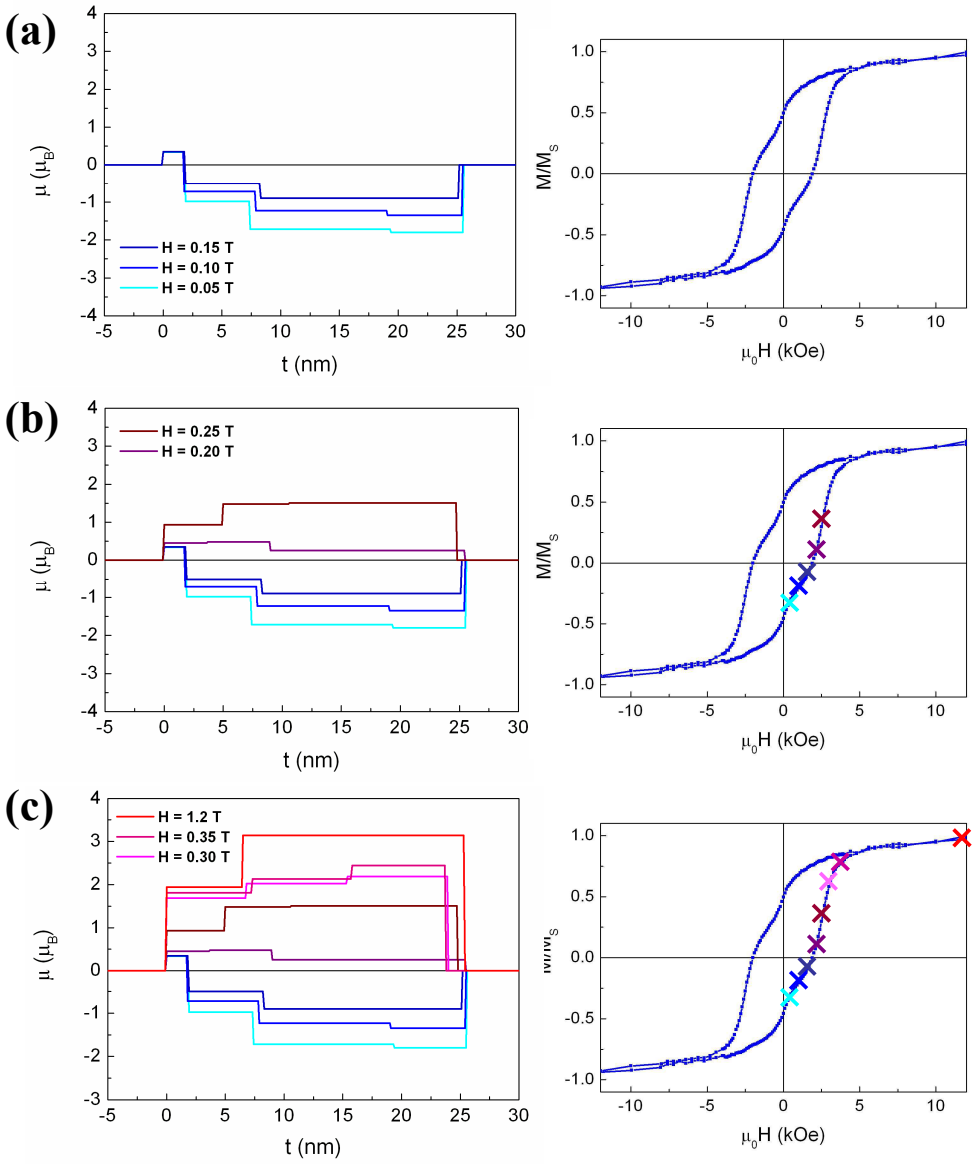

Fig. 6.7: Magnetization depth profiles obtained from room temperature PNR measurements of the same $CoFe_2O_4$(5 nm)/Fe_3O_4(15 nm) sample at different stages of the magnetic hysteresis cycle (i.e. various applied magnetic fields) : (a) In the antiparallel magnetic configuration; (b) About the switching of Fe_3O_4; (c) During the approach to saturation, after the switching of Fe_3O_4. The crosses on the magnetization loops on the right-hand side indicate the point of to each profile measurement.

constituents of the bilayer sample rapidly recover their full magnetization and return to the original bilayer configuration depicted in Figure 6.6-a, only with opposite sign. The series of magnetization depth profiles thus successfully illustrates the step by step dynamics of the magnetic reversal process in the $CoFe_2O_4$(5 nm)/Fe_3O_4(15 nm) system.

6.2 Discussion of the Exchange Coupling Mechanism

The series of VSM, PPMS and PNR experiments on the $CoFe_2O_4$(5 nm)/Fe_3O_4(15 nm) bilayer system illustrate the physical consequences of using an insulating barrier which is both an oxide and magnetic in epitaxial tunnel junction heterostructures. Due to the wide range of complex interface phenomena that such materials may potentially produce, their magnetic (and consequently magneto-transport) properties vary considerably from one magnetic counter electrode to another. In this chapter, we have studied a $CoFe_2O_4$/FM system whose unique magnetization behavior results from the nature of the exchange coupling at the interface. In our $CoFe_2O_4/Fe_3O_4$ bilayers, not only are the structure and chemistry of the two films nearly identical, but their coercive fields as well. The result is a bilayer system whose magnetization reversal behavior is quite unpredictable. In fact, the $CoFe_2O_4$(5 nm)/Fe_3O_4(15 nm) bilayers present a new physical scenario that has never been analyzed before : a FM/FM exchange coupled system in which the distinction between the "hard" and "soft" layers may not be made based only on the intrinsic properties of the individual films. This is in contrast to the well studied FM/FM (or "exchange spring magnet") coupled systems containing one distinctly soft and one hard layer [94, 95]. In the present case, it is not until the $CoFe_2O_4$ and Fe_3O_4 layers are put in contact with each other in a bilayer structure that the role of each material becomes evident.

The discussion presented in this section will attempt to analyze the different results presented in Sections 6.1.3 - 6.1.5, in order to better understand the coupling mechanism and local magnetic configuration at the interface of our $CoFe_2O_4$(5 nm)/Fe_3O_4(15 nm) bilayers. We maintain that the interpretation is somewhat hypothetical, as is often the case when studying complex exchange-coupled systems. The goal here is therefore to describe a physical scenario that we believe is probable given the ensemble of experimental observations and the known structural and magnetic particularities of the family of spinel ferrite thin films.

6.2.1 Switching Order

Before venturing to decipher the nature of the exchange interaction at the $CoFe_2O_4$(5 nm)/Fe_3O_4(15 nm) interface, it is important to emphasize that the originality in this exchange-coupled system containing two ferrimagnets of comparable coercivity lies in the fact that the exchange coupling most dramatically affects the second layer to switch. This is contrary to what is generally reported in traditional exchange spring magnets containing one hard and one soft layer. Judging from the magnetization curves (Figures 6.1 and 6.2), the $CoFe_2O_4$ layer switches readily while the Fe_3O_4 layer follows at an unusually large switching field of 2000-3000 Oe. As far as we know, all previous publications regarding $CoFe_2O_4$/Fe_3O_4 exchange coupled systems agree upon the opposite switching order. This is by all means a correct assumption in systems where the $CoFe_2O_4$ is significantly thicker, consequently exhibiting a large anisotropy field and thus high coercivity [96, 97]. In the typical scenario of a $CoFe_2O_4$ film over 20 nm thick, the distinction between the hard ($CoFe_2O_4$) and soft (Fe_3O_4) layers is unmistakable [98]. However, when the $CoFe_2O_4$ thickness is reduced to a few nanometers, its coercivity dramatically decreases such that it can no longer be considered a hard ferrimagnet with respect to Fe_3O_4. In this situation, which corresponds to that in our samples, the distinction between the two layers is no longer obvious. While in a previous study of a similar epitaxial $CoFe_2O_4$(3 nm)/Fe_3O_4(25 nm) system the $CoFe_2O_4$ layer was intuitively assumed to switch last [77], our VSM, PPMS and PNR results unanimously agree that this assumption is incorrect.

6.2.2 Nature of the Exchange Interaction

Having understood the switching order of the $CoFe_2O_4$ and Fe_3O_4 layers, we continue our analysis by identifying the nature of the exchange interaction, at the atomic level, in between the two—that is whether the exchange coupling is ferromagnetic (F) or antiferromagnetic (AF). Thanks to the oxide/oxide nature of the $CoFe_2O_4$/Fe_3O_4 interface, the exchange mechanism may be analyzed in detail because the dominant magnetic interactions in these ferrimagnetic oxides are superexchange interactions involving distinct 3d and 2p states in the cations and oxygen anions respectively. Nevertheless, the existence of both F and AF superexchange interactions in both layers makes the identification of the exchange coupling at the interface somewhat more complex. The most straight forward approach would be to look for a shift in the minor loop of the magnetization curve in Figure 6.2-a. However, this analysis is not valid in the present case because the exchange coupling

manifests itself via a change in coercivity and not a shift in the minor loops of the two layers. The value of H_{s1} around 100-200 Oe suggests that the interface coupling encourages the early switching of the $CoFe_2O_4$ layer. Such a *facilitation* of the first reversal when starting from a *parallel* magnetic state is a sign of AF coupling. Similarly, the *enhanced* H_{s2} of Fe_3O_4 in the *antiparallel* state is also an indication that the coupling is AF.

In addition to this qualitative consideration of the magnetization curves which favors an AF exchange between $CoFe_2O_4$ and Fe_3O_4, the interpretation is strengthened by evaluating the strength of the different superexchange interactions present in the two spinel ferrites. Assuming that the interface between $CoFe_2O_4$ and Fe_3O_4 is structurally coherent with the bulk of the films, which was indeed confirmed by our TEM investigation in Chapter 4, energy considerations may be used to predict which of the bulk interactions is the most probable at the interface. In both $CoFe_2O_4$ and Fe_3O_4, the magnetic character of these ferrimagnets is dominated by the AF exchange interactions involving cations in tetrahedral (A) and octahedral (B) sites. Not surprisingly, the AF(A-B and A-A) exchange stiffness constants are significantly greater than the FM(B-B) constants. In $CoFe_2O_4$ for example, $J_{AF} = -25k_B$(A-B), $-19k_B$(A-A) and $J_F = 4k_B$ [61]. Similar values are found for Fe_3O_4 [80]. The $CoFe_2O_4/Fe_3O_4$ interface—although structurally coherent—presents a magnetic defect, as the presence of Co^{2+} cations is foreign to the Fe_3O_4 layer (and the presence of Fe^{2+} to the $CoFe_2O_4$). New exchange interactions that do not exist in either of the two ferrite films must therefore form. Based on the notably large difference between J_{AF} and J_F in both materials, it is much more probable, from a purely energetic standpoint, that the new couplings prefer to be AF.

An AF coupling that favors the antiparallel configuration therefore pushes the $CoFe_2O_4$ to switch readily. Once the $CoFe_2O_4$ has switched, the exchange field dominates the Fe_3O_4 layer and stabilizes it in the antiparallel state with respect to the applied field. The strength of the exchange field prohibits the Fe_3O_4 from continuing to switch and leads to the enlarged H_{s2}.

6.2.3 Local Magnetic Configuration at the Interface

After understanding the nature of the coupling and general magnetization reversal mechanism in our $CoFe_2O_4$(5 nm)/Fe_3O_4(15 nm), the next step is to identify that local magnetic configuration at the bilayer interface. Here the interpretation becomes more delicate, as none of the experimental methods described above give direct access to this information. We must therefore carefully examine the different results, and look for subtle signs of a certain magnetic structure at the interface.

To begin, we observe that there is a positive slope in the magnetization curve with respect to the applied field in the range between H_{s1} and H_{s2} both at room temperature and 150 K (Figure 6.2-a). The positive slope is also visible in the tail of $CoFe_2O_4$ minor loop (inset of Figure 6.2-a). This detail leads us to believe that a domain wall is present at the interface for this field range. In fact, such a slope has been previously observed by Canet *et al.* in $Fe_{30}Au_{70}/Fe_{35}Au_{65}$ exchange-coupled bilayers [99], and has been attributed to the compression of the interfacial domain wall as the magnitude of the magnetic field increases. In the case of our $CoFe_2O_4$(5 nm)/Fe_3O_4(15 nm) bilayers, this would suggest that there exists a progressive rotation of the spins, coupled antiferromagnetically on either side of the interface, towards a parallel or antiparallel alignment (depending on the magnitude of the applied magnetic field) far from the interface.

The notion of an interfacial zone possibly containing a domain wall structure is further supported by the magnetization depth profiles in the PNR measurements. In Figure 6.7, we see that all of the profiles obtained in the AP configuration contain an interfacial zone of a few nanometers in thickness, covering part of the $CoFe_2O_4$(5 nm) and part of the Fe_3O_4(15 nm), with a reduced magnetization with respect to the Fe_3O_4. As was mentioned in Section 6.1.5, this interfacial portion of the depth profile could very well be due to a progressive switching of the antiparallel moments in the $CoFe_2O_4$ towards the parallel moments in Fe_3O_4. The reduced negative moment would therefore correspond to the average of the moments in both layers projected along the direction of the applied field, across the entire thickness of this interfacial domain wall. In order to better identify the structure at the interface, one could imagine having fitted the PNR curves with a greater number of sublayers at the $CoFe_2O_4/Fe_3O_4$ interface. However, doing so would introduce a significant number of additional variables into the fitting model, and thus considerably reduce the reliability of the fits. We have therefore chosen not to rely on a more complex model to interpret the PNR results, but on the three sublayer model depicted in Figure 6.7. The interpretation of this simple model indeed suggests that an interfacial zone containing a domain wall structure likely exists between the two layers.

Assuming that the AF coupling at the $CoFe_2O_4/Fe_3O_4$ interface is associated to a domain wall on one or both sides, and that this AF coupling appears as soon as the bilayer is deposited, there are two possible scenarios for the orientation of an AF coupling with respect to the applied magnetic field :

(a) AF coupling *parallel* to H : This scenario leads to a domain wall only in the P state, and predominant in one of the two films (Figure 6.8-a).

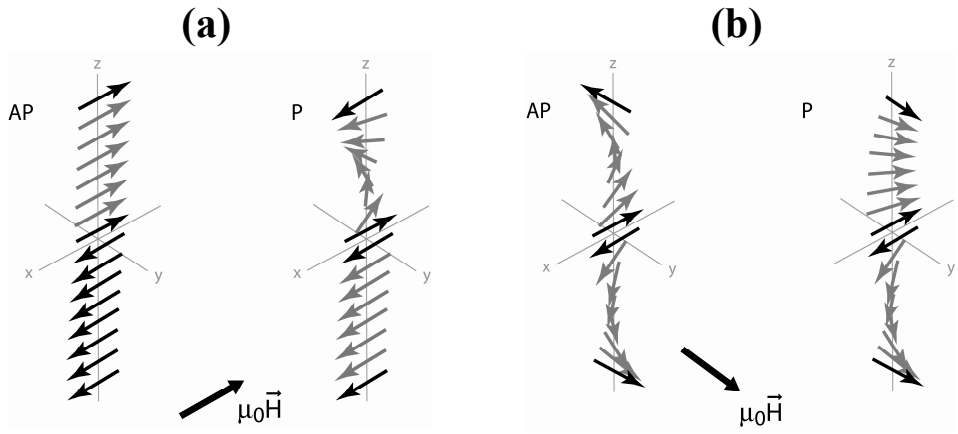

Fig. 6.8: Schematic illustration of two possible scenarios for the alignment of an AF coupling at the $CoFe_2O_4/Fe_3O_4$ interface with respect to an applied magnetic field : (a) Coupling parallel to $\vec{H}$; (b) Coupling perpendicular to $\vec{H}$. In both cases, the expected local magnetic configuration involves the formation of a domain wall on one or both sides of the interface in order to recover a P or AP state far from the interface.

(b) AF coupling *perpendicular* to H : Here the domain wall exists both in the P and AP states and traverses both layers (Figure 6.8-b).

In order to determine which configuration is energetically favorable, we performed a simple analytical calculation which is described in detail below. The result of the calculation indicates that scenario (b)—that is an AF coupling perpendicular to H—is more stable.

Energy Calculation : Spin Configuration at the $CoFe_2O_4/Fe_3O_4$ Interface

The following simple analytic calculation considers the case of two spins, described by the spin operators $\vec{S}_1$ and $\vec{S}_2$, coupled antiferromagnetically in the presence of an applied magnetic field $\vec{H}$. The Zeeman interaction with this applied field causes the spins to cant slightly, leading to an angle between the two that is slightly lower than the ideal 180°, as soon as $H \neq 0$. This is illustrated in Figure 6.9, for both scenarios (a) and (b) described above.

The calculation relies on several assumptions that lead to a situation that is greatly simplified with respect to reality. Nevertheless, they allow us to solve the problem analytically while still gaining valuable information about

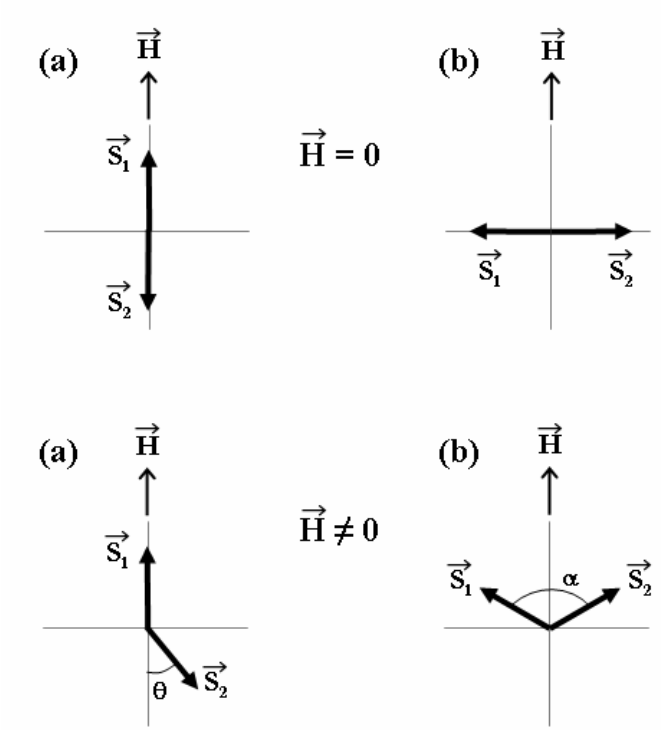

Fig. 6.9: Orientation of the AF-coupled spin operators S_1 and S_2 for scenarios (a) and (b) described above, without and with an applied magnetic field. When the field is non-zero, we expect the spins to cant slightly with respect to the perfect AF alignment, as described by the angles θ and α for scenarios (a) and (b) respectively.

the probable magnetic configuration in our films. These assumptions are :

1. The total energy E contains two contributions : the exchange energy between $\vec{S_1}$ and $\vec{S_2}$, and the Zeeman interaction with $\vec{H}$. The anisotropy energy is therefore neglected.

2. The magnitude of the two spin operators is identical : $|\vec{S_1}| = |\vec{S_2}| = S$

3. The energy contribution from the spin chains forming the domain wall on either side of the AF coupling between $\vec{S_1}$ and $\vec{S_2}$ is negligeable. We therefore base our energy minimization solely on the two AF-coupled spins at the interface, in the presence of an applied field.

We begin by describing the total energy of the system :

$$E = -J\vec{S_1} \cdot \vec{S_2} - \vec{H} \cdot (\vec{S_1} + \vec{S_2}) \tag{6.1}$$

where J is the exchange stiffness constant of the AF coupling.

We next develop the energy equation for scenarios (a) and (b), taking into account the spin canting due to the applied magnetic field, and minimize to find the equilibrium energy. The canting is described by the angles θ and α for scenarios (a) and (b) respectively, as illustrated in Figure 6.9.

Scenario (a)

Total energy :

$$E_a = -JS^2 cos(\pi - \theta) - HS - HScos(\pi - \theta) \tag{6.2}$$

Minimization :

$$\frac{dE_a}{d\theta} = -JS^2 sin\theta - HSsin\theta = 0 \quad \Leftrightarrow \quad \theta = 0 \tag{6.3}$$

$$\boxed{E_a^{min} = JS^2} \tag{6.4}$$

Scenario (b)

Total energy :

$$E_b = -JS^2 cos(\alpha) - 2HScos(\alpha/2) \tag{6.5}$$

Minimization :

$$\frac{dE_b}{d\alpha} = JS^2 sin(\alpha) + HSsin(\alpha/2) = 0 \tag{6.6}$$

$$\boxed{E_b^{min} = \frac{H^2}{2J} + JS^2} \tag{6.7}$$

If we now compare the expressions for E_a and E_b, we see that :

1. For $H = 0$, $E_a = E_b = JS^2$. At zero field both configurations are stable.

2. For $H \neq 0$, the fact that the exchange interaction is AF implies that $J < 0$. E_b is therefore less that E_a regardless of the sign or magnitude of the applied field. E_b is always energetically favorable.

Based on this simple analysis, it becomes evident that the AF coupling at the $CoFe_2O_4/Fe_3O_4$ interface is most likely oriented perpendicular to H. This means that there must exist a progressive rotation of the spins on both sides of the coupling in order to obtain a parallel or antiparallel alignment, with respect to the applied field, in between the $CoFe_2O_4$ and Fe_3O_4 layers. Again, the structure is schematically illustrated in Figure 6.8-b for both the P and AP states. This progressive rotation of the spins on either side of the AF coupling, also referred to as two AF-coupled half spin chains, corresponds perfectly with the hypothesis presented earlier in this section in which a domain wall forms at the $CoFe_2O_4/Fe_3O_4$ interface and spans across both layers.

Furthermore, the magnetization reversal behavior associated with Figure 6.8-b also corresponds very well with the results obtained in the magneto-transport measurements represented in Section 6.1.4. Because the AF coupling at the interface is oriented perpendicular to H, the spins in the $CoFe_2O_4$ layer may rotate freely from P to AP at H_{s1}, without affecting the AF coupling at the interface nor the magnetic order in the Fe_3O_4. We recall that the MR properties of the Fe_3O_4 suggested that this layer maintains the same magnetic configuration starting from the P state at saturation all the way through the switching of the $CoFe_2O_4$ at H_{s1}. This magnetic configuration is different than that in a free layer since the MR curve is significantly modified, again supporting the existence of a domain wall. The MR characteristics only indicate a significant change in magnetic order when the applied field reaches H_{s2}, as one would expect given the configuration depicted in Figure 6.8-b.

As it turns out, the presence of a domain wall structure consisting of two half spin chains coupled antiferromagnetically at an angle of 90° with respect to the applied field is known to be quite common in spinel ferrite thin films. In fact, this local magnetic structure is precisely that associated with the antiphase boundaries (APBs) commonly found in these films [100, 80, 82, 83]. In a certain APBs, the stacking fault created by this type of defect generates an additional AF coupling that is oriented perpendicular to the applied field. Far from the APB, the spins must realign in the same direction as H, and this is achieved via a progressive rotation of the spins on either side of the APB towards the P configuration, exactly as is shown in the P scenario in Figure 6.8-b. In other words, the local magnetic configuration that we predict at the $CoFe_2O_4/Fe_3O_4$ interface when the bilayer system is in the

P or saturated state is in essence equivalent to an APB. In the AP state, the configuration represents a sort of APB in which the two half spin chains rotate in the opposite direction. We therefore believe that the structural and magnetic defect generated by the $CoFe_2O_4/Fe_3O_4$ interface is in fact equivalent to a special type of APB in which the two AF-coupled half spin chains may switch from P to AP depending on the magnitude and direction of the external magnetic field. Finally, the fact that this structure is known to exist in spinel ferrite thin films further strengthens our hypothesis.

Again, it is important to reiterate that the local magnetic configuration proposed in this discussion is surely simplified with respect to reality. In particular, we know that our $CoFe_2O_4$(5 nm)/Fe_3O_4(15 nm) bilayers contain many small magnetic domains generated by the presence of APBs in the films. These domains, having a diameter on the order of a few hundred nanometers, inevitably influence the overall switching behavior in our system. The AF-coupled spin chain configuration proposed above is therefore probably repeated from one domain to another, leading to a situation that is much more complex than that described above. Whether or not these domains act independently of each other is a question that for the moment remains unanswered. Also, we do not know to what extent the boundary conditions imposed by the small domain size affect the spin-chain configuration in each domain. Further theoretical studies to simulate a multidomain system in which each domain contains a spin chain like that described above should significantly improve the understanding of this complex problem.

In Chapter 6, we have seen that the local configuration of the spins on either side of the barrier/electrode interface plays a dominant role in determining the magnetic behavior of the $CoFe_2O_4/Fe_3O_4$ system. We have shown that by directly growing Fe_3O_4 on $CoFe_2O_4$, a two-phase magnetization loop may be obtained *without the insertion of a non-magnetic spacer*. The two-phase switching observed in the $CoFe_2O_4$(5 nm)/Fe_3O_4(15 nm) bilayers is possible thanks to the nature of the exchange interactions that occur exclusively in these ferrimagnetic oxides. As a result, we obtain a bilayer system that, in theory, meets the magnetic prerequisites necessary for insertion into full MTJ structures for TMR measurements.

7. $CoFe_2O_4$-BASED MAGNETIC TUNNEL JUNCTIONS WITH COBALT ELECTRODES

In Chapter 7, we investigate the magnetic and SPT properties of $CoFe_2O_4$-based spin filter MTJs containing Co magnetic electrodes. Because Co is a material that has been used extensively in MTJ systems, its magnetic properties and spin polarization are well known. As a result, the MTJs containing Co electrodes were best suited to unveil the intrinsic SPT characteristics of our $CoFe_2O_4$ spin filters, without the ambiguity of an unfamiliar electrode. As in the previous two chapters, we will begin by describing the magnetic study of the $CoFe_2O_4$/Co-based systems, followed by the results and discussion of our spin-polarized tunneling experiments.

7.1 Magnetic Characterization

7.1.1 $CoFe_2O_4$/Co bilayers

As was already addressed in Chapter 6, the principal motivation behind the magnetic study of our $CoFe_2O_4$/Co bilayers was to understand their switching behavior. Again, the $CoFe_2O_4$ and Co layers must imperatively switch independently in order to be inserted into full MTJ structures. Magnetic hysteresis loops for the $CoFe_2O_4$(5 nm)/Co(15 nm) bilayer samples were therefore measured at room temperature by VSM. The samples consistently showed a magnetic easy axis in the plane of the film, indicating that shape anisotropy effects dominated over the crystalline anisotropy of the Co and $CoFe_2O_4$ (out-of-plane for both Co and $CoFe_2O_4$ in the bulk state). This result could be expected considering the relatively small thickness of the films.

The red curve (open squares) in Figure 7.1 shows the magnetization loop of a typical $CoFe_2O_4$(5 nm)/Co(15 nm) bilayer. As is often the case when a hard ferromagnetic oxide (here $CoFe_2O_4$) is directly in contact with a soft metallic electrode (Co), the magnetization curve for this system does not exhibit independent switching, but rather results in one single hysteresis loop with an H_c of 200 Oe. This coercivity is 10 times greater than that of a 15 nm-thick Co single layer, indicating that the Co electrode has been

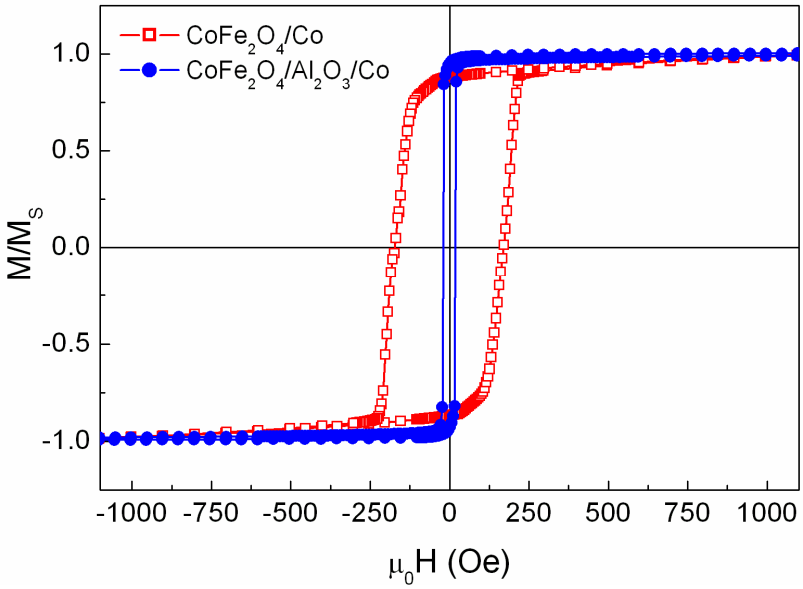

Fig. 7.1: Normalized room temperature magnetization curves for the $CoFe_2O_4$/Co system. The red curve (open squares) corresponds to a $CoFe_2O_4$(5 nm)/Co(15 nm) bilayer and clearly reveals an exchange coupling between the two. The blue curve (filled circles) represents a $CoFe_2O_4$(5 nm)/γ-Al_2O_3(1.5 nm)/Co(15 nm) trilayer in which the effect of the thin γ-Al_2O_3 spacer on the exchange interaction is remarkable.

blocked by the $CoFe_2O_4$ via an exchange coupling at the interface. The result is a system in which the two magnetic layers are aligned parallel regardless of the applied field. The $CoFe_2O_4$(5 nm)/Co(15 nm) bilayers are therefore not suitable, from a magnetic point of view, for insertion into spin filter MTJs, and a solution must be found to eliminate the exchange coupling at the interface.

7.1.2 $CoFe_2O_4$/γ-Al_2O_3/Co trilayers

In an attempt to eliminate the coupling between the two layers and attain an antiparallel magnetic state, we next inserted a crystalline γ-Al_2O_3 layer in between the $CoFe_2O_4$ and Co layers. This insulating spacer had to be continuous, but sufficiently thin to allow for tunneling when combined with the $CoFe_2O_4$ barrier.

The impact of such a 1.5 nm γ-Al_2O_3 spacer is clearly demonstrated by

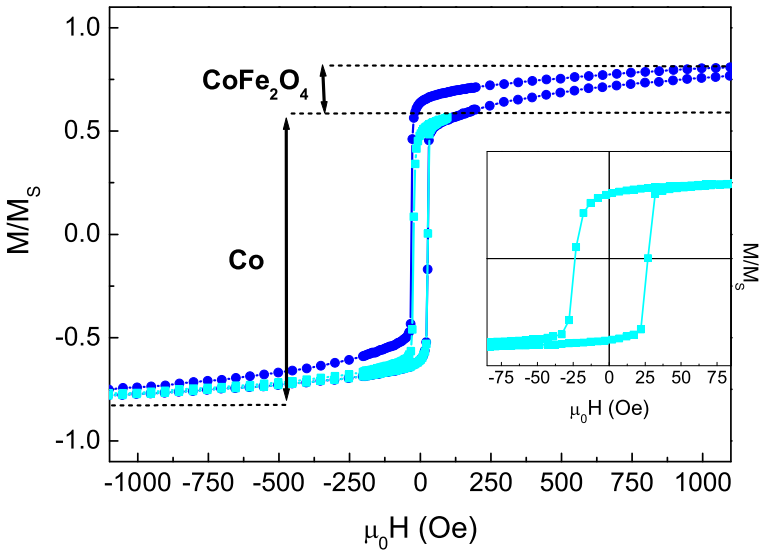

Fig. 7.2: Normalized room temperature magnetization curve for a $CoFe_2O_4/\gamma$-Al_2O_3/Co trilayer where the thickness of the Co was reduced to 3 nm. The major loop is shown in dark blue (circles) and the Co minor loop in light blue (squares). Reducing the thickness of Co allows us to dissociate the signal from each magnetic layer, thus confirming the contribution from the $CoFe_2O_4$.

the blue curve (filled circles) in Figure 7.1. Here the H_c of the Co(15 nm) electrode is reduced to its usual value of about 20 Oe, indicating that the magnetic coupling with the $CoFe_2O_4$ is indeed destroyed. Nevertheless, the magnetization loop still appears to have only one switching event, which may be explained by the fact that the magnetic contribution of the $CoFe_2O_4$ layer in the $CoFe_2O_4$(5 nm)/Al_2O_3(1.5 nm)/Co(15 nm) system is insignificant compared to that of the Co. Taking into consideration the thickness t and saturation magnetization M of the $CoFe_2O_4$ ($M_{CoFe2O4}$ ∼250 kA/m) and Co (M_{Co} ∼1500 kA/m) layers, we may calculate the expected magnetization height ratio :

$$\frac{\mu_{CoFe2O4}}{\mu_{Co}} \approx 0.055$$

from which it becomes immediately clear why the $CoFe_2O_4$ contribution is invisible.

In order to confirm that the $CoFe_2O_4$ contribution was present, we elabo-

rated a second sample where the thickness of the overpowering Co layer was reduced to 3 nm. The result is shown in Figure 7.2, where the major loop of the $CoFe_2O_4$(5 nm)/Al_2O_3(1.5 nm)/Co(3 nm) trilayer is plotted in dark blue (circles) and the minor loop of the Co(3 nm) plotted in light blue (squares). The difference between the major loop and the Co minor loop results from the $CoFe_2O_4$. The magnetic signal of the $CoFe_2O_4$/Al_2O_3/Co trilayer may therefore be decomposed into two independent contributions corresponding to the $CoFe_2O_4$ and Co layers, further confirming the magnetic decoupling of the two. Finally, the resultant magnetization height ratio in this case :

$$\frac{\mu_{CoFe2O4}}{\mu_{Co}} \approx 0.27$$

is in very good agreement with the experimental value obtained from Figure 7.2, demonstrating that the magnetic properties of each individual film are recovered.

Unlike the exchange coupling between $CoFe_2O_4$ and Fe_3O_4 discussed in Chapter 6, the interpretation of the magnetic interaction with Co is much less complex. Regarding the $CoFe_2O_4$/Co samples, the coupling of Co to $CoFe_2O_4$ has been previously observed in spin valve systems where $CoFe_2O_4$ was used as a pinning layer to harden Co [101, 102, 103]. The exchange interaction in this prototypical oxide/metal system is difficult to interpret as the metallic Co atoms have no localized orbital states to interact with the 3d orbitals of the Co^{2+} and Fe^{3+} in $CoFe_2O_4$. From the magnetization curve (Figure 7.1), it is immediately clear that an exchange coupling is present due to its single-phase nature and increased coercivity of the Co film, but one may not determine whether this interaction is ferro- or antiferromagnetic. In the second part of our study, the insertion of a thin γ-Al_2O_3 spacer in between the two layers proves that the coupling between $CoFe_2O_4$ and Co is completely localized at the interface, regardless of the nature of the interaction. The possibility of maintaining an exchange at the $CoFe_2O_4$/Co interface is immediately prohibited, and each film recovers its independent magnetic characteristics. Because it does not take much spacer to prevent the interaction from occurring, it becomes evident that the exchange interaction is restricted to the final planes of the spinel ferrite and the bottom-most atoms of cobalt. This is very encouraging for the realization of full MTJs, as we can be certain that their is no lingering interaction between the two magnetic layers.

7.2 Tunneling Experiments

7.2.1 Resistance Measurements and TMR

Pt/$CoFe_2O_4$/γ-Al_2O_3/Co spin filter MTJs were patterned for SPT measurements by the advanced optical lithography technique described in Chapter 3. The $CoFe_2O_4$ tunnel barriers were all grown with a $P_{O_2}^{plasma}$ of 0.2 Torr. Transport measurements could be carried out in the two terminal configuration because the room temperature junction resistance (R_j) was three orders of magnitude higher than that of the Pt cross strip and contacts. The following paragraphs focus on the results obtained for a Pt(20 mn)/$CoFe_2O_4$(3 nm)/γ-Al_2O_3(1.5 nm)/Co(10 nm) junction whose area was 24 μm^2. These results were systematically reproducible in other junctions of sizes ranging from 12 to 96 μm^2 and on different areas of the 12×8 mm substrate, and were therefore representative of the Pt/$CoFe_2O_4$/γ-Al_2O_3/Co system.

A first indication that tunneling occurred across the $CoFe_2O_4$/γ-Al_2O_3 double barrier was the temperature dependence of R_j. At room temperature the resistance-area product (R_jA) was 0.12 Ωcm^2 and increased to $\sim$10 Ωcm^2 at 2K. This effect could only be explained by tunneling across the $CoFe_2O_4$, as such an increase is not observed in Al_2O_3 tunnel barriers alone. This dramatic increase in R_jA suggests that the tunneling mechanism across the $CoFe_2O_4$ may change from high to low temperature, involving, for example, thermally activated tunneling into the conduction band of the barrier at high temperature. Such an effect would be most probable in the case of a low tunnel barrier height. Finally, the current-voltage ($I-V$) characteristics at both high and low temperature showed typical non-linear tunneling behavior that will be discussed in further detail in Section 7.2.2.

Resistance versus applied magnetic field ($R(H)$) measurements were performed both at low temperature and at room temperature, successfully revealing significant TMR in both cases. Figure 7.3 clearly demonstrates the TMR effect in the Pt/$CoFe_2O_4$/γ-Al_2O_3/Co tunnel junction at 2 K and at 290 K. This result is direct experimental evidence of the spin filter effect in $CoFe_2O_4$ at low temperature and, most importantly, *at room temperature*. Based on the curve at 2 K, we calculated a TMR value of -18% using the relation $TMR = (R_{AP} - R_P)/R_P$ where R_{AP} and R_P are the resistance values in the antiparallel and parallel magnetic configurations. In the same manner, TMR = -3% at room temperature. Both $R(H)$ measurements were performed with a bias voltage (V) of 200 mV, which led to nearly noise-free resistance curves with optimal TMR values (see Section 7.2.3 for more details). The applied magnetic field was -6 T$\leq\mu_0 H\leq$+6 T. This notably high magnetic field was necessary in order to completely saturate the $CoFe_2O_4$

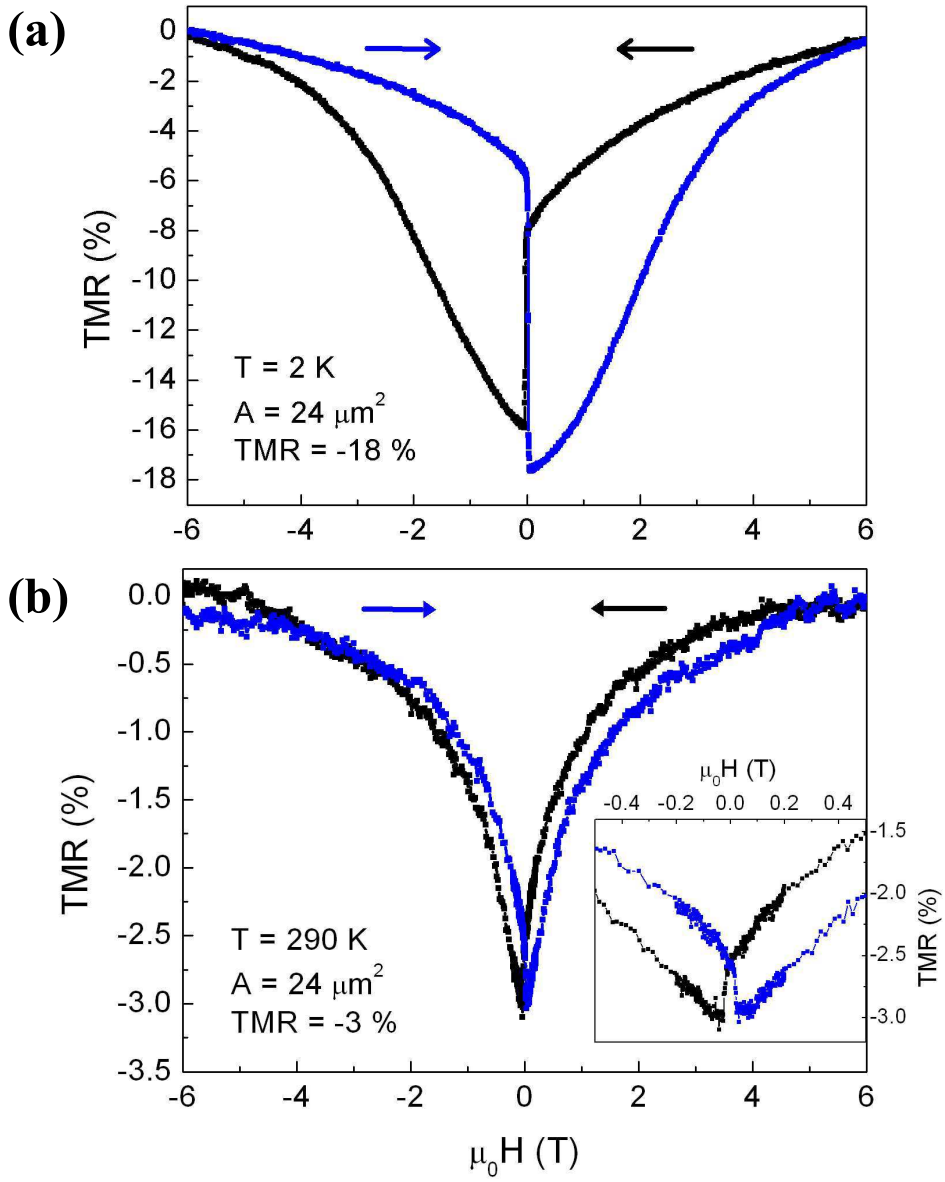

Fig. 7.3: TMR as a function of applied magnetic field for a Pt(20 nm)/$CoFe_2O_4$(3 nm)/γ-Al_2O_3(1.5 nm)/Co(10 nm) tunnel junction at 2 K (a) and at room temperature (b). The applied bias voltage in both cases was 200 mV and the junction area 24 μm^2. A zoom of the Co switching at room temperature is shown in the inset of (b).

layer, whose magnetic properties described in Chapter 5 reveal irreversible hysteresis in fields as high as 7 T.

At 2 K, the abrupt drop in the TMR curve at ±200 Oe corresponds well with the switching of the Co electrode, while the gradual increase back to ±6 T agrees with the progressive switching and lack of saturation in $CoFe_2O_4$ seen by SQUID (see Chapter 5). The switching of the Co electrode (200 Oe) occurs at a magnetic field higher than its bulk coercivity (20-30 Oe) due to geometrical effects resulting from junction patterning down to the micron scale. It is also interesting to note that the TMR effect actually begins well before the switching of Co, due to the low remanence of $CoFe_2O_4$. The result is a "butterfly"-shaped TMR curve that never closes completely. A similar behavior owing to the low remanence of $CoFe_2O_4$ is observed at room temperature, although the TMR curve does close more easily, in good agreement with the room temperature VSM measurements.

Figure 7.3 also clearly reveals a TMR that is negative—that is, that the high and low resistance states correspond to the parallel and antiparallel configurations respectively. The negative sign of the TMR therefore indicates that the $CoFe_2O_4$ spin filter and Co electrode are oppositely polarized. This important result is in very good agreement with what is expected for these two materials : $CoFe_2O_4$ is predicted to have a negative P from band structure calculations [57], and Co, in contact with an Al_2O_3 barrier, has been measured to have a positive P by the Meservey-Tedrow technique [22] (see also Appendix A). Once again, we emphasize that the $P_{CoFe2O4}$ we refer to here is that determined solely from the density of states in the conduction band, or P_N as was discussed in Chapter 5. Taking P_{Co}=40% based on the most recent Meservey-Tedrow studies [104], we may approximate $P_{CoFe_2O_4}$ from the Jullière formula [6] (see Chapter 2) where $P_1=P_{Co}$ and $P_2=P_{CoFe_2O_4}$. This gives $P_{CoFe_2O_4}$=-25% at 2 K and $P_{CoFe_2O_4}$=-4% at room temperature. While these values are already quite fulfilling, they are surely significantly reduced with respect to their intrinsic value due to the low remanence in our $CoFe_2O_4$ films. We could therefore expect to obtain even higher TMR if it were possible to further improve their magnetic properties. This could be done, for example, by reducing the concentration of antiphase boundaries in the ultra-thin films using a substrate other than α-Al_2O_3 or by performing a post-deposition anneal.

Finally, the considerable decrease of $P_{CoFe_2O_4}$ at high temperature could be explained by the thermal excitation of not only the spin-down electrons, but also the spin-up electrons into their corresponding majority spin conduction band, which as a result, would lower the net polarization of the tunneling current. This explanation could be valid under two simultaneous conditions : a low tunnel barrier height, and a small conduction band splitting with

respect to k_BT (see Sections 7.2.2 and 7.2.3).

7.2.2 Current-Voltage Characteristics

The $I-V$ characteristics representative of the Pt/$CoFe_2O_4$/γ-Al_2O_3/Co system are shown in Figure 7.4-a. These are highly asymmetric, with a significantly higher current passing for positive bias—that is, when the electrons tunnel from the Pt to the Co electrode. This observation is completely consistent with the highly asymmetrical nature of the double tunnel barrier, the electrodes, and their *epitaxial* interfaces. In such a complex system, a simple model such as the Brinkmann model which considers tunneling across a trapezoidal barrier of average height $\bar{\varphi}$ and asymmetry $\Delta\varphi$ [12] (see also Chapter 2), is difficult to apply. Not only do we have two barriers, both asymmetric due to their different epitaxial interfaces, but we would expect $CoFe_2O_4$ and γ-Al_2O_3 to have very different barrier heights based on their relative band gaps of 0.8 eV [57] and 8.7 eV [105]. Because the Brinkmann model is only accurate for $\Delta\varphi/\bar{\varphi} < 1$, it is unlikely that it be applicable to the present system. For this reason, we have chosen not to use Brinkmann fitting to extract information about the tunnel barrier height and asymmetry for our $CoFe_2O_4$/γ-Al_2O_3 tunnel barriers.

Nevertheless, we could obtain a reasonable estimation of the tunnel barrier height Φ by analyzing the derivatives of the $I-V$ curves in Figure 7.4-a. The first method, which consists in looking at the second derivative, measures Φ by the voltage at which d^2I/dV^2 deviates from linearity. Figure 7.4-b clearly shows that d^2I/dV^2 is linear for -60 mV $< V <$ 60 mV indicating direct tunneling through the band gap in this regime. However, beyond 60 mV, d^2I/dV^2 rapidly increases, suggesting that the tunneling electrons have sufficient energy to tunnel indirectly across the conduction band. By a second method, which involves analyzing $(dI/dV)/(I/V)$, we also obtain a value of $\Phi = 60$ meV. In this case the $(dI/dV)/(I/V)$ characteristics show an inflection point corresponding to the onset of the conduction band, in good agreement with d^2I/dV^2. The Φ value of 60 meV is quite consistent with the electronic band structure calculations schematized in Figure 7.4-c, which predict $CoFe_2O_4$ to have a small electronic band gap and an intrinsic Fermi level that is close to the first level of the conduction band.

7.2.3 TMR versus Bias Voltage

In addition, the $I-V$ curves provide other remarkable information about the spin polarized transport across the Pt/$CoFe_2O_4$/γ-Al_2O_3/Co tunnel junction. Most notably we observe that the $I-V$ curves obtained in the parallel

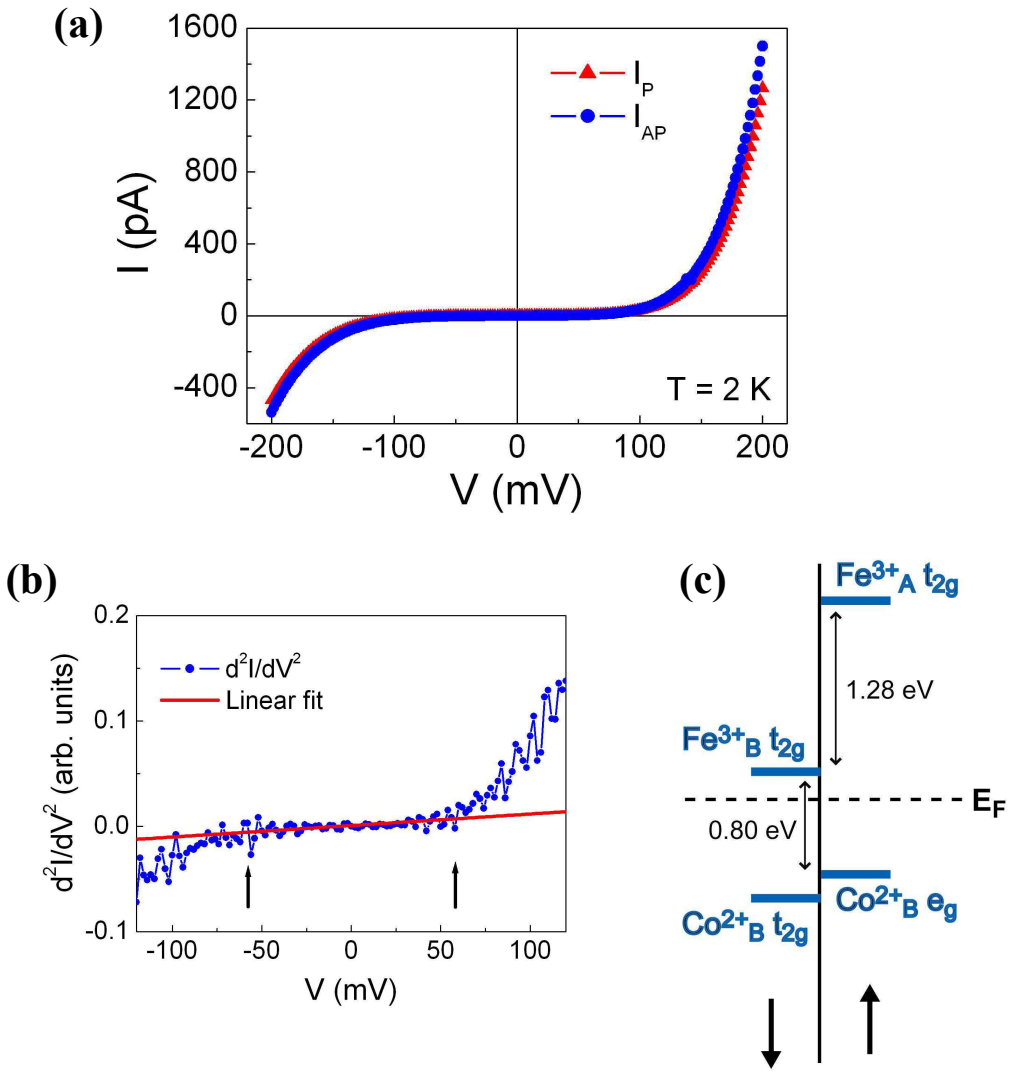

Fig. 7.4: I-V characteristics of a Pt(20 nm)/$CoFe_2O_4$(3 nm)/γ-Al_2O_3(1.5 nm)/Co(10 nm) MTJ. The parallel ($\mu_0 H$ = +6 T) and antipallel ($\mu_0 H$ = -0.08 T) I-V curves are shown in (a). The second derivative of I_{AP} (b) may be fitted linearly for $-60mV \leq V \leq 60mV$, thus giving a good indication of Φ. $\Phi \approx 60$ meV is in good agreement with the electronic band structure schematically illustrated in (c) which is based on first principles studies from [57].

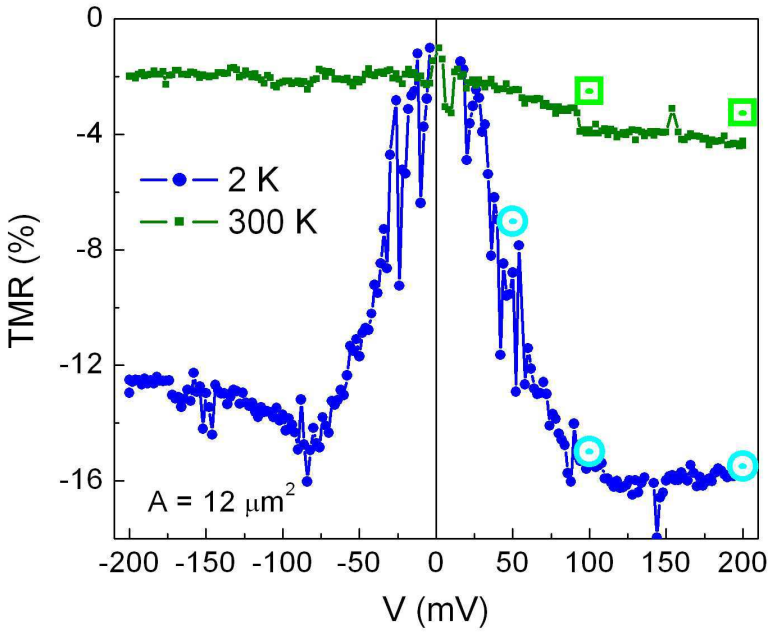

Fig. 7.5: $TMR(V)$ dependence for the same Pt(20 nm)/$CoFe_2O_4$(3 nm)/γ-Al_2O_3(1.5 nm)/Co(10 nm) tunnel junction as 2 K and at 290 K. In both cases, we observe an increasing $TMR(V)$ dependence (in absolute value) for a significant range of applied bias. The open data points correspond to TMR values obtained directly from $R(H)$.

state ($\mp$6 T) and antiparallel state ($\pm$0.08 T) are not superposable (see again Figure 7.4-a). In other words, there is an increase in the tunneling current in the antiparallel state with respect to the parallel state. This is coherent with the observation of negative TMR and once again suggests that spin filtering is present.

By extending the definition of TMR given in Section 7.2.1 to $TMR = (I_P - I_{AP})/I_{AP}$ via Ohm's law, we may extract the TMR versus V dependence from the experimental I_P and I_{AP} curves. The result, shown in Figure 7.5, is a $TMR(V)$ curve that *increases* (in absolute value as we are dealing with negative TMR) with increasing V both at low temperature and at room temperature. This is truly a sign of the excellent quality of our $CoFe_2O_4$ spin filter. More precisely in the low temperature curve, TMR displays a steady increase up to a certain maximum value, beyond which it then slowly decreases for higher biases. This exact behavior was theoretically predicted by A. Saffarzadeh to be the signature of spin filtering in MTJs containing

a magnetic barrier [40], and has only recently been observed experimentally for the first time with EuS at low temperature [44]. However, it has never been verified in higher T_C magnetic oxide tunnel barriers such as $BiMnO_3$ and $NiFe_2O_4$ [51, 54]. Figure 7.5 also contains five experimental TMR data points obtained directly from $R(H)$ measurements at $V = 50$, 100 and 200 mV. All points, both at 2 K and at 290 K, agree well with the $TMR(V)$ curves obtained indirectly via I_P and I_{AP}, thus validating the accuracy of this method for studying the voltage dependence in our spin filter tunnel junctions.

The increasing TMR(V) dependence is opposite to what is observed in conventional MTJs, and may be explained by the spin-split nature of the conduction band in the spin filter. This is schematically illustrated in Figure 7.6. At low bias (Figure 7.6-a), the electrons have no choice but to tunnel directly across the band gap of the barrier. Here, the difference between $\Phi_\uparrow$ and $\Phi_\downarrow$ as well as additional transfer matrix elements determine the polarization of the tunneling current, but do not affect $TMR(V)$ significantly. However, upon the application of sufficient bias, the lower energy spin-down conduction band nears the Fermi level (E_F), creating a preferential tunneling pathway for the spin-down electrons (Figure 7.6-b). This indirect tunneling mechanism if often referred to as Fowler-Nordheim (F-N) tunneling [43]. The result is an increase of the spin-down tunneling probability with respect to spin-up, and thus an increasing TMR(V) dependence. Eventually, the applied V will be high enough that the subsequent spin-up conduction band also approaches E_F (Figure 7.6-c). At this point, both spin-down and spin-up electrons may tunnel preferentially, and the TMR ratio attains its maximum. The gradual decrease thereafter is governed by magnon effects as in the case of standard MTJs.

The onset of spin filtering, given by the region for which TMR increases with V, may be identified from the low temperature curve in Figure 7.5 around ± 30 mV and persists until +130 mV (-100 mV) for positive (negative) bias. In the case of positive bias, these values suggest :

$$\begin{aligned} \Phi_\downarrow &\approx 30\ meV \\ \Phi_\uparrow &\approx 130\ meV \\ \Delta\Phi = \Phi_\downarrow - \Phi_\uparrow &\approx 100\ meV \end{aligned}$$

This semi-quantitative treatment remains approximate because a number of other factors may also influence the features of the $TMR(V)$ curve. For example, the onset of increasing $TMR(V)$ likely occurs before the onset of F-N tunneling because of the exponential difference between $J_\downarrow(\Phi_\downarrow)$ and

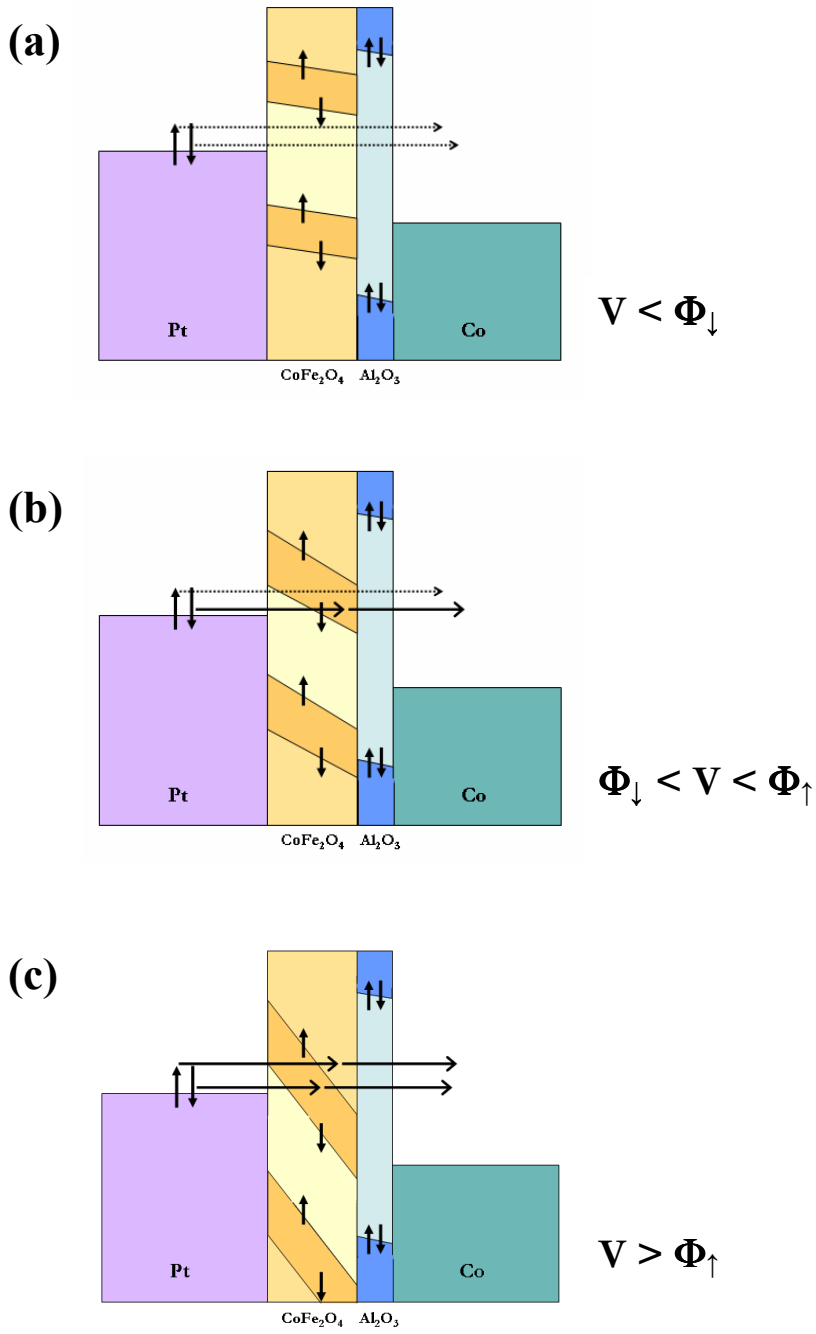

Fig. 7.6: Schematic illustration of the three tunneling regimes in a spin filter MTJ as a function of applied bias voltage : (a) direct tunneling for both spin-down and spin-up electrons; (b) F-N tunneling for only spin-down electrons, resulting in an increasing $TMR(V)$ dependence; (c) F-N tunneling for both spin-down and spin-up electrons with decreasing $TMR(V)$.

$J_{\uparrow}(\Phi_{\uparrow})$. This means that $\Phi_{\downarrow}$ is likely underestimated. Nevertheless, it is in very good agreement with the $\Phi = 60$ meV obtained from the analysis of the $I-V$ characteristics. Secondly, the competition between the magnon effects with the spin filter effect, especially at low temperature, should also have a tendency to cut short the energy range of increasing $TMR(V)$. Once again, $\Phi_{\uparrow}$ and $\Delta\Phi$ are likely underestimated. This second point is further supported by the fact that at 290 K, where magnons are negligible, $TMR(V)$ actually continues to increase beyond 200 mV.

7.2.4 Discussion

Quantitative comparison of the spin filter regime in our TMR(V) curves with the calculations of Szotek *et al.* [57] yields an exchange splitting ($\sim$0.1 eV) that is significantly lower than that predicted for the inverse spinel structure (1.28 eV) (see Figure 7.4-c). This observation is consistent with the temperature sensitivity of the TMR measurement discussed earlier. In addition to magnon effects leading to an underestimation of $\Delta\Phi$, the electronic band structure of the $CoFe_2O_4$ barrier is likely influenced by the presence of structural and/or chemical defects, many of which are difficult to account for in model systems for such calculations. The presence of Co^{3+}, for example, is one defect that has been predicted by Szotek *et al.* to reduce the band gap as well as the conduction band splitting while favoring an energetically stable state. Even a small concentration of Co^{3+} cations, undetectable by standard characterization techniques, could therefore significantly modify the electronic and thus the spin filter properties of the $CoFe_2O_4$ barrier. Secondly, the $CoFe_2O_4$ barrier in the Pt/$CoFe_2O_4$/γ-Al_2O_3/Co MTJs was fabricated with a $P_{O_2}^{plasma}$ of 0.2 Torr, which we know from the SPT measurements in Chapter 5 is not optimal. The presence of oxygen vacancies in this system could therefore have a significant effect on the measured $P_{CoFe2O4}$. Increasing $P_{O_2}^{plasma}$ to 0.26 Torr or higher, thus decreasing the oxygen vacancy concentration, should lead to improved spin filter efficiency. Furthermore, one can not ignore the possible influence of antiphase boundaries as these are known to change the magnetic order in spinel ferrites [80], and thus likely the exchange splitting as well. Further studies are necessary to better quantify the effects of both structural and chemical defects on the spin polarized tunneling across $CoFe_2O_4$.

Finally, it is important to compare the TMR results discussed in this chapter with the SPT characteristics of our $CoFe_2O_4$/γ-Al_2O_3 barriers obtained via the Meservey-Tedrow technique, and presented in Chapter 5. The most obvious discrepancy between the two measurements is the sign of P obtained in each case. As was discussed in Chapter 5, the origin of the

systematically positive P measured by the Meservey-Tedrow technique for $CoFe_2O_4$ is a puzzling question yet to be understood. Even more puzzling is why we measure the opposite sign in the TMR measurements using a Co electrode as the spin analyzer. The fact that our TMR measurements result in a negative P is in good agreement with the numerous existing theoretical studies on $CoFe_2O_4$ and other spinel ferrites which predict the lowest energy level in the conduction band to correspond to spin-down electrons. However, we can not ignore the fact that the Meservey-Tedrow experiment is known to be the most direct, foolproof experimental measurement of the spin polarization of a tunnel current. The question thus remains as to why the two techniques disagree.

In Chapter 5, we discussed the possibility that the definition of P we measure may actually vary from one measurement technique to another, and that the classic P (also called P_N [24]) defined by Equation 1.2, and determined solely by the DOS of a FM electrode or spin filter, may not necessarily be that which dominates in certain tunneling experiments. Depending on the tunneling mechanism present in different SPT measurements, we may in fact be probing two different definitions of P. One key element supporting such a hypothesis and possibly explaining the discrepancy between the TMR and Meservey-Tedrow results involves the difference in bias voltage regime applied in each of the two measurements. In the Merservey-Tedrow technique, a bias of only a few meV is required to observe the BCS gap of the Al SC electrode. In the case of our MTJ experiments, biases ranging from 50 to 200 meV were applied in order to obtain clear, noise-free TMR curves. This means that the Meservey-Tedrow technique is *essentially a zero-bias experiment* with respect to the TMR measurements. This also means that the deformation of the the $CoFe_2O_4$ tunnel barrier is minimal and the tunneling regime is almost certainly that of direct tunneling. As was discussed earlier in Chapter 5, P in this direct tunneling regime may actually be determined by more than just the DOS in the $CoFe_2O_4$ conduction band (integration of $|M_{\uparrow(\downarrow)}|^2$ into P [24]), thus resulting in a preferential tunneling channel for spin-up electrons despite the slightly higher tunnel barrier height. Additional considerations such as spin-dependent electron decay lengths, band symmetry and alignment with the Al counter electrode, or even resonant tunneling could also contribute to the effective P that we measure.

On the other hand, the results from our TMR(V) studies show that transport in this bias voltage range is governed by Fowler-Nordheim tunneling, facilitated by the low tunnel barrier height. This indirect mechanism, different from that in the Meservey-Tedrow experiment, involves tunneling across the conduction band of the $CoFe_2O_4$ spin filter as it passes below the Fermi level [44]. As a result, there will be spin accumulation at the $CoFe_2O_4/\gamma$-

Al_2O_4 interface, which is necessarily negatively spin-polarized because only the DOS matters here. Tunneling is thus a two-step process whose polarization should be determined by the exchange splitting of the energy levels in the conduction band, ignoring all tunnel matrix elements. The DOS definition of $P = P_N$ is therefore the one to consider. In the case of $CoFe_2O_4/\gamma$-Al_2O_3, the expected P_N should lead to a negatively polarized tunneling current, as is observed experimentally.

Finally, it is worth noting that in the TMR(V) curve shown in Figure 7.5, TMR does indeed approach zero with decreasing bias. One could even imagine it switching sign near $V = 0$. Unfortunately, it was impossible for us to extrapolate the TMR(V) curve or obtain a TMR measurement at low bias due to the extremely high resistance of our junctions, and so this hypothesis could not be experimentally verified. We therefore leave this discussion open for future experimental and theoretical studies to follow.

Putting aside the discrepancy in the sign of $P_{CoFe2O4}$, the results from our TMR measurements are quite consistent with those from the Meservey-Tedrow technique on a number of other points. First, in both cases, we observe a three to fourfold increase in R_jA when going from room temperature down to liquid He temperature. As was explained in Section 7.3, this is a clear sign of tunneling across the $CoFe_2O_4$ barrier, as well as an indication of low tunnel barrier height and low exchange splitting. Furthermore, the value of R_jA in both cases is of the same order of magnitude, thus validating both the shadow masking and lithography patterning techniques for tunnel junction fabrication. These common factors between the results obtained from Meservey-Tedrow and TMR, in conjunction with the discrepancies observed due to the different tunneling mechanisms involved, show that they are indeed complementary techniques that provide a thorough analysis of the spin filter properties of $CoFe_2O_4$.

8. CONCLUSIONS AND FUTURE WORK

In this final chapter, we will summarize the ensemble of results presented throughout this thesis in a slightly different order than that used in the previous chapters. Rather than proceeding system by system, as was done in Chapters 5-7, this final chapter will be organized by measurement type (i.e. materials characterization, magnetic measurements, spin-polarized transport), allowing us to directly compare the different $CoFe_2O_4$-based systems. The hope is to show how all of the seemingly different materials and physical studies performed in this work actually do interweave, and that interesting conclusions may be drawn by comparing the different systems. The discussion of the various results will then lead us to consider the future studies left to be done on this exciting new material.

8.1 Conclusions

The study of epitaxial cobalt ferrite ultra-thin films as a potential room temperature spin filter material was broken down into three main steps :

- The study of the epitaxial growth and materials properties of ultra thin $CoFe_2O_4(111)$ films.
- The direct study of $CoFe_2O_4$ single layers as spin filters at low temperature. This was done using a superconducting Al counter electrode as the spin analyzer, also known as the Meservey-Tedrow technique.
- The study of two $CoFe_2O_4$-based multilayer systems for room temperature spin filter magnetic tunnel junctions. These two systems were $Pt/CoFe_2O_4/Fe_3O_4$ and $Pt/CoFe_2O_4/\gamma\text{-}Al_2O_3/Co$.

Both steps two and three involved not only spin-polarized tunneling measurements, but also an in depth study of the magnetic properties of the $CoFe_2O_4$ single layer and multilayer systems. These magnetic studies, particularly in the case of the two MTJ systems, revealed very interesting results about the interaction of $CoFe_2O_4$ with different metallic and oxide magnetic electrodes.

8.1.1 Growth and materials characterization

The growth of $CoFe_2O_4(111)$ epitaxial ultra-thin films was performed by oxygen plasma-assisted molecular beam epitaxy. The in-depth study of the structural and chemical properties of these films, using both *in-situ* and *ex-situ* methods, allowed us to optimize growth conditions in the MBE chamber for the fabrication of our films. The ensemble of the materials characterization techniques revealed fully epitaxial $CoFe_2O_4(111)$ films and $CoFe_2O_4(111)$-based multilayers demonstrating a high quality, two dimensional growth mode, and near-perfect interfaces. In the case of the multilayer systems, both structural and chemical studies confirmed the presence of distinct layers with no interatomic diffusion at the interfaces.

One important result from this study was that proper $CoFe_2O_4$ films could be obtained under a significantly wide range of oxygen plasma pressures—as opposed to other spinel ferrites such as Fe_3O_4 that require very specific oxidation conditions—allowing us to tailor the oxygen vacancy concentration in our films while still maintaining the correct spinel phase. This would later serve as a variable parameter in our spin-polarized transport studies.

Although seemingly straight forward, mastering the growth and materials properties of our $CoFe_2O_4$ layers was undoubtedly the most time-consuming part of this entire thesis. Many months of testing were necessary before the optimal growth conditions were found, and smaller modifications were constantly necessary, even after the general procedure was established. Nevertheless, there is no doubt that this additional time was well spent, as the final result was a set of different samples having uniquely high structural and chemical quality, rarely obtained by other groups working with complex oxide thin films. We strongly believe that the ensemble of magnetic and SPT result to follow owe their success to the excellent quality of our films.

8.1.2 Magnetism

Magnetic studies were performed both on our $CoFe_2O_4$ single layers and on the $CoFe_2O_4/Fe_3O_4$ and $CoFe_2O_4$/Co MTJ systems. In the case of the single layers, the goal was to optimize the magnetic properties when their thickness was reduced to a few nanometers, which was necessary for tunnel barrier applications. In Chapter 5 we indeed saw that $CoFe_4O_4$ films down to 3 nm in thickness demonstrated clear ferromagnetic behavior with magnetic moments comparable to those of thicker layers. Even better magnetic behavior was observed when a Pt(111) buffer layer was inserted between sapphire substrate and the $CoFe_2O_4$. The reduced coercivity ($\sim$ 200 Oe) in these ultra-thin films, likely due to the increased presence of antiphase boundaries,

also favored their integration into spin-filter MTJs for TMR measurements. On the other hand, the rather low remanent magnetization ($\sim 20\%$) was less desirable, and remains a property to further optimize in future studies.

In the case of the bilayer spin filter MTJ systems, the central issue that needed to be considered was that the magnetic barrier and electrode were directly in contact with each other, thus increasing the probability that the two layers would not switch independently. The existence of an antiparallel magnetic state between the $CoFe_2O_4$ barrier and the ferromagnetic electrodes at low applied fields was therefore addressed in our magnetic studies before any transport measurements were performed. The physics of magnetic interfaces changing drastically from one material to another, each electrode in contact with the $CoFe_2O_4$ barrier introduced a whole new set of interface phenomena specific to that system. In particular, we studied two $CoFe_2O_4$/FM systems, where FM = Fe_3O_4 or Co, whose magnetization behavior differed due to the nature of the exchange coupling at their interfaces. This portion of the magnetic study therefore illustrated the physical consequences of using an insulating barrier which is both an oxide and magnetic in epitaxial tunnel junction heterostructures.

The more straightforward of the two systems, $CoFe_2O_4$/Co, represented a classically coupled system in which the hard ferrimagnetic oxide pinned the soft ferromagnetic metal. The coercive fields of the two magnetic layers were radically different, as were their chemical and structural properties. In the second more complex system, $CoFe_2O_4/Fe_3O_4$, not only were the structure and chemistry of the two films nearly identical, but their coercive fields as well. This latter system presented a new physical scenario that had never been analyzed before : an exchange-coupled bilayer in which the distinction between the "hard" and "soft" layers could not be made based on the intrinsic properties of the individual films. This was in contrast to the well studied "exchange spring magnet" systems containing one distinctly soft and one hard layer. In the present case, it was not until the $CoFe_2O_4$ and Fe_3O_4 layers were coupled in a bilayer structure that the role of each material became evident.

The primary difference between the oxide/metal and the oxide/oxide bilayer systems, from a magnetic point of view, lied in the mechanism governing the exchange coupling. In the case of $CoFe_2O_4$/Co samples, the exchange interaction was that of a prototypical oxide/metal system containing one soft layer and one hard pinning layer. The exact mechanism was difficult to interpret as the metallic Co atoms have no localized orbital states to interact with the 3d orbitals of the Co^{2+} and Fe^{3+} in $CoFe_2O_4$. In other words, we could not determine whether the interaction was ferro- or antiferromagnetic. The insertion of a thin γ-Al_2O_3 spacer in between the two layers further proved

that the coupling between $CoFe_2O_4$ and Co was completely localized at the interface, regardless of the nature of the interaction.

Unlike the $CoFe_2O_4$/Co system, the oxide/oxide exchange mechanism at the $CoFe_2O_4/Fe_3O_4$ interface was analyzed in greater detail thanks to the presence of distinct superexchange interactions involving the 3d and 2p orbitals of the atoms in both materials. The result in this exchange-coupled system containing two ferrimagnets of comparable coercivity was an interaction that most dramatically affected the second layer to switch, that is the Fe_3O_4. In fact, the coercivity of the Fe_3O_4 in this bilayer system was found to increase to 3000 Oe at room temperature, and even higher at low temperature, in comparison to the 300 Oe coercivity normally found in Fe_3O_4 single layers. Following a series of magnetic and magneto-transport measurements using a variety of complementary techniques, we were able to propose a possible scenario describing the local magnetic configuration at the $CoFe_2O_4/Fe_3O_4$ interface which was consistent with the experimental results observed. We therefore showed that the local configuration of the spins on either side of the barrier/electrode interface played a dominant role in determining the magnetic behavior of the $CoFe_2O_4/Fe_3O_4$ system. By directly growing Fe_3O_4 on $CoFe_2O_4$, a two-phase magnetization loop was obtained *without the insertion of a non-magnetic spacer*, in contrast with the case of $CoFe_2O_4$/Co, where the two magnetic layers had to be physically separated in order to obtain the desired decoupled switching.

8.1.3 Spin-polarized tunneling

The spin-polarized tunneling characteristics of our $CoFe_2O_4$ tunnel barriers were studied using two complementary experimental methods. The first, known as the Meservey-Tedrow technique, directly measured the spin polarization, at low temperature, of the tunnel current passing through the $CoFe_2O_4$ barrier. This was done in a tunnel junction structure containing a superconducting Al counter electrode as the spin analyzer. In the second technique, a magnetic tunnel junction structure containing Co as the FM counter electrode was used to study the spin polarized tunneling both at low temperature and at room temperature.

The Meservey-Tedrow studies of our Pt(111)/$CoFe_2O_4$(111)/γ-Al_2O_3(111)/Al tunnel junctions revealed asymmetric Zeeman splitting in the quasiparticle density of states of the superconducting Al electrode. This proved that the tunneling current generated by the $CoFe_2O_4$ electrode was indeed spin polarized, thus directly demonstrating the spin filter effect in this material for the first time. Furthermore, a series of samples grown under different oxidation conditions in our MBE chamber revealed a systematic augmentation

of the measured spin polarization with increasing $P_{O_2}^{plasma}$, increasing from 6% at the lower limit to 26% in moderately high oxidation conditions. This very interesting result suggested that the suppression of oxygen vacancies in our $CoFe_2O_4$ spin filters reduced the number of spin scattering defect states in the band structure of the barrier, thus increasing the polarization of the resultant tunneling current. Even more interesting was the fact that the structural and chemical measurement techniques used to characterize our $CoFe_2O_4$ barriers were incapable of detecting this difference in oxygen vacancy concentration. We therefore showed that SPT measurements provide a much more sensitive method of detecting the presence of structural and chemical defects in magnetic tunneling barriers, where classic characterization techniques such as RHEED, XPS and AES do not have the resolution to do so.

In the second of our spin-polarized tunneling experiments, we measured TMR both at low temperature and at room temperature in fully epitaxial MTJs having the structure Pt(111)/$CoFe_2O_4$(111)/γ-Al_2O_3(111)/Co(0001). The exact TMR values were of -18% at 2 K and -3% 300 K. By way of these experiments, we proved that $CoFe_2O_4$ is capable of filtering spins even at room temperature, which is, to our knowledge, the first unambiguous demonstration of room temperature spin filtering in any ferromagnetic insulating material. Furthermore, a more detailed analysis of the current-voltage characteristics in our $CoFe_2O_4$ spin filters revealed an experimental TMR ratio that increased with increasing bias voltage. This unique bias voltage dependence reproduced theoretical studies predicting that an increasing $TMR(V)$ dependence was in fact the signature of spin filtering across a ferromagnetic insulator. The physical origin of this effect could be explained by the preferential tunneling of spin-down electrons through the first spin-down level of the conduction band (Fowler-Nordheim tunneling) for a specific bias-voltage regime related to the amount of exchange splitting in the conduction band of our $CoFe_2O_4$. The striking similarity between our experimental TMR(V) curves and those previously predicted in the literature not only proved the spin filtering capability of $CoFe_2O_4$ both at low temperature and at room temperature, but also contributed to the validation of the theoretical and phenomenological models describing the physics of spin-polarized tunneling across a magnetic insulator.

In comparing the SPT results obtained by the Meservey-Tedrow and TMR experiments, the most intriguing find was that the sign of the spin polarization disagreed from one measurement technique to the other. In particular, the observation of positive $P_{CoFe2O4}$ using the Meservey-Tedrow technique was opposite to that expected from electronic band structure calculations. Although we were not able to provide a definite answer to this puzzling question, the comparison of our experimental results with previous

theoretical and experimental studies did allow us to discuss a few possible explanations. In particular, we considered the possibility that each of the two SPT techniques probed a different definition of P, thus leading to the measurement of opposite signs. In the case of the Meservey-Tedrow experiments, the direct tunneling mechanism present in these low-bias experiments led us to believe that P was determined by more than just the DOS in the $CoFe_2O_4$ conduction band, and that additional factors including the different Fermi velocities associated with the *sp* and *d* channels, band symmetry filtering or even resonant tunneling could modify the transmission of spin-up and spin-down electrons across the barrier. On the other hand, the Fowler-Nordheim tunneling mechanism observed in the higher-bias TMR experiments supported the fact that we probed the purely DOS definition of P, thus measuring negatively polarized spin filtering. Future theoretical and experimental investigations—some of which are discussed in the following section—should help verify this hypothesis.

8.2 Short-term Future Work

Quite often, the end of a doctoral thesis opens the door to a myriad of future studies inspired by the results obtained. Other studies also remain unfinished due to time constraints and other technical issues. In this final section, we will discuss a few future projects on our $CoFe_2O_4$-based spin filter systems that follow directly from the results presented in Chapters 5-7 of this thesis. We will end this chapter with a brief description of some more long-term projects involving $CoFe_2O_4$ spin filter tunnel barriers, which include double spin filter MTJs and spin injection applications into semiconductors and organics.

8.2.1 Meservey-Tedrow experiments on $CoFe_2O_4$ single layers

As we saw in the discussion sections of Chapter 5, the most important unresolved issue resulting from the Meservey-Tedrow measurements on our Pt(111)/$CoFe_2O_4$(111)/γ-Al_2O_3(111)/Al tunnel junctions was the unexpected positive sign of the measured polarization. While a few possible explanations were proposed, further studies are clearly necessary in order to determine whether the origin of this positive P is related to the Al spin detector or to the spin-polarized tunneling characteristics of the $CoFe_2O_4$ barrier itself.

One very interesting experiment to try would be to replace the Al spin analyzer with another superconducting material having an electronic band structure dominated by *d*-states, rather than *s*-states as is the case for Al.

This would lead us to consider the transition metal superconductors, which unfortunately are limited in number. Having available d-states in the superconducting spin analyzer could potentially favor the detection of electrons originating from the d-states in the Pt electrode, and polarized by the d-states in the conduction band of the $CoFe_2O_4$ spin filter. One could expect that the probability of detecting negatively polarized spins would be increased in this scenario. In fact, a few attempts were made during this thesis (and in collaboration with the Francis Bitter Magnet Laboratory at MIT) to replace the Al electrode with Vanadium. However, it rapidly came to our attention that the extremely high oxygen affinity of V would pose serious problems at the the γ-Al_2O_3/V interface. Our preliminary experiments showed that the oxidation of V at this interface rapidly destroyed its superconducting properties, making it impossible to perform a Meservey-Tedrow experiment. Further studies are therefore necessary in order to either engineer this interface such that the V oxidation is avoided, or to incorporate an alternative transition metal superconductor as the spin analyzer in our $CoFe_2O_4$-based tunnel junctions.

In addition to further experimental studies, the results from our preliminary Meservey-Tedrow measurements beg for complementary theoretical calculations of the electronic band structure of $CoFe_2O_4$ as well as the entire Pt(111)/$CoFe_2O_4$(111)/γ-Al_2O_3(111)/Al system. This is by no means an easy task, given the complicated crystal structure of the oxide tunnel barrier. By determining the electronic band structure of the two electrodes, as well as their alignment with the different symmetry channels in the $CoFe_2O_4$ barrier, one might obtain a better picture of what spin channels are actually favored during the tunneling process, thus providing additional information about the tunnel matrix elements and the transmission of sp and d electrons. In particular, an analysis of the different spin-electron decay lengths inside the $CoFe_2O_4$ barrier could eventually explain why we measure a positively polarized current in the Al superconductor after tunneling across the $CoFe_2O_4$/γ-Al_2O_4 barrier. Finally, it would be most interesting to further calculate the band structure for the fully epitaxial Pt(111)/$CoFe_2O_4$(111)/γ-Al_2O_3(111)/Co(0001) MTJ, and compare this with the Pt(111)/$CoFe_2O_4$(111)/γ-Al_2O_3(111)/Al case.

8.2.2 $CoFe_2O_4/Fe_3O_4$ bilayers and MTJs

Our study of the magnetic properties of the fully epitaxial, near-fully oxide, Pt(111)/$CoFe_2O_4$(111)/Fe_3O_4(111) heterostructures left two major topics for future work. The first, and most urgent of course, was the TMR measurements on this system, which unfortunately were never performed

due to time constraints. Having shown that $CoFe_2O_4$ does indeed function as a spin filter barrier in other tunnel junction systems, the question to address in the $Pt/CoFe_2O_4/Fe_3O_4$ case is what effect does the exchange interaction at the $CoFe_2O_4/Fe_3O_4$ interface have on the possibility of measuring a TMR. This is a particularly intriguing issue given the fact that we do observe two individual switching events in the magnetization curves, corresponding to the $CoFe_2O_4$ and Fe_3O_4 layers. Without performing the actual experiment, it is impossible to predict whether this strong antiferromagnetic exchange coupling paired with the local magnetic configuration at the interface would prohibit the observation of any TMR, or result in an extremely high value. Further motivating this study are the results obtained by Santos et al. on Cr/Cu/EuO/Gd/Al spin filter MTJs, where a TMR of 280% was observed in conjunction with an exchange coupling at the EuO/Gd interface [50] (see Chapter 2). Regardless of whether any TMR could be observed in the $Pt/CoFe_2O_4/Fe_3O_4$ system, it would also be important to test the same system modified only by the insertion of a γ-Al_2O_3 spacer in between the two ferrite layers. Because our results in Chapter 7 show that such a spacer inhibited the strong exchange interaction, we would expect there to be a significant modification in the spin-polarized transport properties.

In addition to the unresolved TMR experiments in our $Pt/CoFe_2O_4/Fe_3O_4$ MTJs, further studies are necessary to better understand the complex exchange interaction and local magnetic configuration at the $CoFe_2O_4/Fe_3O_4$ interface. We note that the scenario discussed in Chapter 6 was only a hypothetical prediction based on the ensemble of magnetic and CIP magneto-transport measurements performed on these samples. First and foremost, we propose a complementary theoretical study simulating the AF-coupled half spin chain model discussed at the end of this chapter. Similar analytical calculations have already been resolved in the case of two AF-coupled spin chains that align parallel far from the interface, such is the case at an antiphase boundary [83]. In the present case, the idea would be to repeat the calculation taking the alignment to be antiparallel far from the interface, in the hopes of better resolving the $M(H)$ behavior and $H_{s2}(T)$ dependence discussed in Chapter 6. More detailed computational studies could also help simulate the observed experimental behavior. Finally, we also propose that the ensemble of experimental measurements including low temperature VSM, CIP magneto-transport and PNR be repeated in the case of $CoFe_2O_4/Fe_3O_4$ bilayers deposited on a Pt buffer layer. Because it was observed that the magnetic switching of the $CoFe_2O_4$ and Fe_3O_4 layers was better resolved and more abrupt when deposited on Pt, we believe that the number of structural defects are reduced, leading to larger magnetic domains. If this is the case, we would expect the results from the CIP magneto-transport and PNR ex-

periments to be better resolved as well, possibly allowing for a more definite interpretation of the experimental results.

8.2.3 $Pt/CoFe_2O_4/\gamma$-Al_2O_3/Co MTJs

Finally, regarding our Pt/$CoFe_2O_4$/γ-Al_2O_3/Co MTJs, the successful measurement of TMR both at low temperature and at room temperature opens the door to a number of studies that dig deeper in to the materials issues and physics of this particular system. In particular, one could imagine trying to optimize the magnitude of the measured TMR by varying the oxygen vacancy concentration in the $CoFe_2O_4$ spin filter, as was done for the Meservey-Tedrow experiments. An in-depth study of the effect of structural and chemical defects (i.e. oxygen vacancies, presence of Co^{3+}, antiphase boundaries...) on the spin filter characteristics of the $CoFe_2O_4$ barrier would be extremely useful in understanding the magnitude and sign of the TMR, as well as the dramatic temperature dependence observed in our experiments.

TMR measurements should also be performed in a wider range of applied biases in order to better understand the unique bias voltage dependence in this system, and its correlation to the electronic band structure. Although more difficult to realize experimentally, TMR measurements at significantly lower bias voltages would provide an important base for comparison with the Meservey-Tedrow results, which themselves were obtained near zero bias.

8.3 Long-term Perspectives and Applications

8.3.1 Double spin filter tunnel junctions

Taking into consideration the highly spin-polarized electron currents generated by single spin filter tunnel barriers, Worledge and Geballe [106] went a step further to propose a double spin filter tunnel junction whose functionality was even more enhanced with respect to the single spin filter MTJ. In their model, they proposed a device consisting of two non-magnetic electrodes separated by two adjacent spin filter tunnel barriers whose TMR output could reach as high as 10^5%. A schematic illustration of the double spin filter device proposed by Worledge and Geballe is shown in Figure 8.1. The physics of double spin filter tunnel junctions follows naturally from that of the single spin filter scenario. Assuming that both spin filters have a lower barrier height for spin-up electrons, when the two spin filters are magnetized in the parallel configuration, the spin-up electrons have a lower barrier height with respect to the spin-down electrons resulting in a highly spin-up polarized tunneling current. Conversely, when the two spin filters are magnetized in

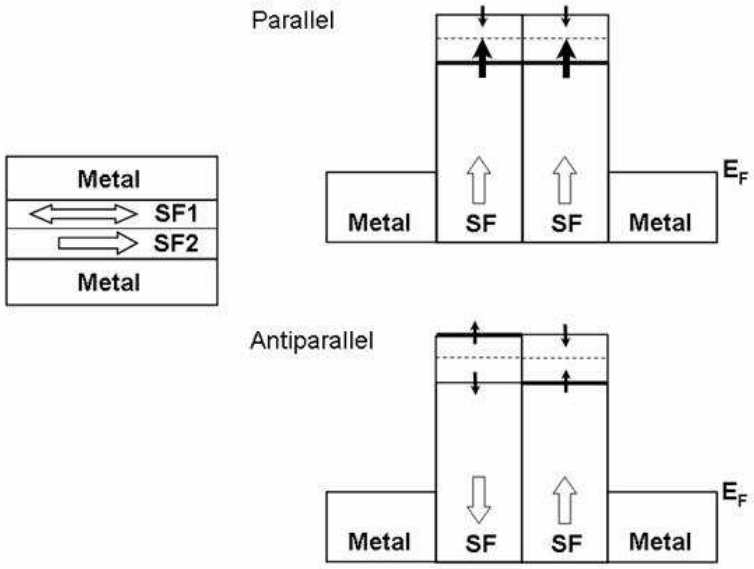

Fig. 8.1: Schematic illustration of a double spin filter tunnel junction in the parallel and antiparallel magnetic alignments, as proposed by Worledge and Geballe [106]. SF1 and SF2 represent two spin filter tunnel barriers, the first being free to switch and the second effectively pinned. In this particular model the two spin filter barriers are assumed to have identical electronic band structures.

the antiparallel configuration, the spin-up and spin-down barrier heights are mismatched such that very little current flows through the device. According to this model, the exponential dependence of the tunneling current on the barrier height should result in exceedingly large TMR when the two spin filter layers are simply toggled from the P to the AP alignment.

Of course, the most challenging issue to overcome in the fabrication of such a device is the magnetic decoupling of the two spin filter barriers which, once again, are in direct contact with each other. In Worledge and Geballe's device, independent switching is achieved by choosing two spin filter materials having different coercive fields, one of the two remaining pinned due to its high H_c. In reality, the high probability of exchange coupling between the two spin filters, especially when working with magnetic oxides, makes the choice of materials much more difficult than just two spin filters with different coercive fields. To prevent the exchange coupling issue, other dou-

ble spin filter devices could be envisioned with a non-magnetic spacer (either insulating or metallic) separating the two spin filter layers.

Another complication arising from the double spin filter device structure is its very high resistance. Because the junction resistance depends exponentially on the barrier thickness, R_j will be much higher than in the thinner, single barrier situation. Furthermore, in the case of two spin filters having different band gaps and exchange splitting, an addition potential barrier could result due to this heterojunction structure, thus increasing R_j even more.

Having proven in this thesis that $CoFe_2O_4$ is indeed a functioning spin filter material, the next natural step would be to integrate it into a double spin filter device. One possibility would be to use another of the spinel ferrite spin filters ($NiFe_2O_4$ [107], $MnFe_2O_4$...) whose structural properties are nearly identical to those of $CoFe_2O_4$. The resultant device would have the following structure : NM/XFe_2O_4/$CoFe_2O_4$/NM. However, the magnetic decoupling of XFe_2O_4 and $CoFe_2O_4$ would surely be difficult to obtain, especially since the magnetic properties of the different spinel ferrites are very similar. Taking a slightly different approach, we propose to take advantage of the exchange coupling between Co and $CoFe_2O_4$ described in Chapter 7 in order to modify the magnetic properties of one $CoFe_2O_4$ layer. We could then create a double spin filter tunnel junction containing *two $CoFe_2O_4$ barriers separated by a γ-Al_2O_3 spacer*: Co/$CoFe_2O_4$/γ-Al_2O_3/$CoFe_2O_4$/NM. In this particular structure, the Co/$CoFe_2O_4$ bilayer would replace one of the NM/SF pairs in the structure proposed by Worledge and Geballe, since these two layers switch in unison. Furthermore, we saw in Chapter 7 that the switching of the Co/$CoFe_2O_4$ bilayer is abrupt—in contrast to the switching of a $CoFe_2O_4$ layer alone—resulting in two spin filter layers with different magnetic properties. In this structure, we could expect to obtain a TMR curve with a similar shape to that in our Pt/$CoFe_2O_4$/γ-Al_2O_3/Co MTJs. Finally, this potential device could be fabricated entirely *in-situ* using our MBE system.

8.3.2 Spin injection into semiconductors and organics

Arguably the most exciting future application of spin filter tunnel barriers is for the injection of spin-polarized currents into semiconductor materials. These may be either classic semiconductors such as Si or GaAs, or organic semiconductors such as Alq_3 or rubrene. Datta et al. first proposed to combine semiconductor electronics with spin electronics in a device which they named the spin field effect transistor or spin-FET [108]. Similar semiconductor spintronics devices have since been proposed using spin filters as the

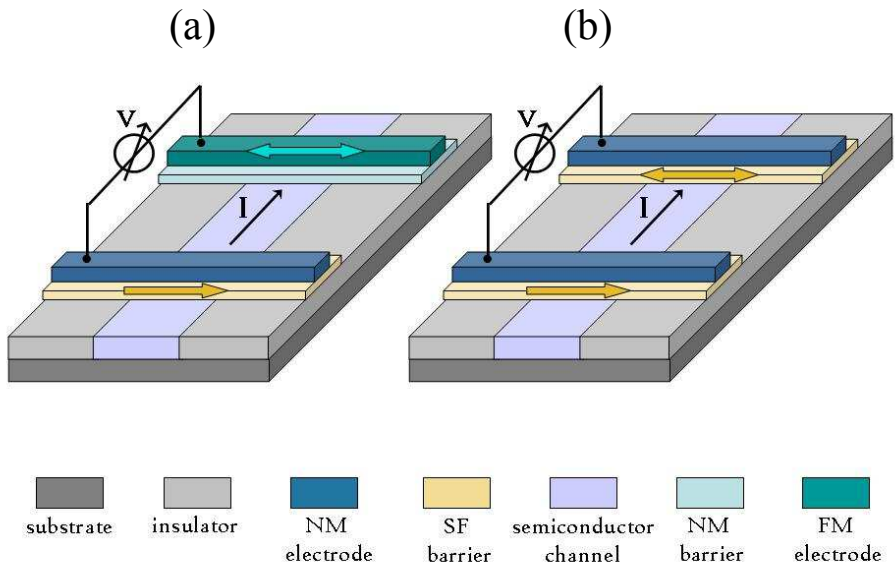

Fig. 8.2: Illustration of two spin valve-type devices that could be potentially used to study the injection of a spin-polarized current from a spin filter barrier into a semiconductor channel. In (a) the spin filter barrier injects spin-polarized current which is then detected by a ferromagnetic electrode. In (b), spin filter barriers act both as a spin-polarized current source and detector.

source and detector of spin-polarized currents [109, 110]. On the experimental side, several studies have now successfully demonstrated spin injection into III-V semiconductors using ferromagnetic electrodes as the polarized electron source [111, 112], and more recently into Si [113]. Although the details of these and numerous other studies are beyond the scope of this thesis, a few points about these device applications are worth noting.

The major obstacle found when injecting spin-polarized currents from a ferromagnetic electrode into a semiconductor arises at the FM/semiconductor interface. In fact, it was observed experimentally [114, 115] and then explained theoretically [116] that the conductivity mismatch between the FM and semiconductor layers at their interface resulted in the near-complete depolarization of the injected current. In order to overcome this conductivity mismatch problem, Rashba [117] theoretically analyzed the advantage of using a Schottky barrier or a tunnel barrier at the FM/semiconductor interface. The optimization of this interface in the case of an MTJ was also analyzed

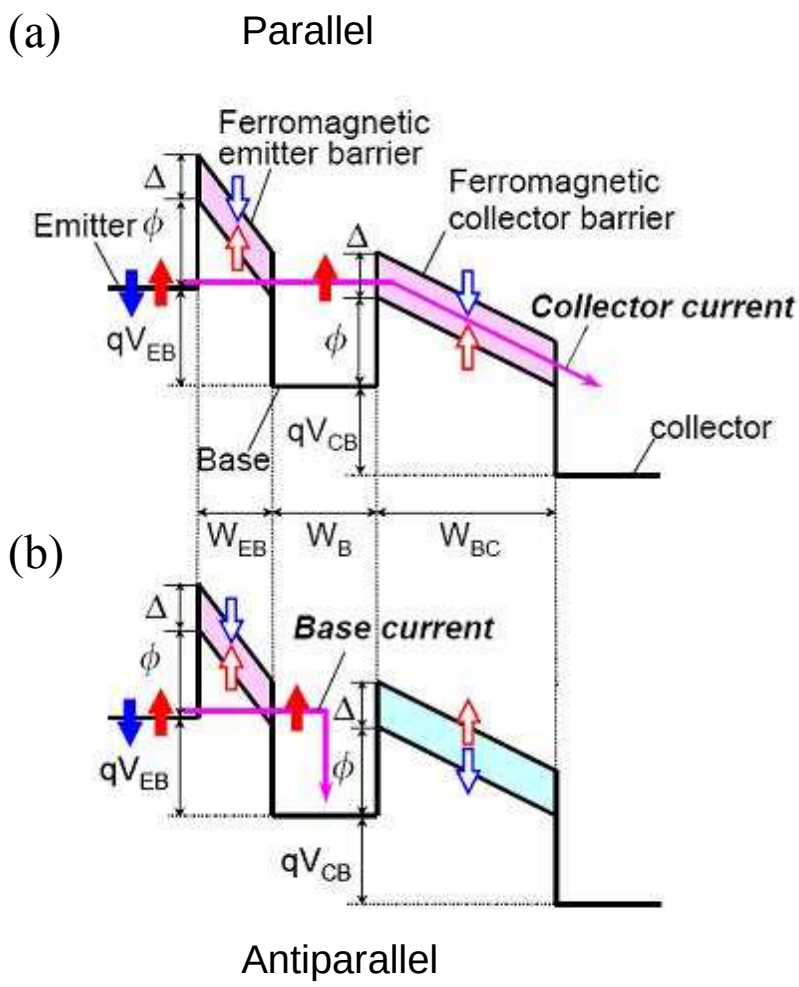

Fig. 8.3: Band diagram representing the spin-filter transistor proposed by Sugahara and Tanaka. In the parallel magnetic configuration of the emitter barrier and collector barrier (a), a high collector current is detected. Conversely, the antiparallel configuration (b) results in no collector current. Figure taken from [109].

by Fert and Jaffrès [118], who proposed a model in which the spin-dependent interface resistance could be a determinant factor in the TMR measurement. While all of the successful demonstrations of spin injection into semiconductors have taken advantage of Rashba's original proposition, one can expect to obtain even higher spin-polarized injector currents using a spin filter tunnel barrier coupled to a non-magnetic metal as the polarized current source. The $CoFe_2O_4$ spin filter is, of course, a particularly interesting candidate because of its potential to function at room temperature.

Before integrating $CoFe_2O_4$ spin filters into complex spin-FET and spin-LED devices, simple studies should be done using spin-valve type structures in which the non-magnetic metallic spacer is replaced by a classic or organic semiconductor. A schematic representation of two such devices are shown in Figure 8.2. In the first (Figure 8.2-a), $CoFe_2O_4$ acts only as the polarized current source, the detector being a FM metal such as Co. In the second (Figure 8.2-b), $CoFe_2O_4$ now acts both as the spin-polarized emitter and detector. The measurement of MR in both cases would be a first indication of the successful spin injection into a semiconductor from a $CoFe_2O_4$ spin filter.

Figure 8.2-b leads us to the final $CoFe_2O_4$-based device proposition, which is directly inspired by Sugahara and Tanaka's spin filter transistor or SFT [109]. A schematic illustration of this devices is shown in Figure 8.3 for both the parallel and antiparallel magnetic configurations of the spin filter barriers. In Sugahara and Tanaka's SFT, a nonmagnetic, semiconducting emitter, base and collector are separated by two spin filter tunnel barriers. Upon application of an emitter-base bias (V_{EB}), the emitter barrier filters the spins tunneling into the base. Similarly, the application of a base-collector bias (V_{BC}) allows the collector barrier to act as a spin-analyzer for the spin-polarized transport through the base. In the parallel magnetic configuration (Figure 8.3-a), the spin-polarized electrons injected through the $CoFe_2O_4$ emitter barrier into the base can continue to tunnel through the second $CoFe_2O_4$ collector barrier, thus resulting in the detection of a collector current. In the antiparallel configuration (Figure 8.3-b), the mismatch between the spin-up and spin-down barrier heights in the $CoFe_2O_4$ emitter and collector barriers prevents a collector current from being detected. Of course, this device will only function if the width of the base (W_B) is less than the spin-flip scattering length. Once again, in the particular device containing two $CoFe_2O_4$ spin filter barriers, these must be engineered such that they switch at different magnetic fields, allowing for both parallel and antiparallel magnetic alignments.

As we can clearly see, the results presented throughout this thesis are

merely a first crucial step towards the integration of spin filters into future spintronics devices. Having demonstrating that spin filtering at room temperature is indeed possible, we may now start thinking about the myriad of more complex devices and applications that take advantage of this exciting physical effect, and how we may integrate novel materials into these systems. Continuing work with $CoFe_2O_4$ and other potential room temperature spin filters will demand a high level of technical finesse and creativity, but the doors to the future are wide open.

APPENDIX

A. CRYSTALLINE Co/α-Al_2O_3(0001) BILAYERS FOR FULLY EPITAXIAL MAGNETIC TUNNEL JUNCTIONS

Research in *fully epitaxial* MTJs has increased greatly following the discovery of giant TMR effects using single crystalline MgO tunnel barriers. An impressive number of studies on systems such as Fe(001)/MgO(001)/Fe(001) [35, 36] have stemmed from the theoretical predictions of Butler *et al.* [32] stating that the spin-coherent tunneling of symmetrical electron wave functions in crystalline MgO barriers could lead to TMR values that defied predictions from Jullière model [6]. The epitaxial Co(001)/MgO(001)/Co(001) system similarly revealed TMR values exceeding 400% at room temperature [119]. However, much less attention has been given to epitaxial systems containing Al_2O_3 tunnel barriers which, in the amorphous form, presided MgO in the first room temperature MTJs [7]. A few theoretical papers have addressed the spin polarization of the epitaxial Co/α-Al_2O_3 system [120, 121, 122], but little is known about spin-coherent tunneling. On the experimental side, the difficulty to grow single crystalline Al_2O_3 tunnel barriers [84] is largely responsible for the lack of results on the spin-polarized tunneling in this model system.

In Appendix A, we present a complete study of the epitaxial growth, structural and chemical characterization, and spin-polarized tunneling properties of single-crystalline Co/α-Al_2O_3(0001) bilayers grown by oxygen plasma-assisted MBE. The optimization of this bilayer system is a crucial step towards the fabrication of fully epitaxial Co/α-Al_2O_3/Co MTJs for future TMR measurements.

A.1 Epitaxial Growth and Materials Characterization

Our Co/α-Al_2O_3(0001) samples were grown in the same UHV MBE system as the $CoFe_2O_4$-based heterostructures described throughout this thesis. Typical thicknesses for the Co and Al_2O_3 layers were 15 nm and 3 nm respectively. Co bottom electrodes were deposited at room temperature on sapphire (α-Al_2O_3(0001)) substrates at a rate of 0.9 Å/min. Because the initial growth revealed itself to be polycrystalline by RHEED, the deposition

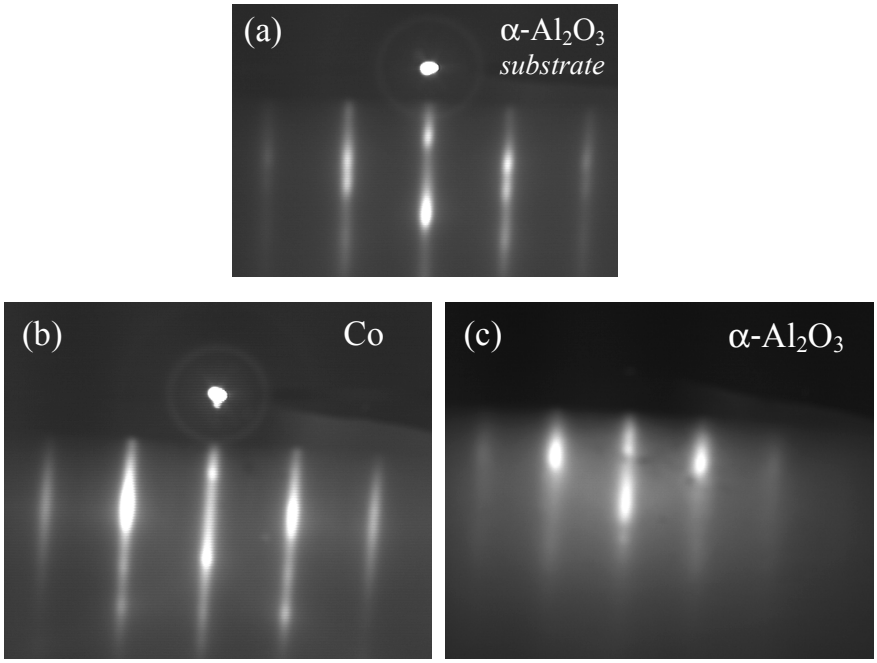

Fig. A.1: In situ RHEED characterization of a Co(0001)(15 nm)/α-Al_2O_3(0001)(3 nm) bilayer, here shown along [1$\bar{1}$00], after MBE growth. The RHEED pattern of the α-Al_2O_3 substrate is shown in (a). Both the RHEED patterns of the Co electrode (b) and α-Al_2O_3 barrier (c) reveal the high crystalline quality of this fully epitaxial system. Comparison of (a) with (c) confirms the hexagonal structure of the α-Al_2O_3 barrier.

of the Co layer was followed by a two-hour anneal at 450°C, resulting in the two-dimensional, single crystalline RHEED pattern shown in Fig.A.1-b. The α-Al_2O_3 barriers were subsequently grown at 450°C by the reactive deposition of metallic aluminum in the presence of the atomic oxygen plasma (total oxide growth rate = 1 Å/min). The RHEED patterns of the Al_2O_3 barriers are characteristic of the hexagonal α-phase, as may be seen by comparing the RHEED patterns of the α-Al_2O_3 substrates (Figure A.1-a) with those of the barriers themselves (Figure A.1-c). These also reveal a high quality, two-dimensional, epitaxial growth mode.

In situ characterization of the Co/α-Al_2O_3(0001) bilayers by AES and XPS directly after sample growth was used to analyze the chemistry of the individual layers before surface contamination and exposure to air. This was especially important in characterizing the oxidation state of the Al, which

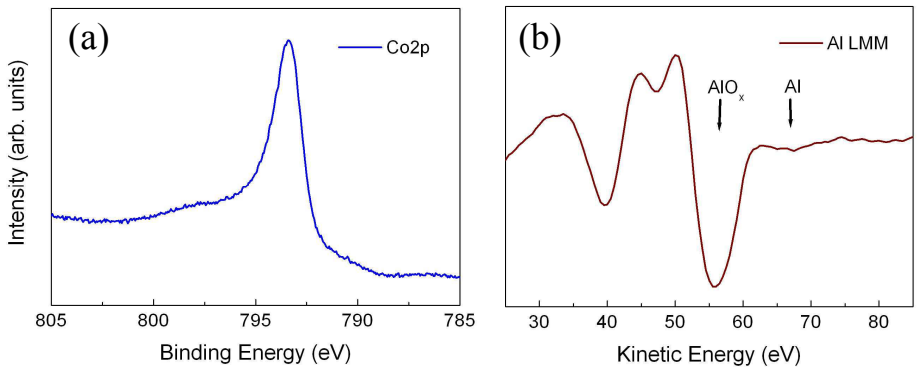

Fig. A.2: In situ chemical study of a Co(0001)(15 nm)/α-Al_2O_3(0001)(3 nm) bilayer. (a) The metallic state of the Co layer is analyzed by XPS, and reveals no sign of undesired oxidation. (b) AES is used to verify the stoichiometry of the α-Al_2O_3 layer, which is clearly fully oxidized. This is shown by the sole presence of a peak at the energy corresponding to AlO_x and not metallic Al.

should ideally be fully oxidized Al^{3+} throughout the entire thickness of the film. For the α-Al_2O_3, AES was therefore most appropriate, not only because of its the surface sensitivity, but because of its chemical sensitivity to the presence of metallic Al. On the other hand, XPS was best suited to study the oxidation state of the Co because the longer escape depth of the photoelectrons ($\sim$ 5 nm) allowed to selectively study the Co atoms localized near the metal/oxide interface. Fig.A.2-a shows the Co2*p* XPS peak as measured at the Co/α-Al_2O_3(0001) interface, revealing a fully metallic Co layer. The LMM transition in the AES spectrum of the α-Al_2O_3 layer is displayed in Fig.A.2-b, and clearly shows the absence of any significant peak in the energy range corresponding to metallic Al. From our *in situ* chemical studies, we may thus conclude that we have a clean metal/oxide interface with no significant diffusion of oxygen from the Al_2O_3 to the Co. Furthermore, this analysis validates the oxidation conditions (rf power, oxygen pressure in the plasma source...) used to grow the crystalline Al_2O_3.

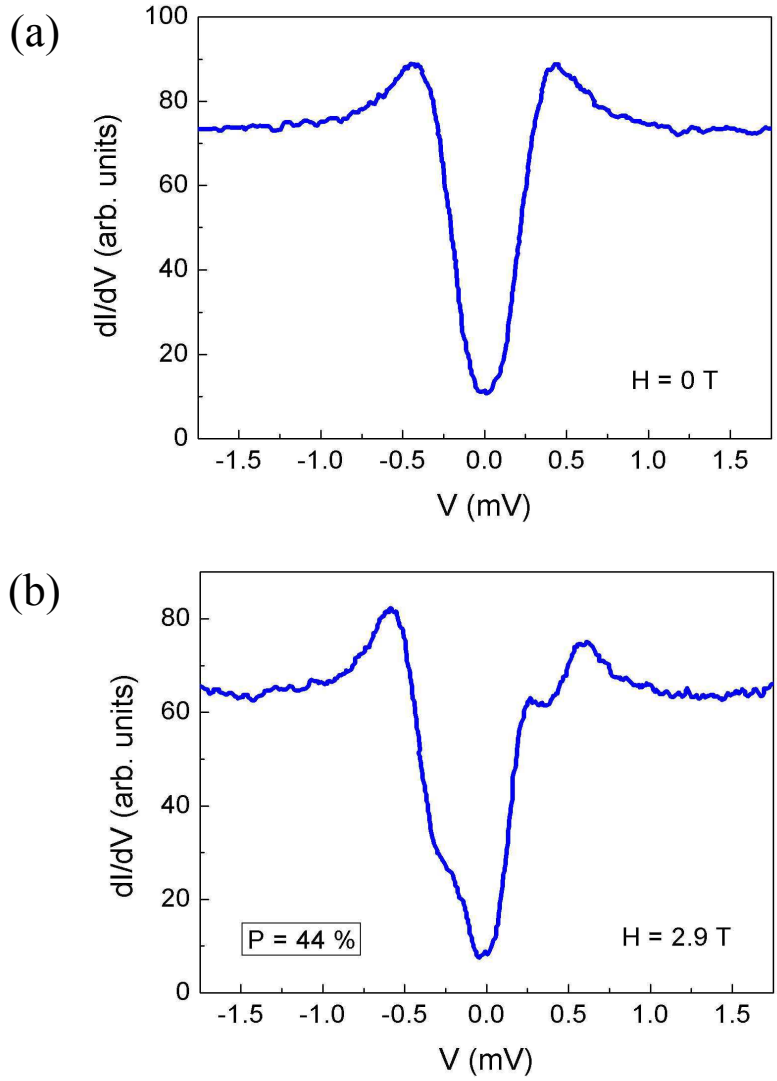

Fig. A.3: Tunneling dynamic conductance curves for a Co(0001)(15 nm)/αAl$_2$O$_3$(0001)(3 nm)/Al(4.2 nm) tunnel junction measured at 0.45 K. The asymmetry in the curve obtained with $H = 2.9$ T corresponds to a spin polarization of 44%.

A.2 Spin-Polarized Tunneling Experiments

The spin polarization of the epitaxial Co/α-Al_2O_3(0001) system was measured by the Meservey-Tedrow technique [17]. As was described in Chapter 2, this experiment uses a superconducting electrode as the spin analyzer in a ferromagnet/insulator/superconductor (FM/I/SC) tunnel junction. The observation of asymmetry in the Zeeman-split BCS density of states of the SC may be translated to a P value corresponding to the tunneling current originating from the FM electrode [39]. The experimental conditions of the Meservey-Tedrow experiment were described in detail in Chapter 3, and are therefore only summarized briefly here. For the Co/α-Al_2O_3(0001) system, superconducting Al (4.2 nm) films deposited by thermal evaporation were again used as the spin analyzer. Co/α-Al_2O_3/Al junctions with an approximate junction area of 150×500 μm were defined by a combination of an amorphous alumina definition layer and a simple shadow mask. The surface of the α-Al_2O_3 barrier was cleaned with an oxygen plasma glow discharge before deposition of the Al top electrode. SPT measurements were performed in a ^{3}He cryostat at 0.45 K (the critical superconducting temperature of our Al films was measured to be 2.6 K), where tunneling dynamic conductance curves were measured in the two-terminal configuration both at zero applied magnetic field and at $H = 2.9$ T.

Fig.A.3 shows the dI/dV curves for a Co(15 nm)/α-Al_2O_3(3 nm)/Al(4.2 nm) tunnel junction with and without applied magnetic field. The zero-field curve contains two symmetric peaks at ± 0.45 mV, delimiting the BCS energy gap of the Al electrode, and thus confirming tunneling transport across the α-Al_2O_3 barrier. In the curve obtained at 2.9 T, each of the two original peaks splits in two, yielding four distinct peaks due to the Zeeman-split spin-up and spin-down quasiparticle states in the Al layer. The asymmetry in the high-field curve is unambiguous, and corresponds to $P = 44\%$. This P value is similar to that obtained by the same technique in Co/Al_2O_3/Al tunnel junctions for which the barrier was amorphous and the Co polycristalline [104]. The SPT measurement therefore confirms the high electrical quality of our Co/α-Al_2O_3(0001)/Al tunnel junction, but also suggests that the crystallinity of the Al_2O_3 does not have a significant effect of the polarization of Co at the interface. Finally, our experimental results confirm the theoretical studies predicting that P at the single crystalline Co/α-Al_2O_3(0001) interface (where Co is the bottom electrode) may have a maximum value of 42.2% when the local atomic bond configurations are optimized [122].

The magnitude and sign of P is attributed to the localized hybridization of the Co-3d and O-2p orbitals at the metal/oxide interface [121], rather than to the crystalline structure of the barrier itself. Therefore, if unique

band symmetry filtering effects are to arise due to the crystalline nature of the α-Al_2O_3 tunnel barrier (i.e. effects related to spin-coherent tunneling), these will only be seen in TMR measurements of MTJs containing epitaxial interfaces *on either side* of the tunnel barrier. Further studies are underway to investigate such potential spin filtering effects in fully epitaxial Co/α-Al_2O_3/Co structures.

A.3 Conclusion

In conclusion, we have successfully developed the epitaxial growth of single-crystalline α-Al_2O_3(0001) tunnel barriers on Co(0001) electrodes for future integration into fully epitaxial, Al_2O_3-based MTJs. A number of *in situ* and *ex situ* characterization techniques confirm the excellent chemical and structural quality of this model system. We have also measured the spin polarization of the epitaxial Co/α-Al_2O_3(0001) interface by the Meservey-Tedrow technique, and have found P to agree well with theoretical calculations on the same system. Our Co/α-Al_2O_3(0001) bilayers are therefore ready to be inserted into complete MTJ structures that will allow us to investigate the effect of a second epitaxial Co electrode on the TMR measurement, and thus spin-polarized tunneling, across a crystalline Al_2O_3 barrier.

BIBLIOGRAPHY

[1] S. A. Wolf, D. D. Awschalom, R. A. Burhmann, J. M. Daughton, S. von Molnar, M. L. Roukes, A. Y. Chtchelkanova, and D. M. Treger. Spintronics: A spin-based electronics vision for the future. *Science*, 294:1488, 2001.

[2] Mark Johnson, editor. *Magnetoelectronics*. Academic Press.

[3] I. Zutic, J. Fabian, and S. Das Sarma. Spintronics: Fundamentals and applications. *Rev. Mod. Phys.*, 76:323, 2004.

[4] M. N. Baibich, J. M. Broto, A. Fert, F. Nguyen Van Dau, F. Petroff, P. Etienne, G. Creuzet, A. Friederich, and J. Chazelas. Giant magnetoresistance of (001)Fe/(001)Cr magnetic superlattices. *Phys. Rev. Lett.*, 61:2472, 1988.

[5] G. Binasch, P. Grunberg, F. Saurenbach, and W. Zinn. Enhanced magnetoresistance in layered magnetic structures with antiferromagnetic interlayer exchange. *Phys. Rev. B*, 39:4828, 1989.

[6] M. Jullière. Tunneling between ferromagnetic films. *Phys. Lett. A*, 54:225, 1975.

[7] J. S. Moodera, L. R. Kinder, T. M. Wong, and R. Meservey. Large magnetoresistance at room temperature in ferroomagnetic thin film tunnel junctions. *Phys. Rev. Lett.*, 74:3273, 1995.

[8] B. Dieny, V. S. Speriosu, S. S. P. Parkin, B. A. Gurney, D. R. Wilhoit, and D. Mauri. Giant magnetoresistive in soft ferromagnetic multilayers. *Phys. Rev. B*, 43:1297, 1991.

[9] E. L. Wolf. *Principles of electron tunneling spectroscopy*. Oxford University Press, London, 1985.

[10] J. Bardeen. Tunnelling from a many-particle point of view. *Phys. Rev. Lett.*, 6:57, 1960.

[11] J. G. Simmons. Generalized formula for the electric tunnel effect between similar electrodes separated by a thin insulating film. *J. Appl. Phys.*, 34:1793, 1963.

[12] W. F. Brinkman, R. C. Dynes, and J. M. Rowell. Tunneling conductance of asymmetrical barriers. *J. Appl. Phys.*, 41:1915, 1970.

[13] I. Giaever. Energy gap in superconductors measured by electron tunneling. *Phys. Rev. Lett.*, 5:147, 1960.

[14] I. Giaever. Electron tunneling between two superconductors. *Phys. Rev. Lett.*, 5:464, 1960.

[15] J. A. Appelbaum and W. F. Brinkman. Theory of many-body effects in tunneling. *Phys. Rev.*, 186:464, 1969.

[16] J. A. Appelbaum and W. F. Brinkman. Interface effects in normal metal tunneling. *Phys. Rev. B*, 2:907, 1970.

[17] R. Meservey and P. M. Tedrow. Spin-polarized electron tunneling. *Phys. Repts.*, 238:173, 1994.

[18] P. LeClair, J. T. Kohlhepp, H. J. M. Swagten, and W. J. M. de Jonge. Interfacial density of states in magnetic tunnel junctions. *Phys. Rev. Lett.*, 86:1066, 2001.

[19] J. M. D. Teresa, A. Barthélémy, A. Fert, J.-P. Contour, F. Montaigne, and P. Seneor. Role of metal-oxyde interface in determining the spin polarization of magnetic tunnel junctions. *Science*, 286:507, 1999.

[20] P. M. Tedrow and R. Meservey. Spin-dependent tunneling into ferromagnetic nickel. *Phys. Rev. Lett.*, 26:192, 1971.

[21] K. Maki. *Superconductivity*, volume 2. Marcel Dekker, New York, 1969.

[22] P. M. Tedrow and R. Meservey. Spin polarization of electrons tunneling from films of Fe, Co, Ni and Gd. *Phy. Rev. B*, 7:318, 1973.

[23] D. A. Papaconstantopoulos. *Handbook of the Band Structures of Elemental Solids*. Plenum, New York, 1986.

[24] I. I. Mazin. How to define and calculate the degree of spin polarization in ferromagnets. *Phys. Rev. Lett.*, 83:1427, 1999.

[25] M. B. Stearns. Simple explanation of tunnelling spin-polarization in Fe, Co, Ni and its alloys. *J. Magn. Magn. Mater.*, 8:167, 1977.

[26] E. Y. Tsymbal and D. G. Pettifor. Modelling of spin-polarized electron tunnelling from 3d ferromagnets. *J. Phys.: Condens. Matter*, 9:L411, 1997.

[27] J. C. Slonczewski. Conductance and exchange coupling of two ferromagnets separated by a tunneling barrier. *Phys. Rev. B*, 39:6995, 1988.

[28] J. Nogués and I. K. Schuller. Exchange bias. *J. Magn. Magn. Magn.*, 192:203, 1999.

[29] J. S. Moodera, L. R. Kinder, T. M. Wong, and R. Meservey. Large magnetoresistance at room temperature in ferromagnetic thin film tunnel junctions. *Phys. Rev. Lett.*, 74:3273, 1995.

[30] E. Y. Tsymbal, O. N. Mryasov, and P. R. LeClair. Spin-dependent tunnelling in magnetic tunnel junctions. *J. Phys.: Condens. Matter*, 15:109, 2003.

[31] J. Hayakawa, S. Ikeda, Y. M. Lee, F. Matsukura, and H. Ohno. Effect of high annealing temperature on giant tunnel magnetoresistance ratio of CoFeB/MgO/CoFeB magnetic tunnel junctions. *Appl. Phys. Lett.*, 89:232510, 2006.

[32] W. H. Butler, X.-G. Zhang, and T. C. Schulthess. Spin-dependent tunneling of Fe/MgO/Fe sandwiches. *Phys. Rev. B*, 63:054416, 2001.

[33] J. Faure-Vincent, C. Tiusan, E. Jouguelet, F. Canet, M. Sajieddine, C. Bellouard, E. Popova, M. Hehn, F. Montaigne, and A. Schuhl. High tunnel magnetoresistance in epitaxial Fe/MgO/Fe tunnel junctions. *Appl. Phys. Lett.*, 82:4507, 2003.

[34] M. Bowen, V. Cross, F. Petroff, A. Fert, C. Martinez Boubeta, J. L. Costa-Kramer, J. V. Anguita, A. Cebollada, F. Briones, J. M. D. Teresa, L. Morellon, M. R. Ibarra, F. Guell, F. Peiro, and A. Cornet. Large magnetoresistance in Fe/MgO/FeCo(001) epitaxial tunnel junctions on GaAs(001). *Appl. Phys. Lett.*, 79:1655, 2001.

[35] S. Yuasa, T. Nagahama, A. Fukushima, Y. Suzuki, and K. Ando. Giant room-temperature magnetoresistance in single-crystal Fe/MgO/Fe magnetic tunnel junctions. *Nature Mater.*, 3:868, 2004.

[36] S. S. P. Parkin, C. Kaiser, A. Panchula, P. M. Rice, B. Hughes, M. Samant, and S.-H. Yang. Giant tunelling magnetoresistance at room temperature with MgO(100) tunnel barriers. *Nature Mater.*, 3:862, 2004.

[37] T. Nagahama and J. S. Moodera. Magnetic tunnel junctions with magnesium oxide barriers. *J. Magnetics*, 11:170, 2006.

[38] J. S. Moodera, R. Meservey, and X. Hao. Variation of the electron-spin polarization in EuSe tunnel junctions from zero to near 100 percent in a magnetic field. *Phys. Rev. Lett.*, 70:853, 1993.

[39] J. S. Moodera, T. S. Santos, and T. Nagahama. The phenomena of spin-filter tunnelling. *J. Phys.: Condens. Matter*, 19:165202, 2007.

[40] A. Saffarzadeh. Spin-filter magnetoresistance in magnetic barrier junctions. *J. Magn. Magn. Mater.*, 269:327, 2004.

[41] J. S. Moodera, J. Nowak, and R. J. M. van de Veerdonk. Interface magnetism and spin wave scattering in ferromagnet-insulator-ferromagnet tunnel junctions. *Phys. Rev. Lett.*, 80:2941, 1998.

[42] X.-F. Han, A. C. C. Yu, M. Oogane, J. Murai, T. Daibou, and T. Miyazaki. Analyses of intrinsic magnetoelectric properties in spin-valve-type tunnel junctions with high magnetoresistance and low resistance. *Phys. Rev. B*, 63:224404, 2001.

[43] R. H. Fowler and L. Nordheim. Electron emission in intense electric fields. *Proc. Roy. Soc. (London)*, A119:173, 1928.

[44] T. Nagahama, T. S. Santos, and J. S. Moodera. Enhanced magnetotransport at high bias in quasimagnetic tunnel junctions with EuS spin-filter barriers. *Phys. Rev. Lett.*, 99:016602, 2007.

[45] G. Sarma. On the influence of a uniform exchange field acting on the spins of the conduction electrons in a superconductor. *J. Phys. Chem. Solids*, 24:1029, 1963.

[46] P. G. de Gennes. Coupling between ferromagnets through a superconducting layer. *Phys. Lett.*, 23:10, 1966.

[47] J. S. Moodera, X. Hao, G. S. Gibson, and R. Meservey. Electron-spin polarization in tunnel junctions in zero applied field with ferromagnetic EuS barriers. *Phys. Rev. Lett.*, 61:637, 1988.

[48] T. S. Santos and J. S. Moodera. Observation of spin filtering with a ferromagnetic EuO tunnel barrier. *Phys. Rev. B*, 69:241203, 2004.

[49] P. LeClair, J. K. Ha, J. M. Swagten, J. T. Kohlhepp, C. H. van de Vin, and W. J. M. de Jonge. Large magnetoresistance using hybrid spin filter devices. *Appl. Phys. Lett.*, 80:625, 2002.

[50] T. S. Santos. *Europium oxide as a perfect electron spin filter*. PhD thesis, Massachusetts Institute of Technology, Dept. of Materials Science and Engineering, 2007.

[51] M. Gajek, M. Bibes, A. Barthélémy, K. Bouzehouane, S. Fusil, M. Varela, J. Fontcuberta, and A. Fert. Spin filtering through ferromagnetic $BiMnO_3$ tunnel barriers. *Phys. Rev. B*, 72:020406, 2005.

[52] M. Bowen, M. Bibes, A. Barthélémy, J.-P. Contour, A. Anane, Y. Lemaître, and A. Fert. Nearly total spin polarization in $La_{2/3}Sr_{1/3}MnO_3$ from tunneling experiments. *Appl. Phys. Lett.*, 82:233, 2003.

[53] M. Gajek, M. Bibes, S. Fusil, K. Bouzehouane, J. Fontcuberta an dA. Barthélémy, and A. Fert. Tunnel junctions with multiferroic barriers. *Nature Mater.*, 6:296, 2007.

[54] U. Luders, M. Bibes, K. Bouzehouane, E. Jacquet, J.-P. Contour, S. Fusil, J. Fontcuberta, A. Barthélémy, and A. Fert. Spin filtering through ferrimagnetic $NiFe_2O_4$ tunnel barriers. *Appl. Phys. Lett.*, 88:082505, 2006.

[55] G. Hu and Y. Suzuki. Negative spin polarization of Fe_3O_4 in magnetite/manganite-based junctions. *Phys. Rev. Lett.*, 89:276601, 2002.

[56] U. Luders, M. Bibes, S. Fusil, K. Bouzehouane, E. Jaquet, C. B. Sommers, J.-P. Contour, J.-F. Bobo, A. Barthélémy, A. Fert, and P. M. Levy. Sbias dependence of tunnel magnetoresistance in spin filtering tunnel junctions : Experiment and theory. *Phys. Rev. B*, 76:134412, 2007.

[57] Z. Szotek, W. M. Temmerman, D. Kodderitzsch, A. Svane, L. Petit, and H. Winter. Electronic structures of normal and inverse spinel ferrites from first principles. *Phys. Rev. B*, 74:174431, 2006.

[58] M. G. Chapline and S. X. Wang. Room-temperature spin filtering in a $CoFe_2O_4/MgAl_2O_4/Fe_3O_4$ magnetic tunnel barrier. *Phys. Rev. B*, 74:014418, 2006.

[59] C. Gatel. *Élaboration et étude d'un système hybride* O*xyde ferrimagnétique/*M*étal non magnétique/*O*xyde ferrimagnétique*. PhD thesis, INSA Toulouse, 2004.

[60] Y. Suzuki, G. Hu, R. B. van Dover, and R. J. Cava. Magnetic anisotropy of epitaxial cobalt ferrite thin films. *J. Magn. Magn. Mater.*, 191:1, 1999.

[61] S. J. Kim, S. W. Lee, and C. S. Kim. Mossbauer studies on exchange interactions in $CoFe_2O_4$. *Jpn. J. Appl. Phys.*, 40:4897, 2001.

[62] L. Horng, G. Chern, M. C. Chen, P. C. Kang, and D. S. Lee. Magnetic anisotropic properties in Fe_3O_4 and $CoFe_2O_4$ ferrite epitaxy thin films. *J. Magn. Magn. Mater.*, 270:389, 2004.

[63] G. Hu, J. H. Choi, C. B. Eom, V. G. Harris, and Y. Suzuki. Structural tuning of the magnetic behavior in spinel-structure ferrite thin films. *Phys. Rev. B*, 62:779, 2000.

[64] S. Gota, J.-B. Moussy, M. Henriot, M.-J. Guittet, and M. Gautier-Soyer. Atomic-oxygen-assisted MBE growth of on α-Al_2O_3(0001): Metastable FeO-like phase at subnanometer thicknesses. *Surf. Sci.*, 482-485:809, 2001.

[65] J.-B. Moussy, S. Gota, A., Bataille, M.-J. Guittet, M. Gautier Soyer, F. Delille, B. Dieny, F. Ott, T. D. Doan, P. Warin, P. Bayle-Guillemaud, C. Gatel, and E. Snoeck. Thickness dependence of anomalous magnetic behavior in epitaxial Fe_3O_4 thin films: Effect of density of antiphase boundaries. *Phys. Rev. B*, 70:174448, 2004.

[66] E. Guiot. *Epitaxie assistée par plasma d'oxygène atomique de couches minces d'oxydes de fer sur* α-Al_2O_3. PhD thesis, Université de Paris VI, 1998.

[67] S. A. Chambers, R. F. C. Farrow, S. Maat, M. F. Toney, L. Folks, J. G. Catalano, T. P. Trainor, and G. E. Brown Jr. Molecular beam epitaxial growth and properties of $CoFe_2O_4$ on MgO(001). *J. Magn. Magn. Mater.*, 246:124, 2002.

[68] M. J. Hytch, J.-L. Putaux, and J.-M. Pénisson. Measurement of the displacement field of dislocations to 0.03 å by electron microscopy. *Nature*, 423:270, 2003.

[69] M. J. Hytch, E. Snoeck, and R. Kilaas. Quantitative measurement of displacement and strain fields from HREM micrographs. *Ultramicroscopy*, 74:131, 1998.

[70] Y. Suzuki, R. B. van Dover, E. M. Gyorgy, J. M. Phillips, V. Korenivski, D. J. Werder, C. H. Chen, R. J. Cava, J. J. Krajewski, and W. F. Peck, Jr. Structure and magnetic properties of epitaxial spinel ferrite thin films. *Appl. Phys. Lett.*, 68:714, 1996.

[71] Y. C. Wang, J. Ding, J. B. Yi, B. H. Liu, T. Yu, and Z. X. Shen. High-coercivity Co-ferrite thin films on (100)-SiO_2 substrate. *Appl. Phys. Lett.*, 84:2596, 2004.

[72] B. H. Liu and J. Ding. Strain-induced high coercivity in $CoFe_2O_4$ powders. *Appl. Phys. Lett.*, 88:042506, 2006.

[73] L. Signorini, L. Pasquini, F. Boscherini, E. Bonetti, I. Letard, S. Brice-Profeta, and P. Sainctavit. Local magnetism in granular iron/iron oxide nanostructures by phase- and site-selective x-ray magnetic circular dichroism. *Phys. Rev. B*, 74:014426, 2006.

[74] J. F. Hochepied, Ph. Sainctavitc, and M. P. Pilenib. X-ray absorption spectra and X-ray magnetic circular dichroism studies at Fe and Co $L_{2,3}$ edges of mixed cobaltzinc ferrite nanoparticles: cationic repartition, magnetic structure and hysteresis cycles. *J. Magn. Magn. Mater.*, 231:315, 2001.

[75] A. Barbier, R. Belkhou, P. Ohresser, M. Gautier-Soyer, O. Bezencenet, M. Mulazzi, M.-J. Guittet, and J.-B. Moussy. Electronic and crystalline structure, morphology, and magnetism of nanometric Fe_2O_3 layers deposited on Pt(111) by atomic-oxygen-assisted molecular beam epitaxy. *Phys. Rev. B*, 72:245423, 2005.

[76] A. Yanase and K. Siratori. Band structure in the high temperature phase of Fe_3O_4. *J. Phys. Soc. Jpn.*, 53:312, 1984.

[77] M. G. Chapline and S. X. Wang. Pulsed laser deposition grown $CoFe_2O_4/Fe_3O_4$ bilayers and their tunneling characteristics. *J. Appl. Phys.*, 97:10C915, 2005.

[78] A. Lisfi and C. M. Williams. Magnetic anisotropy and domain structure in epitaxial $CoFe_2O_4$ thin films. *J. Appl. Phys.*, 93:8143, 2003.

[79] M. D. Sturge, E. M. Gyorgy, R. C. LeCraw, and J. P. Remeika. Magnetic behavior of cobalt in garnets. magnetiocrystalline anisotropy and ferrimagnetic resonance of cobalt-doped yttrium iron garnet. *Phys. Rev.*, 180:413, 1969.

[80] D. T. Margulies, F. T. Parker, M. L. Rudee, F. E. Spada, J. N. Chapman, P. R. Aitchison, and A. E. Berkowitz. Origin of the anomalous magnetic behavior in single crystal Fe_3O_4 films. *Phys. Rev. Lett.*, 79:5162, 1997.

[81] M. Ziese and H. J. Blythe. Magnetoresistance of magnetite. *J. Phys.: Condens. Matter*, 12:13, 2000.

[82] W. Eerenstein, T. T. M. Palstra, S. S. Saxena, and T. Hibma. Spin-polarized transport across sharp antiferromagnetic boundaries. *Phys. Rev. Lett.*, 88:247204, 2002.

[83] A. V. Ramos, J. B. Moussy, M. J. Guittet, A. M. Bataille, M. Gautier-Soyer, M. Viret, C. Gatel, P. Bayle-Guillemaud, and E. Snoeck. Magneto-transport properties of Fe_3O_4 epitaxial thin films: thickness effects driven by antiphase boundaries. *J. Appl. Phys.*, 100:103902, 2006.

[84] A. M. Bataille, J.-B. Moussy, F. Paumier, S. Gota, M.-J. Guittet, M. Gautier-Soyer, P. Warin, P. Bayle-Guillemaud, P. Seneor, K. Bouzehouane, and F. Petroff. Cyrstalline γ-Al_2O_3 barrier for magnetite-based magnetic tunnel junctions. *Appl. Phys. Lett.*, 86:012509, 2005.

[85] W. Eerenstein, T. T. M. Palstra, T. Hibma, and S. Celotto. Diffusive motion of antiphase domain boundaries in Fe_3O_4 films. *Phys. Rev. B*, 68:014428, 2003.

[86] A. Thomas, J. S. Moodera, and B. Satpati. Evidence for positive spin polarization in Co with $SrTiO_3$ barriers. *J. Appl. Phys.*, 97:10C908, 2005.

[87] D. C. Worledge and T. H. Geballe. Negative spin-polarization of $SrRuO_3$. *Phys. Rev. Lett.*, 85:5182, 2000.

[88] M. Muenzenberg and J. S. Moodera. Superconductor-ferromagnet tunneling measurements indicate sp-spin and d-spin currents. *Phys. Rev. B*, 70:060402, 2004.

[89] T. H. Kim and J. S. Moodera. Large spin polarization in epitaxial and polycrystalline Ni films. *Phys. Rev. B*, 69:020403, 2002.

[90] C. Tiusan, J. Faure-Vincent, C. Bellouard, M. Hehn, E. Jouguelet, and A. Schuhl. Interfacial resonance state probed by spin-polarized tunneling in epitaxial Fe/MgO/Fe tunnel junctions. *Phys. Rev. Lett.*, 93:106602, 2004.

[91] E. Y. Tsymbal, A. Sokolov, I. F. Sabirianov, and B. Doudin. Resonant inversion of tunneling magnetoresistance. *Phys. Rev. Lett.*, 90:186602, 2003.

[92] G. Q. Gong, A. Gupta, G. Xiao, W. Qian, and V. P. Dravid. Magnetoresistance and magnetic properties of epitaxial magnetite thin films. *Phys. Rev. B*, 56:5096, 1997.

[93] J. M. D. Coey, A. E. Berkowitz, Ll. Balcells, F. F. Putris, and F. T. Parker. Magnetoresistance of magnetite. *Appl. Phys. Lett.*, 72:734, 1998.

[94] E. Goto, N. Hayashi, T. Miyashita, and K. Nakagawa. Magnetization and switching characteristics of composite thin magnetic films. *J. Appl. Phys.*, 36:2951, 1965.

[95] E. E. Fullerton, J. S. Jiang, M. Grimsditch, C. H. Sowers, and S. D. Bader. Exchange-spring behavior in epitaxial hard/soft magnetic bilayers. *Phys. Rev. B*, 58:12193, 1998.

[96] M. Ziese, R. Hohne, A. Bollero, H. C. Semmelhack, P. Esquinazi, and K. Zimmer. Size and shape dependence of the exchange-bias field in exchange-coupled ferrimagnetic bilayers. *Eur. Phys. J. B*, 45:38054, 2005.

[97] Y. Suzuki, R. B. van Dover, E. M. Gyorgy, J. M. Phillips, and R. J. Felder. Exchange coupling in single-crystalline spinel-structure (Mn,Zn)Fe_2O_4/$CoFe_2O_4$ bilayers. *Phys. Rev. B*, 53:14016, 1996.

[98] E. Snoeck, C. Gatel, R. Serra, G. BenAssayah, J.-B. Moussy, A. M. Bataille, M. Pannetier, and M. Gautier-Soyer. Experimental evidence of the spin dependence of electron reflections in magnetic $CoFe_2O_4$/Au/Fe_3O_4 trilayers. *Phys. Rev. B*, 73:104434, 2006.

[99] F. Canet, C. Bellouard, L. Joly, and S. Mangin. Magnetic behavior of exchange-coupled $Fe_{30}Au_{70}$/$Fe_{35}Au_{65}$ bilayers. *Phys. Rev. B*, 69:094402, 2004.

[100] H. Zijlstra. Coping with brown's paradox: The pinning and nucleation of magnetic domain walls at antiphase boundaries. *IEEE Transactions on Magnetics*, 15:1246, 1979.

[101] S. Maat, M. J. Carey, E. E. Fullerton, T. X. Le, P. M. Rice, and B. A. Gurney. Cobalt-oxide underlayers for cobalt-ferrite pinned spin valves. *Appl. Phys. Lett.*, 81:520, 2002.

[102] M. J. Carey, S. Maat, P. M. Rice, R. F. C. Farrow, R. F. Marks, A. Kellock, P. Nguyen, and B. A. Gurney. Spin valves using insulating cobalt ferrite exchange-spring pinning layers. *Appl. Phys. Lett.*, 81:1044, 2002.

[103] K. V. O'Donovan, J. A. Borchers, S. Maat, M. J. Carey, and B. A. Gurney. Neutron reflectivity on $CoFe_2O_4$ exchange springs for spin valve applications. *J. Appl. Phys.*, 95:7507, 2004.

[104] J. S. Moodera and G. Mathon. Spin polarized tunneling in ferromagnetic junctions. *J. Magn. Magn. Mater.*, 200:248, 1999.

[105] B. Ealet, M. H. Elyakhlouffi, E. Gillet, and M. Ricci. Electronic and crystallographic structure of γ-Al_2O_3 thin films. *Thin Solid Films*, 250:92, 1994.

[106] D. C. Worledge and T. H. Geballe. Magnetoresistive double spin filter tunnel junction. *J. Appl. Phys.*, 88:5277, 2000.

[107] U. Luders, A. Barthélémy, M. Bibes, K. Bouzehouane, S. Fusil, E. Jacquet, J.-P. Contour, J.-F. Bobo, J. Fontcuberta, and A. Fert. $NiFe_2O_4$: A versatile spinel material brings new opportunities for spintronics. *Adv. Mater.*, 18:1733, 2006.

[108] S. Datta and B. Das. Electronic analog of the electrooptic modulator. *Appl. Phys. Lett.*, 56:665, 1990.

[109] S. Sugahara and M. Tanaka. A novel spin transistor based on spin-filtering in ferromagnetic barriers: a spin-filter transistor. *Physica E*, 21:996, 2004.

[110] A. T. Filip, P. LeClair, C. J. P. Smits, J. T. Kohlhepp, H. J. M. Swagten, B. Koopmans, and W. J. M. de Jonge. Spin-injection device based on eus magnetic tunnel barriers. *Appl. Phys. Lett.*, 81:1815, 2002.

[111] Y. Ohno, D. K. Young, B. Beschoten, F. Matsukura, H. Ohno, and D. D. Awschalom. Electrical spin injection in a ferromagnetic semiconductor heterostructure. *Nature*, 402:790, 1999.

[112] R. Fiederling, M. Keim, G. Reuscher, W. Ossau, G. Schmidt, A. Waag, and L. W. Molenkamp. Injection and detection of a spin-polarized current in a light-emitting diode. *Nature*, 402:787, 1999.

[113] I. Appelbaum, B. Huang, and D. J. Monsma. Electronic measurement and control of spin transport in silicon. *Nature*, 447:295, 2007.

[114] P. R. Hammar, B. R. Bennett, M. J. Yang, and M. Johnson. Observation of spin injection at a ferromagnet-semiconductor interface. *Phys. Rev. Lett.*, 83:203, 1999.

[115] S. Gardelis, C. G. Smith, C. H. W. Barnes, E. H. Linfield, and D. A. Ritchie. Spin-valve effects in a semiconductor field-effect transistor: A spintronic device. *Phys. Rev. B*, 60:7764, 1999.

[116] G. Schmidt, D. Ferrand, L. W. Mollenkamp, A. T. Filip, and B. J. van Wees. Fundamental obstacle for electrical spin injection from a ferromagnetic metal into a diffusive semiconductor. *Phys. Rev. B*, 62:4790, 2000.

[117] E. I. Rashba. Theory of electrical spin injection: Tunnel contacts as a solution of the conductivity mismatch problem. *Phys. Rev. B*, 62:16267, 2000.

[118] A. Fert and H. Jaffrès. Conditions for efficient spin injection from a ferromagnetic metal into a semiconductor. *Phys. Rev. B*, 64:184420, 2001.

[119] S. Yuasa, A. Fukushima, H. Kubota, Y. Suzuki, and K. Ando. Giant tunneling magnetoresistance up to 410 percent at room temperature in fully epitaxial Co/MgO/Co magnetic tunnel junctions with bcc Co(001) electrodes. *Appl. Phys. Lett.*, 89:042505, 2006.

[120] Z. Qiu, J. Shang, X. Bi, S. Gong, and H. Xu. Study of electronic structure in $Co/Al_2O_3/Co$ heterostructures from first principles. *Acta. Mater.*, 52:533, 2004.

[121] K. D. Belaschenko, E. Y. Tsymbal, I. I. Oleynik, and M. van Schilfgaarde. Positive spin polarization in $Co/Al_2O_3/Co$ tunnel junctions driven by oxygen adsorption. *Phys. Rev. B*, 71:224422, 2005.

[122] C. Kim and Y.-C. Chung. First principles calculations on magnetic properties of interface-rippled Co/α-Al_2O_3/Co. *Appl. Phys. Lett.*, 88:132512, 2006.

PUBLICATIONS AND PRESENTATIONS

Publications in Refereed Journals

A. V. Ramos, S. Matzen, J.-B. Moussy, F. Ott, M. Viret, *"Artificial antiphase boundary at the interface of ferrimagnetic spinel bilayers"* Phys. Rev. B **79**, 014401 (2009).

A. V. Ramos, T. S. Santos, M.-J. Guittet, G.-X. Miao, J.-B. Moussy, J. S. Moodera, *"Influence of oxidation on the spin-filtering properties of $CoFe_2O_4$ and the resultant spin polarization"* Phys. Rev. B(R) **78**, 180402 (2008).

G. Müller, M. Djordjevic, M. Münzenberg, G.-X. Miao, A. Gupta, **A. V. Ramos**, K. Gehrke, V. Moshnyaga, K. Samwer, J. Schmalhorst, A. Thomas, G. Reiss, J. S. Moodera, *"Measuring the Spin Polarization in Half Metals by fs Spin Excitation"* Nature Materials **8**, 56 (2009).

G.-X. Miao, **A. V. Ramos**, J. S. Moodera, *"Infinite magnetoresistance from spin dependent proximity effect in BCC-Fe/V/Fe heteroepitaxial superconducting spin valves"* Phys. Rev. Lett. **101**, 137001 (2007).

C. Mocuta, A. Barbier, **A. V. Ramos**, M.-J. Guittet, J.-B. Moussy, S. Stanescu, R. Mattana, C. Deranlot, F. Petroff, *"Effect of optical lithography patterning on the crystalline structure of tunnel junctions"* Appl. Phys. Lett. **91**, 241917 (2007).

A. V. Ramos, M.-J. Guittet, J.-B. Moussy, R. Mattana, C. Deranlot, F. Petroff, C. Gatel, *"Room temperature spin filtering in epitaxial cobalt-ferrite tunnel barriers,"* Appl. Phys. Lett. **91**, 122107 (2007).

A. V. Ramos, J.-B. Moussy, M.-J. Guittet, M. Gautier-Soyer, C. Gatel, P. Bayle-Guillemaud, B. Warot-Fonrose, E. Snoeck, *"Influence of a metallic or oxide top layer in epitaxial magnetic bilayers containing $CoFe_2O_4$(111) tunnel barriers,"* Phys. Rev. B **75**, 224421 (2007).

A. V. Ramos, J.-B. Moussy, M.-J. Guittet, A. M. Bataille, M. Gautier-Soyer, M. Viret, C. Gatel, P. Bayle-Guillemaud, E. Snoeck, *"Magneto-transport properties of Fe_3O_4 epitaxial thin films: thickness effects driven by antiphase boundaries,"* J. Appl. Phys. **100**, 103902 (2006).

Conference Presentations

A. V. Ramos, J.-B. Moussy, R. Mattana, F. Petroff, T. S. Santos, G. X. Miao, J. S. Moodera, *"Spin-polarized tunneling study of the room temperature spin filter $CoFe_2O_4$,"* American Physical Society March Meeting, New Orleans (2008).

A. V. Ramos, J.-B. Moussy, R. Mattana, F. Petroff, *"Room temperature spin filtering with epitaxial $CoFe_2O_4$ tunnel barriers,"* Magnetism and Magnetic Materials Conference, Tampa (2007).

A. V. Ramos, J.-B. Moussy, M.-J. Guittet, F. Ott, M. Viret, C. Gatel, B. Warot-Fonrose, *"Magnétisme à l'interface des bicouches épitaxiées à base de $CoFe_2O_4$ (invité),"* Journées Nanomagnétisme, Saclay (2007).

A. V. Ramos, J.-B. Moussy, M.-J. Guittet, M. Gautier-Soyer, R. Mattana, F. Petroff, *"Epitaxial $CoFe_2O_4(111)$-based tunnel junctions for spin filter applications,"* International Conference on Nano Science and Technology, Stockholm (2007).

A. V. Ramos, J.-B. Moussy, M.-J. Guittet, M. Gautier-Soyer, F. Ott, M. Viret, C. Gatel, P. Bayle-Guillemaud, B. Warot-Fonrose, E. Snoeck, *"Croissance épitaxiale de couches minces et de multicouches à base de $CoFe_2O_4(111)$ en vue de leur utilisation comme filtre à spin,"* Colloque Louis Néel 11, Lyon (2007).

A. V. Ramos, J.-B. Moussy, M.-J. Guittet, M. Gautier-Soyer, *"Epitaxial $CoFe_2O_4(111)$-based multilayers for spin filter applications,"* American Phyical Society March meeting, Denver (2007).

A. V. Ramos, J.-B. Moussy, M.-J. Guittet, M. Gautier-Soyer, F. Ott, C. Gatel, P. Bayle-Guillemaud, B. Warot-Fonrose, E. Snoeck, *"$CoFe_2O_4(111)$/ $Fe_4O_4(111)$ bilayers grown by oxygen plasma-assisted molecular beam epitaxy for spintronics applications,"* European Conference on Surface Science, Paris

(2006).

A. V. Ramos, J.-B. Moussy, M.-J. Guittet, M. Gautier-Soyer, F. Ott, C. Gatel, P. Bayle-Guillemaud, B. Warot-Fonrose, E. Snoeck, *"Croissance épitaxiale de couches minces de $CoFe_2O_4(111)$ en vue de leur utilisation comme filtre à spin,"* Journées de la Matière Condensée 10, Toulouse (2006).

A. V. Ramos, J.-B. Moussy, M.-J. Guittet, M. Gautier-Soyer, *"$CoFe_2O_4$ thin films grown by oxygen plasma-assisted molecular beam epitaxy for spintronics applications,"* European Materials Research Society spring meeting, Nice (2006).

Invited Seminars

A. V. Ramos, *"Systèmes multicouches à base de $CoFe_2O_4(111)$ pour le filtrage de spin à température ambiante,"* CEA-Saclay DSM/IRAMIS/SPCSI, Paris (2008).

A. V. Ramos, *"Croissance épitaxiale de couches minces et de multicouches à base de $CoFe_2O_4(111)$ en vue de leur utilisation comme filtre à spin,"* Institut de Nano Sciences de Paris, Paris (2007).

A. V. Ramos, *"Epitaxial $CoFe_2O_4(111)$ for their potential integration into elementary spin filter devices,"* Francis Bitter Magnet Laboratory MIT, Cambridge MA (2006).